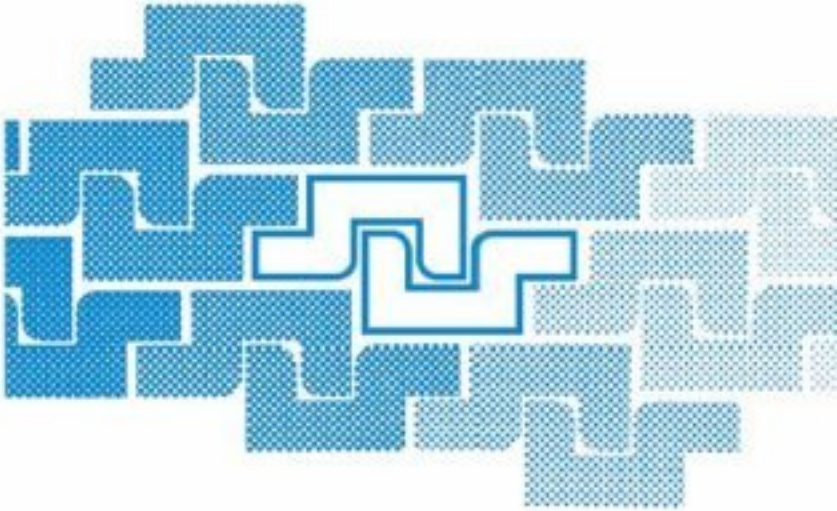

Carbon Nanotubes

Edited by

Valentin N. Popov
and Philippe Lambin

NATO Science Series

II. Mathematics, Physics and Chemistry – Vol. 222

Carbon Nanotubes

NATO Science Series

A Series presenting the results of scientific meetings supported under the NATO Science Programme.

The Series is published by IOS Press, Amsterdam, and Springer in conjunction with the NATO Public Diplomacy Division

Sub-Series

I. Life and Behavioural Sciences	IOS Press
II. Mathematics, Physics and Chemistry	Springer
III. Computer and Systems Science	IOS Press
IV. Earth and Environmental Sciences	Springer

The NATO Science Series continues the series of books published formerly as the NATO ASI Series.

The NATO Science Programme offers support for collaboration in civil science between scientists of countries of the Euro-Atlantic Partnership Council. The types of scientific meeting generally supported are "Advanced Study Institutes" and "Advanced Research Workshops", and the NATO Science Series collects together the results of these meetings. The meetings are co-organized by scientists from NATO countries and scientists from NATO's Partner countries – countries of the CIS and Central and Eastern Europe.

Advanced Study Institutes are high-level tutorial courses offering in-depth study of latest advances in a field.
Advanced Research Workshops are expert meetings aimed at critical assessment of a field, and identification of directions for future action.

As a consequence of the restructuring of the NATO Science Programme in 1999, the NATO Science Series was re-organized to the four sub-series noted above. Please consult the following web sites for information on previous volumes published in the Series.

http://www.nato.int/science
http://www.springer.com
http://www.iospress.nl

Series II: Mathematics, Physics and Chemistry – Vol. 222

Carbon Nanotubes: From Basic Research to Nanotechnology

edited by

Valentin N. Popov
Faculty of Physics,
University of Sofia,
Bulgaria

and

Philippe Lambin
Département de Physique,
Facultés Universitaires Notre-Dame de la Paix,
Namur, Belgium

Springer

Proceedings of the NATO Advanced Study Institute on
Carbon Nanotubes: From Basic Research to Nanotechnology
Sozopol, Bulgaria
21-31 May 2005

A C.I.P. Catalogue record for this book is available from the Library of Congress.

ISBN-10 1-4020-4573-5 (PB)
ISBN-13 978-1-4020-4573-8 (PB)
ISBN-10 1-4020-4572-7 (HB)
ISBN-13 978-1-4020-4572-1 (HB)
ISBN-10 1-4020-4574-3 (e-book)
ISBN-13 978-1-4020-4574-5 (e-book)

Published by Springer,
P.O. Box 17, 3300 AA Dordrecht, The Netherlands.

www.springer.com

Printed on acid-free paper

TABLE OF CONTENTS

Preface……... xi

Scientific Committee…….. xiii

Part I. Synthesis and structural characterization

Arc discharge and laser ablation synthesis of single-walled carbon nanotubes
B. Hornbostel, M. Haluska, J. Cech, U. Dettlaff and S. Roth …….1

Scanning tunneling microscopy and spectroscopy of carbon nanotubes
L. P. Biró and Ph. Lambin …….19

Structural determination of individual singlewall carbon nanotube
by nanoarea electron diffraction
E. Thune, D. Preusche, C. Strunk, H. T. Man, A. Morpurgo, F. Pailloux and A. Loiseau…..……..43

The structural effects on multi-walled carbon nanotubes
by thermal annealing under vacuum
K. D. Behler, H. Ye, S. Dimovski and Y. Gogotsi ……..……45

TEM sample preparation for studying the interface CNTs-catalyst-substrate
M.-F. Fiawoo, A. Loiseau, A.-M. Bonnot, A. Iaia, V. Bouchiat and J. Thibault ……..……47

A method to synthesize and tailor carbon nanotubes
by electron irradiation in the TEM
R. Caudillo, M. José-Yacaman, H. E. Troiani, M. A. L. Marques and A. Rubio ……..……49

Scanning tunneling microscopy studies of nanotube-like structures
on the HOPG surface
I. N. Kholmanov, M. Fanetti, L. Gavioli, M. Casella and M. Sancrotti 51

Influence of catalyst and carbon source on the synthesis
of carbon nanotubes in a semi-continuous injection
chemical vapor deposition method
Z. E. Horváth, A. A. Koós, Z. Vértesy, L. Tapasztó, Z. Osváth, P. Nemes Incze, L. P. Biró, K. Kertész, Z. Sárközi and A. Darabont ……...53

PECVD growth of carbon nanotubes
A. Malesevic, A. Vanhulsel and C. Van Haesendonck ……..……55

Carbon nanotubes growth and anchorage to carbon fibres
Th. Dikonimos Makris, R. Giorgi, N. Lisi, E. Salernitano, M. F. De Riccardis and D. Carbon 57

CVD synthesis of carbon nanotubes on different substrates
Th. Dikonimos Makris, L. Giorgi, R. Giorgi, N. Lisi, E. Salernitano, M. Alvisi and A. Rizzo 59

Influence of the substrate types and treatments on carbon nanotube growth by chemical vapor deposition with nickel catalyst
R. Rizzoli, R. Angelucci, S. Guerri, F. Corticelli, M. Cuffiani and G. Veronese 61

Non catalytic CVD growth of 2D-aligned carbon nanotubes
*N. I. Maksimova, J. Engstler and J. J. Schneide*r 63

Pyrolytic synthesis of carbon nanotubes on Ni, Co, Fe/MCM-41 catalysts
K. Katok, S. Brichka, V. Tertykh and G. Prikhod'ko ……..…...65

A Grand Canonical Monte Carlo simulation study of carbon structural and adsorption properties of in-zeolite templated carbon nanostructures
Th. J. Roussel, C. Bichara and R. J. M. Pellenq ……...…67

Part II. Vibrational properties and optical spectroscopies

Vibrational and related properties of carbon nanotubes
V. N. Popov and Ph. Lambin …….69

Raman scattering of carbon nanotubes
H. Kuzmany, M. Hulman, R. Pfeiffer and F. Simon …….…….89

Raman spectroscopy of isolated single-walled carbon nanotubes
Th. Michel, M. Paillet, Ph. Poncharal, A. Zahab, J.-L. Sauvajol, J. C. Meyer and S. Roth ……..…….121

Part III. Electronic and optical properties and electrical transport

Electronic transport in nanotubes and through junctions of nanotubes
Ph. Lambin, F. Triozon and V. Meunier …….123

Electronic transport in carbon nanotubes at the mesoscopic scale
S. Latil, F. Triozon and S. Roche ……143

Wave packet dynamical investigation of STM imaging mechanism using an atomic pseudopotential model of a carbon nanotube
Géza I. Márk, Levente Tapasztó, László P. Biró and A. Mayer ..……...167

Carbon nanotube films for optical absorption
E. Kovats, A. Pekker, S. Pekker, F. Borondics and K. Kamaras 169

Intersubband exciton relaxation dynamics in single-walled carbon nanotubes
C. Gadermaier, C. Manzoni, A. Gambetta, G. Cerullo, G. Lanzani, E. Menna and M. Meneghetti 171

Peculiarities of the optical polarizability of single-walled zigzag carbon nanotube with capped and tapered ends
O. V. Ogloblya and G. M. Kuznetsova ……...173

Third-order nonlinearity and plasmon properties in carbon nanotubes
A. M. Nemilentsau, A. A. Khrutchinskii, G. Ya. Slepyan and S. A. Maksimenko ……..……175

Hydrodynamic modeling of fast ion interactions with carbon nanotubes
D. J. Mowbray, S. Chung and Z. L. Mišković ……..……177

Local resistance of single-walled carbon nanotubes as measured by scanning probe techniques
B. Goldsmith and Ph. G. Collins ……179

Band structure of carbon nanotubes embedded in a crystal matrix
P. N. D'yachkov and D. V. Makaev ……..……181

Magnetotransport in 2-D arrays of single-wall carbon nanotubes
V. K. Ksenevich, J. Galibert, L. Forro and V. A. Samuilov ……..……183

Computer modeling of the differential conductance of symmetry connected armchair-zigzag heterojunctions
O. V. Ogloblya and G. M. Kuznetsova ……..……...185

Part IV. Molecule adsorption, functionalization and chemical properties

Molecular Dynamics simulation of gas adsorption and absorption in nanotubes
A. Proykova ……...……..187

First-principles and molecular dynamics simulations of methane adsorption on graphene
E. Daykova, S. Pisov and A. Proykova ……..……...209

Effect of solvent and dispersant on the bundle dissociation of single-walled carbon nanotubes
S. Giordani, S. D. Bergin, A. Drury, É. N. Mhuircheartaigh, J. N. Coleman and W. J. Blau ……..211

Carbon nanotubes with vacancies under external mechanical stress and electric field
H. Iliev, A. Proykova and F.-Y. Li ……..213

Part V. Mechanical properties of nanotubes and composite materials

Mechanical properties of three-terminal nanotube junction
determined from computer simulations
E. Belova and L. A. Chernozatonskii ……..……..215

Oscillation of the charged doublewall carbon nanotube
V. Lykah and E. S. Syrkin …….……...217

Polymer chains behavior in nanotubes: a Monte Carlo study
K. Avramova and A. Milchev ……..…….219

Carbon nanotubes as ceramic matrix reinforcements
C. Balázsi, F. Wéber, Z. Kövér, P. Arato, Z. Czigány, Z. Kónya, I. Kiricsi,
Z. Kasztovszky, Z. Vértesy and L. P. Biró ……..……..221

Carbon nanotubes as polymer building blocks
F. M. Blighe, M. Ruether, R. Leahy and W. J. Blau …….……...223

Synthesis and characterization of epoxy-single-wall
carbon nanotube composites
D. Vrbanic, M. Marinsek, S. Pejovnik, A. Anzlovar, P. Umek
and D. Mihailovic ..……..225

Vapour grown carbon nano-fibers – polypropylene composites
and their properties
V. Chirila, G. Marginean, W. Brandl and T. Iclanzan 227

Part VI. Applications

Nanotechnology: challenges of convergence, heterogeneity
and hierarchical integration
A. Vaseashta ……229

Behavior of carbon nanotubes in biological systems
D. G. Kolomiyets …….231

Molecular dynamics of carbon nanotube-polypeptide complexes
at the biomembrane-water interface
K. V. Shaitan, Y. V. Tourleigh and D. N. Golik …….…….233

Thermal conductivity enhancement of nanofluids
A. Cherkasova and J. Shan ……..235

Carbon nanotubes as advanced lubricant additives
F. Dassenoy, L. Joly-Pottuz, J. M. Martin and T. Mieno ……237

Synthesis and characterization of iron nanostructures inside
porous zeolites and their applications in water treatment technologies
M. Vaclavikova, M. Matik, S. Jakabsky, S. Hredzak and G. Gallios …….239

Nanostructured carbon growth by an expanding radiofrequency plasma jet
S. I. Vizireanu, B. Mitu, R. Birjega, G. Dinescu and V. Teodorescu ……...241

Design and relative stability of multicomponent nanowires
T. Dumitrică, V. Barone, M. Hu and B. I. Yakobson 243

Modeling of molecular orbital and solid state packing polymer calculations
on the bi-polaron nature of conducting sensor poly (p-phenylene)
I. Rabias, P. Dallas and D. Niarchos ……..245

Nd:LSB microchip laser as a promising instrument for Raman spectroscopy
V. Parfenov ……..247

Subject Index…...……...…… 249

Author Index……...…… 251

PREFACE

It is about 15 years that the carbon nanotubes have been discovered by Sumio Iijima in a transmission electron microscope. Since that time, these long hollow cylindrical carbon molecules have revealed being remarkable nanostructures for several aspects. They are composed of just one element, Carbon, and are easily produced by several techniques. A nanotube can bend easily but still is very robust. The nanotubes can be manipulated and contacted to external electrodes. Their diameter is in the nanometer range, whereas their length may exceed several micrometers, if not several millimeters. In diameter, the nanotubes behave like molecules with quantized energy levels, while in length, they behave like a crystal with a continuous distribution of momenta. Depending on its exact atomic structure, a single-wall nanotube –that is to say a nanotube composed of just one rolled-up graphene sheet– may be either a metal or a semiconductor. The nanotubes can carry a large electric current, they are also good thermal conductors.

It is not surprising, then, that many applications have been proposed for the nanotubes. At the time of writing, one of their most promising applications is their ability to emit electrons when subjected to an external electric field. Carbon nanotubes can do so in normal vacuum conditions with a reasonable voltage threshold, which make them suitable for cold-cathode devices. Nanotubes are also good candidates for the design of composite materials. They can increase the conductivity, either electrical or thermal, of polymer matrices which they are embedded in at a few weight percents, while improving the mechanical resistance of the materials. Most spectacular, but still far from industrialization, is the nanotube-based field-effect transistor. Here, a single-wall semiconducting nanotube, contacted to two electrodes, may block or may transmit an electric current depending on the potential applied to a gate electrode placed at near proximity. Many other applications are foreseen, among which nanoscopic gas sensing in which one property of the nanotube, sensitive to adsorbed molecules, is measured. Gas selectivity may be realized by a suitable functionalization of the nanotubes. Optical and opto-electronic properties of single-wall nanotubes are also promising for infra-red applications.

While the list of potential applications increases every month, the basic properties of intrinsic nanotubes are well documented and relatively well understood. Only relatively, because there remain several important open issues. Many-body effects, although predicted to occur in one-dimensional systems since a long time, are not clearly evidenced. Luttinger-liquid behavior,

for instance, is not fully recognized by experiments on metallic nanotubes. Excitons in semiconducting tubes constitute another topic of recent, sometimes controversial debates. More important, perhaps, the synthesis and growth mechanisms of the carbon nanotubes are not clearly pinned out. It is remarkable that these beautiful molecules can be produced in such many different physical and chemical conditions (electric arc discharge, catalytic chemical vapor deposition, laser ablation ...). Partly due to that, it is still not possible at the time of writing to produce nanotubes with all the same structure in a controllable way. Large-scale, but detailed characterization of the nanotubes, like with any other nanostructures, remains a great experimental challenge that will need to be overcame.

Whether or not nanotubes will have important industrial applications is not the essential point for the time being. What can be given for sure is that the carbon nanotubes have triggered an intense research activity thanks to which nanotechnology is developing so fast. The nanotubes are indeed ideal objects to deal with in this context before other nanostructures, perhaps, will supplement them and will open the way to real technological applications. In this book, many aspects of the nanotubes are either touched or described in details. The book is a snapshot, incomplete perhaps, of the state of the art at the time where the ASI took place, on the shore of the Black Sea.

We gratefully acknowledge the generous support from the NATO Scientific and Environmental Affairs Division and the University of Namur. We thank all authors for preparing high-quality manuscripts.

V. N. Popov
Sofia
Bulgaria

Ph. Lambin
Namur
Belgium

November 2005

ORGANIZING COMMITTEE

Co-Director

Prof. Philippe Lambin
Département de Physique
Facultés Universitaires Notre-Dame de la Paix
Namur, BELGIUM

Co-Director

Prof. Valentin Popov
Faculty of Physics
University of Sofia
Sofia, BULGARIA

Scientific Chairman

Prof. Hans Kuzmany
Universität Wien
Institut für Materialphysik
Wien, AUSTRIA

Scientific Advisor

Prof. Angel Rubio
Dpto. Fisica de Materiales
Facultad de Quimicas U. Pais Vasco
San Sebastian/Donostia, SPAIN

Scientific Advisor

Prof. Minko Balkanski
Université Pierre et Marie Curie
Paris, FRANCE

Part I. Synthesis and structural characterization

ARC DISCHARGE AND LASER ABLATION SYNTHESIS OF SINGLE-WALLED CARBON NANOTUBES

BJÖRN HORNBOSTEL,* MIRO HALUSKA, JIRKA CECH, URSULA DETTLAFF, SIEGMAR ROTH
Max-Planck-Institute for Solid-State Research, Stuttgart, Germany

Abstract. The laser ablation synthesis of carbon nanotubes is contrasted with the arc discharge method with respect to the synthesis product. A novel combination of two laser systems of different wavelengths for the laser ablation synthesis is presented. The impact of sulfur on the synthesis process is discussed. An excerpt of our quality control protocol is presented.

Keywords: single-walled carbon nanotubes; laser ablation; arc discharge; synthesis; CO_2; Nd:YAG; sulfur; quality control protocol

1. Introduction

The prospects for a wide range of applications of single-walled carbon nanotubes (SWCNT, SWNT) rely on the development of a cost-effective large-scale production. The three main roots for SWNT synthesis are laser ablation (LA), arc-discharge (arcD)[1-3] in a Krätschmer[4] reactor, and chemical vapor deposition (CVD). Besides these, there are plenty of scions where different methods merge into each other, other ambient conditions are used (e.g., submerged arcD[5-8]) or where other supporting energy sources sustain (e.g. PE-CVD[9-12]). Here, only the laser ablation and the standard Krätschmer arc discharge method are regarded. These two synthesis methods in plasma aggregate state rely on the presence of a catalyst for the production of SWNT.

Historically, the arcD method was the first technique for multi-walled carbon nanotubes[1] (MWCNT, MWNT) and single-walled carbon nanotubes.[2,3] By this method one is able to produce roughly 100 mg/min of SWNT-containing soot. However, due to highly fluctuating conditions in the plasma

*To whom correspondence should be addressed. Björn Hornbostel; e-mail: b.hornbostel@fkf.mpg.de

V.N. Popov and P. Lambin (eds.), Carbon Nanotubes, 1–18.

plume of the light arc it is difficult to keep a favorable condition for a long period. There are attempts to keep the conditions stable, which is essential for the production of flawless nanotubes at a high yield. Biggest drawback of the Krätschmer method is the relative high amount of undesired by-products, as fullerenes, graphite and amorphous carbon (a-C).

In 1995 Guo et al.[13] synthesized nanotubes by laser ablation for the first time. The usage of concentrated light directed on a target to evaporate material and to create highly reactive plasma is a mean to engender more controlled conditions in the plume. In the following we will present our way to synthesize SWCNT by ArcD and LA. Therefore, we will recapitulate the state of the art and our own experiences with both methods. Firstly, we will elaborate on the technical equipment and parameters. Later we will describe briefly how we evaluate as-produced and purified SWCNT material by our quality control protocol.

2. Technology and experimental

2.1. DC ARC DISCHARGE TECHNOLOGY

Between a pair of graphite electrodes in an inert gas atmosphere a DC electric arc discharge is ignited by e.g. a short contact between both. As a result, electrons exit from the cathode and form an electron cloud. At this time the voltage is still zero. As dissociating both from each other the resulting empty space between them is filled up by electrons and by the ambient gas. The electrons are accelerated towards the anode and on their way they ionize the gas molecules cascade-like by impact ionization. Positive charge carriers move to the negative counter pole. As soon as enough charge carriers are situated in the conducting channel, the arc ignites. At the moment of electrode separation the voltage source has to deliver full voltage. The incoming electrons give up their kinetic energy to the anode which causes the material to sublimate. The cathode will be cooled by discharge work of the electrons. The electrodes are typically water-cooled graphite rods separated by few mm. A bias voltage of 15 to 35V is applied at currents between 50 and 120A.

Achieving stable discharge plasma is the main factor in generating an environment favorable to nanotube growth. This is not so easy, as the anode is consumed and therefore has to be tracked towards the cathode continuously. Furthermore, the stability of an electric arc is limited due to its moving nature on the cathode and anode surface. Additionally, after already a few minutes the resulting uneven consumption of the anode and build-up of material on the cathode side causes a further instability in the DC arc. The rate of synthesis of a lab Krätschmer reactor can surpass 100 mg/min.

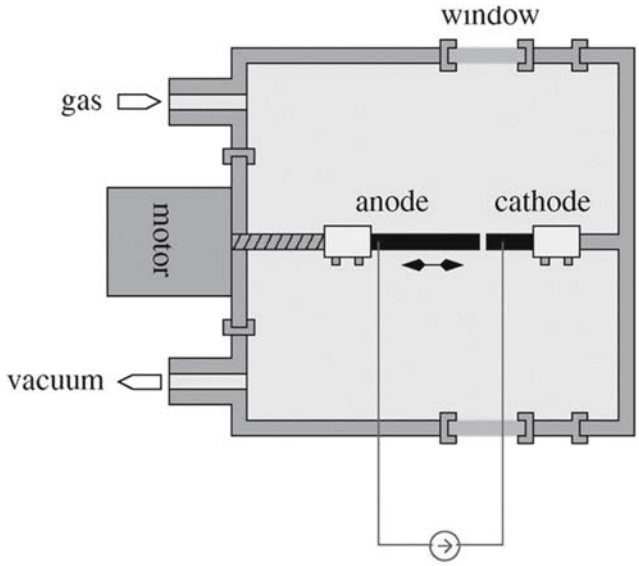

Figure 1. Schematic of a standard DC Krätschmer reactor (arc discharge).

A vast amount of studies on the fundamental technical parameters to optimize the arcD method has been accomplished and people are still working on it. Apparently, the yield and the properties of the nanotubes are not just dependent on the anode composition, the background gas pressure, the gas composition, ... but also linked to the apparatus size and its geometry, the thermal gradients and other influences of the sublimation system. Due to sometimes total different results (yields) at same parameter sets in different reactors it is hard to deduce a general rule for an optimized production.

2.2. ARC DISCHARGE PARAMETERS

The catalysts can be introduced by either drilling a hole into the anode or filling it up with a catalyst-carbon mixure or by intermixing a larger portion of C and catalyst and then pressing to a rod. As for the laser ablation (LA) it was found that using bi-material plus C mixtures of Co, Ni, Y, and Fe favors the production of larger quantities of SWNT. Furthermore, people agree upon Co/Y and Ni/Y intermixtures being the most effcient. Recently, Itkis et al.[14] published their results on optimum anode compositions.

Helium at around 500-800 mbar is most favorable for the SWCNT-production. Additional gases (e.g. H_2) or substances (e.g. S) are able to influence the yield, the diameter distribution and the quality of the product. We currently exploit the advantage of sulfur in the process.

In the arc discharge production method sulfur functions as a SWNTs growth promoter and surfactant when added together with Ni/Fe/Co,[15] Ni/Co,[15,16] Ni/Y/Fe or Ni/Ce/Fe[17] catalysts into the anode. Sulfur is used as promoter in other nanotube production methods as well, like in the solar energy evaporation method[18] with Ni/Co and in the laser vaporization method[19] with Ni/Co/Fe. It was found that sulfur alone without metal catalysts does not catalyze the SWNTs growth process.[20]

Typically for all methods mentioned and all catalysts used, the addition of sulfur increases the yield of nanotubes and broadens the tube diameter distribution to extend out to 6 nm. Exception is the formation of nanotubes with small diameters in the range of 0.9-1.1 nm as reported by Alvarez et al.[18]

Our work is focused on the influence of the S concentration added to Fe/Y catalysts on the yield of nanotubes and their properties. We chose Fe instead of Ni because it is much easier to remove it from the arc product. Our primary aim is to find satisfactorily high yields of high quality SWNT web material. One of the growth controlling parameters is the distance of the electrodes during the arc process. It influences the evaporation rate (temperature of anode) and the yield of web product. The highest the yield was obtained for the distance ~ 2 mm. The anode evaporation rate was 1.2 g/min.

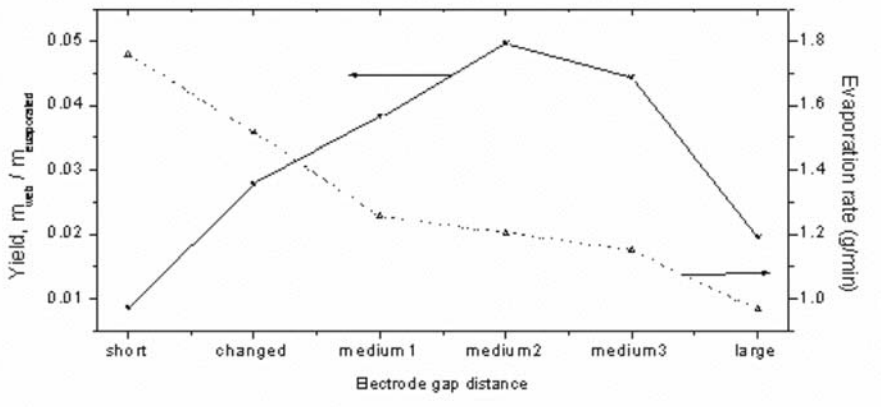

Figure 2. The yield and the evaporation rate dependences on the electrode gap distance.

As it was discussed in the above mentioned publications sulfur does not dissolve in the bulk of the transition metals but adsorbs on the surface. The metal-sulfur interactions change surface tension and melting point of small droplets of metals. This can support the creation of SWNTs for metals which in pure form catalyze badly. The overcritical concentration of S has a poisoning effect on SWNTs growth similar as for many other catalytically controlled processes. The highest yield of web product containing the smallest

concentration of metals was obtained for the sample C where the composition of the anode is Fe:Y:S:C 6.6 at.%:1.1 at.%:1.6 at.%:90.7 at.%. A more detailed overview on this work is presented in.[21]

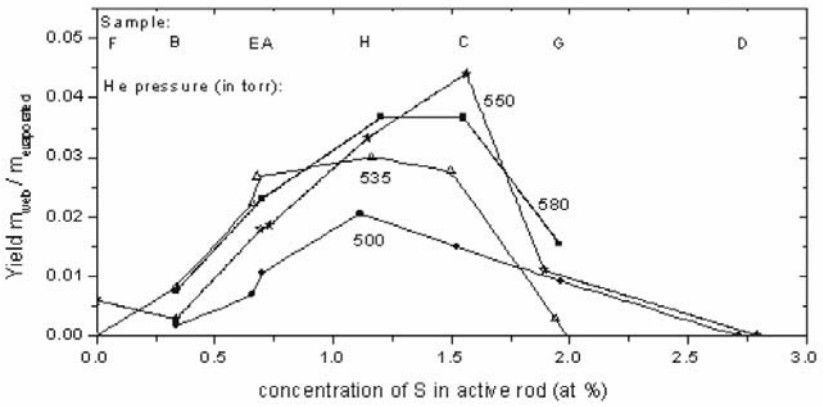

Figure 3. The yield dependence over the concentration of sulfur.

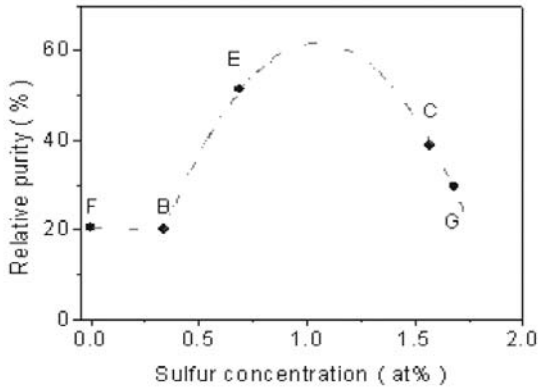

Figure 4. The relative purity determined by NIR-spectroscopy.[13,14] A dashed line depicts the trend. Sulfur was used to attain better results. The background pressure was 550mbar.

2.3. LASER ABLATION TECHNOLOGY

The standard SWNT growth setup consists of a quartz tube (~25 mm diameter, 1000-1500mm length) mounted inside a hinged tube furnace that can operate at a temperature of 1200°C. The quartz tube is sealed to vacuum components. The laser beam enters the quartz tube through a Brewster window, which should be

plated by some anti-reflex layer for the incoming beam. Inert gas, e.g., Argon, or mixed gas compositions are introduced at the upstream side of the tube. The gas feeding is controlled by a mass flow controller and the pressure by a preassure controller downstream. Before the gas exits the system it passes a water-cooled brass collector and a filter to collect the SWNTs. The brass collector is inserted into the quartz tube and positioned just outside the furnace. A rotating rod is led through the water-cooled collector. A target consisting of carbon and metall catalysts is attached to it. This is to ensure a more homogenious ablation of the target. In addition it is appropriate to have the laser beam scanning over the target. The carrier gas-flow sweeps most of the carbon species produced by the laser evaporation out of the furnace zone depositing it as soot on a water-cooled copper rod. Usually the ablation laser is a Nd:YAG opperating at 1064 nm or 532 nm, respectively. Specific values of those Nd:YAG systems are between 300 mJ and 1.5 J per pulse at <10 ns FWHM. The beam is usually focused to a 3-8 mm diameter spot.

A different approch for laser synthesis of SWCNT is the exertion of CO_2-laser.[21-25] Here, laser ablation at 10.6 μm, with 250W and a spot size of 0.8-1mm produces a notable quantity of carbon nanotubes. Maser et al.[26] reported a maximum ablation rate of 200 mg/h. In case of a pure CO_2-laser process a furnace is not inevitably necessary. The energy for the evaporation of the targert can be delivered completely by the beam itself. Maser et al.[26] found no big difference betweeen Nd:YAG and CO_2-laser systems concerning yields and structural characteristics of the produced SWNT. However, they consider the scaling-up possibility of CO_2-laser systems to be easier by far.

The fundamental limitation which is inherent to today's laser ablation systems is their restriction of milligram-quantity per day. This is far too low to sustain more than laboratory-scale levels of development. Thess et al.[27] reported optimization of a Nd:YAG-Laser ablation process. The initial laser pulse (532 nm, 250 mJ, 10 Hz, 5 mm diameter spot) was followed 50 ns later by a second pulse (1064 nm, 300 mJ, 10 Hz, in a 7 mm diameter spot coaxial with the first laser spot). This provides a more uniform evaporation of the target resulting in increased SWNT yields. They used a 25mm-diameter quartz tube. Since the SWNT production rate of this laser-oven set-up was only 80 mg/day, Rinzler et al.[28] scaled it up by more powerful laser systems. They found that the generation of material containing more than 50 vol.% SWNTs requires a geometry which mimics the original 25mm-diameter tube. They added a 25mm-diameter quartz tube coaxial with the 50mm-tube extending from 4 mm ahead of the graphite target. The SWNT yield soared up 90 vol.% and an amount of 1g/day carbonaceous nano-material could be synthesized. This configuration of the set-up enables the evaporation plume to be lifted off from the target and to

extend far within the 25 mm tube. Nucleation and SWNT growth could now be carried out inside this tube.

Kingston et al.[29] were able to enhance the yield considerably by using two Nd:YAG lasers, one (1.5J) operating in the pulsed-mode to ablate and the other one in cw-mode to alter the rate of cooling of the condensing plume. The synthesis rate of black soot surpassed 400mg/h.

Our set-up consists also of two different laser systems. For the first time (as much as we know) a Nd:YAG and a small 100W cw-CO_2-laser are used simultanously. While the Nd:YAG (1.0J, 1064nm, 20Hz, 7ns) is used to ablate material from the target, the CO_2-laser systems is meant to influence the cooling of the condensing plume as the cw-laser does in Kingston's et al. system. We use a 40mm-diameter quartz tube as reaction chamber and the already above mentioned 25mm coaxial inner tube.

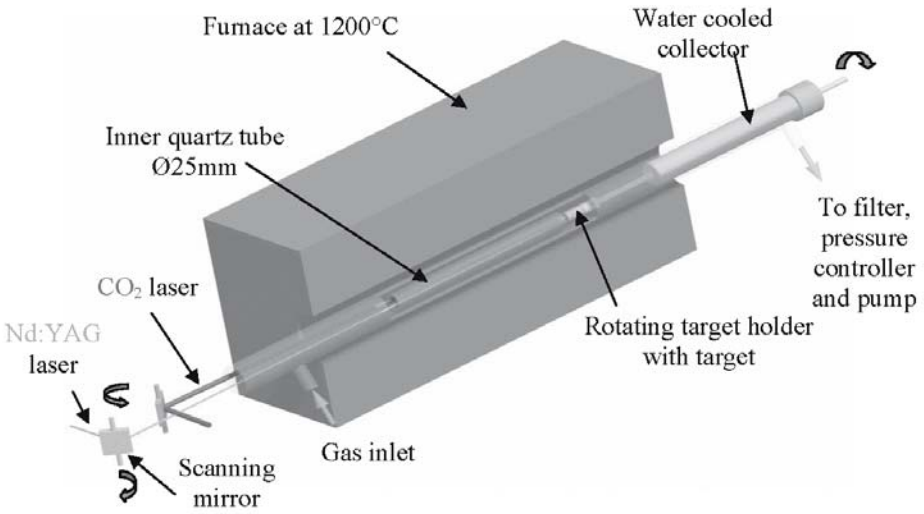

Figure 5. A novel LA set-up using a CO_2 and a Nd:YAG laser system simultaneously. Mass flow and pressure control units as well as auxiliary devices are not depicted in this schematic.

2.4. LASER ABLATION PARAMETERS

The flow in the reaction tube should be kept constant in the range between 100 and 350 sccm. While ablating a pressure of 250 to 550 Torr is to be maintained. Below 100 Torr the formation of amorphous carbon is favored. Munoz et al.[23] observed gas and pressure effects on the local temperature conditions. Using pure helium no SWNT are formed. Helium and light gases are more efficient for cooling so that the resulting temperature gradient is too large to favor

SWNT growth. In opposition, argon and nitrogen are heavy enough to keep the temperature gradient at a point where suitable growth conditions prevail. Increasing the pressure above 400 Torr will soar-up the collision propability of the evaporated material with the gas molecules. This will diminish the capabiltity of SWNT forming.

Adding no catalyst to the graphite target no SWNT will be formed. In case of a small amout of Ni or other metal given to the target SWNT-forming will occur. Possible transition metals may be Ni > Co >> Fe > Pt, where yields decrease by a few percent in the same order. The synthesized tubes are few, isolated and often covered by a-C. In case of a bi-material combination a web-like structure is produced where thick and relatively clean bundels of SWNT can be observed. Yields may be over a hundred times higher than achieved with one-dopant targets. Guo et al. found the following sequence for bi-material compositions and Nd:YAG systems: Ni/Co ~ Co/Pt > Ni/Pt >>Co/Cu. Munoz et al.[24] examined bi-material mixtures for CO_2-laser systems and concluded Ni/Co~Ni/Y>>Ni/Fe~Ni/La~Co/Ni.

For our initial experiments we use mainly Ni/Y (4.2at.%/1at.%), Ni/Y (2at.%/0.5at.%) and Ni/Co (2at.%/2at.%) plus carbon compositions. One target is around 8g in weight. The very dryed mixture is mixed by a tooth-pick first before we put it into a tumbling machine for at at least 48h to assume a macroscopic homogenious intermixture. Afterwards a 15mm-diameter pellet is pressed in a 150°C warm tool at 8kN. The optimum operation parameters of our laser-furnace set-up, concerning preassure, carrier gas, flow and temperature as well as applied laser power will be puplished elsewhere as soon as our experiments are completed. Our momentary production record at a quite acceptaple quality is at 200mg/h without S. With only Nd:YAG we attchieved only 60mg/h. This is a triplication of the production rate. The composition of the target was C:Ni:Co 96 at.%: 2 at.% : 2 at.%. The pure Ar gas flow was controlled to be 350 sccm.

3. Synthesis product evaluation

Our experience is that a highly optimized process for arcD may yield up to 55 vol.% SWNT. The ArcD process delivers in contrast to LA rather short carbon nanotubes (some microns) with a quite broad diameter distribution. Laser ablated SWNTs are remarkably uniform in diameter and self-organized into bundles via van-der-Waals forces. Consisting of 100 to 500 SWNTs, their diameters range from 10 to 20 nm and their lengths can reach values between 10 and some 100 μm. In the synthesis of arcD tubes quite low defect densities can be observed. The high temperatures in the plasma usually ensure a complete closure of the tube lattices. An even lower defect density can be expected in

single-walled nanotubes produced in the laser ablation set-up. Here, the few and minor fluctuations in the process conditions are less important. The more stable conditions are also the reason for the longer, more identical tubes and for the higher purity. The energy in the arcD process is high enough to evaporate the material carefully. But due to the alternating conditions a favorable condensation of the material is hindered. By TEM one can observe structural differences between both synthesis products concerning the catalysts: ArcD tubes usually encase the catalyst particle with which help the tube grows. In LA material it is more common to have the particle somewhere in the soot but not encased or attached to the tube. For getting rid of the catalyst content in the end-product more easily this cartelistic is opportune.

The production rate in the arcD is by far higher. While the rate of an arcD process is usually measured on the 100 mg/min scale the production rate in the LA is expressed by the 10mg/h or 100mg/h scale. But one has to keep in mind that the yield of SWNT in the as produced arcD soot does not surpass 55 vol.% today. Of course, today it is not possible to produce SWNT of LA quality by ArcD.

There are possibilities to clean the soot from all unwanted content, like catalysts, a-C, fullerenes and graphite by purification. However, according to our experiences so far, this might be applicable for small quantities or for a-C and fullerenes but in case of an overall purification and a mass production these cleaning steps for arcD material would turn out to be the most cost intensive. Furthermore, by running through certain purification steps, not just the unwanted material will be attacked but also the SWNTs will be harmed to some extent.

Quality characterization in the SWNT field is a complicated issue. To ensure the comparability of our measurements we have been working on a protocol for quality control of single-walled carbon nanotube material. This protocol is regularly updated.[30] The momentary version of the protocol includes standards for homogenization, bucky paper preparation, composites, electrical, x-ray diffraction SEM, TEM, optical spectroscopy and Raman measurements. We stress the importance of working with large homogenized batches (Presently, we use 100 g batches of ArcD material, whenever possible). A short excerpt of our protocol is presented here.

3.1. ELECTRICAL MEASUREMENTS

Figure 6 shows a simple device to measure the conductivity of bucky papers and of thin composite films using the 4 leads method. A strip punched off from a bucky paper or a composite film is placed under the two outer (current) electrodes and held with 5 mm wide clamps. Two inner (voltage) electrodes

with 10mm distance are put onto the sample orthogonally to the surface and pressed with a constant force of 0.6 N. To this end a weight made of a stainless steal block is placed on the body holding and separating the measuring electrodes (insulating PTFE/PE, 10^{18} Ωcm).

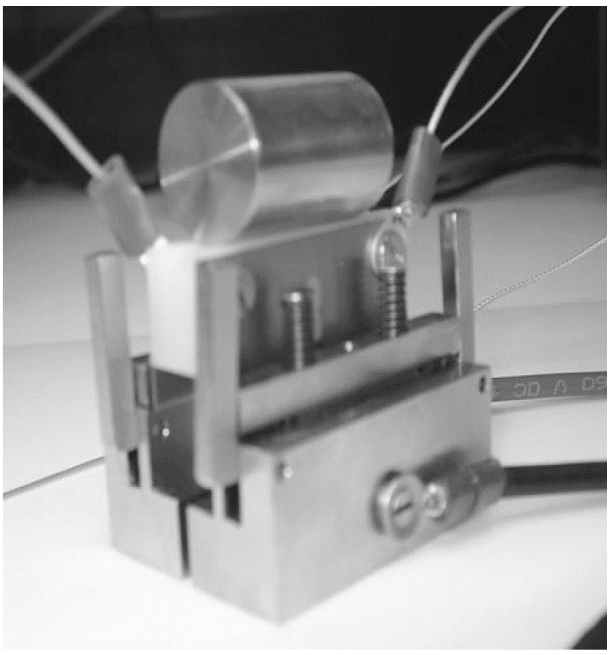

Figure 6. Device to measure the electric conductivity with the four-leads-method.

Measurement: Constant current (mA) is applied to determine the voltage drop between the inner electrodes. The thickness of the strip (usually between 60 and 100 µm) is measured. At least three strips of one bucky paper should be measured to estimate the mean electrical conductivity and the standard deviation. The conductivity[1] is calculated as follows:

$R = \Delta U / I$	
$\sigma = 1/R \cdot L/(T*W)$	≈ conductivity in Siemens per centimeter [S/cm = $(\Omega cm)^{-1}$]
L = 10 mm	≈ distance between the inner electrodes (constant)
W = 2 or 5 mm	≈ width of the sample (constant)
T	≈ lowest thickness of the bucky paper strip

[1] Remark: A strong scattering of the conductivity values (larger than 15%) is evidence of problems in the preparation of bucky paper and the preparation should be repeated.

3.2. ELECTRON MICROSCOPY

Note that electron microscopy (SEM and TEM) is not well suited to characterise large batches. Sample preparation and image evaluation is very "selective", i.e. the result depends on the skill and patience of the spectroscopist and on what he hopes to see. Usually "best" data are shown rather than "representative" data. But the methods are very useful to check whether in a particular sample "there are nanotubes at all". When new synthetic routs for nanotube production are developed, SEM very often gives the first positive hint of success. SEM characterization can be carried out on powder deposited on the sticky side of scotch tape or on a bucky paper.

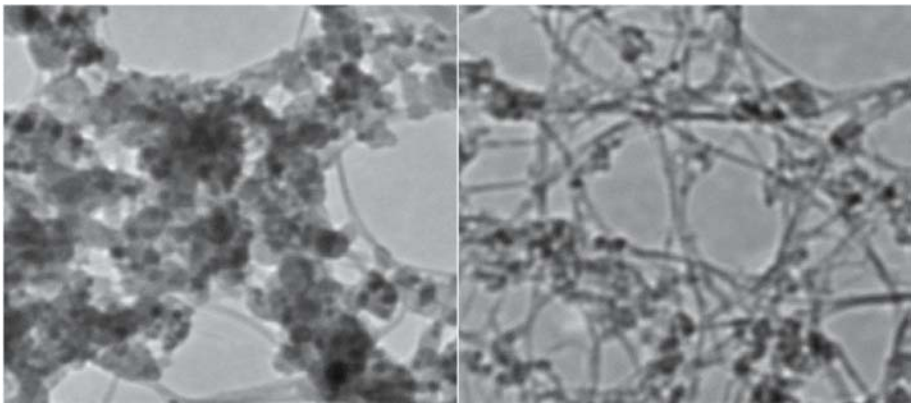

Figure 7. Visual comparison of SWNT-material produced by ArcD (left) and LA (right). Both TEM-pictures were taken at same magnification. In the ArcD material dirt and irregular large particles are clearly recognizable.

3.3. X-RAY POWDER DIFFRACTION

We execute x-ray measurements in two ways. The first one is to use a Lindeman tube. Here, the nanotube powder is filled into a Lindeman tube (thin glass capillary, as commonly used for X-ray powder diffraction), diameter 0.3 or 0.5 mm. The second possibility is to use a flat bed sample holder. About 5 mg of powder is distributed on a scotch tape and put into the sample holder. Both sample holders rotate while measuring. Fig. 8 (left) shows a typical powder diffractogram of carbon arc material after various purification steps (Copper Kα radiation, 20 minutes exposure time, Lindeman tube, multidetector). If there are nanotube bundles in the sample, a peak will show up at 6°, which originates from the triangular lattice of the tubes in the bundle (lattice constant about 10 Å). The central curve shows a slight indication of such a peak. The peak at ~26° corresponds to graphite. At higher scattering angles there are the peaks of metal (raw material) or metal oxides (after heating

in air). For quantitative measurements the SWNT material is mixed in a ratio of 1:1 with fullerene C_{60}. X-ray powder diffraction patterns are recorded using the flat bed method (By filling into a Lindeman tube the sample would de-mix). The area of the graphite peak at 26° is compared with that of the second fullerene peak at 16° (which is used as a marker).

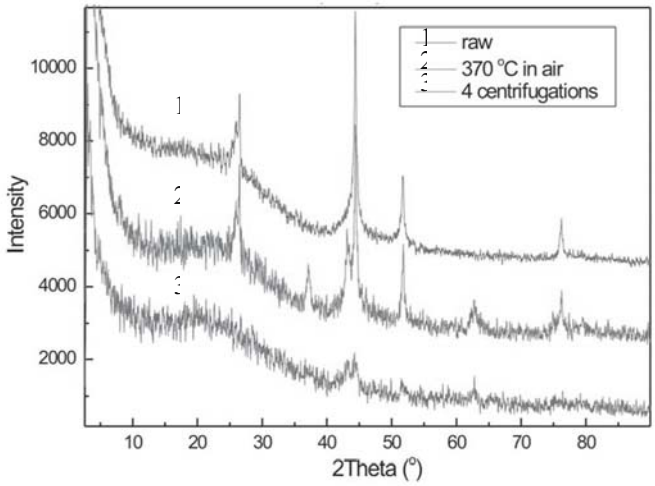

Figure 8. A typical powder diffractogram of ArcD material after various purification steps.

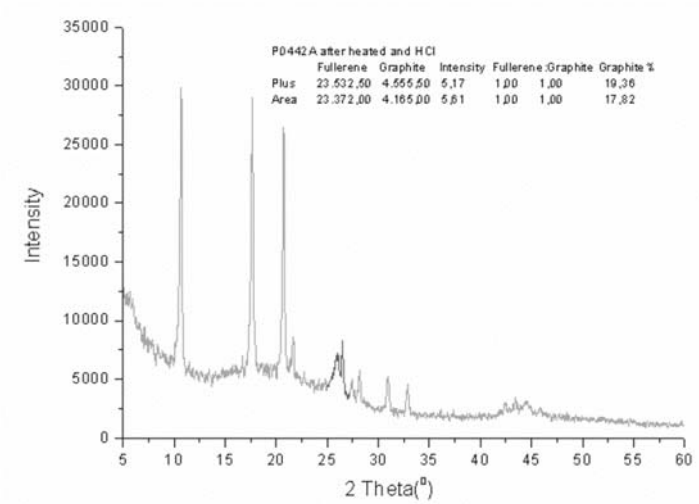

Figure 9. The pattern of a sample with unknown graphite concentration is shown. Now the peak area between graphite and fullerene marker compare like 1 to 5, indicating that the sample contains about 20% of graphite contamination (In addition to crystalline graphite there probably also is an important contamination of turbostratic graphite leading to the broad peak between 15° and 25°).

3.4. OPTICAL SPECTROSCOPY

For a first orientation, absorption spectra of films sprayed onto a glass substrate are useful. Therefore, SWNTs are suspended in 1% SDS aqueous solution and sprayed onto microscope slides using the airbrush technique. Fig. 9 shows the spectrum of SWCNT after subtraction of an appropriate baseline. The peaks are assigned to transitions between the van Hove spikes in the electronic density of states of nanotubes. S11 and S22 are related to semi-conducting tubes and M11 originates from metallic tubes. S11 depends very much on the chemical environment of the sample (e.g. doping) and is not well suited for a quantitative analysis. The background is due to carbonaceous by-products, like amorphous carbon and graphitic particles, and also to excitations in the nanotubes themselves (but not directly related to the van Hove spikes). For a quantitative analysis we follow Itkis et al. method.[30,31] This analysis only yields relative nanotube concentrations, relative to a standard of known concentration. For ArcD material we use the standard ($A(S_{22})/A(T) = 0.141$) published in.[31] For LA material we use $A(S_{22})/A(T) = 0.211$, a value which we measured on some material which was delivered by FZ Karlsruhe (Germany) and purified by ourselves. NIR spectroscopy and electrical measurements in bucky paper correlate well as can be seen in Figure 10.

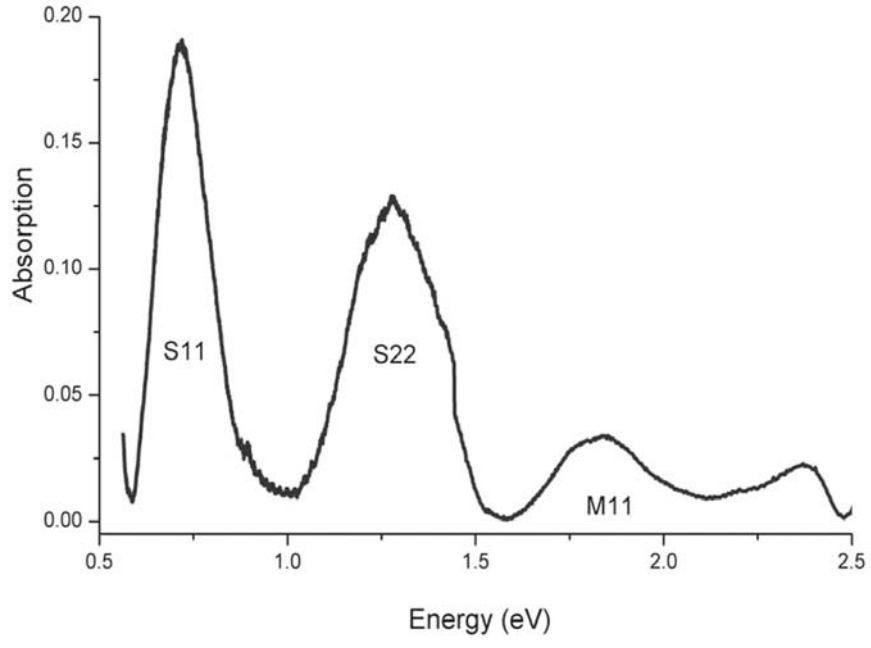

Figure 10. Spectrum of SWCNT after the subtraction of a proper baseline.

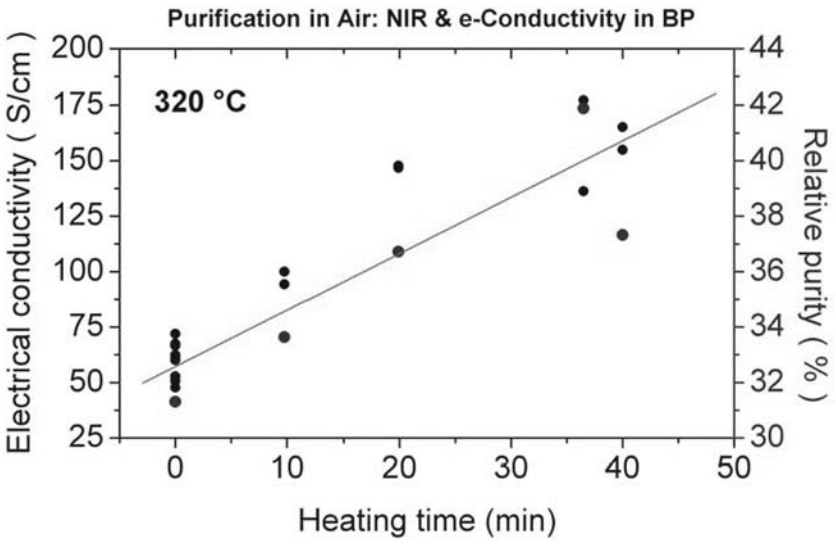

Figure 11. NIR spectroscopy in solution and electrical measurements in bucky paper correlate well. Here we purified ArcD material in a hot furnace at a set temperature for differently long periods.

3.5. RAMAN SPECTROSCOPY

Figure 12 shows a Raman spectrum measured by a Raman microscope, excitation line $\lambda = 632$ nm. The double line at ≈1600 cm^{-1} is the so called G-line coming from the stretching of conjugated double bonds. The lines around 200 cm^{-1} are from the radial breathing mode (RBM) and depend on the nanotube diameter, the line at 1300 cm^{-1} (D-line) is from the multiple phonon scattering and from the nanotubes defects. Spectra are normalized to the D*-mode (2600 cm^{-1}). Note that Raman spectra are resonance enhanced and depend very much on the excitation line. For our believe, Raman spectra are not useful for quantitative analysis, but the intensity of the D-line is often taken as evidence of many defects on the tube or of the presence of amorphous carbon in the sample. In addition, like SEM and TEM images, Raman spectra often give the first hint of the presence of single-walled carbon nanotubes in a sample and then justify further investigations.

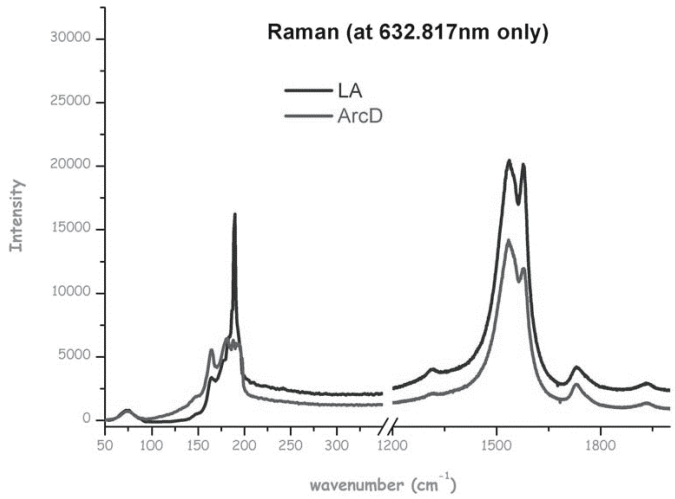

Figure 12. Raman lines from ArcD and LA material at 632.817nm. LA nanotubes have a narrower diameter distribution.

4. Summary

In comparison to the laser ablation method, the arc discharge SWCNT synthesis is still the most efficient method to produce large quantities of nanotubes. Additionally, it is also the most widly used one which also traces back to the relative simple basic set-up. In combination of optimized process parameters and additional ingredients like sulfur yield and quality can be influenced positively. Although the relative amount of SWCNT in the soot can be increased by varying the process parameters and by gas/ingredient variations the synthesis process regime is difficult to control. Hence, in case of need for very pure material with a narrow diameter distribution the laser ablation method is the process of choice. Our approach to use a Nd:YAG system at 1064nm and a CO_2 system at 10.6 microns simultaneously is already capable to triple the production rate to 200mg/h. A main question is whether laser ablation may ever be a synthesis method to produce bulk quantities or if it stays a method for nanotubes for specialized applications. For the evaluation of SWNT material we developed a protocol[34] which is regularly updated. It is one of the most important means for our work on synthesis and purification.

References

1. S. Iijima, Helical microtubules of graphitic carbon, *Nature* 354, 56–58 (1991).
2. S. Iijima and T. Ichihashi, Single-shell carbon nanotubes of 1-nm diameter, *Nature* 363, 603–605 (1993).
3. D. S. Bethune, C. H. Kiang, M. S. de Vries, G. Gorman, R. Savoy, J. Vazquez, and R. Beyers, Cobalt-catalysed growth of carbon nanotubes with single-atomic-layer walls, *Nature* 363, 605–607 (1993).
4. W. Krätschmer, L. O. Lamb, K. Fostiropoulos, and D. R. Huffman, Solid C60: a new form of carbon, *Nature* 347, 354–358 (1990).
5. Y. L. Hsin, K. C. Hwang, F.-R. Chen, and J.-J. Kai, Production and *in-situ* metal filling of carbon nanotubes in water, *Advanced Materials* 13(11), 830-833 (2001).
6. H. W. Zhu, X. S. Li, B. Jiang, C. L. Xu, Y. F. Zhu, D. H. Wu and X. H. Chen Formation of carbon nanotubes in water by the electric-arc technique. *Chem. Phys. Lett.* 366, 664-669 (2002).
7. H. Lange, M. Sioda, A. Huczko, Y. Q. Zhu, H. W. Kroto and D. R. M. Walton, Nanaocarbon production by arc discharge in water, *Carbon* 41, 1617-1623 (2003).
8. L. P. Biró, Z. E. Horváth, L. Szalmás, K. Kertész, F. Wéber, G. Juhász, G. Radnóczi and J. Gyulai, Continuous carbon nanotube production in underwater AC electric arc, *Chemical Physics Letters* 372, 399-402 (2003).
9. Ch. Bower, O. Zhou, W. Zhu, D. J. Werder, and S. Jin, Nucleation and growth of carbon nanotubes by microwave plasma chemical vapor deposition, *Applied Physics Letters* 77, 2767-2769 (2000).
10. M. Chhowalla, K. B. K. Teo, C. Ducati, N. L. Rupesinghe, G. A. J. Amaratunga, A. C. Ferrari, D. Roy, J. Robertson, and W. I. Milne, Growth Process Conditions of Vertically Aligned Carbon Nanotubes Using Plasma Enhanced Chemical Vapor Deposition, *J. Appl. Phys.* 90(10), 5308-5317 (2001).
11. L. Delzeit, C. V. Nguyen, R. M. Stevens, J. Han, and M. Meyyappan, Growth of carbon nanotubes by thermal and plasma chemical vapour deposition processes and applications in microscopy, *Nanotechnology* 13, 280-284 (2002).
12. J. Han, J.-B. Yoo, C. Y. Park, H.-J. Kim, G. S. Park, M. Yang, I. T. Han, N. Lee, W. Yi, S. G. Yu, and J. M. Kim, Tip Growth Model of Carbon Tubules Grown on the Glass Substrate by Plasma Enhanced Chemical Vapor Deposition, *J. Appl. Phys.* 91, 483-486 (2002).
13. T. Guo, P. Nikolaev, A. Thess, D. T. Colbert, and R. E. Smalley, Catalytic growth of single-walled nanotubes by laser vaporization, *Chem. Phys. Lett.* 243, 49–54 (1995).
14. M. E. Itkis, D. E. Perea, S. Niyogi, J. Love, J. Tang, A. Yu, C. Kang, R. Jung, and R. C. Haddon, Optimization of the Ni-Y Catalyst Composition in Bulk Electric Arc Synthesis of Single-Walled Carbon Nanotubes by Use of Near-Infrared Spectroscopy, *J. Phys. Chem. B* 108*,* 12770-12775 (2004).
15. Y. S. Park, K. S. Kim, H. J. Jeong, W. S. Kim, J. M. Moon, K. H. An, D. J. Bae, Y. S. Lee, G.-S. Park, and Y. H. Lee, Low pressure synthesis of single-walled carbon nanotubes by arc discharge, *Synthetic Metals* 126, 245-251 (2002).
16. C. Liu, H. M. Cheng, H. T. Cong, F. Li, G. Su, B. L. Zhou, M. S. Dresselhaus. Synthesis of macroscopically long ropes of well-aligned single-walled carbon nanotubes, *Advanced Materials* 12, 1190-1192 (2000).
17. H. W. Zhu, B. Jiang, C. L. Xu, and D. H. Wu, Synthesis of High Quality Single-walled Carbon Nanotube Silks by the Arc-discharge Technique, *J. Phys. Chem. B* 107, 6514-6518 (2003).

18. L. Alvarez, T. Guillard, J. L. Sauvajol, G. Flamant, and D. Laplaze, Solar production of single-wall carbon nanotubes: growth mechanisms studied by electron microscopy and Raman spectroscopy, *Appl. Phys. A* 70(2), 169–173 (2000); L. Alvarez L., Guillard T., Sauvajol, G. Flamant, and D. Laplaze, Growth mechanisms and diameter evolution of single wall carbon nanotube, *Chem. Phys. Lett.* 342, 7-14 (2001).
19. S. Lebedkin, P. Schweiss, B. Renker, S. Malik, F. Hennrich, M. Neumaier, C. Stoermer, and M. M. Kappes, Single-wall Carbon Nanotubes with Diameters Approaching 6 nm Obtained by Laser Vaporization, *Carbon* 40, 417- 423 (2002).
20. C.-H. Kiang, W. A. Goddard III, R. Beyers, J. R. Salem, D. S. Bethune, Catalytic Synthesis of Single-Layer Carbon Nanotubes with a Wide Range of Diameters, *J. Phys. Chem.* 98, 6612-6618 (1994).
21. M. Haluska, V. Skakalova, D. L. Carroll, and Z. Roth, The Influence of Sulfur Promoter on the Production of SWCNTs by the Arc-Discharge Process, in: *Electronic Properties of Novel Materials*, H. Kuzmany, J. Fink, M. Mehring, S. Roth (eds.), American Institute of Physics, New York, 2005, AIP Conference Proceedings, in print.
22. W. K. Maser, E. Munoz, M. T. Martınez, A. M. Benito, and G. F. de la Fuente, Study of parameters important for the growth of single wall carbon nanotubes, *Opt. Mater.* 17, 331–334 (2001).
23. E. Munoz, W. K. Maser, A. M. Benito, M. T. Martınez, G. F. de la Fuente, Y. Maniette, A. Righi, E. Anglaret, and J. L. Sauvajol, Gas and pressure effects on the production of single-walled carbon nanotubes by laser ablation, *Carbon* 38, 1445–1451 (2000).
24. E. Munoz, W. K. Maser, A. M. Benito, M. T. Martınez, G. F. de la Fuente,A. Righi, E. Anglaret, and J. L. Sauvajol, The influence of the target composition in the structural characteristics of single walled carbon nanotubes produced by laser ablation, *Synth. Metals* 121, 1193–1194 (2001)..
25. A. P. Bolshakov, S. A. Uglov, A. V. Saveliev, V. I. Konov, A. A. Gorbunov, W. Pompe, and A. Graff, A novel CW laser-powder method of carbon single-wall nanotubes production, *Diam. Rel. Mater.* 11, 927–930 (2002).
26. W. K. Maser, A. M. Benito, E. Muñoz, G. M. de Val, M. T. Martínez, Á. Larrea, and G. F. de la Fuente, Production of carbon nanotubes by CO_2-laser evaporation of various carbonaceous feedstock materials, *Nanotechnology* 12, 147-151 (2001).
27. A. Thess, R. Lee, P. Nikolaev, H. Dai, P. Petit, J. Robert, C. Xu, Y. H. Lee, S. G. Kim, A. G. Rinzler, D. T. Colbert, G. E. Scuseria, D. Tomanek, J. E. Fischer, and R. E. Smalley, Crystalline ropes of metallic carbon nanotubes, *Science* 273, 483–487 (1996).
28. A. G. Rinzler, J. Liu, H. Dai, P. Nikolaev, C. B. Huffman, F. J. Rodrıguez-Macıas, P. J. Boul, A. H. Lu, D. Heymann, D. T. Colbert, R. S. Lee, J. E. Fischer, A. M. Rao, P. C. Eklund, and R. E. Smalley, Large-scale purification of single-wall carbon nanotubes: process, product, and characterization, *Appl. Phys. A* 67, 29–37 (1998).
29. Ch. T. Kingston, Z. J. Jakubek, S. Denommee, and B. Simard, Efficient laser synthesis of single-walled carbon nanotubes through laser heating of the condensing vaporization plume, *Carbon* 42, 1657–1664 (2004).
30. U. Dettlaff-Weglikowska, J. Wang, J. Liang, B. Hornbostel, and S. Roth, Purity Evaluation of Bulk Single Wall Carbon Natotube Materials, in: *Electronic Properties of Novel Materials*, H. Kuzmany, J. Fink, M. Mehring, S. Roth (eds.), American Institute of Physics, New York, 2005, AIP Conference Proceedings, in print.
31. M. E. Itkis, D. Perea, S. Niyogi, S. Rickard, M. Hamon, H. Hu, B. Zhao, and R. C. Haddon, Purity Evaluation of As-Prepared Single-Walled Carbon Nanotube Soot by Use of Solution Phase Near-IR Spectroscopy, *Nano Lett.* 3, 309-314 (2003).

32. W. K. Maser, E. Munoz, A. M. Benito, M. T. Martınez, G. F. de la Fuente, Y. Maniette, E. Anglaret, and J.-L. Sauvajol, Production of high-density single-walled nanotube material by a simple laser-ablation method, *Chem. Phys. Lett.* 292, 587–593 (1998).
33. F. Kokai, K. Takahashi, M. Yudasaka, and S. Iijima, Emission Imaging Spectroscopic and Shadow graphic Studies on the Growth Dynamics of Graphitic Carbon Particles Synthesized by CO_2 Laser Vaporization, *J. Phys. Chem.* 103, 8686-8693 (1999).
34. This protocol is a guidance for sample characterization and quality control within the SPANG consortium. It is hoped that by applying this protocol, reproducible results will be obtained at the different laboratories. To facilitate cooperation with other consortia and quite general with colleagues worldwide, the protocol is also spread outside the EU project SPANG. The protocol is regularly updated. We appreciate any interest for the protocol and any feedback from colleagues working in the field.

SCANNING TUNNELING MICROSCOPY AND SPECTROSCOPY OF CARBON NANOTUBES

LÁSZLÓ P. BIRÓ*
Research Institute for Technical Physics and Materials Science, H-1525, POB 49, Budapest, Hungary

PHILIPPE LAMBIN
Facultés Universitaires Notre-Dame de la Paix, B-5000, Rue de Bruxelles 61, Namur, Belgium

Abstract. This paper briefly reviews scanning tunneling microscopy with emphasis on the particularities that have the most significant influence on the STM and STS characterization of both single-wall and multi-wall carbon nanotubes. The experimental results obtained on these carbon nanotubes are surveyed together with computer modeling of the STM images of carbon nanotubes and the role of structural defects is discussed.

Keywords: scanning tunneling microscopy (STM); scanning tunneling spectroscopy (STS); carbon nanotubes; computer modeling; structural defects

1. Introduction

Carbon nanotubes (CNTs) are perhaps one of the most exciting members of the family of carbon nanostructures. The very quick development of this family was initiated by the discovery of fullerene almost two decades ago[1]. The very promising properties of the CNTs[2,3] brought single-wall carbon nanotubes (SWCNTs) and multi-wall carbon nanotubes (MWCNTs) in the focus of the attention of researchers in various fields ranging from nanoelectronics to composite materials. The straight carbon nanotubes were discovered by Iijima in 1991 (Ref. [4]). Later on, other more complex, but tubular type structures built of layers of sp^2 hybridized carbon, like Y-junctions, helical coils and

*To whom correspondence should be addressed: László P. Biró, Nanotechnology Department, Research Institute for Technical Physics and Materials Science, H-1525, POB 49, Budapest, Hungary; e-mail: biro@mfa.kfki.hu

V.N. Popov and P. Lambin (eds.), Carbon Nanotubes, 19–42.

multiple coils have been predicted theoretically[5-8] and soon observed experimentally by transmission electron microscopy (TEM) and scanning tunneling microscopy (STM).[9-13]

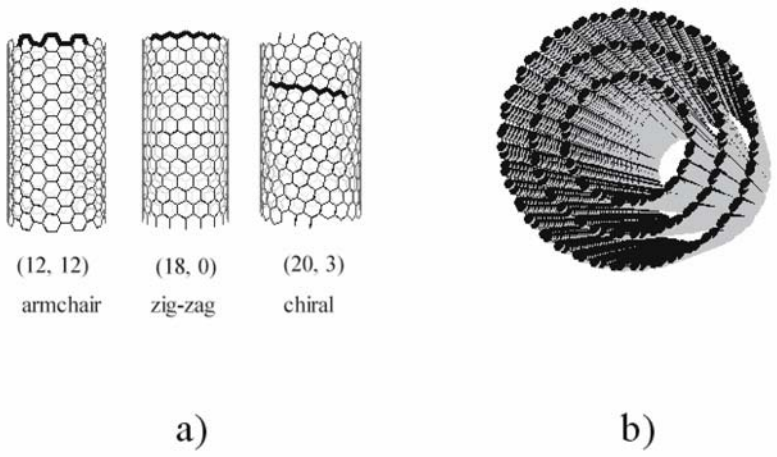

Figure 1. Structural models of carbon nanotubes: a) varieties of SWCNTs depending on the wrapping of the graphene layer; b) a MWCNT composed of three concentric SWCNTs (with permission from http://www.photon.t.utokyo.ac.jp/~maruyama/agallery/agallery.html).

A SWCNT is constituted from a one atomic layer thick sheet with graphite-like structure (graphene sheet) rolled into a perfect cylinder (Fig. 1a), while MWCNTs are built of a set of graphene cylinders (which can be regarded as individual SWCNTs) with increasing diameter, concentrically placed in each other (Fig. 1b). The diameter and helicity of a defect-free SWCNT are uniquely characterized by the vector $\mathbf{C} = n\mathbf{a}_1 + m\mathbf{a}_2 \equiv (n,m)$ called the rolling (or wrapping) vector, that connects crystallographically equivalent sites on the two-dimensional graphene sheet. Here $\mathbf{a}_1$ and $\mathbf{a}_2$ are the graphene lattice vectors, and n and m are integer numbers (see Fig. 2). The interlayer spacing of MWCNTs is consistent with the characteristic one for turbostratic graphite of 0.34 nm (Ref. [14]). The typical diameter values of SWCNTs are around 1 nm, while MWCNTs have diameters of a few tens of nanometers. Their structure confers the nanotubes with special properties, very closely determined by the way in which the C-C bonds in the graphene sheet are oriented with respect the nanotube axis, and by the diameter of the tube[2,3] (Fig. 1). As a typical example: depending on the way in which the graphene sheet is wrapped into a cylinder, SWCNTs may be metallic or semiconducting.[2] One third of all possible SWCNTs shows metallic behavior, i.e., their electronic density of state (DOS) at the Fermi energy is different from zero, while two thirds exhibit semiconducting behavior with zero DOS around the Fermi energy. Normally,

MWCNTs are constituted from a random alternation of semiconducting and metallic layers.[15] Due to the strong relation between the atomic structure and the electronic properties, atomic resolution topographic STM images and scanning tunneling spectroscopy (STS) are very useful in the investigation and in the understanding of physical properties of carbon nanotubes. Presently, the STM is the only tool able to give information about both the atomic arrangement and electronic structure of the very same nanotube.

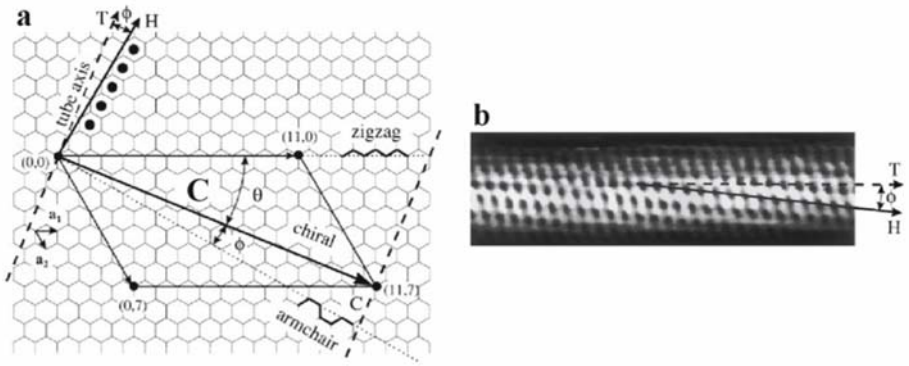

Figure 2. Schematic drawing showing the wrapping of a (11,7) SWCNT and its topographic STM image (after Ref. [47]). a) wrapping of the graphene sheet using a (11,7) wrapping vector **C**, the wrapping angle Φ, the vector **T** defining the tube axis and the vector **H** defining the direction of a row of hexagons appearing as dark spots on the STM image, b) atomic resolution, topographic STM image showing the relation of vectors **T** and **H**.

2. Brief overview of STM

The basic concept of the STM is simple (Fig. 3): an atomically sharp metallic tip is brought in the proximity of a flat conducting sample within a distance *s* of the order of a few tenths of a nanometer. As their behavior is governed by the laws of quantum mechanics, electrons may tunnel with equal probability from the tip to the surface and vice versa. When an external bias *V* is applied between the surface and the tip, preferential tunneling will be imposed in one of the directions (depending on the polarity of *V*), which will yield an average tunneling current I_t. For maintaining continuous tunneling, the tip-sample distance *s* has to be regulated using a piezo actuator and a feedback loop. The tunneling current measured at a given moment is taken as input signal for the feedback loop and compared with a preset value. The actuator will increase or reduce the gap between sample and tip depending on whether the difference of measured value of I_t is larger or smaller than the preset value.

A comprehensive overview of the theoretical models used to describe the tunneling through a one dimensional potential barrier, the simplest case of tunneling, is given by Wiesendanger.[16] Two major conclusions arise from the various models:

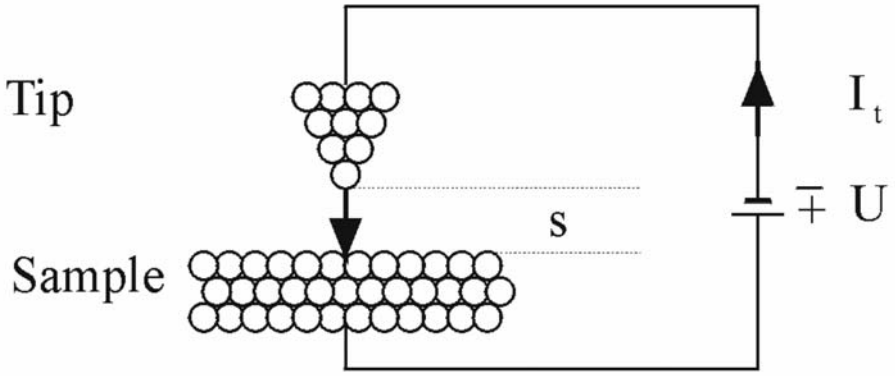

Figure 3. Principle of operation of the STM.

The transmission T of electrons through a one dimensional potential barrier depends exponentially on the width s of the barrier

$$T \propto e^{-2\chi s}. \tag{1}$$

The decay rate χ, characterizing the decrease of the probability of the electron to cross over the barrier, is

$$\chi = \frac{2\pi[2m(V_0 - E)]^{1/2}}{h}, \tag{2}$$

where V_o is the average height of the barrier, E is the energy of the tunneling electron. Independently of the exact shape of the barrier, the strong exponential dependence of T with the barrier width s and the square root of the effective barrier height, $(V_o - E)^{1/2}$ is typical of tunneling. The exponential dependence makes that the tunneling channel will be very narrow, thus making possible the atomic resolution.

The tunnel current flowing between the tip and the sample at a bias voltage V will be:

$$I(V) \propto \int_0^{eV} \rho_s(E)\rho_t(E - eV)T(E)dE, \tag{3}$$

where ρ_s is the sample electronic DOS, ρ_t is the DOS of the tip and T the transmission coefficient of the barrier. From Eq. 3, one may observe that the STM offers the opportunity to acquire not only topographic information about the sample but also information regarding the DOS of the sample. If the tip DOS is flat and the transmission coefficient T may be taken as constant, then Eq. 3 reduces to:

$$I(V) \propto \int_0^{eV} \rho_s(E)dE. \tag{4}$$

Then, the quantity dI/dV, named differential resistance, will be proportional to $\rho_s(V)$, the sample electronic DOS. However, T may be regarded as constant only in the limit of small voltage variations but it gives deviation from this simple dependence at large bias values.

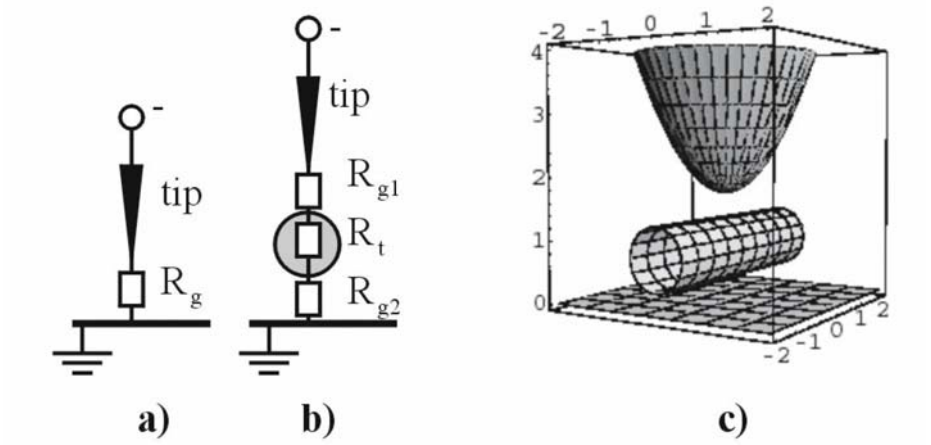

Figure 4. Schematic representation of the STM-nanotube-substrate system: a) the STM tip when tunneling directly into the substrate; b); the STM tip when tunneling through a carbon nanotube (showed in transversal cross section), the shaded circle stands fro the carbon nanotube; c) 3D presentation of the STM tip, nanotube, substrate system, dimensions are in nanometers. Note that the nanotube is not integral part of the substrate.

In reality, the STM measurement is quite different from the simple case of tunneling through a one dimensional potential barrier. First of all, in the case of a sharp tip, one has a three-dimensional potential barrier instead of a one-dimensional one. The shape of real potential barriers may strongly differ from the rectangular shape assumed in deducing Eqs. 1 and 2. A widely used model for the interpretation of experimental STM images is the model given by

Tersoff and Hamann.[17] In their theory, the tip is treated as a single *s orbital*, a constant DOS is assumed for it, and the tunnel current is taken as being proportional to the sample DOS computed at the location of the apex of the STM tip at the Fermi energy and taking a vanishingly small bias. A more comprehensive and detailed treatment of tunneling is given in the book on STM edited by Wiesendanger and Güntherodt.[18]

In the practical STM instrumentation, the positioning and scanning of the STM tip is usually achieved by piezoelectric actuators. It is important to emphasize that the generated image opposite to other image generating techniques, like analog photography, is constituted of pixels (256 x 256, 512 x 512, etc.). Therefore, zooming in using software tools into a recorded image unavoidably is reducing the amount of "measured" information. An STM can operate in several regimes; the three most important ones are as follows:

Topographic (constant current) imaging: the width of the STM gap is controlled by a feedback loop keeping the value of the tunneling current at a setpoint value selected by the operator. The image is generated from the values of the voltage applied to the piezo-actuator to maintain the constant value of the tunneling current. Provided the electronic structure at the sample surface is homogeneous, the topographic profile of the surface will be generated.

Current-voltage spectroscopy, frequently called scanning tunneling spectroscopy (STS). The scanning and the feedback loop are switched off, the value of the tunneling gap is fixed, and the bias voltage is ramped from $-U$ to $+U$, and the corresponding current variations are recorded. The function dI/dV gives information about the local DOS of the sample.

Current-voltage spectroscopy and imaging (CITS): the feedback loop is switched on and of. While it is on, the scanning is done and image information is acquired (as in topographic imaging), in each image point, after the position of the tip has stabilized, the feedback loop is switched off and the full STS spectrum is acquired followed by switching on the feedback loop and continuing scanning.

To understand the results of the STM imaging of carbon nanotubes, it is useful to keep in mind a few particularities of the tunneling system specific to this case:

In order to be able to image a nanoscopic object, like a carbon nanotube in an STM, the object has to be placed on an atomically flat conducting surface: the substrate. Highly oriented pyrolitic graphite (HOPG), or Au (111) terraces are the most frequently used substrates.[19]

When a carbon nanotube is imaged, as opposite to the case of tunneling into a bulk sample, the electrons have to cross two tunnel gaps: one between the STM tip and the nanotube, the other between the nanotube and its support[20,21] as shown in Fig. 4b.

The electronic structure of the carbon nanotube and its support may be different. As it follows from Eq. 3, the different values of $\rho_{s(support)}(V)$, and $\rho_{s(nanotube)}(V)$, will yield different values of tunneling current, thus having influence on the height values measured from topographic images.[22]

When the STM tip comes very close to the nanotube or when switching from pure tunneling to point contact imaging regime occurs,[23] the STM tip may induce the elastic deformation of the nanotube. By changing the imaging conditions like I_t or V, if the mechanical contact was not as strong as to damage the tip or the sample, the point contact imaging can be "switched" on and off[24] (Fig. 5).

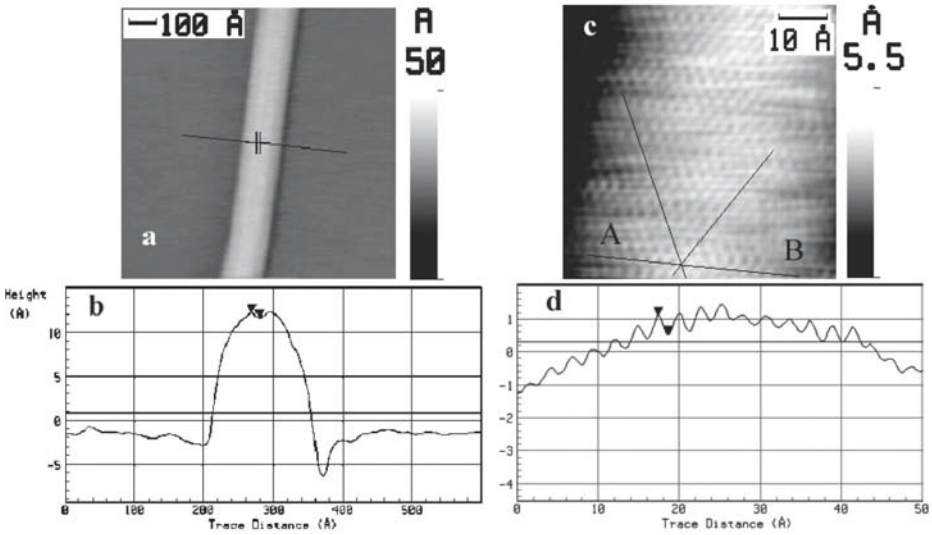

Figure 5. A STM image taken on a MWCNT in conditions under which switchover to point contact imaging occurs. a) low magnification topographic image I_t = 1.2 nA, V = 100 mV. Note the depression in the top part of the MWCNT; b) line-cut along the line marked in panel a), the depression of 0.1 nm depth is clearly visible in the topmost part of the nanotube; c) an atomic resolution image taken on the same nanotube with the same STM tip using I_t = 1.0 nA and V = 100 mV: the typical structure of graphite is well observed, the three axes running through the tunneling current maxima make an angle of 60°; d) line-cut along the line marked in c) by AB: the curvature of the MWCNT is well observed. Note the corrugation amplitude of 0.05 nm equal to half of that characteristic for HOPG.

Convolution effects, arising between the shape of a nanometric object and the shape of the STM tip, may have a significant influence on the recorded STM image. This phenomenon may cause a significant apparent lateral broadening of the imaged tube[25] (see Fig. 6).

The apparent diameter D may be related to the apparent height h of the tube by the approximate relation $D = (8Rh)^{1/2}$, where R is the curvature radius of the tip.[23] The height of the topographic profile h may be regarded as being close to the geometric diameter of the tube and h is often used as a measure of d, the geometric diameter of the tube. But the measured apparent height depends on a few factors: the adsorption distance of the nanotube above the substrate; on the difference between the tunneling distances above the tube and over the substrate arising from their different electronic properties; and on the possible compression of the tube by the STM tip. The magnitude of these effects is not known with precision. Using the apparent height h of the nanotube seems to *underestimate* the actual diameter by as much as 0.2–0.5 nm[26] which may cause a significant error for a SWCNT, while it may be tolerable for a MWCNT. A fitting procedure of the tunneling current has been proposed[27] for the better determination of the diameter from the measured height.

Figure 6. Illustration of the distortion due to tip-sample convolution effects for objects with different shapes. When the object becomes sharper than the tip, the object will generate the image of the tip.

Distortion effects may also arise from a "floppy" tip. Such a tip may be produced when the rigid STM tips picks up a highly flexible carbon nanotube from the sample.[28] In this case the attached nanotube will act as the tip generating the image. Such a tip may cause in the topographic STM image reduced apparent height and dips on the sides of the imaged nanotube.

3. STM and STS of multi-wall carbon nanotubes

The nanotubes discovered by Iijima[4] in 1991 were MWCNTs, Fig. 1b. STM was perhaps the best suited tool to characterize the topography and the electronic properties of these nano-objects which at that time were produced in extremely small quantities. Topographic and voltage dependent STM imaging of arc-grown MWCNTs in a bundle was first reported by Zhang and Lieber.[29] The bundles were found to be composed of a parallel arrangement of closely packed nanotubes with diameters on the order of 10 nm. The first STS

measurement on individual carbon nanotubes was reported by Olk and Heremans.[30] The experiment was carried out in air on MWCNTs grown by the electric arc method. The nanotubes were transferred onto an Au substrate using a suspension in ethanol prepared by ultrasonication. Both semiconductor and metallic carbon nanotubes were found. The comparison of measured energy gap and experimental diameter values with gap values predicted by theory[31,32] showed an increasing deviation with decreasing tube diameter. The possible sources of this deviation are: the unavoidable error introduced in the measured diameter by tip/sample convolution effects (Fig. 6), the more complex structure of the tunneling region than in the well known case of a flat homogeneous sample[20,22] (Fig. 4) and effects arising from the multiple walls of the MWCNTs (Fig. 1b). The role that the inner layers of a MWCNT may play during STM imaging is not fully clarified yet. Theoretical calculations show that the smaller inner layers of a MWCNT may rotate in the larger diameter outer layer.[33] However, the first atomic resolution STM image was reported by Ge and Sattler[34] on MWCNTs. Disregarding the curvature of the imaged object, a similar atomic resolution STM image was obtained as in the case of flat HOPG. The triangular lattice characteristic for HOPG (Fig. 7b) is caused by the nonequivalence of the carbon atoms (in the Bernal graphite stacking) due to interlayer interaction.[35, 36] Thus a similar atomic resolution pattern in the case of a MWCNT like that of HOPG is an indication of an interlayer arrangement resembling that of HOPG. Additionally Ge and Sattler[34] found a periodicity of 16 nm along the tube axis superimposed on the atomic lattice. This was interpreted as arising from the misorientation of the outer two layers of the MWCNT, analogous to the generation of Moiré patterns known in geometric optic. The STM observation of Moiré patterns on HOPG[37] is well known experimentally.

Despite that MWCNTs were discovered first, both their experimental and theoretic understanding is behind that of SWCNTs. Atomic resolution images acquired on MWCNTs grown by CVD[22] were interpreted in a similar way like in the work by Ge and Sattler.[34] The comparison of atomic resolution images of SWCNTs, MWCNTs and HOPG, taken within the same series of experiments, showed that the atomic resolution images on MWCNTs and HOPG are similar.[38] Moreover, the difference between α and β sites (β sites do not have a neighbor in the layer below) was evidenced by STS too.[38] Most of the atomic resolution STM images on MWCNTs have been obtained on large diameter tubes while on small diameter tubes only low-quality atomic resolution was reported,[22] The latter may be related to the difficulty to achieve a HOPG-like stacking of the layers at small diameters.

The particularities in the DOS in the region of closed MWCNT ends were investigated using spatially resolved scanning tunneling spectroscopy and tight-binding calculations. Sharp resonant valence band states were found at the tube ends dominating the valence band edge and filling the band gap. Calculations show that the strength and position of these states with respect to the Fermi level depend sensitively on the relative positions of pentagons and their degree of confinement at the tube ends.[39,40] In accordance with theoretical predictions,[41] CITS measurements on MWCNTs grown directly on the HOPG support for STM measurements[42] showed that the MWCNTs with diameter over 30 nm do not have significant differences in their STS spectrum as compared to the HOPG support[43] (Fig. 8).

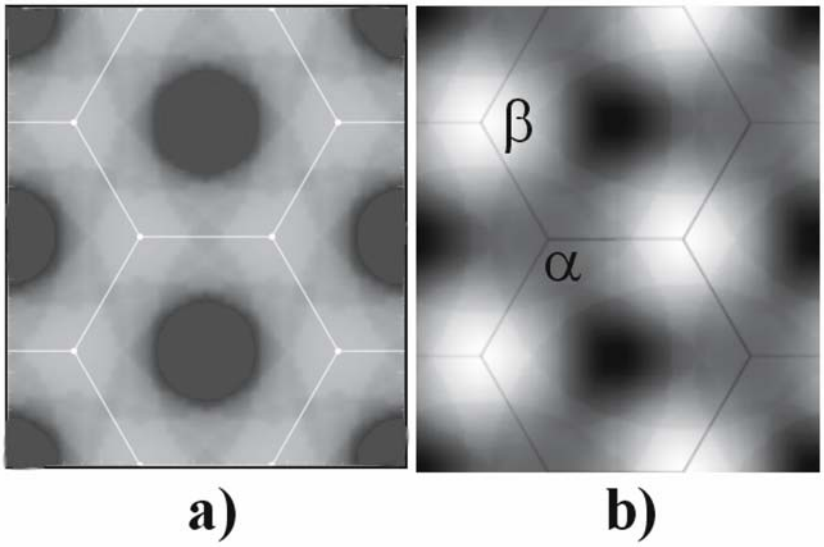

Figure 7. Computed STM images: a) a single layer of graphene, which can be regarded as the equivalent of the SWCNT and b) HOPG, which can be regarded as the equivalent of MWCNT. (After Ref. 44).

STS was successfully used to investigate the effect of mechanical strain on the electronic structure of MWCNTs on a support. The spectroscopic data show that opposite to small deformations, high strain like that due to abrupt substrate morphology change showed drastic perturbation in the local electronic structure of the tube.[45] This experimental finding is an agreement with theoretical work on the effects of defects produced by strain in the STM image of SWCNTs and alterations in their transport properties.[46]

4. STM and STS of single-wall carbon nanotubes

The first atomic resolution topographic STM images and STS results on SWCNTs were reported simultaneously by two groups.[47,48] Both groups used SWCNTs grown by laser ablation and the samples were imaged in a low temperature UHW STM on Au substrate. The atomic resolution images allow the determination of the chiral angle Φ, between the tube axis and the centers of the closest row of hexagons appearing in the STM (Fig. 2). As already discussed above, the hexagons will appear with a dark center (tunneling current minimum), while the bonds linking carbon atoms will show up as tunneling current maxima (Fig.7 and Fig. 9). However, caution is needed in the determination of the chiral angle from STM images, specially in the case of SWCNTs in bundles[49] or nanotubes trapped in debris, like in Fig. 9, where the SWCNT may be twisted in a way that the angles between the tube axis **T** and the vector **H** (Fig. 2) may be altered with respect to those characteristic for a free tube. For a more detailed discussion see Ref. 49.

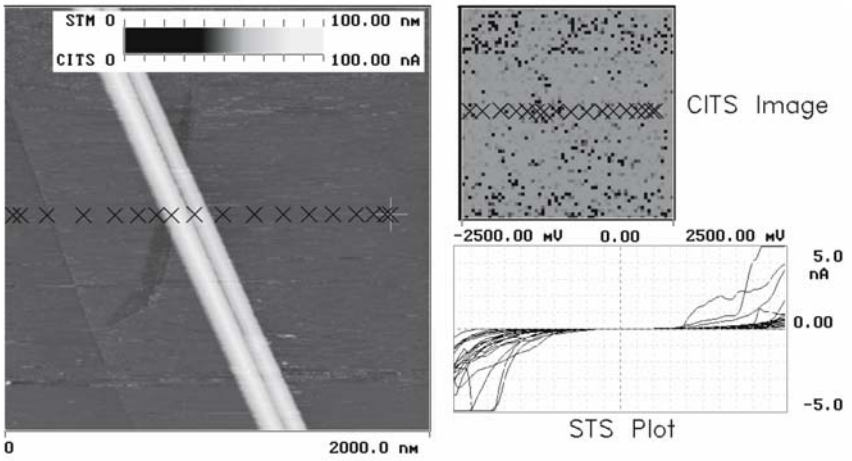

Figure 8. Topographic and CITS image of two multi-wall carbon nanotubes on HOPG. The CITS image does not reveal differences in the electronic structure. In the STS plot, the *I-V* curves recorded in the points marked by crosses are shown. In the range of –1 to 1 V all curves are practically coincident.

Another factor that may influence the precise determination of the chiral angle was identified by Venema et al.[26] and is illustrated in Fig. 10. The distortion originates from the planar scan over a cylindrical object.

Given the correct diameter and correct chirality, one may attempt the structural identification of the nanotube.[2] On the basis of this identification, the

calculated and measured DOS may be compared. The electronic structure of the SWCNTs has one dimensional character, which means that in their electronic DOS are present sharp maxima, the so-called van Hove singularities.[2] The STS results[47,48] are in good agreement with the calculated densities of states of SWCNTs,[2,50,51] the experimental DOS. The quantity dI/dV, called differential tunneling resistance, calculated according to Eq. 4, matches nicely the theoretical predictions. Both metallic and semiconductor carbon nanotubes were found. The typical forbidden gap values were in the range of 0.5 eV for semiconductor nanotubes with diameters in the 1.2 to 1.9 nm range, while the metallic carbon nanotubes with diameters in the range of 1.1 to 2.0 nm had subband separations of the order of 1.7 eV (Ref. [47]) (see also Fig. 11). The semiconducting SWCNTs were found to have gap values proportional to $1/d_t$, where d_t is the diameter of the nanotube. In first approximation, the distances between van Hove singularities across the gap ΔE_{11} of a semiconduting SWCNT are found to respect the rule $\Delta E_{33} = 4 \times \Delta E_{11}$ and $\Delta E_{22} = 2 \times \Delta E_{11}$, while for metallic nanotubes, the rule is $\Delta E_{33} = 3 \times \Delta E_{11}$ and $\Delta E_{22} = 2 \times \Delta E_{11}$ (Refs. [51,52]), ΔE_{11} being the subband separation. This relationship may be very useful in the experimental identification SWCNTs from often noisy STS data.

Due to work function differences, the Au substrate may produce the doping of the nanotube by charge transfer.[47] Therefore, this effect has to be taken into account in the interpretation of the spectroscopic data. The center of the gap that separates the first two van Hove singularities may be offset towards the valence band by as much as 0.2 – 0.3 eV.

Pronounced peaks in the LDOS were found at the end of an atomically resolved metallic SWCNT. Comparison of these data with calculations suggests that the topological arrangement of pentagons is responsible for the localized features in the experiment.[53]

Atomic resolution images of SWCNTs have been also obtained on the top of a rope.[49,54,55] The achieved resolution made it possible to compare the chiralities of the tubes that belong to the same rope. In some cases it was reported that the nanotubes have different chiralities and some of them may be twisted. In other cases, nearly uniform diameter and chirality were observed. Spectroscopic data taken on bundles show that the I-V curve may vary a lot along the same nanotube, and the spectra may exhibit a pronounced asymmetry.[56] The variation of the noise level of constant current topographic images taken at the same values of positive and negative bias, confirm the asymmetric character of the spectra. The asymmetric shape of the STS spectra was explained by wave-packet dynamical simulations of the tunneling process[23] showing that the asymmetry may arise from the shape of the electrode emitting the electrons.

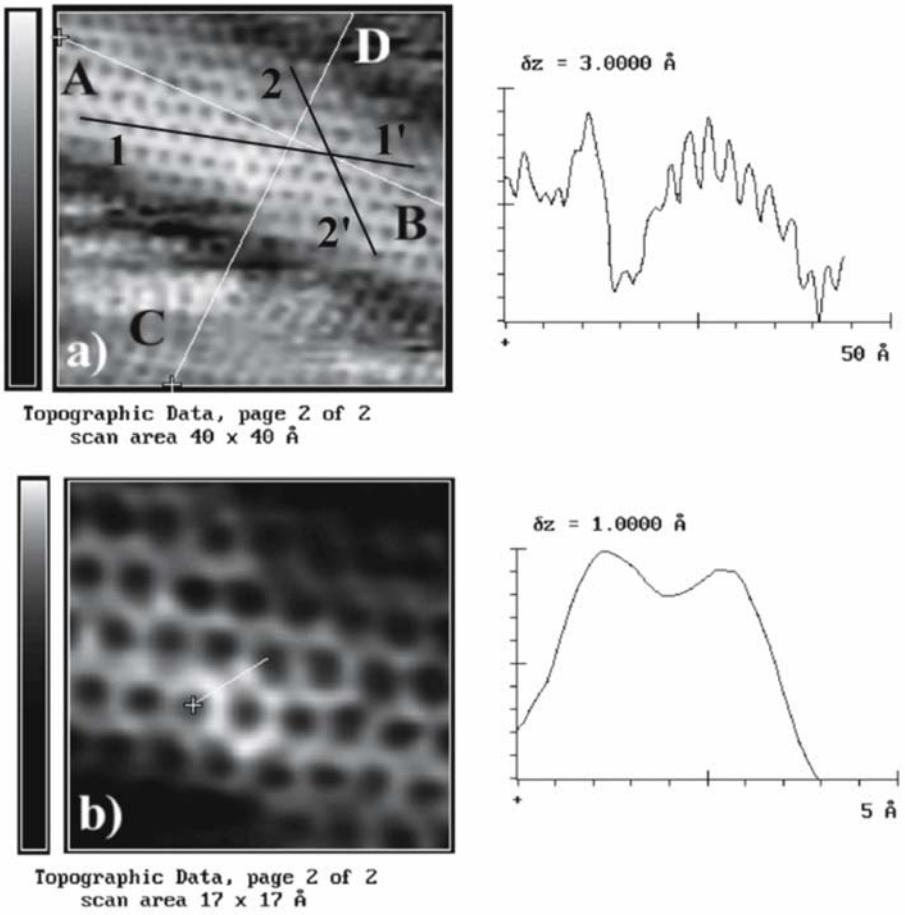

Figure 9. Atomic resolution, constant-current STM images of a twisted zig-zag nanotube trapped in surrounding material: a) the white line labeled AB is parallel with the tube axis while the line CD is passing through a row of hexagons (as seen in the line cut shown at the right hand side of the image), lines AB and CD are orthogonal, the black lines 11' and 22' are also drawn along rows of hexagons (dark spots) as clearly seen in the image but they make different angles with line CD, such a situation is indicating twist in the tube; b) physically zoomed detail of a), note a well-resolved hexagon close to the center of the image, the line-cut along a C-C bond is shown on right side, it indicates a slightly increased distance of 0.16 nm.

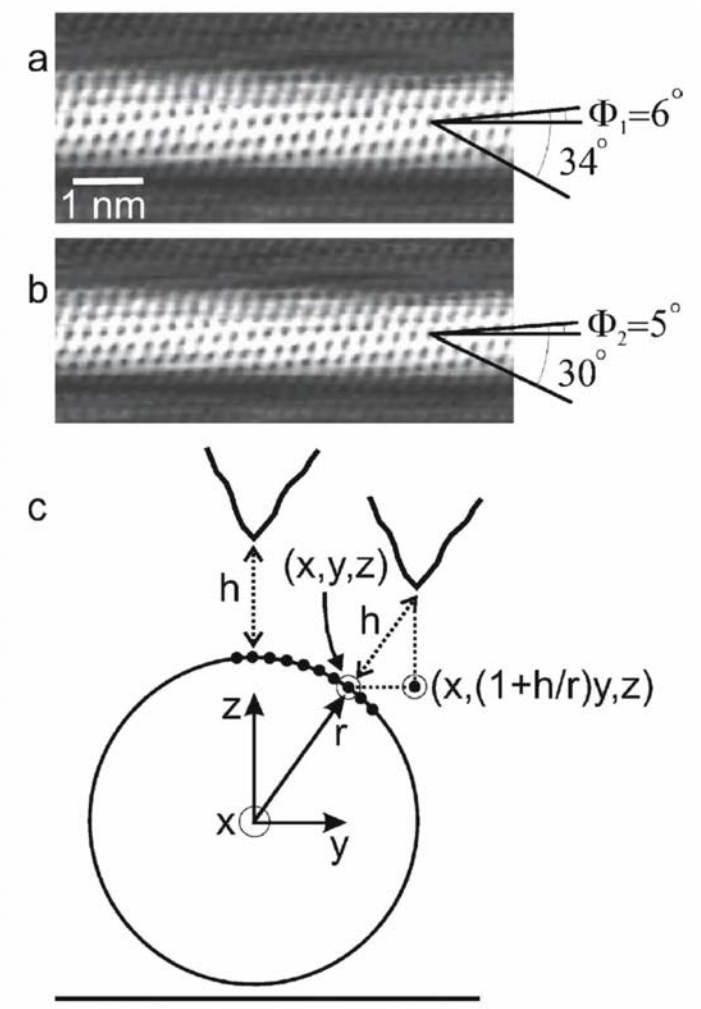

Figure 10. Illustration of the image distortion mechanism for nanotubes and a correction method. The 1-nm bar indicates the scale for both images in a) and b): a) An uncorrected image with an angle between armchair and zigzag directions of 34° instead of 30°. This is attributed to a distortion effect, which stretches the atomic lattice in the direction perpendicular to the tube. The apparent angle $\phi_1 = 6°$; b) The same image as a), corrected for the distortion. This is done by decreasing the image in the perpendicular direction to the tube axis to obtain a 30° difference between the zigzag and armchair directions. A chiral angle $\phi_2 = 5°$ is determined from this corrected image; c) a sketch illustrating the geometrical distortion mechanism. A nanotube with radius *r* lies in the *xy* plane with its axis in the *x* direction. When the STM tip tunnels to the side of the nanotube, an atom at position (*x*,*y*,*z*) is projected in the STM image at [*x*,(1+1*h*/*r*)*y*,*z*]. (After Ref. 26)

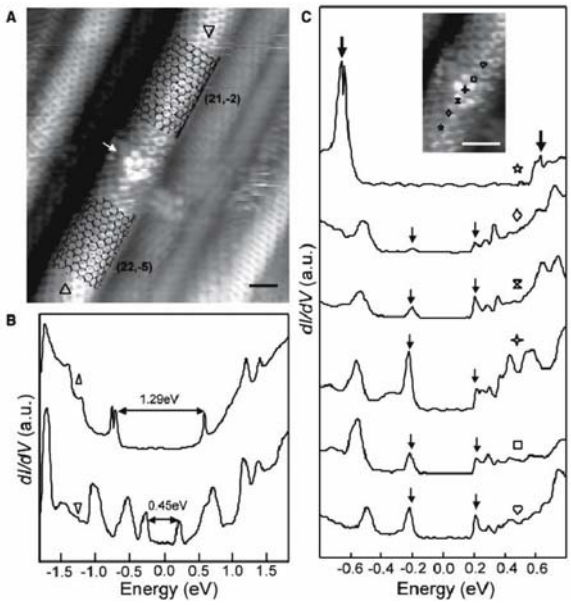

Figure 11. Structure and spectroscopy of a nanotube junction. (A) Atomically-resolved STM image of a SWNT containing the junction; the position is highlighted with a white arrow. Black honeycomb meshes corresponding to (21,–2) and (22,–5) indices are overlaid on the upper and lower portions of the nanotube, respectively, to highlight the distinct atomic structures of these different regions. The image was recorded in a low temperature, UHV STM in constant-current mode with electrochemically etched tungsten tips at bias voltage V_b = 650 mV and I_t = 150 pA; (B) Tunneling conductance, dI/dV recorded at the upper (▼) and lower (▲) locations indicated in (A). The energy difference between first VHS gap in the upper semiconducting segment, 0.45 eV, and lower metallic segment, 1.29 eV, are shown. (C) Spatially resolved dI/dV acquired across the junction at the positions indicated by the six symbols on the high-resolution image (inset) of the junction interface. The small arrows highlight the positions of the first VHS of the semiconducting (21,22) structure and emphasize their spatial decay across the junction; the large arrows highlight the first VHS of the metallic (22,–5) structure. (From Ref. [67])

Figure 12. Constant-current (topographic) STM images calculated using a tight-binding Hamiltonian and a point-like tip for an armchair (10,10), a chiral (13, 7), and a zig-zag (18, 0) nanotube. (From Ref. [69])

The STM can be used as "tool" to modify the nanotube. SWCNTs were cut to desired size by applying a voltage pulse of the order of 4V, no polarity dependence was found.[57] After shortening to a length of 30 nm, the STS spectrum of the nanotube piece taken at 4 K showed non-equidistant, step-like features absent before the cutting. The observed effect was interpreted as arising from discrete electron stationary waves observed as periodic oscillations in the differential conductance as a function of the position along the tube axis, with a period that differed from that of the atomic lattice. Similar studies were also devoted to chiral metallic and semiconducting nanotubes shortened to a few nanometers.[58,59] In contrast to the metallic nanotubes, no significant length dependence is observed in finite-sized semiconducting nanotubes down to 5 nm. The STS data obtained from the center of the shortened tubes showed a striking resemblance to the spectra observed before cutting.[59]

STS was used to investigate the effects of the ambient atmosphere on SWCNT samples. It was found that some semiconducting samples exhibit metallic behavior upon exposure to oxygen, while in the case of other samples the effect of O_2 is restricted to the modification of the apparent density of states at the valence band edge.[60] The investigation of the electrical response of semiconductor SWCNTs to gas molecules showed that while NH_3 produces a sharp decrease in conductance, NO_2 has an opposite effect.[61]

Statistical evaluation of nanotube diameters in a SWCNT mat (buckypaper) from the measured gap values and the comparison of these values with statistics obtained from TEM images demonstrated that the evaluation of diameters from gap values has to be done with caution because the gap is not always sharply defined in the STS spectrum.[62] When examined in a large enough bias interval, the positions of the peaks in DOS corresponding to the van Hove singularities form a fingerprint of the wrapping indices *n* and *m* of the nanotube, which can be used to better estimate the diameter.[63] Effects arising from interaction with the substrate[64] and possible charge transfer[47,65] have to be taken carefully into account. These effects may shift the Fermi level as mentioned above but do not affect too much the local DOS on the topmost part of the nanotube, which is the part that is scanned by the STM tip.[64]

Curvature effects in carbon nanotubes studied analytically as a function of chirality show that the π orbitals are found to be significantly rehybridized in all tubes so that they are never normal to the tube surface. This results in a curvature-induced gap in the electronic band structure of the metallic tubes. The tilting of the π orbitals should be observable by atomic resolution scanning tunneling microscopy measurements.[66] Recent STS measurements confirm the existence of the predicted gaps in the case of metallic zig-zag nanotubes and the presence of pseudo-gaps produced by tube-tube interaction in bundles.[59,67]

5. Computer modeling of STM images

As already emphasized in the previous sections, the interpretation of experimental data obtained in a complex tunneling system, constituted of a supported nano-object sandwiched between two tunneling gaps, is far from being straightforward. Therefore, computer modeling of the expected STM images is of great help in the correct evaluation of the experimental data. Modeling the atomic resolution images has been carried out by Meunier and Lambin. Their method is based on a tight-binding π-electron Hamiltonian for the case of a point-like tip in combination with a self-supported nanotube.[68] The calculated images confirm the different image symmetries observed experimentally (see Fig. 12). In the case of armchair tubes, the honeycomb structure is easily observable with all bonds looking similar. For zig-zag tubes, a strong anisotropy of the bonds is found with the ones parallel with the tube axis appearing much more stronger.[26] For chiral tubes, stripes spiraling around the nanotube are observed[19] which reverse orientation on bias reversal[69,70] in the case of semiconducting tubes as indeed observed experimentally in some occasions.[71] Calculated atomic resolution images of semiconductor SWCNTs show that the angle between the stripes spiraling around the nanotube and the tube axis changes gradually with the changing of the chiral angle. The two distinct classes of semiconductor tubes $n - m = M(3) + 1$ and $n - m = M(3) - 1$ exhibit complementary behavior. The image acquired with a negative tip in the first case is similar to the image acquired with positive tip bias for the second group of tubes. The complementarities of the two families of tubes is produced by the change in the occupied/unoccupied character of the HOMO and LUMO when changing from $n - m = M(3) + 1$ to $n - m = M(3) - 1$ due to the phase change imposed by the periodic boundary condition along the circumferential direction.[72] These calculated STM images of SWCNTs may prove to be extremely useful for the quick identification of nanotubes while acquiring experimental data.

The method based on the tight-binding π-electron Hamiltonian is suitable for calculating the expected STM images of 5 - 7 defects and other defects on carbon nanotubes as well.[68] An overview of the method and of the main results has been given recently.[73] A similar calculation technique was used[67] to identify the particular arrangement of the non hexagonal rings which may generate the intramolecular junction, seen in Fig. 11.

A wave-packet dynamical method for the simulation of the geometric and charge spreading effects during tunneling in supported carbon nanostructures was developed and applied successfully for getting insight in the particularities of tunneling in two-dimensional (2D) representations[20] and more recently in full three-dimensional (3D) tunneling through carbon nanotubes.[74,75]

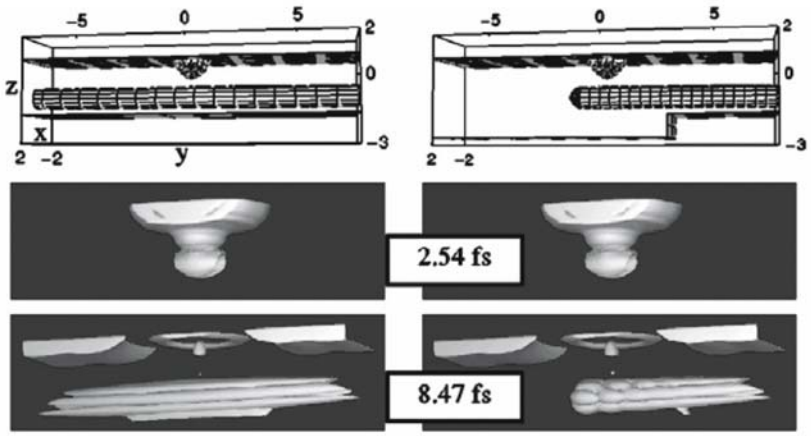

Figure 13. Model geometries for the case of an infinite nanotube on flat substrate and for a capped nanotube protruding from a step. The time evolution clearly shows the different ways in which tunneling occurs. While at 2.54 fs after the wave-packet is launched, the two systems are are practically identical; at 8.47 fs major differences are produced, due to the existence of the cap and the absence of the substrate within tunneling range under the STM tip. (From Ref. [75])

In this method the current density flowing through the STM tip-nanotube-support system is calculated based on the scattering of the wave-packets incident on the barrier potential. The geometric effects are well described by electrodes and nanotube treated in the jellium-potential approximation. The STM topographic profile through a carbon nanotube was calculated. It shows that as long as the electronic structure of the supported object and that of the support may be regarded as similar, the major image distortions arise from pure geometric tip-shape convolution[20] already discussed above. With increasing differences in the electronic structure of the nanotube and that of the support, larger distortions are expected. The incidence angle- and energy-dependent transmission of wave-packets through single and bundled carbon nanotubes were calculated, the effects arising from point-contact imaging and tip shape were analyzed, and STS curves were modeled.[23] As already mentioned above, for tip positive bias, the angular dependence of the transmission depends strongly on the nature of the nanosystem in the STM gap. While the transmission of the STM tunnel junction without nanotube can be well represented by a one dimensional model, all other geometries cause large normal-transverse momentum mixing of the wave packet. Recently, an overview and comparison of the tight-binding and wave packet dynamical methods has been given.[36] The usefulness of the wave-packet dynamical method is completely revealed when it is used in full three-dimensional (3D) simulation.[36,74,75]

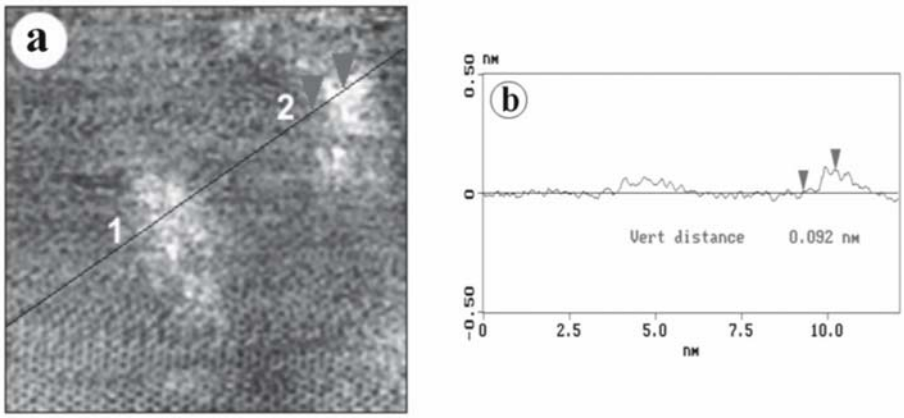

Figure 14. Topographic STM images of defects created on a MWCNT by irradiation with 30 keV Ar^+ ions: a) defects created by irradiation so called "hillocks"; b) line-cut along the line in a) on may note that an apparent height of around 1 nm is measured for the defects. (From Ref. [79])

The computer simulation clearly shows that during tunneling, the charge spreads along the nanotube. As a result, while the tunnel junction between the STM tip and the nanotube is a zero-dimensional junction, the tunnel junction between the nanotube and the support will be a linear one-dimensional junction (Fig. 13). The consequences of the spreading will affect the tunneling situations when the nanotube is only partly supported or is placed over a non-homogeneous substrate.[74,75]

6. Structural defects

As already reveled by early theoretic papers, structural defects like 5 –7 pairs, vacancies, isolated pentagons and heptagons may have dramatic effects on the structure and electronic properties of carbon nanotubes.[5-8,76,77] More recent calculations[78] predict similar effects for defects produced by ion irradiation. Irrespective of its nature, a defect in a SWCNT gives rise to backscattering of the electron wave function. Interference of the incoming and backscattered waves leads to a standing wave pattern, which can extend far away from the defect because of the one-dimensionality of the nanotube. This is the case, for example, for the junction of the two tubes, shown in Fig. 11 or for defects created on purpose by ion irradiation[79] (Fig. 14).

7. Summary and outlook

Scanning tunneling microscopy and spectroscopy proved to be the most suitable methods for truly revealing the characteristic electronic properties of carbon nanotubes arising from their one-dimensional character and nanometric size. A remarkable agreement between the theoretically computed results and experiment was achieved in the case of SWCNTs. Many basic level questions concerning the STM investigation of multi-wall carbon nanotubes are still open. The advance of this field is expected as suitable techniques emerge for the selective production of few wall carbon nanotubes like double wall carbon nanotubes. The variety of novel carbon nanostructures, not discussed in this chapter like Y-junctions, coils, and multiple coils, will pose a new challenge both for theoreticians and experimentalists.[80-82]

A new class of carbon nanomaterials emerges with the discovery of the peapods. The first experimental results already indicate that STM will be an extremely useful tool in getting deeper insight in the properties of these new materials.[83]

Last but not least, a very wide field of research opens up with the functionalization of carbon nanotubes. As the first results already demonstrate, STM and STS are the ideal tools for understanding the way in which the chemical moieties are coupled to the nanotubes.[84,85] A close collaboration between physicists, chemists and materials scientist will be needed in this field.

ACKNOWLEDGMENT

This work was partly funded by the Inter-University Attraction Pole (Grant No. IUAP P5/1) on "Quantum-size effects in nanostructured materials" of the Belgian Science Programming Services and partly by OTKA Grant T 043685 in Hungary. L.P.B. gratefully acknowledges the Belgian Fonds National de la Recherche Scientifique and the Hungarian Academy of Sciences for financial support.

References

1. H. W. Kroto, J. R. Heath, S. C. O'Brien, R. F. Curl, and R. E. Smalley, C_{60}: Buckminsterfullerene, *Nature* 318, 162-163 (1985).
2. M. S. Dresselhaus, G. Dresselhaus, and P. C. Eklund, *Science of Fullerenes and Carbon Nanotubes*, (Academic Press, San Diego, 1996).
3. *Carbon Filaments and Nanotubes: Common Origins, Different Applications?* edited by L. P. Biró, C. A. Bernardo, G. G. Tibbetts and Ph. Lambin (Kluwer Acad. Publ., Dordrecht, 2001).

4. S. Iijima, Helical microtubules of graphitic carbon, *Nature* 354, 56 -58 (1991).
5. G. E. Scuseria, Negative curvature and hyperfullerenes, *Chem. Phys. Lett.* 195, 534-536 (1992).
6. L. A. Chernozatonskii, Carbon nanotube connectors and planar jungle gyms, *Phys. Lett. A* 172, 173 (1992).
7. B. I. Dunlap, Connecting carbon tubules, *Phys. Rev. B* 46, 1933-1936 (1992).
8. S. Ihara, S. Itoh, and J. Kitakami, Helically coiled cage forms of graphitic carbon, *Phys. Rev. B* 48, 5643-5647 (1993).
9. S. Amelinckx, X. B. Zhang, D. Bernaerts, X. F. Zhang, V. Ivanov, and J. B. Nagy, A formation mechanism for catalytically grown shaped graphite nanotubes, Science 265, 635-639 (1994).
10. J. Li, C. Papadopoulos, and J. M. Xu, Nanoelectronics: Growing Y-junction carbon nanotubes, *Nature* 402, 253-254 (1999).
11. L. P. Biró, S. D. Lazarescu, P. A. Thiry, A. Fonseca, J. B. Nagy, A. A. Lucas, and Ph. Lambin, Scanning tunneling microscopy observation of tightly wound, single-wall coiled carbon nanotubes, *Europhys. Lett.* 50, 494 (2000).
12. L. P. Biró, R. Ehlich, Z. Osváth, A. Koós, Z. E. Horváth, J. Gyulai, and J. B.Nagy, Room temperature growth of single-wall coiled carbon nanotubes and Y-branches, *Mat. Sci. Eng. C* 19, 3 (2002).
13. L. P. Biró, G. I. Márk, A. A. Koós, J. B.Nagy, Ph. And Lambin, Coiled carbon nanotube structures with supraunitary nonhexagonal to hexagonal ring ratio, *Phys. Rev. B* 66, 165405 (2002).
14. D. Reznik, C. H. Olk, D. A. Neumann, and J. R. D. Copley, X-ray powder diffraction from carbon nanotubes and nanoparticles, *Phys. Rev. B* 52, 116-124 (1995).
15. Ph. G. Collins, M. S. Arnold, and Ph. Avouris, Engineering Carbon Nanotubes and Nanotube Circuits Using Electrical Breakdown, *Science* 292, 706-709 (2001).
16. R. Wiesendanger, *Scanning Probe Microscopy and Spectroscopy*, Cambridge University Press, Cambridge (1994).
17. J. Tersoff and D. R. Hamann, Theory of the scanning tunneling microscope, *Phys. Rev. B* 31, 805-813 (1985).
18. R. Wiesendanger and H.-J. Güntherodt (Editors), *Scanning Tunneling Microscopy III*, Spriger-Verlag, (1993).
19. W. Clauss, Scanning tunneling microscopy of carbon nanotubes, *Appl. Phys. A* 69, 275-281 (1999).
20. G. I. Márk, L. P. Biró, and J. Gyulai, Simulation of STM images of three-dimensional surfaces and comparison with experimental data: Carbon nanotubes, *Phys. Rev. B* 58, 12645-12648 (1998).
21. Animated computer simulations showing the tunneling through a supported nano-object are available at: *http://www.mfa.kfki.hu/int/nano/*
22. L. P. Biró, J. Gyulai, Ph. Lambin, J. B.Nagy, S. Lazarescu, G. I. Márk, A. Fonseca, P. R. Surján, Zs. Szekeres, P. A. Thiry, and A. A. Lucas, Scanning tunneling microscopy (STM) imaging of carbon nanotubes, *Carbon* 36, 689-696 (1998).
23. G. I. Márk, L. P. Biró, J. Gyulai, P. A. Thiry, A. A. Lucas, and Ph. Lambin, Simulation of scanning tunneling spectroscopy of supported carbon nanotubes, *Phys. Rev. B* 62, 2797-2805 (2000).
24. L. P. Biró and G. Márk, *STM investigation of Carbon Nanotubes*, in Ref. 3, pp. 219-231
25. L. P. Biró, S. Lazarescu, Ph. Lambin, P. A. Thiry, A. Fonseca, J. B. Nagy, and A. A. Lucas, Scanning tunneling microscope investigation of carbon nanotubes produced by catalytic decomposition of acetylene, *Phys. Rev. B* 56, 12 490-12498 (1977).

26. L. C. Venema, V. Meunier, Ph. Lambin, and C. Dekker, Atomic structure of carbon nanotubes from scanning tunneling microscopy, *Phys. Rev. B* 61, 2991-2996 (2000).
27. Ph. Kim, T. W. Odom, J. Huang, and Ch. M. Lieber, STM study of single-walled carbon nanotubes, *Carbon* 38, 1741-1744 (2000).
28. F.-X. Zha, D. L. Carroll, R. Czerw, A. Loiseau, H. Pascard, W. Clauss, and S. Roth, Electronic effects in scanning tunneling microscopy of dendritic, Cr-filled carbon nanotubes, *Phys. Rev. B* 63, 165432-165437 (2001).
29. Z. Zang and Ch. M. Lieber, Nanotube structure and electronic properties probed by scanning tunneling microscopy, *Appl. Phys. Lett*. 62, 2792-2794 (1993).
30. Ch. H. Olk and J. P. Heremans, Scanning tunneling spectroscopy of carbon nanotubes, *J. Mater. Res*. 9, 259-262 (1994).
31. J. W. Mintmire, B. I. Dunlap, and C. T. White, Are fullerene tubules metallic? *Phys. Rev. Lett*. 68, 631-634 (1992).
32. R. Saito, M. Fujita, G. Dresselhaus, and M. S. Dresselhaus, Electronic structure of chiral graphene tubules, *Appl. Phys. Lett*. 60, 2204-2206 (1992).
33. Y. K. Kwon and D. Tománek, Electronic and structural properties of multiwall carbon nanotubes, *Phys. Rev. B* 58, R16001-R16004 (1998).
34. M. Ge and K. Sattler, Vapor-condensation generation and STM analysis of fullerene tubes, *Science* 260, 515-518 (1993).
35. D. Tománek and S. G. Louie, First-principles calculation of highly asymmetric structure in scanning-tunneling-microscopy images of graphite, *Phys. Rev. B* 37, 8327-8336 (1988).
36. G. I. Márk, L. P. Biró, and Ph. Lambin, in *Frontiers of Multifunctional Nanosystems*, edited by E. Buzaneva and P. Scharff, Kluwer Academic Publishers, Dordrecht (2002), p. 43.
37. J. Jxhie, K. Sattler, M. Ge, N. Verkateswaran, Giant and supergiant lattices on graphite, *Phys Rev. B* 47, 15835-15841 (1993).
38. Ph. Lanbin, V. Meunier, and A. Rubio, *Simulation of STM images and STS spectra of carbon nanotubes*, in: *"Science and application of nanotubes"* Ed. D. Tomanek and R. J. Endbody (Kluwer Academic/Plenum Publishers, New York, 2000) pp. 17 -33.
39. A. Hassanien, A. Mrzel, M. Tokumoto, and D. Tománek, Imaging the interlayer interactions of multiwall carbon nanotubes using scanning tunneling microscopy and spectroscopy, *Appl. Phys. Lett.* 79, 4210-4212 (2001).
40. D. L. Carroll, P. Redlich, P. M. Ajayan, J. C. Charlier, X. Blase, A. De Vita, and R. Car, Electronic Structure and Localized States at Carbon Nanotube Tips, *Phys. Rev. Lett*. 78, 2811-2814 (1997)
41. T. Tamura and M. Tsukada, Electronic states of the cap structure in the carbon nanotube, *Phys. Rev. B* 52, 6015-6026 (1995).
42. M. S. Dresselhaus, in *Carbon Filaments and Nanotubes: Common Origins, Different Applications?* edited by L. P. Biró, C. A. Bernardo, G. G. Tibbetts and Ph. Lambin, Kluwer Academic Publishers, Dordrecht (2001), p. 11
43. L. P. Biró, R. Ehlich, R. Tellgmann, A. Gromov, N. Krawez, M. Tschaplyguine, M.-M. Pohl, Z. Véretsy, Z. E. Horváth, and E. E. B. Campbell, (1999) Growth of carbon nanotubes by fullerene decomposition in the presence of transition metals, *Chem. Phys. Lett*. 306, 155 – 162.
44. L. P. Biró and G. I. Márk in *Carbon Filaments and Nanotubes: Common Origins, Different Applications?* edited by L. P. Biró, C. A. Bernardo, G. G. Tibbetts and Ph. Lambin, Kluwer Academic Publishers, Dordrecht (2001), p. 219
45. D. Tekleab, D. L. Carroll, G. G. Samsonidze, and B. I. Yakobson, Strain-induced electronic property heterogeneity of a carbon nanotube, *Phys. Rev. B* 64, 035419-035424 (2001).

46. D. Orlikowski, M. B. Nardelli, J. Bernholc, and Ch. Roland, Theoretical STM signatures and transport properties of native defects in carbon nanotubes, *Phys. Rev. B* 61, 14194-14203 (2000).
47. J. W. G. Wildöer, L. C. Venema, A. G. Rinzler, R. E. Smalley, and C. Dekker, Electronic structure of atomically resolved carbon nanotubes, *Nature* 391, 59-62(1998)
48. T. W. Odom, J-L. Huang, Ph. Kim, and Ch. M. Lieber, Atomic structure and electronic properties of single-walled carbon nanotubes, *Nature*, 391, 62-64 (1998).
49. W. Clauss, D. J. Bergeron, and A. T. Johnson, Atomic resolution STM imaging of a twisted single-wall carbon nanotube, *Phys. Rev. B* 85, R4266-R4269 (1998).
50. N. Hamada, S. Sawada, and A. Oshiyama, New one-dimensional conductors: Graphitic microtubules, *Phys. Rev. Lett.* 68, 1579-1581 (1992).
51. J.-C. Charlier and Ph. Lambin, Electronic structure of carbon nanotubes with chiral symmetry, *Phys. Rev. B* 57, R15037-R15039 (1998).
52. C. T. White and J. W. Mintmire, Density of states reflects diameter in nanotubes, *Nature* 394 29-30 (1998).
53. Ph. Kim, T. W. Odom, J-L. Huang, and Ch. M. Lieber, Electronic Density of States of Atomically Resolved Single-Walled Carbon Nanotubes: Van Hove Singularities and End States, *Phys. Rev. Lett*. 82, 1225-1228 (1999).
54. E. D. Obraztsova, V. Yu. Yurov, V. M. Shevluga, R. E. Baranovsky, V. A. Nalimova, V. L. Kuznetsov, and V. I. Zaikovski, Structural investigations of close-packed single-wall carbon nanotube material, *Nanostruct. Mater.* 11, 295-306 (1999).
55. A. Hassanien, M. Tokumoto, Y. Kumazawa. H. Kataura, Y. Maniwa, S. Suzuki, and Y. Achiba, Atomic structure and electronic properties of single-wall carbon nanotubes probed by scanning tunneling microscope at room temperature, *Appl. Phys. Lett*. 73, 3839-3841 (1998).
56. L. P. Biró, P. A. Thiry, Ph. Lambin, C. Journet, P. Bernier, and A. A. Lucas, Influence of tunneling voltage on the imaging of carbon nanotube rafts by scanning tunneling microscopy, *Appl. Phys. Lett.* 73, 3680-3682 (1998).
57. L. C. Venema, J. W. G. Wildöer, H. L. J. Temminck Tuinstra, C. Dekker, A. G. Rinzler, and R. E. Smalley, Length control of individual carbon nanotubes by nanostructuring with a scanning tunneling microscope, *Appl. Phys. Lett*. 71, 2629-2631 (1977).
58. T. W. Odom, J. L. Huang, Ph. Kim, and C. M. Lieber, Structure and Electronic Properties of Carbon Nanotubes, *J. Phys. Chem. B*, 104, 2794-2809 (2000).
59. T. W. Odom, J. L. Huang, and C. M. Lieber, STM studies of single-walled carbon nanotubes, *J. Phys. Condens. Mat.* 14, R145-R167 (2002).
60. Ph. G. Collins, K. Bradley, M. Ishigami, and A. Zettl, Extreme Oxygen Sensitivity of Electronic Properties of Carbon Nanotubes, *Science* 287, 1801-1804 (2000).
61. J. Kong, N. R. Franklin, Ch. Zhou, M. G. Chapline, S. Peng, K. Cho, and H. Dai, Nanotube Molecular Wires as Chemical Sensors, *Science* 287, 622-625 (2000).
62. I. Wirth, S. Eisebitt, G. Kann, and W. Eberhardt, Statistical analysis of the electronic structure of single-wall carbon nanotubes, *Phys. Rev. B* 61, 5719-5723 (2000).
63. R. Saito, G. Dresselhaus, and M. S. Dresselhaus, Trigonal warping effect of carbon nanotubes, *Phys. Rev. B* 61, 2981-2990 (2000).
64. A. Rubio, Spectroscopic properties and STM images of carbon nanotubes, *Appl. Phys. A* 68, 275-282 (1999).
65. Y. Xue and S. Datta, Fermi-Level Alignment at Metal-Carbon Nanotube Interfaces: Application to Scanning Tunneling Spectroscopy, *Phys. Rev. Lett*. 83, 4844-4847 (1999).
66. A. Kleiner and S. Eggert, Curvature, hybridization, and STM images of carbon nanotubes, *Phys. Rev. B*, 64, 113402-113406 (2001).

67. M. Ouyang, J-L. Huang, C. L. Cheung, and Ch. M. Lieber, Energy Gaps in "Metallic" Single-Walled Carbon Nanotubes, *Science* 292, 702-705 (2001).
68. V. Meunier and Ph. Lambin, Tight-Binding Computation of the STM Image of Carbon Nanotubes, *Phys. Rev. Lett*. 81, 5588-5591 (1999).
69. Ph. Lambin, A. Loiseau, C. Culot, and L. P. Biró, Structure of carbon nanotubes probed by local and global probes, *Carbon* 40, 1635-1648 (2002).
70. C. L. Kane and E. J. Mele, Broken symmetries in scanning tunneling images of carbon nanotubes, *Phys. Rev. B* 59, R12759-R12762 (1999).
71. W. Clauss, D. J. Bergeron, M. Freitag, C. L. Kane, E. J. Mele, and A. T. Johnson, Electron backscattering on single-wall carbon nanotubes observed by scanning tunneling microscopy, *Europhys. Lett.* 47, 601-607 (1999).
72. P. Lambin, G. I. Márk, V. Meunier, L. P. Biró, Computation of STM Images of Carbon Nanotubes, *Int. J. Quant. Chem.* 95, 493–503 (2003).
73. Ph. Lambin and V. Meunier, in *Carbon Filaments and Nanotubes: Common Origins, Different Applications?* edited by L. P. Biró, C. A. Bernardo, G. G. Tibbetts and Ph. Lambin, Kluwer Academic Publishers, Dordrecht (2001), p. 233.
74. G. I. Márk , A. Koós , Z. Osváth , L. P. Biró , J. Gyulai , A. M. Benito , W. K. Maser, P. A. Thiry, and Ph. Lambin, Calculation of the charge spreading along a carbon nanotube seen in scanning tunnelling microscopy (STM), *Diam. Rel. Mat.* 11, 961-963 (2001).
75. G. I. Márk, Ph. Lambin, and L. P. Biró, Calculation of axial charge spreading in carbon nanotubes and nanotube Y junctions during STM measurement, *Phys. Rev B* 70, 115423/1-10 (2004).
76. A. L. Macky and H. Terrones, Diamond from graphite, *Nature* 352, 762-762 (1991).
77. 77 J-C. Charlier, T. W. Ebbesen, and Ph. Lambin, Structural and electronic properties of pentagon-heptagon pair defects in carbon nanotubes, *Phys. Rev B* 53, 11108-11113 (1996).
78. A. V. Krasheninnikov, K. Nordlund, M. Sirviö, E. Salonen, and J. Keinonen, Formation of ion-irradiation-induced atomic-scale defects on walls of carbon nanotubes, *Phys. Rev. B* 63, 245405-245411 (2001).
79. Z. Osváth, G. Vértesy, L. Tapasztó, F. Wéber, Z. E. Horváth, J. Gyulai, and L. P. Biró, Atomically resolved STM images of carbon nanotube defects produced by Ar irradiation, *Phys. Rev B* 72, 045429/1-6 (2005).
80. Z. Osváth, A. A. Koós, Z. E. Horváth, J. Gyulai, A. M. Benito, M.T. Martínez, W. K. Maser, and L. P. Biró, Arc-grown Y-branched carbon nanotubes observed by scanning tunneling microscopy (STM), *Chem. Phys. Lett.* 365, 338-342 (2002).
81. L. P. Biró , R. Ehlich , Z. Osváth , A. Koós , Z. E. Horváth , J. Gyulai , and J. B. Nagy, From straight carbon nanotubes to Y-branched and coiled carbon nanotubes, *Diam. Rel. Mat.* 11, 1081-1085 (2002).
82. Ph. Lambin, G. I. Márk and L. P. Biró, Structural and electronic properties of coiled and curled carbon nanotubes having a large number of pentagon–heptagon pairs, *Phys. Rev B* 67, 205413/1-9 (2003).
83. D. J. Hornbaker, S.-J. Kahng, S. Misra, B. W. Smith, A. T. Johnson, E. J. Mele, D. E. Luzzi, and A. Yazdani, Mapping the One-Dimensional Electronic States of Nanotube Peapod Structures, *Science* 295, 828-831(2002).
84. K. F. Kelly, I. W. Chiang, E. T. Mickelson, R. H. Hauge, J. L. Margrave, X. Wang, G. E. Scuseria, C. Radloff, N. J. Halas, Insight into the mechanism of sidewall functionalization of single-walled nanotubes: an STM study, *Chem. Phys. Lett.* 313, 445-450 (1999).
85. Z. Kónya, I. Vesselenyi, K. Niesz, A. Demortier, A. Fonseca, J. Delhalle, Z. Mekhalif, J. B.Nagy, A. A. Koós, Z. Osváth, A. Kocsonya, L. P. Biró, and I. Kiricsi, Large scale production of short functionalized carbon nanotubes, *Chem. Phys. Lett.* 360, 429-435(2002).

STRUCTURAL DETERMINATION OF INDIVIDUAL SINGLEWALL CARBON NANOTUBE BY NANOAREA ELECTRON DIFFRACTION

E. THUNE, D. PREUSCHE, C. STRUNK*
Institut für Experimentelle und Angewandte Physik, Universität Regensburg, Universitätsstr. 31, D-93040 Regensburg, Germany

H. T. MAN, A. MORPURGO
Kavli Institute of NanoScience, Delft University of Technology, Lorentzweg 1, NL-2628 CJ Delft, The Netherlands

F. PAILLOUX
Laboratoire de Métallurgie Physique, Université de Poitiers, Bd M. & P. Curie, F-86962 Chasseneuil-Futuroscope Cedex, France

A. LOISEAU
Laboratoire d'Etudes des Microstructures, CNRS-ONERA, 29 avenue de la Division Leclerc, F-92322 Châtillon Cedex, France

Abstract. The determination of the exact values of (n,m) or equivalently (d, ϑ) for an individual singlewall nanotube (SWNT) is of great importance, in particular for comparison with transport measurements. In this study, the selected area electron diffraction technique is used to investigate the structure of individual carbon nanotubes grown by chemical vapor deposition (CVD) directly on TEM-Si_3N_4 membranes.

Keywords: SWNT; SAED; chiral indices

As grown, singlewall nanotubes (SWNTs) usually have a dispersion of chirality and diameter[1] because the nanotube structural energy is only weakly dependent on chirality.[2] For a quantitative comparison of the measured electric transport properties with theoretical predictions, it is highly desirable to identify the chiral indices of individual SWNTs. A complete determination of the structure (diameter and helicity) with enough spatial resolution to identify an individual

*To whom correspondence should be addressed. Christoph Strunk; e-mail: christoph.strunk@physik.uni-regensburg.de

V.N. Popov and P. Lambin (eds.), Carbon Nanotubes, 43–44.

nanotube is in practice a difficult task. The indices (*n*,*m*) of an individual nanotube can be identified using selected area electron diffraction (SAED).[3]

In this study, we grow carbon SWNTs directly on TEM-Si_3N_4 membranes previously decorated by electron beam lithography (EBL) with (a) a pattern of gold (Au) alignment marks in order to locate individual nanotubes, (b) with a pattern for catalyst particles for nanotube growth by chemical vapor deposition (CVD), and (c) with a pattern of iron-palladium (Fe-Pd) contact structures.

Atomic Force Microscopy (AFM) (Fig. 1, left) and High Resolution Transmission Microscopy (HRTEM) (Fig. 1, middle) characterizations were achieved and showed the presence of isolated SWNTs, 1-5 nm in diameter, with low contamination of amorphous carbon. The background from the amorphous Si_3N_4 membrane covers the weak signal of individual SWNT (see Fig. 1, middle) and does not allow us to determine the chirality of the nanotubes.

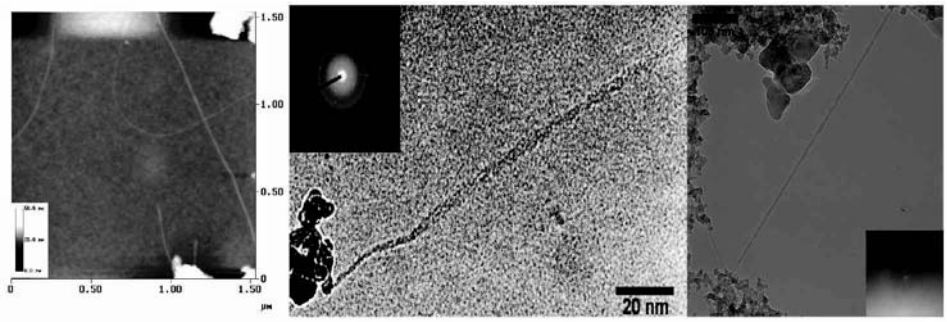

Figure 1. Left: AFM height image of isolated nanotubes on Si_3N_4 membrane. Middle: HRTEM image of an individual SWNT grown on Si_3N_4 membrane and its corresponding diffraction pattern. Right: TEM image of an individual SWNT on a ***perforated*** Si_3N_4 membrane and its corresponding diffraction pattern.

To avoid the Si_3N_4 background, the selected area electron diffraction requires an energy filter or use perforated membranes. Figure 1, right, shows an individual SWNT (5.5 nm in diameter) grown on perforated membranes. But, up to now, since individual SWNTs produce very low intensities, it was difficult to determine their chiral indices.

References

1. R. Saito, G. Dresselhaus, and M. S. Dresselhaus, *Physical properties of carbon nanotubes* (Imperial College Press, London, 1998).
2. J. W. Mintmire and C. T. White, Electronic and structural properties of carbon nanotubes, *Carbon* 33, 893- 902 (1995).
3. M. Gao, M. Zuo, R. D. Twesten, I. Petrov, L. A. Nagahara, and R. Zhang, Structure determination of individual single-wall carbon nanotubes by nanoarea electron diffraction, *Appl. Phys. Lett.* 82, 2703-2705 (2003).

THE STRUCTURAL EFFECTS ON MULTI-WALLED CARBON NANOTUBES BY THERMAL ANNEALING UNDER VACUUM

K. D. BEHLER, H. YE, S. DIMOVSKI, Y. GOGOTSI
Drexel University, Philadelphia, PA 19103, USA

Abstract. Characterization of Vacuum Thermal Annealing of a new variety of Multiwalled Carbon Nanotubes (MWCNT) produced in a Catalytic Chemical Vapor Deposition (CCVD) process by Arkema, France, was preformed by Raman Spectroscopy (RS) and Transmission Electron Microscopy (TEM).

Keywords: Nanotube; Raman; Transmission Electron Microscopy; Annealing

Recently, small tubes, having advantages with respect to mechanical and thermal properties over larger tubes, expect to see manufacturing capabilities allowing large scale quantities that may dominate the market within 2-3 years.

The effects of heat treatment were noticeable for the nanotubes when compared to the as-received tubes. The tubes were vacuum annealed (10^{-6} atm) for 3 hours at 1800°C and 2000°C. Catalyst removal can be seen in Figure 1. The as-received tubes encompass the metal catalyst (Fig. 1a); whereas catalyst removal occurs after vacuum annealing (Fig. 1b).

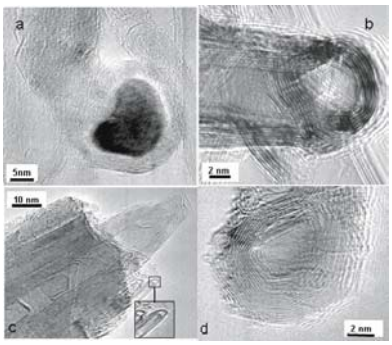

Figure 1. TEM of MWCNTs.

Individual tubes appear to be more graphitic after the 1800°C treatment and even more so after the treatment at 2000°C as evidenced by the RS, Figure 2

V.N. Popov and P. Lambin (eds.), Carbon Nanotubes, 45–46.

(excitation energy of 1.96 eV). A separation of the G and D' begins to occur, as seen in the inset, as the treatment temperature increases, implying that the tubes are transforming to a more graphitic structure.

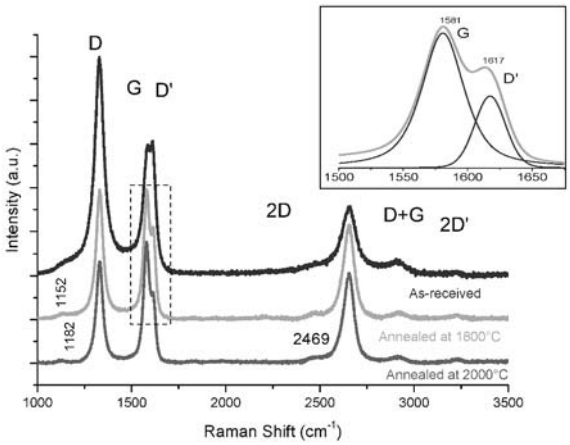

Figure 2. Raman Spectra of MWCNTs.

Some tubes after treatment also show overgrowth, as shown in Figure 1c. The original tube, which is currently in the center of tube, has a sheath-like growth that is enclosing the original structure. Thickening of the tubes indicates mass transfer occurs during the annealing process. The observed tubes show a polygonal graphite structure as the tube walls start to become less cylindrical (Fig 1d) similar to graphite polyhedral crystals.[1] There is also an elimination of dangling bonds nanotube tips through the "lip+lip" interactions as seen in the inset of Figure 1c. The graphene sheets are connecting to other sheets and forming a loop,[2] preventing bonding at the end of the tube by reducing the number of possible bonding sites and thus eliminating dangling bonds. Such nanotubes are expected to be less chemically active.

Vacuum annealing leads to catalyst removal, polygonization and graphitization of MWCNT. It may lead to higher conductivity and improved electrical properties. Excessive over growth and polygonization occur above 1800°C.

References

1. Y. Gogotsi, J. A. Libera, N. Kalashnikov, and M. Yoshimura, Graphite polyhedral crystals. *Science* 290, 317-320 (2000).
2. S. Rotkin and Y. Gogotsi, Analysis of non-planar graphitic structures: from arched edge planes of graphite to nanotubes, *Mat. Res. Innovat*. 5, 191-200 (2002).

TEM SAMPLE PREPARATION FOR STUDYING THE INTERFACE CNTS-CATALYST-SUBSTRATE

MARIE-FAITH FIAWOO, ANNICK LOISEAU
LEM UMR 104 CNRS/ONERA, 92322 Châtillon, France

ANNE-MARIE BONNOT, ANTONIO IAIA
LEPES-CNRS UPR11, 38042 Grenoble, France

VINCENT BOUCHIAT
CRTBT-CNRS UPR5001, 38042 Grenoble, France

JANY THIBAULT
TECSEN CNRS UMR 6122, Univ. Paul Cézanne, 13397 Marseille, France

Abstract. We study by Transmission Electron Microscopy (TEM) in-situ self-assembled carbon nanotubes (CNTs) grown by the Hot Filament Chemical Vapor Deposition (HFCVD) process on silicon substrates used for electronic devices. We present the different methods we have developed for extracting CNTs and studying their interface with the substrate as they are observable by TEM.

Keywords: TEM preparation technique, nanotubes, SACT, cleavage, ion milling

For studying specimens by TEM and performing analysis (EFTEM, EELS), the sample needs to be thin (20 to 30 nm), transparent to electrons, smaller than 3 nm diameter to fit in the TEM holder and keep its intrinsic features. We want to study the interface CNTs-catalyst-substrate in localized CNTs synthesis (Marty et al., 2002) aiming to understand the CNTs growth by Chemical Vapor Deposition (CVD) process like previously done for high temperature synthesis (Loiseau et al., 2004). Here we present different preparation methods which we tried in order to reach the required thickness necessary for the study of the interface of nanotubes with a single crystal silicon substrate.

Four types of preparation have been tested: scratching the sample, ion milling, Si_3N_4 membrane system, and small angle cleavage technique (SACT).

*To whom correspondence should be addressed. Marie-Faith Fiawoo; e-mail: fiawoo@onera.fr

V.N. Popov and P. Lambin (eds.), Carbon Nanotubes, 47–48.

Some of them enable plane view, cross-section observations or both. Scratching the sample with a tweezer or a diamond scribe to deposit on a TEM grid seldom enables observations of the interface because of the thickness of the piece scratched. Ion milling technique involves a mechanical polishing before thinning the sample by pulling out atoms of the sample with an ion beam of argon Ar+ (Fig. 1, left). A disadvantage of this technique is the introduction of artifacts. The Si_3N_4 membrane with a rectangular hole has CNTs grown on the membrane as well as across the hollow. Unfortunately, the hole's edge in not thin enough to see the interface. SACT consists in cleaving the sample along the (120) and (110) planes, which form an angle of 18.43° (Fig. 1, right). This small angle of the apex of the sample allows its transparency to electrons (Walck et al., 1997). The disadvantage of this technique is the small area transparent to electrons, which is not adapted for a sample having a few CNTs.

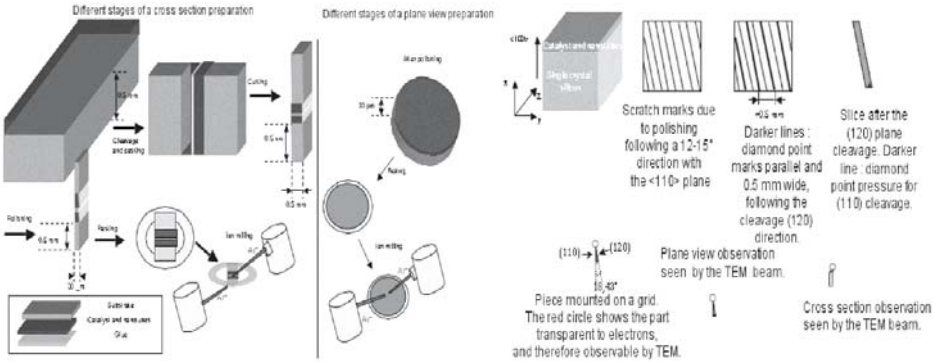

Figure 1. Left: Ion milling preparation stages; Right: Different stages of SACT.

For the time being, the ion milling technique is the only one, which enables the systematical observation and analysis of the interface. Further investigations, such as focused ion beam cutting and other membrane systems, are presently being carried out.

References

Marty, L., Bouchiat, V., Bonnot, A.M., Chaumont, M., Fournier, T., Decossas, S., and Roche, S. 2002, Batch processing of nanometer-scale electrical circuitry based on in-situ grown single-walled carbon nanotubes, *Microelectronic Engineering* **61-62:**485-489.

Loiseau, A., Gavillet, J., Ducastelle, F., Thibault, J., Stéphan, O., Bernier, P., and Thair, S., 2004, Nucleation and growth of SWNT: TEM studies of the role of the catalyst, *C. R. Physique* **4:**975-991.

Walck, S.D., and McCaffrey, J.P, 1997, The small angle cleavage technique applied to coatings and thin films, *Thin Solid Films* **308-309:**399-405.

A METHOD TO SYNTHESIZE AND TAILOR CARBON NANOTUBES BY ELECTRON IRRADIATION IN THE TEM

R. CAUDILLO,* M. JOSÉ-YACAMAN
Materials Science and Engineering and Texas Materials Institute, University of Texas at Austin, 1 University Station C2201, Austin, Texas 78712, USA

H. E. TROIANI
Centro Atómico Bariloche and Instituto Balseiro, CNEA and UNC, 8400 Bariloche, Rio Negro, Argentina

M. A. L. MARQUES, A. RUBIO
Donostia International Physics Center, Paseo Manuel Lardizábal 4, 20018 San Sebastián, Spain

Abstract. Carbon nanotubes (CNTs) can be synthesized from amorphous carbon thin films by electron irradiation in the transmission electron microscope (TEM). We propose that irradiation effects impart a tensile stress and introduce defects to a CNT thus formed and show that the CNTs can be made to fracture by a brittle or ductile mechanism. We also report a healing of the carbon film that is observed after some critical amount of irradiation.

TEM is normally only used to characterize CNTs synthesized by standard techniques, such as arc discharge, laser ablation, or chemical vapor deposition (CVD); however, Troiani et al.[1,2] have shown that it is also possible to use electron irradiation in a TEM to construct single-walled carbon nanotubes (SWCNT) from an amorphous carbon film. In this method, two through-holes are created in an amorphous carbon film using electron-beam irradiation in a TEM. A thin graphitic fiber forms in between the two holes and is narrowed until forming a SWCNT. Here we show that by controlling the current density on a CNT formed by this technique, it is possible to cause fracture and to observe the fracture mechanism in the TEM. We observe that the CNT fractures either by a brittle or ductile fracture mechanism, depending on the amount of current density on the sample.

*To whom correspondence should be addressed. Roman Caudillo; email: rcaudillo@mail.utexas.edu

V.N. Popov and P. Lambin (eds.), Carbon Nanotubes, 49–50.

We propose two mechanisms working to achieve the narrowing of the bridge: (1) deformation in response to an axial stress resulting from a contraction of the film due to radiation-induced graphitization and (2) creation of defects in the bridge due to irradiation, resulting in vacancy clustering that leads to brittle fracture or atomic rearrangements that lead to plastic fracture. Figure 1 shows CNT formation at the neck of a bridge and the formation of a linear chain of carbon atoms during the ductile deformation of the CNT.

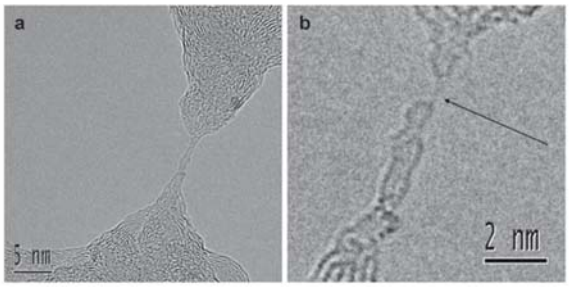

Figure 1. (a) TEM image showing the formation of a CNT at the neck of a bridge, (b) TEM image showing the formation of a linear chain of carbon atoms (signaled by arrow) in a CNT neck that has undergone ductile deformation.

We also observe a surprising phenomenon during prolonged irradiation of carbon nanotubes and carbon nanofibers formed by electron irradiation in the TEM, in which a sudden diffusion of carbon atoms to the bridge structure and periphery of the holes results in a reconstruction of the carbon film, which in some cases results in a complete closing of the holes.[3]

These results indicate that CNTs, as well as other carbon nanostructures, can be synthesized and tailored by electron irradiation, and suggests the possibility of larger scale, carbon nanostructure design by e-beam lithography and complementary techniques.

References

1. H. E. Troiani, M. Miki-Yoshida, G. A. Camacho-Bragado, M. A. L. Marques, A. Rubio, J. A. Ascencio, and M. Jose-Yacaman, Direct observation of the mechanical properties of single-walled carbon nanotubes and their junctions at the atomic level, *Nano Letters* 3(6), 751-755 (2003).
2. M. A. L. Marques, H. E. Troiani, M. Miki-Yoshida, M. Jose-Yacaman, and A. Rubio, On the breaking of carbon nanotubes under tension, *Nano Letters* 4(5), 811-815 (2004).
3. R. Caudillo, H. E. Troiani, M. Miki-Yoshida, M. A. L. Marques, A. Rubio, and M. Jose-Yacaman, A viable way to tailor carbon nanomaterials by irradiation-induced transformations, *Radiation Physics and Chemistry* (In Press) (2005).

SCANNING TUNNELING MICROSCOPY STUDIES OF NANOTUBE-LIKE STRUCTURES ON THE HOPG SURFACE

I. N. KHOLMANOV,[1,2] M. FANETTI,[1] L. GAVIOLI,[1]
M. CASELLA,[1] M. SANCROTTI[1,3]

[1]*INFM and Dipartimento di Matematica e Fisica, Università Cattolica del Sacro Cuore, Via dei Musei 41, 25121 Brescia, Italy*
[2]*Thermophysics Department, Academy of Sciences, Katartal str., 28, 700135 Tashkent, Uzbekistan*
[3]*Laboratorio Nazionale TASC-INFM, Strada Statale 14, Km 163.5, Basovizza, I-34012 Trieste, Italy*

Abstract. We have studied the scanning tunneling microscopy tip interaction with the naturally formed nanotube-like (NTL) structures on highly oriented pyrolytic graphite (HOPG) surface. Shape variations of the NT-like structures, caused by the modulation of scanning parameters, were observed and analyzed.

Keywords: STM; highly oriented pyrolytic graphite; nanotube-like structures

Scanning tunneling microscopy (STM) and spectroscopy (STS) are widely employed to obtain information on local electronic properties, surface geometry, and nanostructure-surface interactions.[1]

We report on STM studies of the NTL structures formed on HOPG surface. STM (OMICRON ultra-high vacuum (UHV) system) measurements have been carried out in UHV at room temperature, in constant-current mode using tungsten tips. HOPG specimen has been prepared by cleaving (adhesive tape) in air, and annealed in UHV chamber at 900 °C.

Naturally-formed NTL structures located on steps were formed by the spontaneous folding of the HOPG graphene sheets, or by STM tip manipulation.[2] The NTL, presented in Fig. 1, is located at a HOPG step edge, with an apparent width of 1.77 nm. The height difference of the graphene layers between the right and left side of the NTL structure is 0.86 nm, quite close to

V.N. Popov and P. Lambin (eds.), Carbon Nanotubes, 51–52.

the height of two graphene sheets. The image has been acquired with two different tunneling currents, corresponding to region *A* (0.1 nA) and *B* (0.2 nA), respectively. Region *A* corresponds to the typical appearance of the NTL structure with continuity of the distorted graphite lattice on the curved structure.

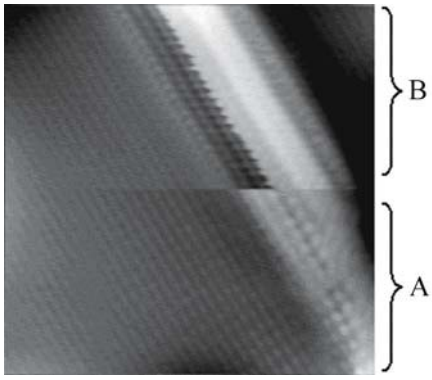

Figure 1. STM image (8×8 nm2) of NTL structure on the step edge of the HOPG graphene sheet. Scanning parameters: gap voltage +0.253 V and current 0.1 nA (region *A*) and 0.2 nA (region *B*).

Variation of tunneling parameters leads to dramatic changes of the NTL apparent shape. In region *B*, the NTL presents a large modification of the NTL curvature that becomes a large depression in the graphite structure. The maximum depth of the depression, with respect to the unmodified structure, is 0.4 nm. Such variation is not observed when the tip is moving from right side to left side of Fig.1, i.e., the backward direction. Hence the shape change behavior is asymmetric. The NTL recovers its original shape by simply restoring a lower current, without presenting any hysteresis in the apparent height variation.

These observations suggest that the deformations may actually be induced by the modification of the tip-substrate interaction strength, and that the NTL structure reacts in an elastic way to the STM tip. Although these features may support deformation-based mechanism of the shape-changes, further detailed analysis is required to elucidate the obtained experimental results. The results suggest a possible development of STM as a tool to investigate the mechanical properties of nanosystems.

References

1. T. W. Odom, J. H. Hafner, Ch. M. Lieber, in: *Carbon Nanotube: Synthesis, Structures, Properties and Applications*, edited by M. S. Dresselhaus, G. Dresselhaus and Ph. Avouris (Springer-Verlag, Berlin, 2001) pp. 177-215.
2. H.-V. Roy, C. Kallinger, B. Marsen, and K. Sattler, J. Appl. Phys. 83, 4695-4699 (1998).

INFLUENCE OF CATALYST AND CARBON SOURCE ON THE SYNTHESIS OF CARBON NANOTUBES IN A SEMI-CONTINUOUS INJECTION CHEMICAL VAPOR DEPOSITION METHOD

Z. E. HORVÁTH, A. A. KOÓS,* Z. VÉRTESY, L. TAPASZTÓ, Z. OSVÁTH, P. NEMES INCZE, L. P. BIRÓ
Research Institute for Technical Physics and Materials Science, P.O. Box 49, H-1525, Budapest, Hungary

K. KERTÉSZ, Z. SÁRKÖZI, AL. DARABONT
Babes-Bolyai University, Faculty of Physics, Kogãlniceanu 1, RO-3400, Cluj-Napoca, Romania

Abstract. The injection chemical vapor deposition (CVD) method allows the semi-continuous production of pure multi-wall carbon nanotubes (MWCNTs). In order to find the most efficient catalyst material and carbon source, we investigated the quality and quantity of carbon nanotubes, when different metallocenes (ferrocene, cobaltocene and nickelocene) and hydrocarbons (benzene, toluene, xylene, cyclohexane, cyclohexanone, n-hexane, n-heptane, n-octane and n-pentane) are injected into the reaction furnace. The obtained samples were analyzed by Transmission Electron Microscopy (TEM). The highest yield and the best quality were obtained when a mixture of ferrocene-nickelocene was used as catalyst and xylene as carbon source. The weight of purified carbon nanotubes was higher than 50% of the weight of catalyst material for xylene and reached the 10% for all investigated carbon sources.

Keywords: carbon nanotubes; chemical vapour deposition; electron microscopy

The major advantage of the injection CVD method is the *in-situ* and continuous generation of catalytic particles throughout the entire growth cycle. Therefore, the injection CVD method does not need a catalyst synthesis step and can be scaled up for continuous or semi-continuous production. We investigated the quality and quantity of carbon nanotubes when different metallocenes and hydrocarbons were injected into the reaction furnace.

*To whom correspondence should be addressed. Antal Koós; e-mail: koos@mfa.kfki.hu

V.N. Popov and P. Lambin (eds.), Carbon Nanotubes, 53–54.

We used the following reaction parameters: 6 g metallocene in 100 ml hydrocarbon catalyst concentration (except for the cases when the solubility of the metallocene in the hydrocarbon was too low), 1 ml/min solution flow-rate, 875 °C furnace temperature and 500 l/h Ar (carrier gas) flow-rate. The samples were purified using a 45% HNO_3 aqueous solution.

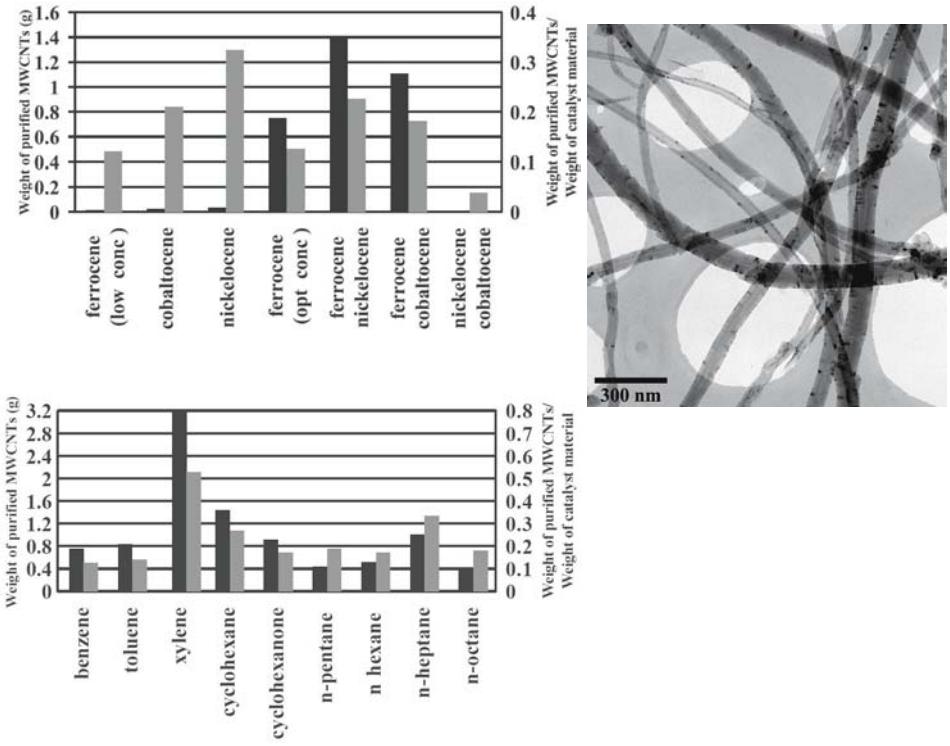

Figure 1. Left: comparison of the weight of purified carbon nanotubes produced with different catalysts and carbon sources (black) and the weight of purified carbon nanotubes normalized to the weight of the catalyst material (grey). Right: TEM image of MWCNTs prepared using xylene as a carbon source.

Pure MWCNTs were grown. The MWCNTs were produced with maximum yield when ferrocene – nickelocene catalyst mixture was used and xylene was found to be the most efficient carbon source. For xylene, the weight of purified carbon nanotubes normalized to the weight of catalyst material was higher than 50%.

Work supported by the Sapientia Research Programs Institute in the framework of Fellowships 822/2001 K/513/2003.03.25, and by the MTA-MEH Grant "Nanogas" and by OTKA through Grant nr. T043685 and M 041689.

PECVD GROWTH OF CARBON NANOTUBES

ALEXANDER MALESEVIC,* A. VANHULSEL
Flemish Institute for Technological Research, Boeretang 200, 2400 Mol, Belgium

C. VAN HAESENDONCK
Solid State Physics, KULeuven, Celestijnenlaan 200 D, 3001 Heverlee, Belgium

Abstract. We report on the growth of carbon nanotubes by plasma-enhanced chemical vapor deposition (PECVD). We used acetylene and ammonia gas mixtures with a process pressure of 1 Torr for the growth of carbon nanotubes on nickel layers. The metal catalyst, just a few nanometers thick, was patterned on oxidized silicon substrates by electron beam lithography. Our aim was to develop a cheap mass production method to grow high quality, aligned carbon nanotubes. We used different plasma setups and scanned individual growth parameters in order to achieve that goal. In this work, we compare the different results obtained by direct current (DC) plasma deposition.

Keywords: carbon nanotubes; plasma-enhanced chemical vapor deposition; DC plasma deposition; mass production

Whereas most groups concentrate on only one particular type of plasma for the growth of carbon nanotubes, we have built a unique setup which combines DC, radio-frequency (RF) and inductively-coupled (ICP) plasma sources. A scheme of the setup is drawn in Fig. 1, left. In the case of a DC or RF bias, we apply a negative voltage to a resistively heated electrode and ignite plasma between the electrode and the grounded reactor walls. A dense RF-ICP source can be used in addition to or in combination with the DC or RF substrate biasing.

In order to compare the results of different types of plasma, we started to grow carbon nanotubes with the DC plasma enhanced chemical vapor deposition (PECVD) technique.

*To whom correspondence should be addressed. Alexander Malesevic, VITO Materialen, Boeretang 200, 2400 Mol; email: alexander.malesevic@vito.be

V.N. Popov and P. Lambin (eds.), Carbon Nanotubes, 55–56.

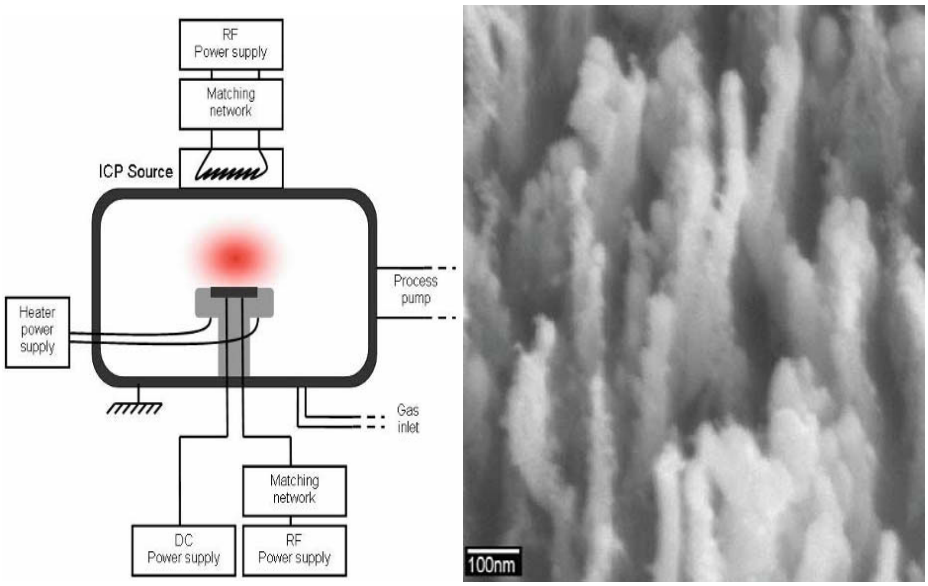

Figure 1. Left: Schematic view of a PECVD setup. Right: SEM image of carbon nanotubes obtained with an acetylene to ammonia ratio of 25/100 sccm.

The samples consist of a 5 nm thick nickel layer that is deposited by a conventional molecular beam epitaxy (MBE) technique on a silicon (100) substrate with a silicon oxide buffer layer of 200 nm. The samples were placed on the electrode and the reactor is pumped down to a base pressure of 10^{-6} mBarr. The electrode was resistively heated up to 700°C in a continuous flow of 100 sccm ammonia at 1 mBarr. The samples were annealed at 700°C during 10 minutes and afterwards pretreated in ammonia plasma of 600 V during 10 minutes. The growth was initiated by allowing the carbon containing gas, diluted with ammonia, in the reactor for 20 minutes.

As carbonaceous gas, we used acetylene, methane, propane and butadiene in combination with ammonia. We varied the ratio of the carbonaceous gas to ammonia from 15/100 to 33/100 sccm. The combination acetylene with ammonia was each time successful for the growth of carbon nanotubes, independent of the gas ratio. A typical result is presented in Fig. 1, right. Among the other gas mixtures, only the combination of methane with ammonia yielded carbon nanotubes.

CARBON NANOTUBES GROWTH AND ANCHORAGE TO CARBON FIBRES

TH. DIKONIMOS MAKRIS,* R. GIORGI, N. LISI, E. SALERNITANO
ENEA Casaccia Research Centre, 00060 Rome, Italy

M. F. DE RICCARDIS, D. CARBONE
ENEA Brindisi Research Centre, 72100 Brindisi, Italy

Abstract. A novel material made of carbon fabrics with a uniform three-dimensional (3D) distribution of carbon nanotubes (CNTs) on the surface was synthesized by an electrochemical deposition (ELD) process.

Keywords: carbon nanotubes; electrochemical deposition

The CNT exceptional tensile strength and modulus are deemed to improve the tensile properties of a polymeric matrix composite. In order to fully utilise the mechanical properties and the lightness of CNT, a sufficient volume fraction should be dispersed into the matrix.[1] The problems are connected with the CNT aggregation and floating. The 3D distribution achieved by coating fabrics of carbon fibres with CNT could provide a way for dispersing the CNT across the composite. Moreover, CNT could further enhance the mechanical properties of composite materials traditionally reinforced with carbon fibres by enhancing the interfacial bonding between polymer and carbon fibre acting as fillers of micropores.[2]

ELD process was used to deposit Ni catalyst on PAN and Pitch based carbon fibres. Different deposition conditions were tested in order to optimise the dimension, morphology, and density of the Ni clusters.[3,4] A Hot Filament assisted CVD reactor was used for the CNT growth.[5,6] On both PAN and Pitch based carbon fibres, independently of the cluster size, density and morphology, clean CNT with low impurity content and rather smooth walls were grown.[6] A high density of CNT was obtained on carbon fibres fabric (see Fig. 1, left), even at the critical cross over regions, as shown in Fig. 1, center. This result indicates

*To whom correspondence should be addressed. Th. Dikonimos Makris; e-mail: dikonimos@casaccia.enea.it

V.N. Popov and P. Lambin (eds.), Carbon Nanotubes, 57–58.

that all fabric fibres were coated by the catalyst giving rise to such a dense CNT network. Mechanical test usually performed to measure the adhesion of thin films on a substrate are not reliable in this case due to the peculiar nature of the substrate and the coating itself. Pseudo-mechanical tests, based on the idea of exposing the three-component material (carbon fibre plus metallic cluster plus carbon nanotubes) to stressing environments were performed.[7] Samples were treated by immersion, magnetic stirring, centrifugation and ultrasonic bath in four different liquids (deionised water, ethanol, n-butanol, and acetone). After the treatment, the Ni clusters remained anchored to the fibres. As illustrated in Fig. 1, right, for the ultrasonic bath test in acetone, CNT were still present with high density on the fibre surface.

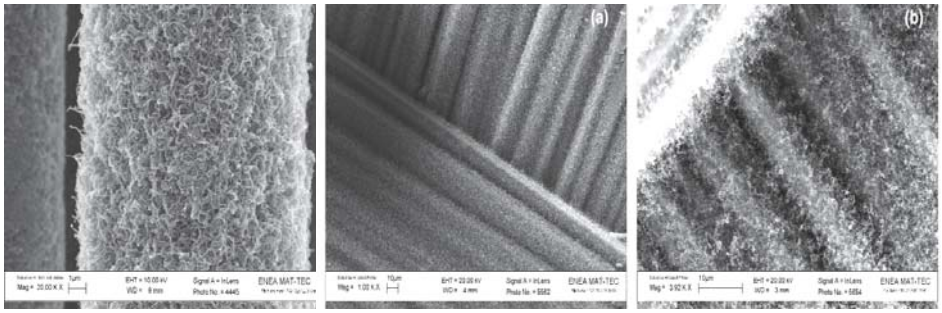

Figure 1. Left and center: high density CNT grown on carbon fibres fabrics. Right: carbon fibres after ultrasonic bath in acetone for 5 minutes.

References

1. C. Bower, R. Rosen, L. Jin, J. Han, and Q. Zhou, Deformation of carbon nanotubes in nanotube-polymer composites, *Appl.Phys.Lett.*74(22), 3317-3319 (1999).
2. E. T. Thostenson, W. Z. Li, D. Z. Wang, Z. F. Ren, and T. W. Chou, Carbon nanotube/carbon fibre hybrid multiscale composites, *Journal of Applied Physics* 91, 6034-6037 (2002).
3. E. Gómez, R. Pollina, and E. Vallés, Morphology and structure of nickel nuclei as function of the conditions of electrodeposition, *J. of Electroanalytical Chemistry* 397, 111-118 (1995).
4. E. Gómez, R. Pollina, and E. Vallés, Nickel electrodeposition on different metallic substrates, *J. of Electroanalytical Chemistry* 386, 45-46 (1995).
5. Th. Dikonimos Makris, R. Giorgi, N. Lisi, L. Pilloni, E. Salernitano, F. Sarto, and M. Alvisi, Carbon nanotubes growth by HFCVD: effect of the process parameters and catalyst preparation, *Diamond and Related Materials* 13, 305-310 (2004).
6. Th. Dikonimos Makris, R. Giorgi, N. Lisi, L. Pilloni, E. Salernitano, and F. De Ricardis, Carbon nanotubes growth on PAN and Pitch based carbon fibres by HFCVD, *Fullerenes, Nanotubes and Carbon Nanostructures* 13(1), 383-392 (2005).
7. M. F. De Riccardis, D. Carbone, Th. Dikonimos Makris, R. Giorgi, N. Lisi, and E. Salernitano, Anchorage of carbon nanotubes grown on carbon fibres, *Carbon* (2005) (submitted).

CVD SYNTHESIS OF CARBON NANOTUBES ON DIFFERENT SUBSTRATES

TH. DIKONIMOS MAKRIS, L. GIORGI, R. GIORGI, N. LISI, E. SALERNITANO
ENEA Casaccia Research Centre, 00060 Rome, Italy

M. ALVISI, A. RIZZO
ENEA Brindisi Research Centre, 72100 Brindisi, Italy

Abstract. Carbon nanotubes (CNTs) were grown using three different chemical vapor deposition (CVD) processes. Optimized conditions were studied.

Keywords: carbon nanotubes; chemical vapor deposition process

CNTs were grown on differently supported Ni catalytic nanoparticles on flat and bulk substrates using H_2 and CH_4 as precursors. The different behavior of the same metal catalyst in the presence of the same precursor varying the gas activation by different energy sources, using Hot Filament, Plasma Enhanced (PE), and pure Thermal CVD processes, was studied. By properly choosing the process parameters, dense CNTs were grown by HFCVD on 3 nm Ni thin film deposited by Evaporation and Radio-frequency (RF) Sputtering onto flat Si substrates coated with an intermediate SiO_2 layer[3] (Fig. 1a). Prior to the growth, the samples were heated in H_2 atmosphere and the Ni clusters distribution shown in Fig. 2a was obtained. No CNT growth was obtained on the same sample in the thermal CVD reactor, but only cluster coalescence was observed (Fig. 2b). CNT grew sparsely in the PE CVD reactor. The different results were ascribed to: i) the catalytic decomposition of the precursors was more efficient where an additional activation source was present; ii) weak interaction between the Ni cluster and the SiO_2 substrate could favour cluster coalescence, which was the dominant effect in the thermal CVD process.

Flat Al_2O_3 substrate coated by a 3nm Ni film, deposited by RF Sputtering, were subjected to the same clustering and CNT growth process in Thermal and PE CVD. The thermal process failed as in the previous case giving rise to

*To whom correspondence should be addressed: Th. Dikonimos Makris; e-mail: dikonimos@casaccia.enea.it

V.N. Popov and P. Lambin (eds.), Carbon Nanotubes, 59–60.

aggregation of Ni clusters distributed on alumina grain surfaces. On the opposite, in the PE reactor, a dense distribution of Ni nanoclusters was obtained (Fig. 2c), followed by a dense CNT growth (Fig. 1b).

The commercial catalyst, consisting of Ni nanoparticles supported on alumina microparticles, was tested in the thermal CVD process for CNT growth (Fig. 1c). This catalyst exhibited a high productivity and a yield of 15mgC/mgNi was obtained.[4] The reason for this could be attributed to the higher metal dispersion on highly porous material. Moreover, the stronger interaction existing between the catalyst and the support prevented metal particles from aggregating and forming unwanted large particles. It could not be excluded that even an electronic interaction existed and it was responsible for the lowering of the catalyst activation barrier.

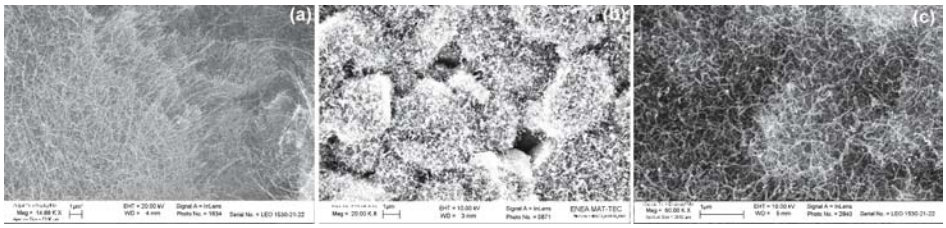

Figure 1. CNT growth on $Ni/SiO_2/Si$ flat sample in HFCVD (a), on Ni/Al_2O_3 flat sample in PECVD (b) and on Ni/Al_2O_3 pellet in Thermal CVD (c).

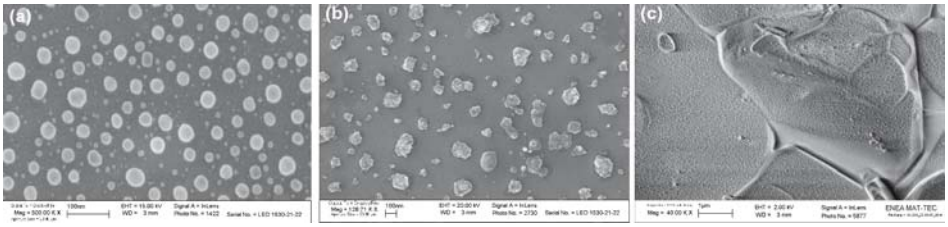

Figure 2. Cluster distribution on $Ni/SiO_2/Si$ flat sample in HFCVD (a) and Thermal CVD (b) and on Ni/Al_2O_3 flat sample in PECVD.

References

1. S. Hoffmann, B. Kleinsorge, C. Ducati, A. C. Ferrari, and J. Robertson, Low-temperature plasma enhanced chemical vapour deposition of carbon nanotubes, *Diamond and Related Materials* 13, 1171-1176 (2004).
2. K. Hernadi, Z. Konya, A. Siske, J. Kiss, A. Oszko, J. B. Nagy, and I. Kiricsi, On the role of the catalyst support and their interaction in synthesis of carbon nanotubes by CCVD, *Mater. Chem.Phys*. 77, 536-541 (2002).
3. Th. Dikonimos, R. Giorgi, N. Lisi, E. Salernitano, L. Pilloni, M. Alvisi, and F. Sarto, Carbon nanotubes growth by HFCVD: effect of the process parameters and catalyst preparation, *Diamond and Related Materials* 13, 305-310 (2004).
4. Th. Dikonimos, L. Giorgi, R. Giorgi, N. Lisi, and E. Salernitano, CNT growth on alumina supported nickel catalyst by thermal CVD, *Diamond and Related Materials* 14, 815-9 (2005).

INFLUENCE OF THE SUBSTRATE TYPES AND TREATMENTS ON CARBON NANOTUBE GROWTH BY CHEMICAL VAPOR DEPOSITION WITH NICKEL CATALYST

R. RIZZOLI, R. ANGELUCCI, S. GUERRI, F. CORTICELLI
CNR - IMM Bologna, via P. Gobetti 101, 40129 Bologna, Italy

M. CUFFIANI, G. VERONESE
Department of Physics, University of Bologna, viale Berti Pichat 6/2, 40127 Bologna, Italy

Abstract. Our investigation aimed at the development of a process capable of producing well ordered, vertically aligned carbon nanotubes (CNTs) arrays, with reproducible properties, for applications such as a position particle detector and a cold cathode emitter for storage devices. The results on catalyst nanoparticles formation from a thin Ni film evaporated on SiO_2 and Si_3N_4 substrates are presented. The substrate-catalyst layers have been processed in several gaseous atmospheres and in the temperature range 700-900°C in order to obtain the most appropriate morphology, size and density of the nanoparticles for the subsequent CNTs growth. The smallest nanoparticles have been obtained on the SiO_2 substrate in H_2 atmosphere and at the lowest temperature 700°C. However, the best vertically aligned and well graphitized CNTs resulted from the NH_3 annealing process followed by the deposition of CNTs at 900°C in C_2H_2 and NH_3.

Keywords: Carbon nanotubes; Ni catalyst; chemical vapor deposition synthesis

Ni thin films, 2 nm thick, were deposited by e-gun evaporation on SiO_2 / Si and Si_3N_4 /Si substrates. The Ni nanoparticles (NPs) formation was studied varying the gas atmosphere (Ar, NH_3 and H_2) and the temperature (in the range 700°C-900°C) applied during the warm-up and annealing steps prior to the CNTs deposition step. Vertically aligned CNTs were grown by atmospheric pressure chemical vapor deposition in C_2H_2 + NH_3 gas mixtures at temperatures in the range 750-900°C.

V.N. Popov and P. Lambin (eds.), Carbon Nanotubes, 61–62.

The investigation on the formation of Ni NPs, starting from a 2 nm thick Ni film, showed that the NP dimensions are mainly affected by the nature of the substrate layer. The NPs average diameter is smaller on SiO_2 than on Si_3N_4 substrates. The use of a reducing (H_2 or NH_3) or inert (Ar) gas atmosphere during the NPs thermal treatment had a strong impact on their properties: size, morphology and chemical composition of subsurface layers both of the NPs and of the underlying substrate. For each gas atmosphere, with increasing the annealing temperature in the range 700° - 900°C on Si_3N_4 substrates, the NPs size decreases, while on SiO_2, it remains almost unchanged. The smallest NPs, shown in the SEM image of Fig. 1, were obtained on SiO_2 after annealing in H_2 at 700°C (scale bar on the bottom left side corresponds to 100 nm).

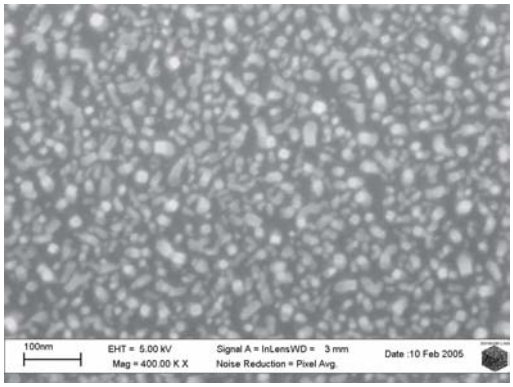

Figure 1. SEM images of Ni NPs on a SiO_2 substrate after annealing at 700°C in H_2 .

However, the best multiwalled CNTs, vertically aligned and well graphitized, resulted from the NH_3 annealing process followed by the deposition of CNTs in 5% C_2H_2 in NH_3 at 900°C, on a SiO_2 substrate. SEM and HRTEM images of these CNTs are displayed in Fig. 2.

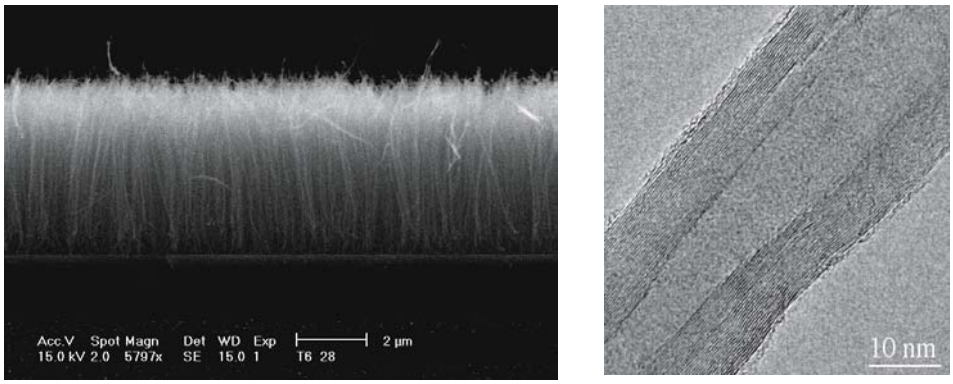

Figure 2. Left: cross-section SEM image of CNTs grown in C_2H_2 + NH_3 at 900°C on Ni NPs formed in NH_3; Right: HRTEM micrograph of one of these MWNTs.

NON CATALYTIC CVD GROWTH OF 2D-ALIGNED CARBON NANOTUBES

NADEZDA I. MAKSIMOVA, JORG ENGSTLER, JORG J. SCHNEIDER*
Dept of Chemistry, Eduard-Zintl Inst. of Inorganic and Physical Chemistry, Tech. University, 64287 Darmstadt, Germany

Abstract. Aligned carbon nanotubes (CNTs) were grown in the channels of porous alumina membranes via a non-catalytic chemical vapor deposition (CVD) method. The morphology of the samples was studied.

Keywords: carbon nanotubes; non-catalytic chemical vapor deposition method

Carbon nanotubes (CNTs) produced by catalytic methods contain metal nanoparticles that cannot be removed completely and may have negative effect on the performance of the CNTs for microelectronic applications.[1] Herein, we present an optimized synthesis procedure for well-aligned CNT arrays. It includes a new post-process purification approach to remove carbonaceous by-products.

Aligned CNT arrays were grown in the tubular channels of porous anodic alumina oxide (PAOX) membranes (Anodisc 25, Whatman) with different pore diameters at 900°C by a CVD method based on propylene decomposition.[2] The morphology of the samples was examined using scanning electron microscopy (Philips XL-30 FEG).

In the non-catalytic CVD process, the carbon atoms or reactive -C- fragments within a PAOX template are directly deposited on the surface of PAOX membrane (Fig. 1, left). In this case, the growth of CNTs is mainly controlled by the shapes of the membrane pores and the catalytic action of the PAOX template.[3] Besides the CNT growth inside the pores (Fig. 1, center), there is deposition of carbon by-products on the PAOX membrane surface that cannot be prevented. This carbon deposit has to be removed before any application of CNTs could be considered. The presence of at least three carbon layers on the PAOX surface, i.e., a thick amorphous carbon overgrowth layer, a

*To whom correspondence should be addressed: Jorg J. Schneider

V.N. Popov and P. Lambin (eds.), Carbon Nanotubes, 63–64.

layer of high molecular hydrocarbons (tar, pitch, resin, etc.) penetrated on the PAOX surface, and a surface graphitic overlayer, was detected (Fig. 1, right). This allowed us to develop a controllable removal of PAOX template: (i) the surface carbon layer was oxidized in a controlled fashion at 550°C in air; (ii) high molecular hydrocarbon by-products were removed by boiling in benzene for 3 hours; (iii) the PAOX template was removed via dissolution in concentrated HF or H_3PO_4 during 4 hours. After these procedures, free-standing CNTs were obtained, however, still stuck to each other and connected via a surface graphitic overlayer.[2] The complex structural composition of the deposited carbon products is an evidence for the complicated mechanism of the non-catalytic metal-free CVD process containing only one precursor.

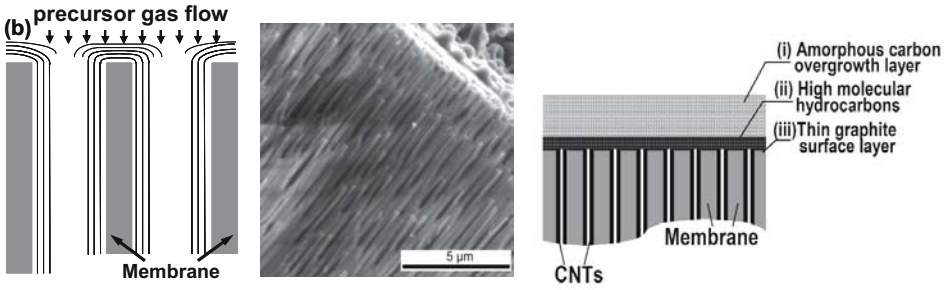

Figure 1. Scheme of the mechanism of CNT growth within the pores of a PAOX membrane by CVD with (left) and without catalyst (center). Right: cross-section of the PAOX membrane with CNTs inside the pores (a); scheme of carbon layers on the PAOX membrane surface (b).

In the present work, CNTs were produced within the pores of PAOX membranes by a non catalytic CVD method. The presence of three different carbon layers on the PAOX membrane surface after CVD process was proven and the three-step purification procedure was developed to receive the free-standing aligned CNT arrays.

We acknowledge support of the Volkswagen Foundation (grant no. 53200034).

References

1. W. A. de Heer, A. Chatelain and D. Ugarte, A Carbon Nanotube Field-Emission Electron Source, *Science* 270, 1179-1180 (1995).
2. J. J. Schneider, N. I. Maksimova and J. Engstler (unpublished).
3. L. Zhi, J. Wu, J. Li, U. Kolb, and K. Müllen, Carbonization of disclike molecules in porous alumina membranes: Toward carbon nanotubes with controlled graphene-layer orientation, *Angew. Chem. Int. Ed.* 44, 2120-2123 (2005).

PYROLYTIC SYNTHESIS OF CARBON NANOTUBES ON Ni, Co, Fe/MCM-41 CATALYSTS

KSENIIA KATOK,* SERGIY BRICHKA, VALENTYN TERTYKH, GENNADIY PRIKHOD'KO
Institute of Surface Chemistry of National Academy of Sciences of Ukraine, 17 Naumov Str., 03680 Kyiv-164, Ukraine

Abstract. The purpose of the accomplished work was to use the advantages (ordered porous structure and high surface area) of mesoporous MCM-41 silicas in the pyrolytic synthesis of carbon nanostructures. MCM-41 matrices were used for chemisorption of volatile nickel, cobalt, and iron acetylacetonates with following metal reduction. The synthesis of carbon nanotubes was carried out by two routes: (a) MCM-41 treatment with $Ni(acac)_2$ or $Co(acac)_2$ vapor at 150°C, metal reduction with H_2 at 450°C, C_2H_2 pyrolysis over the catalyst at 700°C; (b) MCM-41 modification with $Co(acac)_2$ or $Fe(acac)_2$, reduction of supported metal complexes with C_2H_2, and pyrolysis at 700°C (*in situ* reduction). The TEM data showed that carbon nanotubes were formed with external diameter 10-35 nm for Ni-, 42-84 nm for Co-, and 14-24 nm for Fe-containing matrices. In the absence of metals, low yield of nanotubes (up to 2%) was detected.

Keywords: mesoporous MCM-41 silica; metal acetylacetonates; acetylene; pyrolysis; carbon nanotubes; *in situ* reduction

The unique properties of the carbon nanotubes and the prospects of their possible applications continue to attract the attention of the researchers. The pyrolysis of hydrocarbons on the surface of inorganic matrices is one of the possible routes of carbon nanotubes synthesis. In this regard, the ordered mesoporous matrices, such as MCM-41, are of great importance.

The synthesis of carbon nanotubes was carried out by two routes: (a) MCM-41 treatment with $Ni(acac)_2$ or $Co(acac)_2$ vapour at 150°C, metal reduction with H_2 at 450°C, C_2H_2 pyrolysis over the catalyst at 700°C; (b) MCM-41

*To whom correspondence should be addressed. Kseniia Katok, Institute of Surface Chemistry of National Academy of Sciences of Ukraine 17 Naumov Str., 03164 Kyiv, Ukraine; e-mail: smpl@ukr.net

V.N. Popov and P. Lambin (eds.), Carbon Nanotubes, 65–66.

modification with $Co(acac)_2$ or $Fe(acac)_2$, reduction of supported metal complexes with C_2H_2, and pyrolysis at 700°C (*in situ* reduction). During the pyrolysis of acetylene, a deposition of decomposition products of black color on silica matrices was observed. The synthesized composite was treated with a solution of hydrofluoric acid at ambient temperature for removal of the silica phases. As a result, insoluble carbon fraction was obtained. The carbon nanotubes were identified using a transmission electron microscope.

Cetyltrimethylammonium bromide was used as a template for the synthesis of MCM-41 silica with specific surface area 905 m^2g^{-1} and total volume of pores 0.87 cm^3g^{-1}. The average diameter of the pores, determined by the BJH-method, was about 39 Å. The characterization of the mesoporous silica was performed by nitrogen adsorption measurements at 77 K.

In order to provide the homogeneous catalyst deposition, the silicas were treated with volatile cobalt (II) nickel (II) and iron (II) acetylacetonates at moderate temperature. At these conditions, acetylacetonates of metals are chemisorbed on the silica surface due to reaction with the surface silanol groups with eliminating one of the ligands.

The removal of the ligands from the metal complexes supported on the silica was studied in air by the thermogravimetric technique. The destruction of the residual ligands of acetylacetonates (after interaction with silanol groups) occurred at about 445°C. As a result, formation of complex oxides of cobalt and iron occurred on the silica surface.

The pyrolysis of acetylene on the surface of MCM-41 silicas containing metallic catalysts was studied. The application of matrices with supported metals as catalysts enabled us to attain rather high yields of carbon nanostructures (20–30% of the process product). The electron microscopy data provided evidence for the formation of nanotubes with an external diameter of 42–84 nm in the case of cobalt catalyst and 14–24 nm in the case of iron catalyst. The formation of carbon fibers with diameters in the interval 80–110 nm for nickel catalyst was also observed. Here it is appropriate to mention that in the absence of a catalyst on such matrices, small yields (up to 2%) of carbon nanotubes were attained.

A GRAND CANONICAL MONTE CARLO SIMULATION STUDY OF CARBON STRUCTURAL AND ADSORPTION PROPERTIES OF IN-ZEOLITE TEMPLATED CARBON NANOSTRUCTURES

TH. J. ROUSSEL, C. BICHARA, R. J. M. PELLENQ

Centre de Recherche sur la Matière Condensée et Nanosciences – CNRS, Campus de Luminy, 13288 Marseille CEDEX 9, France

Abstract. We used the Grand-Canonical Monte-Carlo technique (GCMC) to simulate the vapor deposition of carbon in the porosity of various zeolitic nanopores (Silicalite, AlPO4-5, faujasite). The carbon-carbon interactions were described within a Tight-Binding formalism (TB) and the carbon-matrix interactions were assumed to be physisorption. Depending on the pore size and topology, various carbon structures can be obtained.

Keywords: adsorption; Grand Canonical Monte-Carlo simulation; carbon nanotubes; zeolite; FAU; $AlPO_4$-5; Tight-Binding

Zeolites are now involved in the process of manufacturing metallic or semi-conductor nanostructures (clusters, nanowires and nanotubes). The basic idea is the deposition of an element from vapour or liquid phase inside the porosity of such crystalline materials that have a narrow pore size distribution. Then, nanostructures of the deposited element can be obtained after matrix removal. In our simulations, the carbon-carbon interactions are described in the tight binding approximation (TB) that is a parameterized version of the Hückel theory. The interaction of carbon with Si, Al, P and O atoms comprising the different zeolite frameworks considered in this work, is assumed to remain weak in the physisorption energy range using a PN-TrAZ potential.[1]

Experimental results for carbon adsorption in zeolites can be found in a series of papers[2] where the synthesis of ultra-small Single Wall Carbon Nanotubes (SWNTs) in the 0.73 nm channels of zeolite $AlPO_4$-5 was described. We show (Fig.1, left) that the narrowest single wall nanotube can be synthesized in the cylindrical channel of $AlPO_4$-5 zeolite (pore diameter 0.7 nm) in agreement with the experimental work of Tang et al.[2] We further show

V.N. Popov and P. Lambin (eds.), Carbon Nanotubes, 67–68.

that this ultra small nanotube (0.4 nm diameter) is defective but stable after template removal. Another example is the case of adsorption in zeolite silicalite.[3] This purely siliceous zeolite possesses two types of intercrossing channels of 0.55 nm in diameter. We also demonstrate that such zeolite with smaller diameter of the channels does not allow obtaining nanotubes but a mesh of intercrossing carbon chains (Fig. 1, middle).

Carbon adsorption was also attempted in the porosity of faujasite:[4] a zeolite that has a porous network made of cages of 1 nm in diameter, interconnected with 0.7 nm large windows. The pore topology of faujasite (made of tetrahedrally coordinated spherical cavities) allows making a highly porous ordered carbon material (C-Na-Y) adopting a diamond-like structure that was subsequently tested for H_2 storage (Fig. 1, right).

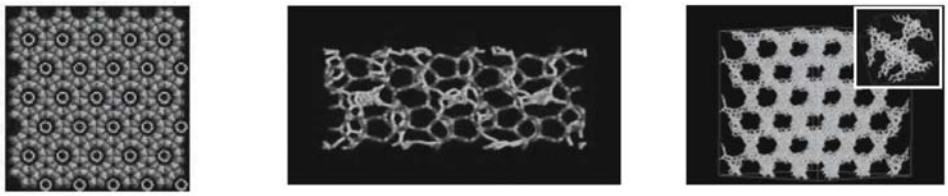

Figure 1. Left: SWNTs in $AlPO_4$-5; Middle: carbon in silicalite; Right: Na-Y replica (inset: unit cell).

The GCMC results show that carbon adsorption in $AlPO_4$-5 allows the formation of an ultra small defective nanotube of 0.4 nm diameter. Our simulations show that this tube is stable upon matrix removal. In the case of silicalite, we only obtain a mesh of intercrossing carbon chains but no aromatic carbon structures indicating that the smallest host cavity size for growing aromatic carbon nanostructures is around 0.7 nm. The C-Na-Y material is a porous carbon structure, which is very stable upon matrix removal and keeps the topology of the template, and is a possible gas storage device for hydrogen.

References

1. R. J.-M. Pellenq and D. Nicholson, Intermolecular potential function for the physical adsorption of rare gases in silicalite-1, *J. Phys. Chem.* 98, 13339-13349 (1994).
2. N. Wang, Z. K. Tang, G. D. Li, and J. S. Li, Single-walled 4 Angstrom Carbon Nanotube Array, *Nature* 408, 50-51 (2000).
3. C. Bichara, R. J.-M. Pellenq, and J.-Y. Raty J.-Y., Adsorption of selenium wires in silicalite-1 zeolite: a first order transition in a microporous system, *Phys. Rev. Lett.* 89, 1610 (2002).
4. T. Kyotani, T. Nagai, S. Inoue, and A. Tomita, Formation of New Type of Porous Carbon by Carbonization in Zeolite Nanochannels, *Chem. Mater.* 9, 609-615 (1997).

Part II. Vibrational properties and optical spectroscopies

VIBRATIONAL AND RELATED PROPERTIES OF CARBON NANOTUBES

VALENTIN N. POPOV*
Faculty of Physics, University of Sofia, 1164 Sofia, Bulgaria
PHILIPPE LAMBIN
Facultés Universitaires Notre-Dame de la Paix, 5000 Namur, Belgium

Abstract. The symmetry-adapted approach to the study of the vibrational and related properties of carbon nanotubes is presented. The usually very large number of carbon pairs in the unit cell of the nanotubes, that hinders most of the microscopic studies, is conveniently handled in this approach by using the screw symmetry of the nanotubes and a two-atom unit cell. This allows the systematic simulation of various properties (vibrational, mechanical, thermal, electronic, optical, dielectric, etc.) of all nanotubes of practical interest: The application of symmetry-adapted models to the study of some of these properties is illustrated in this review in two cases: a force-constant approach and a tight-binding approach.

Keywords: phonons; phonon dispersion; force-constant model; tight-binding model

1. Introduction

The discovery of the carbon nanotubular structures in 1991 led to an avalanche of theoretical and experimental work motivated by their unusual properties and the possibility for their industrial application.[1] Nowadays, carbon nanotubes are components of composite materials, various field-effect devices, field-emitters in displays, hydrogen storage devices, gas sensors, etc. The theoretical study of the nanotubes is based on the use of an idealized structure: a uniform cylinder or an atomic structure with one-dimensional periodicity. The practical

* To whom correspondence should be addressed. Valentin N. Popov, Faculty of Physics, University of Sofia, 5 J. Bourchier Blvd., 1164 Sofia, Bulgaria; e-mail: vpopov@phys.uni-sofia.bg

V.N. Popov and P. Lambin (eds.), Carbon Nanotubes, 69–88.

calculations in the latter case face an often insurmountable obstacle arising from the necessity to deal with a large number of carbon atoms. This hindrance can be overcome considering a usually neglected symmetry of the ideal nanotubes, the screw symmetry.

In this review, we show how the explicit use of the screw symmetry allows the easy computational handling of practically all existing nanotube types. This is illustrated on the example of the lattice dynamics of nanotubes developed within a force-constant approach (Sec. 3) and a tight-binding approach (Sec. 4). The theoretical part is appended with results of calculations, which are compared to available experimental data.

2. The nanotube structure and screw symmetry

The ideal single-walled carbon nanotube can be viewed as obtained by rolling up an infinite graphite sheet (graphene) into a seamless cylinder leading to coincidence of the lattice point O at the origin and another one A defined by the chiral vector $\mathbf{C}_h = (L_1,L_2)$ (see Fig. 1). Each tube is uniquely specified by the pair of integer numbers (L_1,L_2) or by its radius R and chiral angle θ. The latter is defined as the angle between the chiral vector $\mathbf{C}_h$ and the nearest zigzag of carbon–carbon bonds with values in the interval $0 \le \theta \le \pi/6$. The tubes are called achiral for $\theta = 0$ ("zigzag" type) and $\theta = \pi/6$ ("armchair" type), and chiral for $\theta \ne 0$, $\pi/6$. Every nanotube has a translational symmetry with primitive translation vector $\mathbf{T} = (N_1,N_2)$ (see Fig. 1) where $N_1 = \left(L_1 + 2L_2\right)/d$ and $N_2 = -\left(2L_1 + L_2\right)/d$. Here d is the greatest common divisor of $2L_1 + L_2$ and $L_1 + 2L_2$. The total number of atomic pairs in the unit cell is $N = N_1L_2 - N_2L_1$.

All the carbon atoms of a tube can be reproduced by use of two different screw operators[2,3] (see Fig. 2). The screw operator $\{S|\mathbf{t}\}$ rotates the position vector of an atom at an angle φ about the tube axis and translates it at a vector $\mathbf{t}$ along the same axis. Thus, the equilibrium position vector $\mathbf{R}(\mathbf{l}k)$ of the kth atom of the lth atomic pair of the tube is obtained from $\mathbf{R}(k) \equiv \mathbf{R}(\mathbf{0}k)$ by using of two screw operators $\{S_1|\mathbf{t}_1\}$ and $\{S_2|\mathbf{t}_2\}$

$$\mathbf{R}(\mathbf{l}k) = \{S_1|\mathbf{t}_1\}^{l_1}\{S_2|\mathbf{t}_2\}^{l_2}\mathbf{R}(k) = S_1^{l_1}S_2^{l_2}\mathbf{R}(k) + l_1\mathbf{t}_1 + l_2\mathbf{t}_2. \quad (1)$$

Here $\mathbf{l} = (l_1,l_2)$, l_1 and l_2 are integer numbers labeling the atomic pair, and $k = 1$, 2 labels the atoms in the pair. It is convenient to adopt the compact notation $S(\mathbf{l}) = S_1^{l_1}S_2^{l_2}$ and $\mathbf{t}(\mathbf{l}) = l_1\mathbf{t}_1 + l_2\mathbf{t}_2$, and rewrite Eq. 1 as $\mathbf{R}(\mathbf{l}k) = S(\mathbf{l})\mathbf{R}(k) + \mathbf{t}(\mathbf{l})$.

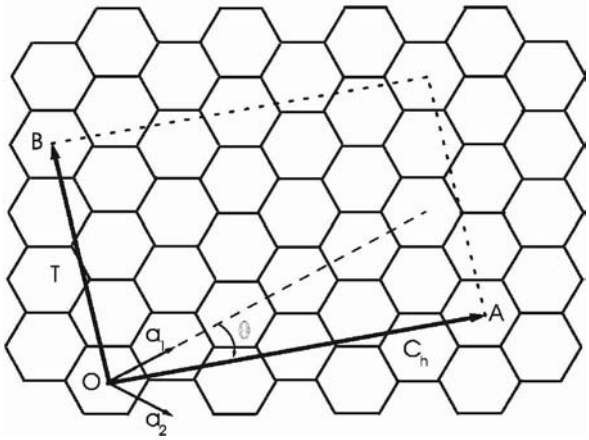

Figure 1. The honeycomb lattice of graphene. The lattice points O and A define the chiral vector $\mathbf{C}_h$ and the points O and B define the primitive translation vector **T** of the tube. The rectangle formed by the two vectors defines the unit cell of the tube. The figure corresponds to tube (4,2) with $\mathbf{C}_h$ = (4,2) and **T** = (4,–5).

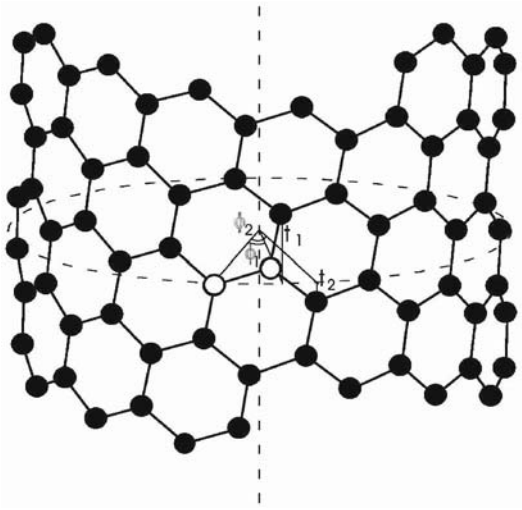

Figure 2. A front view of a nanotube. The closed dashed line is the circumference and the straight dashed line is the axis of the tube. The nanotube can be constructed by mapping of the two atoms of the unit cell (depicted by empty symbols) unto the entire cylindrical surface using two different screw operators. [2]

This "rolled" nanotube structure can be relaxed within tight-binding or *ab-initio* models. In the relaxation procedure, one usually imposes the following constraints: preservation of the translational symmetry of the tubes, keeping all atoms on one and the same cylindrical surface. As parameters of the relaxation one can choose the tube radius, the primitive translation of the tube, and the angle of rotation and the translation of the screw operation for mapping the first atom of the two-atom unit cell unto the second one. The relaxed structure can be used to obtain refined values of various quantities.

3. Lattice dynamics of carbon nanotubes: force-constant approach

The symmetry-adapted lattice dynamical model for nanotubes can be constructed as a Born model of the lattice dynamics based on a two-atom unit cell. In the adiabatic approximation, the atomic motion is conveniently decoupled from the electronic one. For small displacements $\mathbf{u}(\mathbf{l}k)$ of the atoms from their equilibrium positions, it is customary to use the harmonic approximation and represent the atomic Hamiltonian as a quadratic form of $\mathbf{u}(\mathbf{l}k)$. The equations of motion of the atoms are then readily derived in the form

$$m_k \ddot{u}_\alpha(\mathbf{l}k) = -\sum_{\mathbf{l}'k'\beta} \Phi_{\alpha\beta}(\mathbf{l}k,\mathbf{l}'k')u_\beta(\mathbf{l}'k'). \tag{2}$$

Here m_k are the atomic masses and $\Phi_{\alpha\beta}(\mathbf{l}k,\mathbf{l}'k')$ are the force constants.

The screw symmetry of the nanotube suggests searching for a solution of the type

$$u_\alpha(\mathbf{l}k) = \frac{1}{\sqrt{m_k}} \sum_\beta S_{\alpha\beta}(\mathbf{l}) e_\beta(k|\mathbf{q}) \exp i\left(\mathbf{q}\cdot\mathbf{l} - \omega t\right), \tag{3}$$

which represents a wave with wavevector $\mathbf{q} = (q_1,q_2)$ and angular frequency $\omega(\mathbf{q})$. The atomic displacements remain unchanged under integer number tube translations at distance T and integer number rotations at an angle of 2π. These two conditions lead to the following constraints on the wavevector components

$$q_1 L_1 + q_2 L_2 = 2\pi l, \tag{4}$$

$$q_1 N_1 + q_2 N_2 = q. \tag{5}$$

Here l = 0, 1,..., N-1 and $-\pi \le q < \pi$. Using Eqs. 4 and 5, the atomic displacement Eq. 3 can be written as

$$u_\alpha(\mathbf{l}k) = \frac{1}{\sqrt{m_k}} \sum_\beta S_{\alpha\beta}(\mathbf{l}) e_\beta(k|ql) \exp i\left(\alpha(\mathbf{l})l + z(\mathbf{l})q - \omega t\right), \tag{6}$$

Here

$$\alpha(\mathbf{l}) = 2\pi(l_1 N_2 - l_2 N_1)/N_c$$

and

$$z(\mathbf{l}) = (L_1 l_2 - L_2 l_1)/N_c$$

are dimensionless coordinates of the origin of the *l*th cell along the circumference and along the tube axis, respectively. Substituting Eq. 6 in Eq. 2, we get a system of six linear equations of the form

$$\omega^2(ql)e_\alpha(k|ql) = \sum_{k'\beta} D_{\alpha\beta}(kk'|ql)e_\beta(k'|ql), \tag{7}$$

where the dynamical matrix is defined as

$$D_{\alpha\beta}(kk'|ql) = \frac{1}{\sqrt{m_k m_{k'}}} \sum_{\mathbf{l}'\gamma} \Phi_{\alpha\gamma}(\mathbf{0}k, \mathbf{l}'k') S_{\gamma\beta}(\mathbf{l}') \exp i\left(\alpha(\mathbf{l}')l + z(\mathbf{l}')q\right). \tag{8}$$

The eigenfrequencies $\omega(ql)$ are solutions of the characteristic equation

$$\left\| D_{\alpha\beta}(kk'|ql) - \omega^2(ql)\delta_{\alpha\beta}\delta_{kk'} \right\| = 0. \tag{9}$$

Substituting the solutions $\omega^2(qlj)$ in Eq. 7, one can obtain the corresponding eigenvectors $e_\alpha(k|qlj)$ (j = 1, 2,…, 6). For each q there are $6N$ vibrational eigenmodes (phonons) but the number of the different $\omega^2(qlj)$ can be lesser due to degeneracy. Using Eq. 8 it can be proven that D is Hermitian and therefore $\omega^2(qlj)$ are real and $e_\alpha(k|qlj)$ can be chosen orthonormal.

Due to the explicit accounting for the screw symmetry of the tubes in the presented symmetry-adapted scheme, the computation time for each q scales as 6^3N. This ensures great advantage for phonon calculations of tubes with very large N in comparison to the approach that does not use the screw symmetry where the computation time scales as $(6N)^3$. Practically, all observable nanotubes can be handled with the presented lattice dynamical model with respect to the numerical stability of the computations as well as to the computer memory and CPU time.

3.1. PHONON DISPERSION, ZONE-CENTER PHONONS, AND RAMAN INTENSITY OF THE RBM

The phonon dispersion of two nanotubes, calculated using force constants of valence force-field type,[2,3] is shown in Fig. 3. The small number of force fields used does not allow for the precise modeling of the high-frequency branches. In particular, the "overbending" of the in-plane bond-stretching vibrations in

graphene cannot be reproduced well, which results in an incorrect order of the zone-center tangential phonons in nanotubes. However, this does not affect much the low-frequency branches in nanotubes.

The phonons with wavevector q inside the Brillouin zone are waves along the tube with wavelength $\lambda = 2\pi/q$. The zone-center phonons are atomic motions repeating in all unit cells along the tube. The atomic displacements for chiral tubes are not generally restricted to definite directions in space. However, the displacements for achiral tubes can be classified as radial (R), circumferential (C), and axial (A).

The zone-center phonons of chiral tubes belong to the following symmetry species of point groups D_N (Ref. 4)

$$\Gamma=3A_1+3A_2+3B_1+3B_2+6E_1+6E_2+6E_3+...6E_{N/2-1}, \qquad (10)$$

where modes $A_{1,2}$ and $B_{1,2}$ correspond to $l = 0$ and $N/2$, and modes E_i correspond to $l = i$. The E_i modes have $2l$ nodes around the tube circumference. The $A_{1,2}$ modes are nodeless and the $B_{1,2}$ ones have N nodes. Armchair and zigzag tubes have additional symmetry elements and the modes are classified by the irreducible representations of point group D_{2nh}.

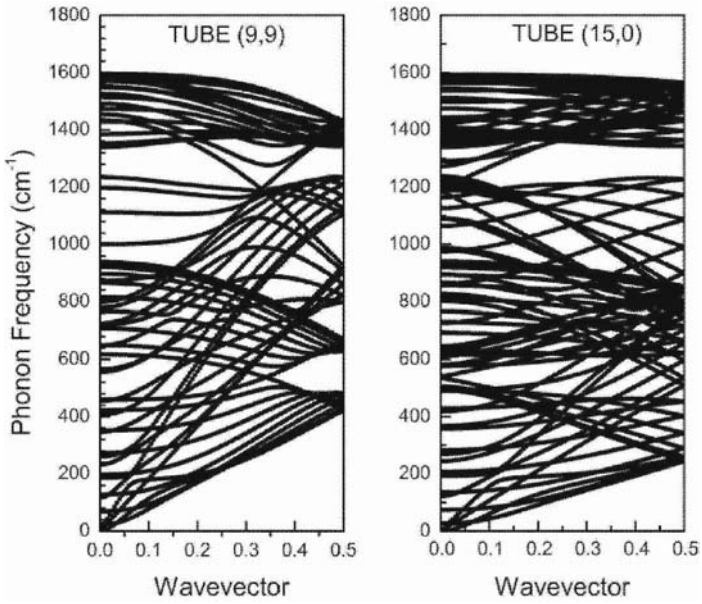

Figure 3. The phonon dispersion of nanotubes (9,9) and (15,0) obtained using force constants of the valence force field type. Notice the large number of phonon branches: 108 and 180.

Among the various zone-center phonons, some are infrared-active ($A_2 + 5E_1$ in chiral tubes, $3E_{1u}$ in armchair tubes, and $A_{2u} + 2E_{1u}$ in zigzag tubes), others are Raman-active ($3A_1 + 5E_1 + 6E_2$ in chiral tubes, $2A_{1g} + 2E_{1g} + 4E_{2g}$ in armchair tubes, and $2A_{1g} + 3E_{1g} + 3E_{2g}$ in zigzag tubes), and the rest are silent. The $A_{1(g)}$, $E_{1(g)}$, and $E_{2(g)}$ phonons are observed in the scattering configurations ($xx + yy$, zz), (xz, yz), and ($xx - yy$, xy), respectively, for z axis along the tube. (The used here Porto notation (x_1x_2) means incident light polarized along x_1 axis and scattered light polarized along x_2 axis.)

Largest Raman signal is observed for parallel scattering configuration and it originates from the following $A_{1(g)}$ modes:

- one mode with a uniform radial atomic displacement (so-called radial-breathing mode or RBM) with frequency following roughly the power law $230/d$ (in cm^{-1}; d is the tube diameter in nm);
- one high-frequency mode of about 1580 cm^{-1}, which is purely circumferential in armchair tubes and purely axial in zigzag tubes (or two neither purely circumferential, nor purely axial modes in chiral tubes).

The Raman signal due to $E_{1(g)}$ and $E_{2(g)}$ phonons is usually very weak. Apart from lines due to single-phonon processes, bands arising from more complex processes are often observed in the Raman spectra. An example of such band is the D band (i.e., disorder band) due to the presence of impurities and defects in the nanotubes.

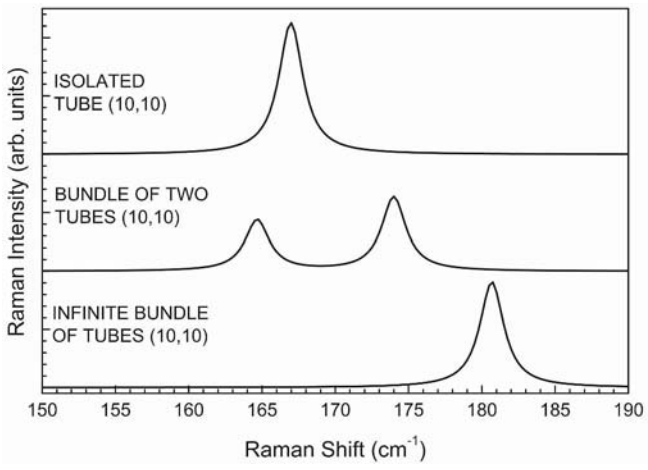

Figure 4. Non-resonant Raman intensity of an isolated nanotube, a bundle of two nanotubes, and an infinite bundles of nanotubes (10,10) calculated within a bond-polarizability model.[5,6]

The Raman lines of the high-frequency $A_{1(g)}$ modes of the different tubes are closely situated and modified by electron-phonon and electron-impurity interactions. The modeling of the latter ones also faces the problem of considering far enough neighbors in order to reproduce correctly the overbending of the phonon branches of graphene, from which these modes originate. On the other hand, the lines of the RBMs in the measured spectra are often well-separated and can be used for structural characterization of the nanotube samples.

In bundles of nanotubes and multiwalled nanotubes, there are many breathinglike phonon modes having different Raman line intensities.[5-7]. This is illustrated in Fig. 4, where the Raman intensity of such modes of an isolated and bundled nanotubes, calculated within a bond-polarizability model, is displayed. It is clearly seen that in bundles there are more than one breathinglike mode and that the intertube interactions generally upshifts their frequencies. It has to be noted that while the bond-polarizability model describes well the non-resonant spectra of most semiconductors, the Raman spectra of nanotubes are usually measured under resonant conditions and non-resonant spectra are rarely observed because of the low signal. Any realistic calculations of the spectra should take into account the electronic band structure of the tubes (see Sec. 3).

3.2. MECHANICAL AND THERMAL PROPERTIES

The force constants are invariant under infinitesimal translations along and perpendicular to the tube axis that leads to the translational sum rules and to three zone-center zero-frequency modes.[3] The infinitesimal rotation invariance condition imposed on the force constants gives rise to a rotational sum rule and to an additional zero-frequency mode. The former three modes are translations along and perpendicular the tube, and the latter mode is a rotation of the tube about its axis. These four modes belong to the four acoustic modes of the tube. The longitudinal and rotational acoustic branches have linear dispersion at the zone center. The corresponding acoustic wave velocities v_L and v_R can be associated with Young's and shear moduli of the tubes, Y and G, as $v_L = \sqrt{Y/\rho}$ and $v_R = \sqrt{G/\rho}$ with ρ being the mass density. The transverse waves have quadratic dispersion at the zone center and zero group velocity there. The estimations of the two moduli within force-constants, tight-binding, and *ab-initio* models yield approximately the same value for the moduli per unit tube circumference (in-plane moduli) of about 350 J/m^2 and 150 J/m^2, close to the values for graphite. The Poisson ratio is given by $v = (Y/2 - G)/G$ and, for the calculated moduli, it is about 0.17. The use of different definitions for the cross-sectional area of the nanotubes can yield quite different values for the

moduli. Thus, assuming a cross-section as a ring of width 0.34 nm, one obtains 1030 GPa and 440 GPa slightly dependent on the tube type. For a cross-section as a full disk with radius R, the moduli with decrease with the increase of the radius, etc. In the case of bundles of many tubes, the cross-section should be chosen as a hexagon with area $\sqrt{3}\left(2R+d\right)^2/2$ with d being the intertube separation resulting again in decreasing of Y with increasing tube radius. In practice, in order to make use of the large moduli of the nanotubes, e.g., in composite materials, it is necessary to bind covalently the nanotubes in ropes and/or to the other constituents of these materials.

The bulk modulus K of infinite bundles of nanotubes can be derived in a similar way as the elastic moduli of isolated tubes.[8] For small-radius tubes, $K = K_W$ is determined by the intertube forces and increases with the increase of the tube radius. For large-radius tubes, $K = K_T$ is predominantly due to the tube elasticity and decreases with the increase of the radius. For intermediate radii, K can be expressed approximately as $K_W K_T/(K_W + K_T)$. The calculated K from the slopes of the acoustic branches of infinite bundles of tubes agrees well with the results of the molecular-dynamics simulations.[9] The disagreement for $R > 15$ Å is due to the assumption of circular cross-section of the tubes in the former model while the intertube interactions polygonize the cross-section of large-radius tubes.

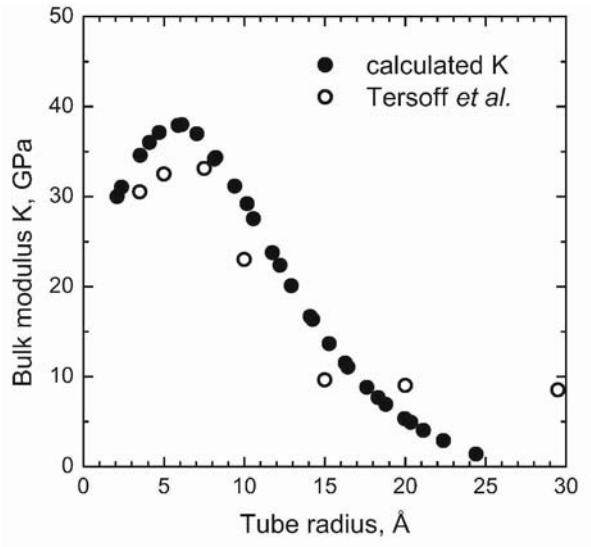

Figure 5. Bulk modulus K of infinite bundles of achiral SWNTs, calculated within a force-constant model,[8] in comparison to the one, derived in molecular dynamics simulations.[9]

The specific heat and thermal conductivity of carbon nanotubes are determined mainly by the phonons while the electronic contribution is usually negligible.

The phonon specific heat of carbon nanotubes C_v can be derived using the phonon frequencies calculated within the lattice-dynamical model by means of the expression[10]

$$C_v(T) = k_B \int_0^\infty \frac{\left(\hbar\omega / k_B T\right)^2 \exp\left(\hbar\omega / k_B T\right)}{\left[\exp\left(\hbar\omega / k_B T\right) - 1\right]^2} D(\omega) d\omega, \tag{22}$$

where $D(\omega)$ is phonon density of states. At high temperature, C_v tends to the classical limit $2k_B/m \approx 2078$ mJ/gK (m is the atomic mass of carbon). At low temperature, C_v is determined by the dispersion of the lowest-energy acoustic branches. For one-dimensional systems, these are the transverse acoustic ones with quadratic dispersion and, therefore, $D(\omega) \propto 1/\sqrt{\omega}$ and $C_v \propto \sqrt{T}$. As it can be seen from Fig. 6, this behavior can be observed below about 1 K. This behavior is essentially different from that of graphene ($C_v \propto T$) and graphite and infinite bundles ($C_v \propto T^3$).

The low-temperature thermal conductivity has the same temperature behavior as the specific heat. At high temperature, scattering from the tube boundaries and *Umklapp* processes become dominant.

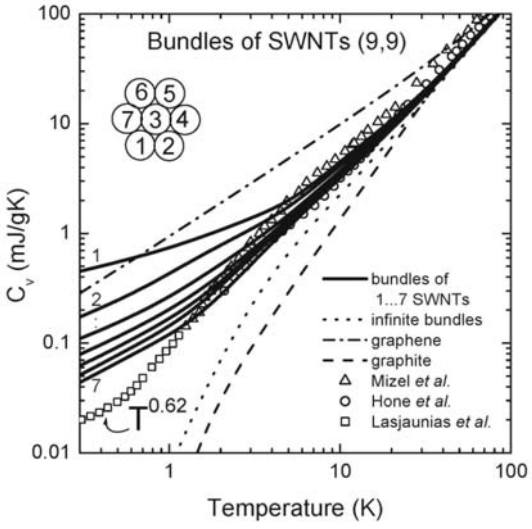

Figure 6. Specific heat of SWNTs and ropes of SWNTs, calculated within a force-constant model,[10], in comparison with that of graphene and graphite, and available experimental data.[11,12,13]

4. Lattice dynamics of carbon nanotubes: tight-binding approach

4.1. THE SYMMETRY-ADAPTED TIGHT-BINDING MODEL

The electronic band structure of a periodic structure is usually obtained in the independent-electron approximation solving the one-electron Schrödinger equation

$$\left[-\frac{\hbar^2\nabla^2}{2m}+V(\mathbf{r})\right]\psi_{\mathbf{k}}(\mathbf{r})=E_{\mathbf{k}}\psi_{\mathbf{k}}(\mathbf{r}), \tag{10}$$

where m is the electron mass, $V(\mathbf{r})$ is the effective periodic potential, $\psi_{\mathbf{k}}(\mathbf{r})$ and $E_{\mathbf{k}}$ are the one-electron wavefunction and energy depending on the wavevector $\mathbf{k}$. This equation can be solved by representing $\psi_{\mathbf{k}}(\mathbf{r})$ as a linear combination of basis functions $\varphi_{\mathbf{k}r}(\mathbf{r})$

$$\psi_{\mathbf{k}}(\mathbf{r})=\sum_r c_{\mathbf{k}r}\varphi_{\mathbf{k}r}(\mathbf{r}). \tag{11}$$

In the tight-binding approach, the φ's are constructed from atomic orbitals centered at the atoms. Let us denote by $\chi_r(\mathbf{R}(\mathbf{l})-\mathbf{r})$ the rth atomic orbital centered at an atom with position vector $\mathbf{R}(\mathbf{l})$ in the $\mathbf{l}$th unit cell.

Similarly to the vibrational problem considered above, the screw symmetry of the tube allows one to solve the electronic problem working with a two-atom unit cell.[14] In this case, Bloch's condition for the basis functions φ is satisfied for the following linear combination of χ's

$$\varphi_{\mathbf{k}r}(\mathbf{r})=\frac{1}{\sqrt{N_c}}\sum_{\mathbf{l}r'}e^{i\mathbf{k}\cdot\mathbf{l}}T_{rr'}(\mathbf{l})\chi_{r'}(\mathbf{R}(\mathbf{l})-\mathbf{r}). \tag{12}$$

where $\mathbf{k}$ is a two-dimensional wavevector, $\mathbf{k}=(k_1, k_2)$, and N_c is the number of unit cells in the tube. $T_{rr'}(\mathbf{l})$ are appropriate rotation matrices rotating a given atomic-type orbital to the same orientation with respect to the nanotube surface for all atoms. The wavevector components are subject to the following constraints arising from the rotational and translational symmetry of the tube

$$k_1L_1+k_2L_2=2\pi l, \tag{13}$$

$$k_1N_1+k_2N_2=k. \tag{14}$$

Here k is the one-dimensional wavevector of the tube ($-\pi \le k < \pi$) and the integer number l labels the electronic energy levels with a given k (l = 0,1, …, N–1). The other symbols are defined in Sec. 2. Using Eqs. 13 and 14, the expansion functions can be rewritten as

$$\varphi_{klr}(\mathbf{r}) = \frac{1}{\sqrt{N_c}} \sum_{\mathbf{l}} e^{i(\alpha(\mathbf{l})l + z(\mathbf{l})k)} T_{rr'} \chi_{r'}(\mathbf{R}(\mathbf{l}) - \mathbf{r}). \tag{15}$$

After substitution of Eqs. 11 and 15 in Eq. 10, the electronic problem is transformed into the matrix eigenvalue problem

$$\sum_{r'} H_{klrr'} c_{klr'} = E_{kl} \sum_{r'} S_{klrr'} c_{klr'}, \tag{16}$$

where the matrix elements of the Hamiltonian $H_{klrr'}$ and the overlap matrix elements $S_{klrr'}$ are given by

$$H_{klrr'} = \sum_{\mathbf{l}r''} e^{i(\alpha(\mathbf{l})l + z(\mathbf{l})k)} H_{rr''}(\mathbf{l}) T_{r''r'}(\mathbf{l}), \tag{17}$$

$$S_{klrr'} = \sum_{\mathbf{l}r''} e^{i(\alpha(\mathbf{l})l + z(\mathbf{l})k)} S_{rr''}(\mathbf{l}) T_{r''r'}(\mathbf{l}). \tag{18}$$

Here $H_{kl}(\mathbf{l})$ and $S_{kl}(\mathbf{l})$ are matrix elements of the Hamiltonian and the overlap matrix elements between χ's. The set of linear algebraic equations Eq. 16 has non-trivial solutions for the coefficients c only for energies E which satisfy the characteristic equation

$$\left\| H_{klrr'} - E_{kl} S_{klrr'} \right\| = 0. \tag{19}$$

The solutions of Eq. 19, E_{klm}, are the electronic energy levels; the energy bands are labeled by the composite index lm (m = 1, 2,…, 8 for 4 electrons per carbon atom). The corresponding eigenvectors c_{klmr} are determined from Eq. 16.

Like with phonons, the symmetry-adapted approach for calculation of the electronic band structure of nanotubes has the important advantage of large reduction of the computational time. Indeed, the calculation of the band energies for a given k needs time scaling as the cube of the size of the two-atom eigenvalue problem (8^3 for 4 electrons per carbon atom) times the number of the two-atom unit cells N. On the other hand, the straightforward calculation of the same band energies will require time scaling as the cube of the size of the $2N$-atom eigenvalue problem, i.e., $(8N)^3$.

For structural relaxation of a nanotube one needs the expressions for the total energy and the forces acting on the atoms. The total energy of a nanotube (per unit cell) is given by

$$E = \sum_{klm}^{occ} E_{klm} + \frac{1}{2} \sum_i \sum_j \phi(r_{ij}), \tag{20}$$

where the first term is the band energy (the summation is over all occupied states) and the second term is the repulsive energy, consisting of repulsive pair

potentials $\phi(r)$ between pairs of nearest neighbors. The band contribution to the force in α direction on the atom with a position vector $\mathbf{R}(\mathbf{0})$ is given by the Hellmann-Feynman theorem

$$F_\alpha = \sum_{klm}^{occ} \frac{\partial E_{klm}}{\partial R_\alpha(\mathbf{0})} = \sum_{klm}^{occ} \sum_{rr'} c^*_{klmr} \frac{\partial \left(H_{klrr'} - E_{klm} S_{klrr'} \right)}{\partial R_\alpha(\mathbf{0})} c_{klmr'} \,. \tag{21}$$

The repulsive contribution is the first derivative of the total repulsive energy with respect to the position vector $\mathbf{R}(\mathbf{0})$.

According to the simplest tight-binding model with one valence electron per carbon atom (the π-band TB model), tubes with residual of the division of L_1 - L_2 by 3 equal to zero are metallic (M-tubes), and the remaining tubes with residual 1 and 2, denoted further with Mod1 and Mod2, are semiconducting (S-tubes). The band-structure calculations within more sophisticated models show that only armchair tubes are strictly metallic, while the remaining M-tubes are tiny-gap semiconductors. The results of the calculations of the band structure and the electronic density of states (DOS) for two SWNTs within a non-orthogonal tight-binding model[14,15] (NTB model) are shown in Fig. 7. Tube (10,10) is metallic with small finite density of states at the Fermi energy defined as zero. Tube (17,0) is semiconducting with a small energy gap of about 0.6 eV. The DOS spikes have characteristic $1/\sqrt{E}$ singularity at the optical transitions.

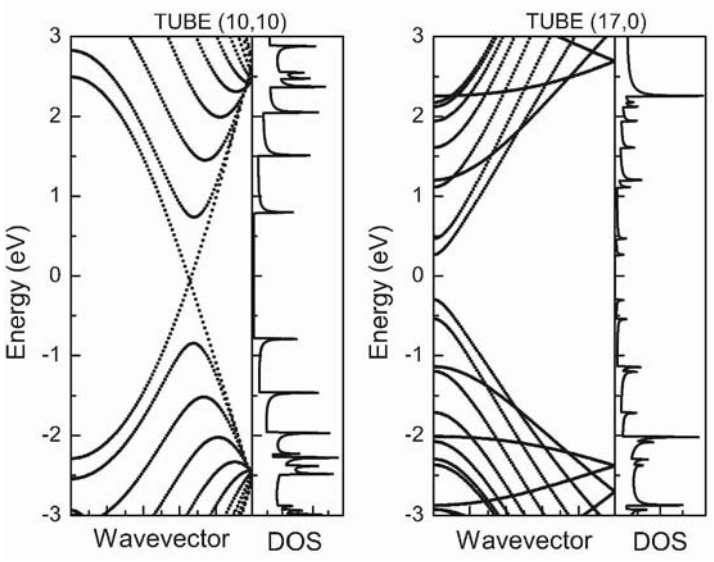

Figure 7. Band structure and electronic density of states of SWNTs (10,10) and (17,0). Notice the characteristic $1/\sqrt{E}$ spikes in the DOS.

4.2. DIELECTRIC PROPERTIES

The imaginary part of the dielectric function in the random-phase approximation is given by[14]

$$\varepsilon_2(\omega) = \frac{4\pi^2 e^2}{m^2\omega^2} \sum_{l'clv} \frac{2}{2\pi} \int dk \left| p_{kl'cklv,\mu} \right|^2 \delta\left(E_{kl'c} - E_{klv} - \hbar\omega \right), \tag{22}$$

where $\hbar\omega$ is the photon energy, e is the elementary charge, and m is the electron mass. The sum is over all occupied (v) and unoccupied (c) states. $p_{kl'cklv,\mu}$ is the matrix element of the component of the momentum operator in the direction μ of the light polarization

$$p_{kl'cklv,\mu} = \int d\mathbf{r}\, \psi^*_{kl'c}(\mathbf{r}) \hat{p}_\mu \psi_{klv}(\mathbf{r}) . \tag{23}$$

Substituting Eqs. 11 and 15 in Eq. 23, one obtains the non-zero matrix elements

$$p_{kl'cklv,\mu} = f_{ll'\mu} \sum_{rr'} c^*_{kl'cr'} c_{klvr} \sum_{\mathbf{l}r''} e^{-i(\alpha(\mathbf{l})l + z(\mathbf{l})k)} p_{r'r'',\mu}(\mathbf{l}) T_{rr''}(\mathbf{l}) , \tag{24}$$

where

$$p_{rr',\mu}(\mathbf{l}) = \int d\mathbf{r}\, \chi_r(\mathbf{R}(\mathbf{0}) - \mathbf{r}) \hat{p}_\mu \chi_{r'}(\mathbf{R}'(\mathbf{l}) - \mathbf{r}) . \tag{25}$$

For z-axis along the tube axis, the quantities $f_{ll',\mu}$ are given by $f_{ll'x} = f_{ll',y} = (\delta_{l',l+1} + \delta_{l',l-1})/2$ and $f_{ll',z} = \delta_{ll'}$. The latter two relations express the selection rules for allowed dipole optical transitions, namely, optical transitions are only allowed between states with the same l for parallel light polarization along the tube axis and between states with l and l' differing by 1 for parallel polarization, which is perpendicular to the tube axis. In the latter case, the electronic response is much weaker than in the former due to the depolarization effect. Therefore, much of the efforts have been directed to the calculation of the dielectric function for parallel polarization.

The optical transition energies can be determined from the spikes of the imaginary part of the dielectric function calculated within a NTB model.[14,15] The derived energies for parallel light polarization are shown in Fig. 8 for HiPco samples and for the most frequently used laser excitation energies. The points on the plot form strips belonging to either M- or S-tubes. With increasing the energy, one crosses strips of points for transitions 11 in S-tubes (Mod1, Mod2), 22 in S-tubes (Mod2 and Mod1), 11 and 22 in M-tubes (only transition 11 in armchair tubes), and so on. In each strip, the arrangement of the points show family patterns for $L_1 + 2L_2$ = integer number (connected with lines).

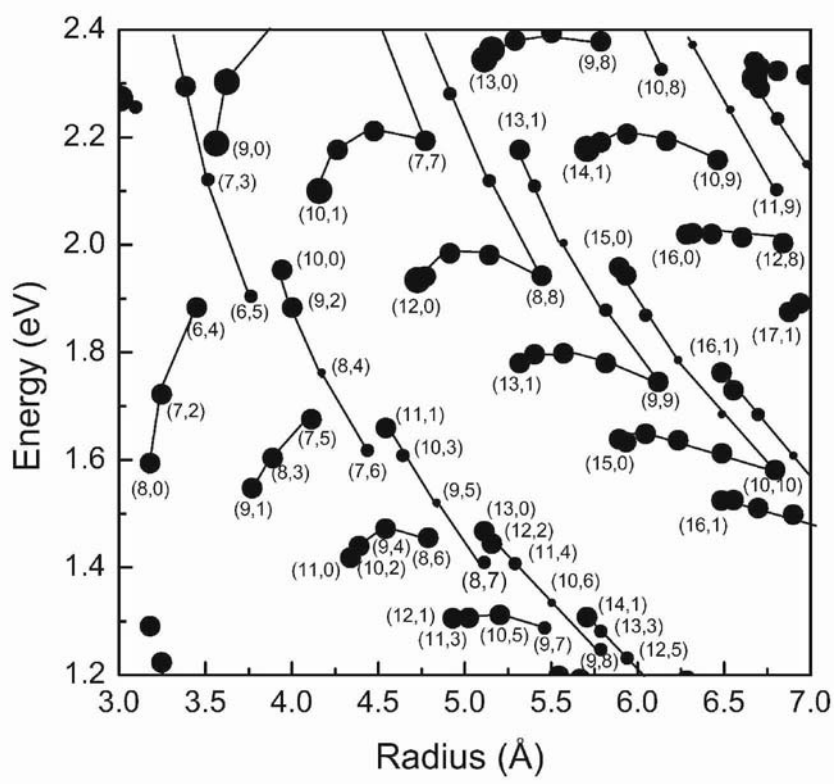

Figure 8. The resonance chart: transition energy vs tube radius. Only the part, containing the points that correspond to the HiPco samples and the most frequently used laser excitation energies, is shown.

4.3. THE DYNAMICAL MATRIX

The dynamical matrix of the nanotubes can be obtained from the expression of the total energy by considering the change of the energy arising from a given static lattice deformation[16] (a phonon). The derivation is too involved to be placed here and the same holds true for the final expression of the dynamical matrix. Here, it suffies to provide results of the calculations for particular nanotubes. We note that this method is not applicable to armchair tubes because the dynamical matrix has a logarithmic singularity at the band crossing at the Fermi energy. The tiny-gap M-tubes require large number of *k*-points to ensure convergence of the sum over the Brillouin zone in the expression of the

dynamical matrix. This problem does not normally appear for S-tubes where a moderate number of *k*-points is sufficient.

The calculated phonon dispersion of graphene within the NTB model overestimates the measured one by about 10 %. The calculated frequencies, multiplied by 0.9, are shown in Fig. 9. It is clear that the overbending of the highest-frequency branches is well reproduced while the out-of-plane optical branch is now underestimated. Since we are rather interested in the former one, the underestimation for the latter one will not be important.

As it was mentioned above, the RBM is of primary importance for the structural characterization of the samples. In Fig. 10, the calculated RBM frequency of all tubes in the radius range from 2 Å to 12 Å is shown in comparison with available *ab-initio* results for strictly radial atomic displacements. The points follow a power law $1141/R$ (in cm^{-1}, R in Å).

In the presence of impurities and structural disorder, there is an additional light-scattering mechanism, so-called double resonance mechanism. It is responsible for the specific Raman line broadening and the position shift with the laser excitation energy especially observed for the D (disorder), G, and G' bands. The review of this mechanism lies outside the scope of this paper.

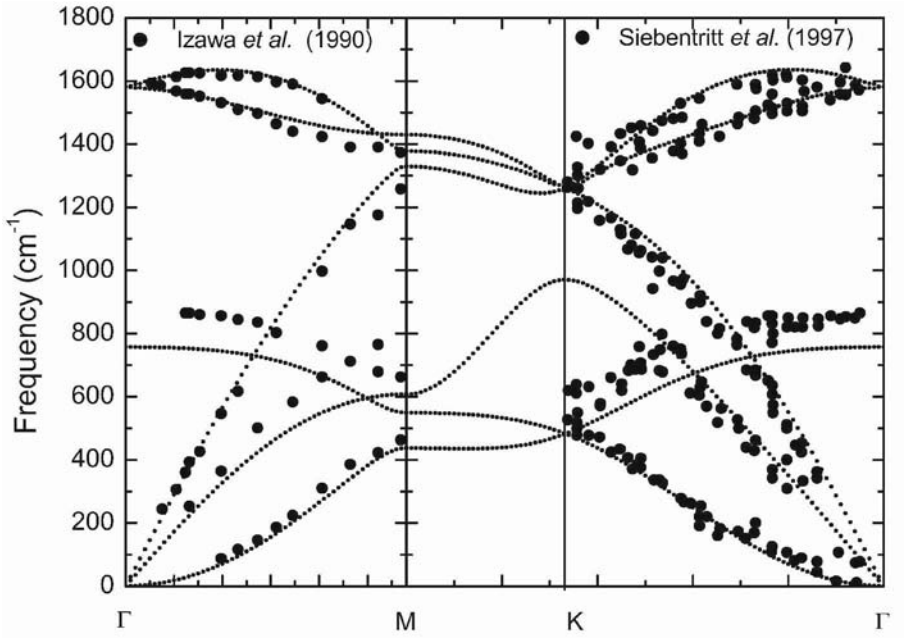

Figure 9. Phonon dispersion of graphite calculated within a NTB model and scaled by a factor of 0.9 (Ref. 16) in comparison with available experimental data.[17,18]

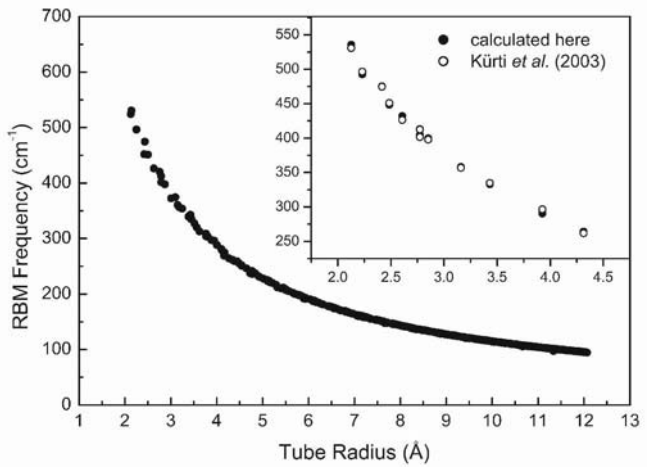

Figure 10. Calculated RBM frequencies within a NTB model vs tube radius.[16] The comparison with *ab-initio* results[19] reveals disagreement less than 5 cm^{-1} (see inset).

4.4. THE RESONANT RAMAN INTENSITY

The Raman-scattering process can be described quantum-mechanically considering the system of the electrons and phonons of the tube and the photons of the electromagnetic radiation and their interactions.[20] The most resonant Stokes process includes a) absorption of a photon (energy E_L, polarization vector $\boldsymbol{\varepsilon}_L$) with excitation of the electronic subsystem from the ground state with creation of an electron-hole pair, b) scattering of the electron (hole) by a phonon (frequency ω_o, polarization vector **e**), and c) annihilation of the electron-hole pair with emission of a photon (energy $E_S = E_L - \hbar\omega_o$, polarization vector $\boldsymbol{\varepsilon}_S$) and return of the electronic subsystem to the ground state. The Raman intensity for the Stokes process per unit tube length (the so-called resonance Raman profile or RRP) is given by[21] (up to a slightly tube-dependent factor)

$$I(E_L,\omega_o) \propto \left| \frac{1}{L} \sum_{cv} \frac{p_{cv}^S D_{cv} p_{cv}^{L*}}{\left(E_L - E_{cv} - i\gamma_{cv}\right)\left(E_S - E_{cv} - i\gamma_{cv}\right)} \right|^2 , \qquad (26)$$

where L is the length of the tube containing N_c unit cells, E_{cv} is the vertical separation between two states in the valence band $v = klm$ and the conduction band $c = klm'$, and γ_{cv} is the excited state width. $p^{L,S}{}_{cv}$ is the matrix element of the component of the momentum in the direction of the polarization vector $\boldsymbol{\varepsilon}^{L,S}$. The electron-phonon coupling matrix element D_{cv} is determined by the scalar

product of the derivative of E_{cv} with respect to the atomic displacement vector **u** and the phonon eigenvector **e**

$$D_{cv} \propto \sqrt{\frac{\hbar}{2m\omega_o}} \sum_{i\gamma} e_{i\gamma} \frac{\partial E_{cv}}{\partial u_{i\gamma}}. \tag{27}$$

Here m is the mass of the carbon atom and $u_{i\gamma}$ is the γ-component of the displacement of the ith atom in the two-atom unit cell. The derivatives with respect to the atomic displacements for the considered phonon can be calculated using the Hellmann-Feynman theorem.

The estimation of the Raman intensity can be simplified for well-separated features of the RRPs within two approximation schemes. In the first scheme, one considers the matrix elements in Eq. 26 as k-independent and pulls them out of the summation. The remaining summation can be performed analytically. The obtained RRPs reproduce within 5% the results of the full calculations using Eq. 26. In the second scheme, one considers the matrix elements as k-independent and tube-independent (i.e., constants) and evaluates the remaining sum analytically. Based on extensive calculations, it was shown that the tube-independent scheme often leads to erroneous predictions of the Raman intensity and should therefore be avoided.[21,22] This is illustrated in Fig. 11 in the case of three tubes with close radii.

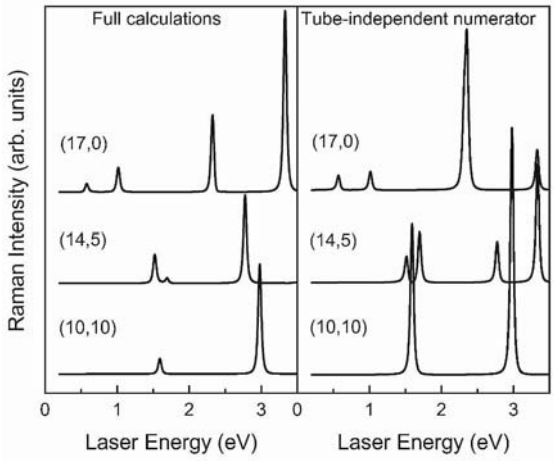

Figure 11. RBM resonance Raman profiles of three different tubes with radius of about 6.7 Å: (17,0), (14,5), and (10,10). The results of the full calculations (Eq. 26) are compared to those of the frequently used tube-independent numerator approximation.[22]

Once the RRPs are evaluated for all nanotube types present in the measured samples, the Raman spectra for different laser excitation energies can be simulated using the following expression[21]

$$I_{tot}(E_L,\omega)=\sum gI(E_L,\omega_o)\frac{1}{\left(\omega-\omega_o\right)^2+\gamma_o^2}, \qquad (28)$$

where g is the tube distribution function for the given sample, γ_o is phonon HWHM, and the summation is carried out over all tube types. The usually adopted Gaussian distribution does not describe sufficiently well the tube types present in the samples. In this case, Eq. 28 can be fit to the measured spectra at several laser excitation energies to obtain the distribution function.

The maximum Raman intensities can be plotted for better visualization as circles with size proportional to the logarithm of the intensity on the transition energy - tube radius plot. As seen in Fig. 8, the lower part of the points of each strip has larger intensity than the upper one. Thus, the points belonging to transitions 11 in S-tubes (Mod1), 22 in S-tubes (Mod2), 11 in M-tubes (Mod0) including transitions 11 in armchair tubes have larger intensity than their counterparts in the strips. This general behavior is corroborated by recent Raman data.[23,24]

5. Conclusions

It is shown that the atomistic approach to the study of the vibrational, mechanical, thermal, electronic, optical, dielectric, etc., properties of ideal nanotubes can be successful when exploiting the screw symmetry of the nanotubes. The results of the calculations of some of these properties within the symmetry-adapted approach are discussed in comparison with available data.

ACKNOWLEDGEMENTS

V.N.P. was supported partly by the Marie-Curie Intra-European Fellowship MEIF-CT-2003-501080. Both authors were supported partly by the NATO CLG 980422. Work performed within the IUAP P5/01 Project "Quantum-size effects in nanostructured materials" funded by the Belgian Science Programming Services.

References

1. *Carbon nanotubes: Synthesis, Structure, Properties, and Applications*, edited by M. S. Dresselhaus, G. Dresselhaus, and Ph. Avouris (Springer-Verlag, Berlin, 2001).
2. V. N. Popov, V. E. Van Doren, and M. Balkanski, Lattice dynamics of single-walled carbon nanotubes, *Phys. Rev. B* 59, 8355-8358 (1999).
3. V. N. Popov, V. E. Van Doren, and M. Balkanski, Elastic properties of single-walled carbon nanotubes, *Phys. Rev. B* 61, 3078-3084 (2000).

4. O. E. Alon, Number of Raman- and infrared-active vibrations in single-walled carbon nanotubes, *Phys. Rev. B* 63, 201403/1-3 (2001).
5. V. N. Popov and L. Henrard, Evidence for the existence of two breathinglike phonon modes in infinite bundles of single-walled carbon nanotubes, *Phys. Rev. B* 63, 233407-233410 (2001).
6. L. Henrard, V. N. Popov, and A. Rubio, Influence of Packing on the Vibrational Properties of Infinite and Finite Bundles of Carbon Nanotubes, *Phys. Rev. B* 64, 205403/1-10 (2001).
7. V. N. Popov and L. Henrard, Breathinglike phonon modes in multiwalled carbon nanotubes, *Phys. Rev. B* 65, 235415/1-6 (2002).
8. V. N. Popov, V. E. Van Doren, and M. Balkanski, Elastic properties of crystals of single-walled carbon nanotubes, *Solid State Commun.* 114, 395-399 (2000).
9. J. Tersoff and R. S. Ruoff, Structural Properties of a Carbon-Nanotube Crystal, *Phys. Rev. Lett.* 73, 676-679 (1994).
10. V. N. Popov, Low-temperature specific heat of nanotube systems, *Phys. Rev. B* 66, 153408/1-4 (2002).
11. A. Mizel, L. X. Benedict, M. L. Cohen, S. G. Louie, A. Zettl, N. K. Budraa, and W. P. Beyermann, Analysis of the low-temperature specific heat of multiwalled carbon nanotubes and carbon nanotube ropes, *Phys. Rev. B* 60, 3264-3270 (1999)
12. J. Hone, B. Batlogg, Z. Benes, A. T. Johnson, and J. E. Fischer, Quantized Phonon Spectrum of Single-Wall Carbon Nanotubes, *Science* 289, 1730-1733 (2000).
13. J. C. Lasjaunias, K. Biljaković, Z. Benes, J. E. Fischer, and P. Monceau, Low-temperature specific heat of single-wall carbon nanotubes, *Phys. Rev. B* 65, 113409/1-4 (2002).
14. V. N. Popov, Curvature effects on the structural, electronic and optical properties of isolated single-walled carbon nanotubes within a symmetry-adapted non-orthogonal tight-binding model, *New J. Phys.* 6, 17.1-17.17 (2004).
15. V. N. Popov and L. Henrard, Comparative study of the optical properties of single-walled carbon nanotubes within orthogonal and non-orthogonal tight-binding models, *Phys. Rev. B* 70, 115407/1-12 (2004).
16. V. N. Popov (unpublished).
17. T. Izawa, R. Souda, S. Otani, Y. Ishizawa, and C. Oshima, Bond softening in monolayer graphite formed on transition-metal carbide surfaces, *Phys. Rev. B* 42, 11469-11478 (1990).
18. S. Siebentritt, R. Pues, K.-H. Rieder, A. M. Shikin, Surface phonon dispersion in graphite and in a lanthanum graphite intercalation compound, *Phys. Rev. B* 55, 7927-7934 (1997).
19. J. Kürti, V. Zólyomi, M. Kertesz, and G. Sun, The geometry and the radial breathing mode of carbon nanotubes: beyond the ideal behaviour, *New J. Phys*. 5, 125.1-125.21 (2003).
20. R. Loudon, Theory of the first-order Raman effect in crystals, *Proc. Roy. Soc. (London)* 275, 218-232 (1963).
21. V. N. Popov, L. Henrard, and Ph. Lambin, Resonant Raman intensity of the radial breathing mode of single-walled carbon nanotubes within a non-orthogonal tight-binding model, *Nano Letters* 4, 1795-1799 (2004).
22. V. N. Popov, L. Henrard, and Ph. Lambin, Electron-phonon and electron-photon interactions and the resonant Raman scattering from the radial-breathing mode of single-walled carbon nanotubes, submitted to *Phys. Rev. B* (2005).
23. C. Fantini, A. Jorio, M. Souza, M. S. Strano, M. S. Dresselhaus, and M. A. Pimenta, Optical Transition Energies for Carbon Nanotubes from Resonant Raman Spectroscopy: Environment and Temperature Effects, *Phys. Rev. Lett*. 93, 147406/1-4 (2004).
24. H. Telg, J. Maultzsch, S. Reich, F. Hennrich, and C. Thomsen, Chirality Distribution and Transition Energies of Carbon Nanotubes, *Phys. Rev. Lett.* 93, 177401/1-4 (2004).

RAMAN SCATTERING OF CARBON NANOTUBES

H. KUZMANY,* M. HULMAN, R. PFEIFFER, F. SIMON
Fakultät für Physik der Universität Wien, Wien, Austria

Abstract. The present state of Raman scattering from carbon nanotubes is reviewed. In the first part of the presentation, the basic concepts of Raman scattering are elucidated with particular emphasis on the resonance scattering. The classical and the quantum-mechanical descriptions are presented and the basic experimental instrumentation and procedures are described. Special Raman techniques are discussed. Eventually, a short review on the electronic structure of single-wall carbon nanotubes (SWCNTs) is given. The second part of the presentation deals with Raman scattering from SWCNTs. The group theoretical analysis and the origin of the basic Raman lines are described. For the radial breathing mode, the observed quantum oscillations and the unusual strong Raman cross section are discussed. For the G-line, the resonance behavior and the response to doping are demonstrated and the calculated dependence of the line frequency on the tube diameter is summarized. For the D-line and for the G'-line, the dispersion is demonstrated and its origin from a triple resonance mechanism is described. Finally, the response from pristine and doped peapods is elucidated. In the third part, most recent results are reported from Raman spectroscopy of double-wall carbon nanotubes (DWCNTs). The unusual narrow lines with widths down to 0.4 cm^{-1} indicate clean room conditions for the growth process of the inner tubes. The (*n*,*m*) assignment of these lines and the high curvature effects are discussed. Results for DWCNTs, where the inner tubes are highly ^{13}C-substituted, are reported with respect to Raman and NMR spectroscopy. Eventually, it is demonstrated that the RBM Raman lines of the inner tubes cluster into groups of up to 14 lines where each member of the cluster represents a pair of inner-outer tubes.

Keywords: Raman scattering; single-wall carbon nanotubes; peapods; double-wall carbon nanotubes; nano clean room; isotope effects

*To whom correspondence should be addressed. Hans Kuzmany; e-mail: hans.kuzmany@univie.ac.at

V.N. Popov and P. Lambin (eds.), Carbon Nanotubes, 89–120.

1. Preface

Raman scattering has developed into one of the key analytical tools to investigate carbon nanotubes. This holds in particular as far as single-wall carbon nanotubes (SWCNTs) are concerned. There are several reasons for this. Firstly, the structure of the tubes is rather simple and many properties can be derived to a first approximation from the study of zone-folded planar graphene. Secondly, the Raman spectra of carbon phases are very well known and easy to record. Thirdly, for the SWCNTs, resonance conditions are easily met for lasers operating in the visible spectral range. As a matter of fact, under good resonance conditions, the Raman response from the tubes has the highest cross section of all materials known so far. Finally, many of the physical properties of the SWCNTs scale with the diameter and depend on the helicity of the tubes, like some of the Raman lines. Therefore the latter are appropriate for deriving information on such properties.

In this series of lectures, three major subjects will be discussed:

- Fundamentals of Raman scattering
- Raman scattering of single-wall carbon nanotubes
- Raman scattering of double-wall carbon nanotubes

2. Fundamentals of Raman scattering

Raman scattering in solids is the inelastic scattering of light from interaction with quasi-particles with an optical type of dispersion. This means that for these particles $\omega(q) \neq 0$ even for $q = 0$. This contrasts the Raman process to Brillouin scattering where interaction of light is with quasi-particles with acoustic dispersion such that $\omega(q) = 0$ for $q = 0$. A general description of Raman scattering can be found in Refs. [1-5].

2.1. FORMAL AND MATHEMATICAL DESCRIPTION OF THE RAMAN PROCESS

The classical approach to the scattering from solids considers the modulation of the susceptibility $\chi_{jl}(\omega)$ by phonons. It is expanded with respect to the normal coordinate Q_k of phonon k. The first expansion coefficient is the Raman tensor. Thus we obtain for the polarizability (in As/m^2) induced by the phonon k

$$P^D{}_j = \chi_{jl,k}(\omega,\Omega_k,t)\varepsilon_0 E_l(\omega,t) = \frac{1}{2}\varepsilon_0 \chi_{jl,k}(\omega,\Omega_k) Q_k E_{l0} Cos(\omega \pm \Omega_k)t \qquad (1)$$

with

$$\chi_{jl,k} = \frac{\partial \chi_{jl}}{\partial Q_k}.$$

Assuming that the induced polarizations act as the source of the evanescent radiation in the form of a Hertzian dipole, we obtain for the emitted Raman light and a 90° scattering geometry as depicted in Fig.1, after thermal averaging,

$$\Phi_{yx,\overline{\Omega}} = \frac{\hbar(\omega \pm \Omega_k)^4 V_u \chi_{yx,k}{}^2 (n_k + 1)V}{32\pi^2 c_0{}^4 \Omega_k} I_i \tag{2}$$

in [W/Ster], where I_i, V_u, V and n_k = exp($\hbar\Omega_k/k_BT$) are the intensity of the incident light, the unit cell volume, the scattering volume, and the average Bose occupation number, respectively. From Eq. 2 we define the Raman cross section of the form

$$\sigma = \frac{1}{VI_i} \frac{d\Phi_{yx}}{d\overline{\Omega}} , \tag{3}$$

where $d\overline{\Omega}$ is a differential solid angle.

In the quantum mechanical description, the incident photon excites an electron-hole pair from a ground state |0⟩ to an intermediate state |i⟩. This transition does not need energy conservation. In the intermediate state a phonon is generated (or absorbed), either from the excited electron or from the excited hole, by electron-phonon interaction. This takes the system to another intermediate state |f'⟩, from where the electron-hole pair can recombine to the final state |f⟩. This state is higher (lower) in energy as compared to the original ground state |0⟩ by one phonon. Overall energy has to be conserved. In solids

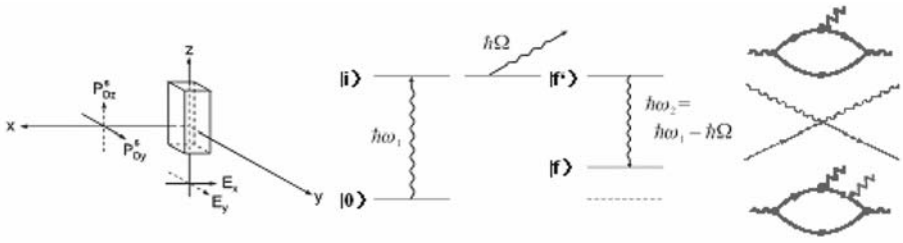

Figure 1. Left: geometry for a 90^0 Raman scattering experiment. Incident and scattered light are either parallel or perpendicular polarized to the scattering plane; Center: quantum-mechanical states involved in the scattering process; Right: Feynman graphs for the H_{pA} interaction (phonon scattering, top), the H_{AA} interaction (electron scattering, center), and for a two-phonon process (bottom).

wave vector conservation is also required. This means: $\mathbf{k}_i = \mathbf{k}_s \pm \mathbf{q}$ where $\mathbf{k}_i$ and $\mathbf{k}_s$ are the wave vectors of the incident and scattered light, respectively, and $\mathbf{q}$ is the wave vector of the phonon. Accordingly, due to the small value of the wave vectors of visible light, in first order, only phonons with $q \sim 0$ (Γ-point phonons) can contribute to the scattering process.

For the quantitative description of the quantum-mechanical formulation, we can use the Feynman diagrams of Fig. 1 (right). For the one-phonon Stokes process this yields

$$K_{2f,10} = \sum_{i,f} \frac{\langle \omega_2, f | H_{er} | 0, f \rangle \langle 0, f' | H_{ep} | 0, i \rangle \langle 0, i | H_{er} | \omega_1, 0 \rangle}{(E_1 - E_i - i\hbar\gamma)(E_2 - E_f - i\hbar\gamma)} \tag{4}$$

Where H_{er} and H_{ep} are the electron-radiation and the electron-phonon interaction Hamiltonians, respectively, E_1 and E_2 are the energy of the incident and scattered light, E_i and E_f represent all transition energies from the ground state and to the final state involved, and γ is an inverse life time constant. The absolute square of this expression is proportional to the Raman cross section. The four indices of the symbol on the left hand side of the equation represent the two states $|0\rangle$ and $|f\rangle$ and the two phonons ω_1 and ω_2 involved.

If one or several transitions from Eq. 5 are close to a real eigenstate, the cross section will be strongly enhanced and is easier to calculate as it will be dominated by these transitions. This case is particularly important for solids where the transition energies often exhibit a continuum in the visible spectral range, known as the *joint density of states* $g_{jds}(\varepsilon)$. In this case we can replace the sum in Eq. 4 by an integral and obtain for the Raman cross section

$$\begin{aligned} \sigma(\omega_1) \propto \left| \int \frac{M_f M_{ph} M_0 \, g_{jds}(\varepsilon) \, d\varepsilon}{(\hbar\omega_1 - \varepsilon - i\hbar\gamma)(\hbar\omega_2 - \varepsilon - i\hbar\gamma)} \right|^2 \approx \\ \approx |M|^2 \left| \int \frac{g_{jds}(\varepsilon) \, d\varepsilon}{(\hbar\omega_1 - \varepsilon - i\hbar\alpha)(\hbar\omega_2 - \varepsilon - i\hbar\alpha)} \right| \end{aligned} \tag{5}$$

where M stands for the product of the three matrix elements on the left side.

2.2. RAMAN SCATTERING, EXPERIMENTAL

On the experimental side, four basic components are needed for Raman scattering: a very narrow band light source, a light focusing and light collection optics, a monochromator system with very good stray light suppression and a very sensitive photon detector. A schematic of a Raman experiment is depicted in Fig. 2.

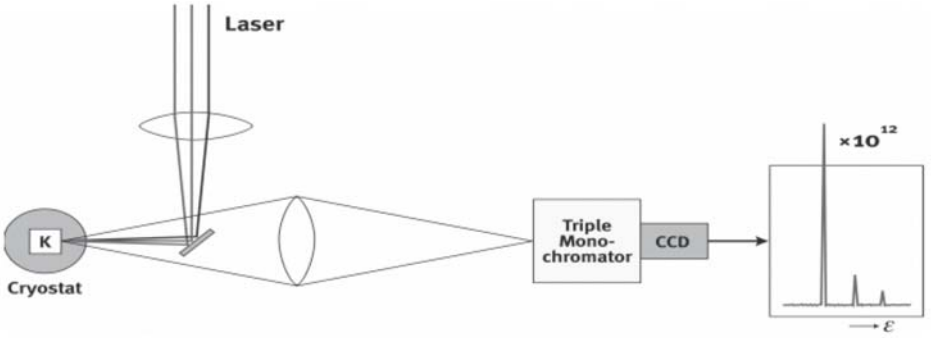

Figure 2. Experimental set up for a Raman experiment, consisting of several lasers for excitation, a light focusing and light collection optic, the sample, the monochromator and an appropriate detector.

As a light source almost exclusively lasers are used in the visible or near visible spectral range. A few mW of power are enough. Tunable lasers such as dye-lasers or Ti-Sapphire lasers have great advantage if resonance scattering is the goal. The focusing and light collection system is either a conventional bright optics or a microscope. In special cases, near-field optics can be used. In this case, the spatial resolution goes down to about 40 nm. For the spectral analysis, usually triple monochromators are used which can be operated in an additive or in a subtractive mode. In the former, the spectral resolution is higher and allows for a spectral band pass down to 0.5 cm^{-1} for red lasers. In the subtractive mode, the stray light suppression is much better which allows measuring Raman shifts down to the one wave number region. Recently, single monochromators have also come in use (confocal Raman systems) in combination with very sharp cutting notch filers. The advantage of such systems is their very high brightness but each laser needs its own notch filter. For the detection of the Raman light, almost exclusively nitrogen cooled, back-thinned, and, if necessary, blue enhanced CCD detectors are used.

Raman scattering has been widely applied to study crystalline and non-crystalline materials with respect to their structures, bonding, symmetries, morphologies, phase transitions, etc. From the many applications, two are selected here as they will be important for the following. Figure 3 depicts Raman spectra of various well-known carbon phases. Diamond has cubic crystal symmetry and two atoms per unit cell. Therefore, it has only one, but threefold degenerated optical mode. Graphite, at least as far as the graphene plane is concerned, has also two atoms per unit cell but the symmetry is only hexagonal. Therefore, it has two optical modes, one non-degenerated A_g species and one twofold degenerated E_{2g} species. The latter is located at ≈1600 cm^{-1} and

is usually called the G-line. The other two lines, which we see in Fig. 3 for the graphitic material, are the D-line and the overtone of the D-line. The D-line is defect-induced and only observed if at least some disorder is present in the material.

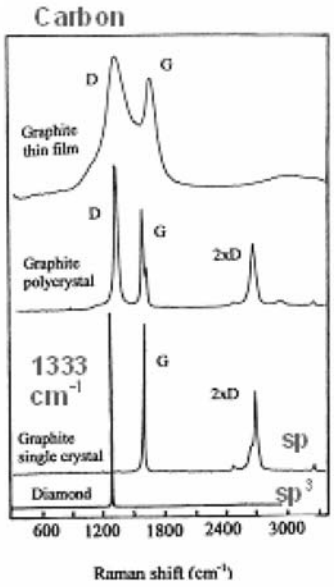

Figure 3. Raman spectra for various carbon phases. Bottom: sp^3 bonded diamond, second, third, and fourth from bottom: sp^2-bonded carbons with increasing disorder.

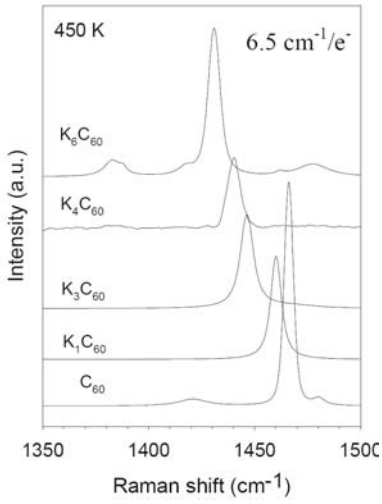

Figure 4. Raman line of the pentagonal pinch mode in C_{60} fullerene for various states of doping.

Interestingly, the overtone of this line is not defect-induced. Neither lines originate from Γ-point phonons and are very famous in sp^2 carbon systems. Figure 4 depicts Raman spectra of the pentagonal pinch mode of C_{60}. In pristine material, this line is strongly resonantly enhanced, particularly in the green-blue spectral range, and located at 1468 cm^{-1}. If electron donors such as, e.g., alkali metals are intercalated, electrons are transferred from the metal to the fullerene orbitals and the conduction band fills up. This causes a quasi-linear downshift of the pentagonal pinch mode by about 6.5 cm^{-1} per transferred electron. This downshift has been used widely to determine the charge state of C_{60} in charge transfer C_{60} compounds.

2.3. SPECIAL TECHNIQUES IN RAMAN SCATTERING

2.3.1. *Resonance excitation*

Since Raman scattering involves not only electron-phonon interaction but also light induced electronic transitions, information on the latter can be obtained. This is in particular so for resonance scattering. A resonance profile of a Raman line represents the cross section as a function of excitation energy. Since all components of the Raman equipment are sensitive to the light energy, careful calibration is needed. This is usually done by measuring the spectrometer response of a well-known cross section such as, e.g., the one of the 520 cm^{-1} Raman line in Si. In this way, electronic transition energies can be determined even from powdered material or from thick, non-transparent films.

2.3.2. *Fano-Breit-Wigner line shape*

Another interesting possibility is the observation of Raman scattering from free electrons in metals or degenerate semiconductors. In this case, the H_{AA}-term of the perturbation Hamiltonian becomes relevant and the excited Raman states exhibit a continuum. Unfortunately, the H_{AA} perturbation is very small and the electronic Raman effect is therefore difficult to observe. However, if the electronic continuum couples to a phonon, interference effects deform the line shape of the latter and the response of the electron continuum becomes observable. The situation is depicted in Fig. 5. It shows the response from a Si crystal doped to various hole concentrations and excited with a red laser. For weak interaction (low doping), the Raman line becomes asymmetric and broadened. For stronger interaction, the line shape almost inverts.

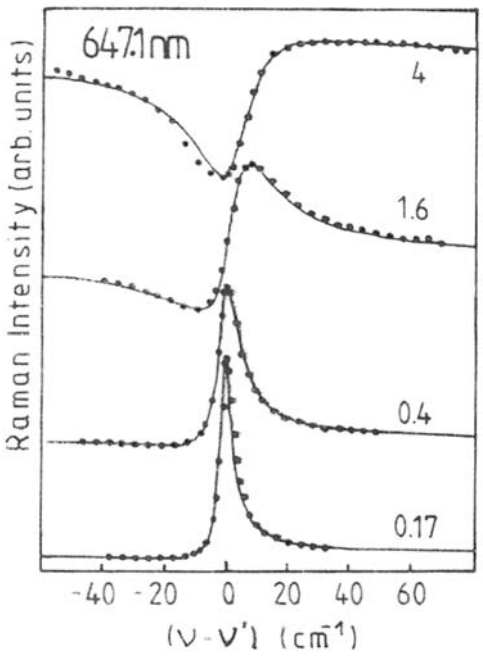

Figure 5. Fano-Breit-Wigner line shapes for the F_{2g} mode in Si doped to various concentrations as indicated in units of 10^{20} cm^{-3} (after Ref. [6]).

2.3.3. *Dispersive modes*

According to the Raman concept, the distance of the Raman line from the exciting laser should be independent of the laser energy. This is not always the case. If the Raman shift depends on the energy of the exciting laser, we talk about *dispersive Raman lines.* There can be several reasons for a dispersion of the Raman lines as for example

- Photo-selective resonance scattering in optically inhomogeneous material;
- Carrier depletion at surfaces combined with light penetration effects;
- Scattering from non Γ–point phonons where the dispersion of the phonon mode becomes relevant and double resonance scattering applies.

In optically inhomogeneous material, the laser depicts predominately such parts where its energy matches to the optical gap. Since the vibrational frequencies often also scale with the optical inhomogeneity, dispersion is observed for such lines.

Depletion of carriers happens at surfaces of semiconductors by surface state effects. This means that any contribution of the carriers to the phonon force

constants is modulated with the distance from the surface. Since the penetration of light depends on its energy, light of different energies will probe different regions of the crystal with respect to the distance from the surface and line dispersion will be observed. An example is shown in Fig.6 for p-doped Ge.

Line dispersion for scattering from non Γ-point phonons is very famous for the D-line in graphite and plays an important role for SWCNTs. Figure 7 depicts an experimental result for the shift of the D-line with laser excitation. The shift is approximately 43 cm^{-1}/eV, independent from the amount of disorder. The D-line represents a *K*-point phonon, which becomes Raman allowed by a double-resonance scattering. The individual intermediate steps of the scattering processes are depicted in the insert of the figure. First, an electron–hole pair is excited under resonance conditions. Then a *K*-point phonon is generated and scatters the electron from *K* to *K'*, again in resonance, since it ends up at an eigenstate of the graphene bands. In order to satisfy **q**-vector conservation, an electron is now elastically and non-resonantly backscattered to the *K*-point region by an impurity. From there it recombines non-resonantly with the hole. This double-resonance scattering process is well known from semiconductor Raman scattering experiments[7]. In the case of overtone Raman scattering, which leads to the G'-line in graphite, backscattering of the electron is established by another phonon. Therefore, no impurity scattering is required.

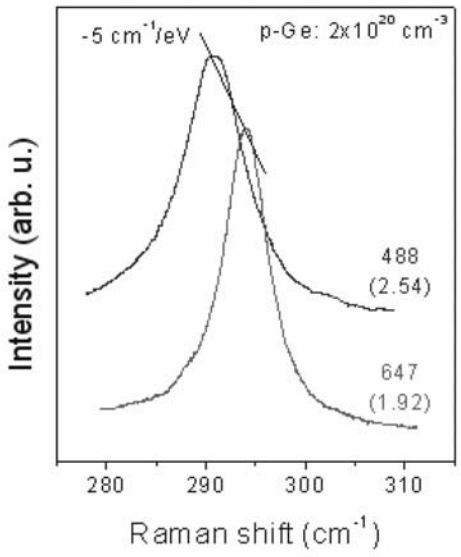

Figure 6. Raman line of *p*-doped Ge as excited by two different laser lines (after Ref. [8]).

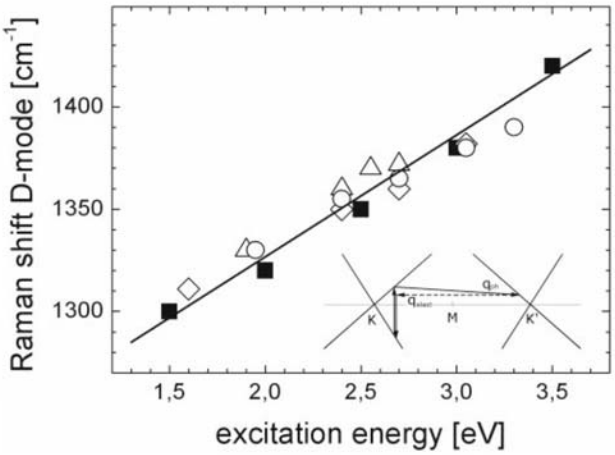

Figure 7. Shift of the D-line in polycrystalline graphite versus laser excitation energy (after Ref. [9]). The insert depicts the graphite band structure close to the *K*- and *K*'-points of the Brillouin zone and the scattering process for the double resonance.

2.4. THE ELECTRONIC STATES OF SINGLE WALL CARBON NANOTUBES

2.4.1. *Results from zone folding*

Zone-folding in the graphene plane is the simplest way to obtain the band structure of SWCNTs. This process will not be described here in detail, since other reports deal with it sufficient explicitly. General descriptions of the electronic properties of SWCNTs can be found in Refs. [10-12]. Only properties with immediate connection to the Raman or resonance Raman process will be described.

By the zone-folding process, a discrete set of curves is cut out from the band structure of graphene which represent the band structure of the SWCNTs. Maxima and minima in these $\varepsilon(k)$ relations lead to the set of van Hove singularities in the density of electronic states which determine, at least in a first approximation, the optical and resonance Raman behavior of the tubes. Figure 8 depicts the density of states for two selected tubes in a narrow energy range around the Fermi level. The (10,10) tube is clearly metallic and the (11,9) tube is semi-conducting. In this approximation only transitions between symmetric Van Hove singularities are allowed and usually assigned as E_{ii}^{S} or E_{ii}^{M} for the semi-conducting and metallic tubes, respectively. The energies E_{ii}^{S} and E_{ii}^{M} scale with the inverse tube diameter approximately as

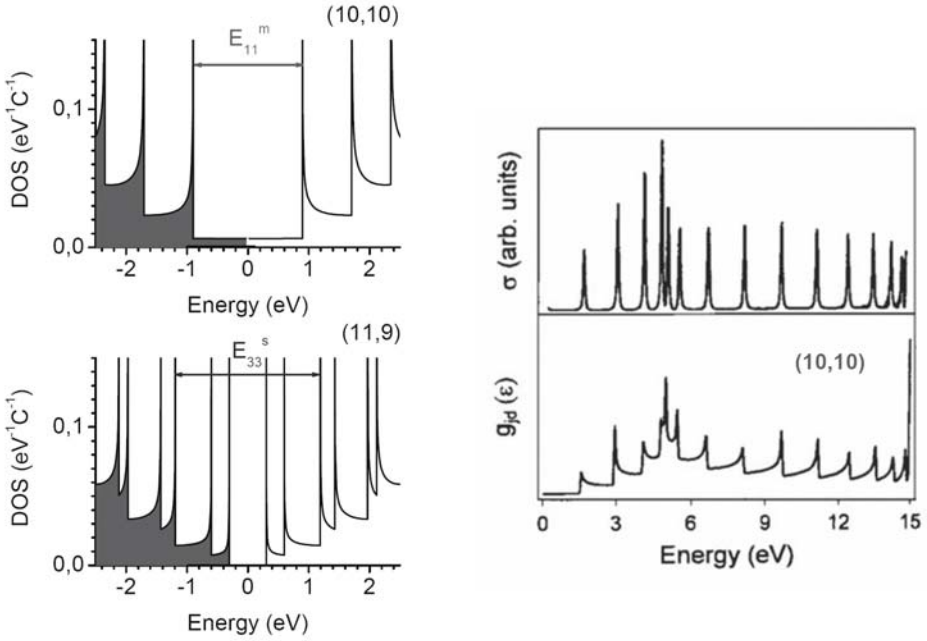

Figure 8. Van Hove singularities for a (10,10) and for a (11,9) tube (left panel) and calculated joint density of states and Raman cross section for a (10,10) armchair tube (right panel).

$$E_{ii}^{\ S} = \frac{2V_0 a_{cc} i}{D} = \frac{0.85i}{D}, \qquad E_{ii}^{\ M} = \frac{6V_0 a_{cc} i}{D} = \frac{2.55i}{D} \tag{6}$$

where $V_0 = 2.9$ eV is the $\pi\pi$-orbital overlap and $a_{C\text{-}C} = 0.144$ nm is the carbon-carbon distance in graphene. There is a hierarchy if corrections to these values for the real tube states are accounted for. These corrections include: trigonal warping in the graphene band structure, chirality effects, curvature effects, and electron correlation (excitonic behavior). For the quantitative analysis of the tubes, these corrections are important as it will be discussed later.

For the achiral tubes, the joint density of states can be evaluated analytically in the zone folding approximation. For armchair tubes (n,n) it yields

$$g_{jds}^{AC}(\varepsilon, n) = \sum_q \frac{\varepsilon}{\pi a \gamma_0^{\ 2} \sin\left[k_q(\varepsilon) a / 2(\cos(q\pi / n) - 2\cos(k_q(\varepsilon) a / 2) \right]} \tag{7}$$

where the sum runs over all sub-bands. This relation allows calculating the Raman scattering cross section explicitly using Eq. 6. The result of the integration is depicted in Fig. 8, right panel.

2.4.2. *The Kataura plot*

The linear relation between the transition energies and the inverse tube diameter allows plotting the whole set of transition energies on a map called Kataura plot[13] as shown in Fig. 9. The straight lines represent the relations of Eq. 5. The deviation of the points from the lines originates from trigonal warping and from chirality effects.

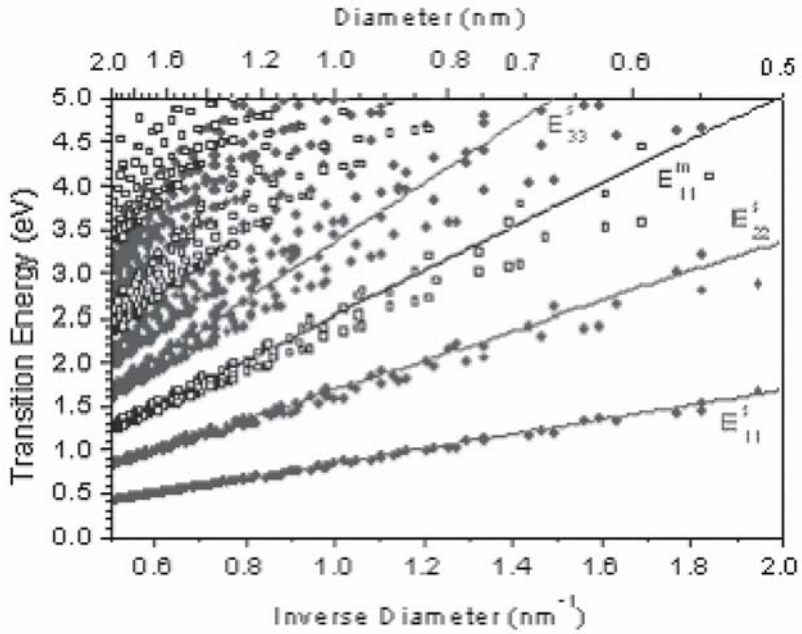

Figure 9. Linear relation between transition energies and inverse tube diameter. Each symbol represents one transition in one particular tube. Full circles are semi-conducting tubes, open squares represent metallic tubes.

3. Raman scattering of single-wall carbon nanotubes

Due to its strong resonance character, the Raman spectrum of SWCNTs is easily recorded and has very pronounced lines. The latter discriminates the SWCNT spectra from those of multi-wall carbon nanotubes where usually only a broad G-line and a rather broad D-line, together with its overtone, is observed. For the SWCNTs each Raman line behaves in a special way as it will be

discussed below. The discussion will also be extended to filled tubes, especially for filling with fullerenes.

3.1. BASIC RAMAN LINES OF SINGLE WALL CARBON NANOTUBES

The Raman spectrum of SWCNTs has four characteristic lines: the radial breathing mode (RBM), the defect induced line (D-line), the graphitic line (G-line), and the overtone of the D-line (G'-line). The D-, G-, and G'-lines are correspond to lines in graphite but the RBM does not exist there (or has zero

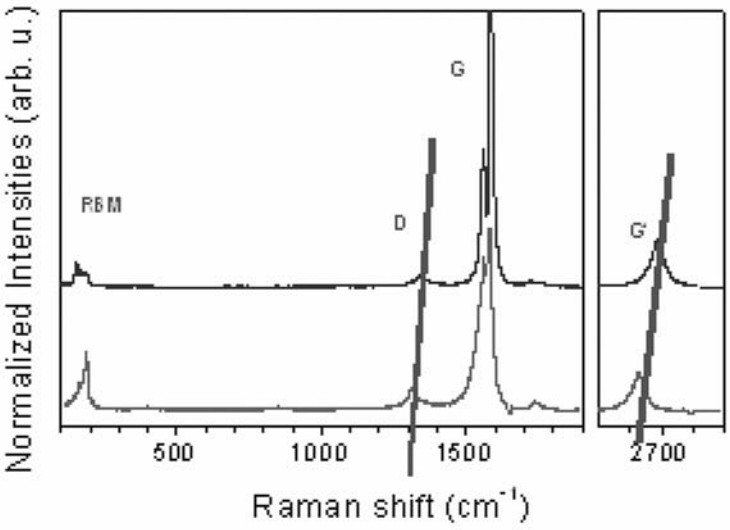

Figure 10. Raman spectra of SWCNTs with a mean diameter of 1.36 nm as excited with 488 nm laser (upper spectrum) and 647 nm (lower spectrum).

frequency). Figure 10 depicts two Raman spectra of laser ablation grown SWCNTs as excited with two different lasers. The four characteristic modes are assigned. The inclined lines passing through the peaks of the D- and G'-lines indicate the dispersive behavior of these modes.

The position of the RBM scales as $1/D$ where D is the tube diameter. This, together with the above described scaling of the transition energies, leads to a dispersive behaviour which manifests itself in a dependence of the line shape on the laser energy. The G-line has also some structure which will be discussed in detail below. Like in graphite, the intensity of the D-line increases with defect concentration whereas the G'-line is independent of defects.

The group-theoretical approach is an important one for the Raman spectra analysis. In principle, line groups are needed to describe the symmetry properties of the tubes. The symmetry elements, point groups and number of

species of Raman active modes are summarized in Table 1. Each nanotube has in addition to the trivial translations a rotation axis and a screw axis parallel to the tube axis. The counting of the rotation axis is determined by the number of lattice points n(LP) on the chiral vector. This number is given by the greatest common divisor between m and n. In addition to the rotational axes along the tube axis, each tube has two types of twofold rotation axes perpendicular to the tube axis. Achiral tubes have some additional symmetry elements. Since we are mainly interested in $\mathbf{q} = 0$ phonons, we can study the isogonal point groups related to the line groups which are D_n and D_{nh} for the chiral and for the achiral tubes, respectively, with $n = N(R) = N_R$. N_R is the number of hexagonal rings in the unit cell. In this way we find 8 and 14 Raman active modes for the achiral and chiral tubes, respectively. The Raman tensors are tabulated in classical textbooks like, e. g., Ref. [3]. The RBM is totally-symmetric and has A_{1g} (A_1) symmetry. The G-line has A_{1g}, E_{1g}, and E_{2g} (A_1, E_1, and E_2) components.

Table 1. Summary of group-theoretical properties of SWCNTs. The lower right graph depicts calculated Raman lines for a set of metallic SWCNTs (after Ref. [14]).

Symmetry elements:	Point groups:
Line groups with SE T: translations, $C_{n(\mathrm{LP})}^{s}$: rotations, $2\pi/n$(LP), parallel $C_{n(\mathrm{LP})}^{w}$: screw axes, π/n(LP) + a/2, parallel U, U': rotations, π, perpendicular σ_h, σ_v, σ_h^{g}, σ_h^{rrfl}: additional mirror planes, one mirror glide plane, and one roto-reflexion plan, only for achiral tubes	For $\mathbf{q} = 0$ modes, only the isogonal point groups to the line groups are relevant. Theses are $D_{N(R)}$ and $D_{N(R)h}$ for the chiral and achiral tubes, respectively, where $N(R)$ is the number of rings in the unit cell Irreducible representations for D_n and D_{nh}: only 1-dimensional and 2-dimensional: A, B, E achiral tubes have center of inversion -> g, u e.g. chiral tubes: A_1, A_2, B_1 B_2, E_1, E_2 ... $E_{N(R)/2\,-\,1}$
Raman active modes: $\Gamma_Z^{\mathrm{Raman}} = 2A_{1g} + 3E_{1g} + 3E_{2g}$, zigzag $\Gamma_A^{\mathrm{Raman}} = 2A_{1g} + 2E_{1g} + 4E_{2g}$, armchair $\Gamma_C^{\mathrm{Raman}} = 3A_1 + 5E_1 + 6E_2$, chiral	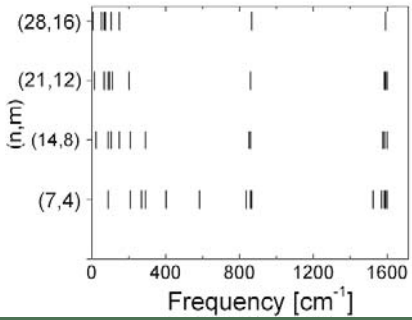

The calculated frequencies in the lower right part of the table were obtained from zone-folding of the graphene plane (except for the RBM mode). As SWCNTs tend to assemble into bundles where tube-tube interaction has some

influence on the frequencies, such frequencies may not immediately correspond to measured Raman modes.

3.2. SPECIAL RAMAN MODES

Now we will discuss the four special Raman modes in some detail.

3.2.1. *The Radial breathing mode*

The RBM suffers to some extent from the tube-tube interaction in the bundles. Therefore, its experimentally observed frequency is formally described by

$$\nu_{RBM} = C_1 / D^x + C_2 \tag{10}$$

where C_1 and C_2 are constants and x is very close to 1. Unfortunately, both constants vary from report to report in a rather wide range which makes it difficult to determine the tube diameter from the observed frequencies, even if Raman experiments were carried out on individual tubes. On the other hand, the Raman response from the RBM mode of a sample with distributed diameters exhibits an interesting oscillatory dispersion as depicted in Fig. 11, left panel. In the figure, the RBM Raman line patterns are plotted for a large number of exciting lasers. The origin of the oscillations is explained in the right panel of the figure. The straight lines on the right represent the Kataura plot. The dashed line on the left represents Eq. 8, without the constant C_2. If a red laser excites a tube resonantly with transition ε_3, a RBM frequency will be observed as given by the dashed line connection. Shifting the laser energy upwards, the observed RBM frequency will also move upwards as thinner tubes will get into resonance. However, at some point the laser will also be able to excite in resonance rather large tubes with the next higher electronic transition, which would be ε_4 in the assignment of the figure. Then, the first moment of the total RBM response will start to decrease. Thus, the observed oscillations in frequency can be traced back to the jamming of the electronic states into van Hove singularities.

The well-defined response of the RBM mode to the distribution of the tube diameters can be used to determine the diameter distribution function. In fact, by analyzing the first and the second moment of the RBM response and assuming a Gaussian distribution for the tube diameters, one can evaluate the mean and the variance of the Gaussian function.[15] An even better and more reliable way is to measure the RBM response with two or three different lasers and obtain in a redundant manner the parameters for the Gaussian function from this procedure.

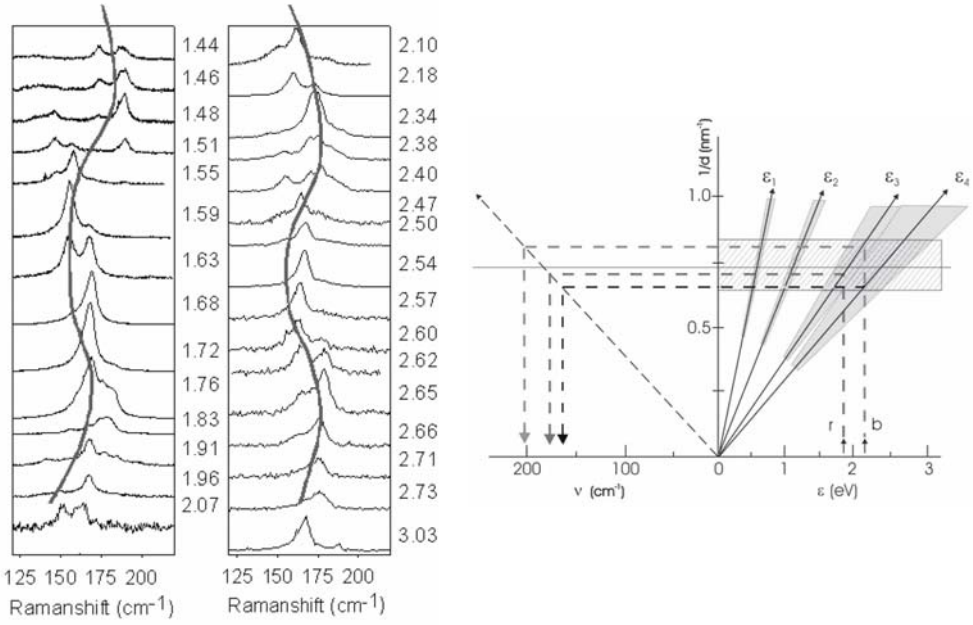

Figure 11. Raman response of the RBM as excited for many different lasers (after Ref. [15]). The wavy line is a guide for the eye (left); The right panel depicts a schematic for the resonance excitations. E_{ii} are the transition energies, r and b represent red and blue lasers. υ is the RBM frequency.

Recently some more detailed Raman experiments were carried out for the HiPco material. These tubes have usually a mean tube diameter of only 1 nm but a rather large width for the distribution function. Results for the RBM response are depicted in Fig. 12, left panel, as exited for various lasers. The oscillatory behavior is certainly also observed but a lot of individual lines appear, wide spread on the frequency axis. It is possible to measure the resonance profile for each of the peaks. The results can be plotted on a two-dimensional grid of frequency and laser excitation energy. As a result we obtain the so-called "Raman chart". An example for a Raman chart is depicted in Fig. 12.

Another important result for the Raman response comes from spectra recorded for individual tubes. Since the resonance cross-section was large, the spectra could be measured from a scattering volume as low as 10^{-6} μm^3. This is the volume of one SWCNT in a laser focus of 500 nm diameter. Figure 13 gives an example. The line from Si originates from an impurity-activated mode and is

about 50 times smaller than the Raman response of the Si optical mode. Estimating the scattering volume for Si to be 0.2 μm^3 we find the Raman cross section of SWCNTs more than a factor 10^6 larger as compared to Si.

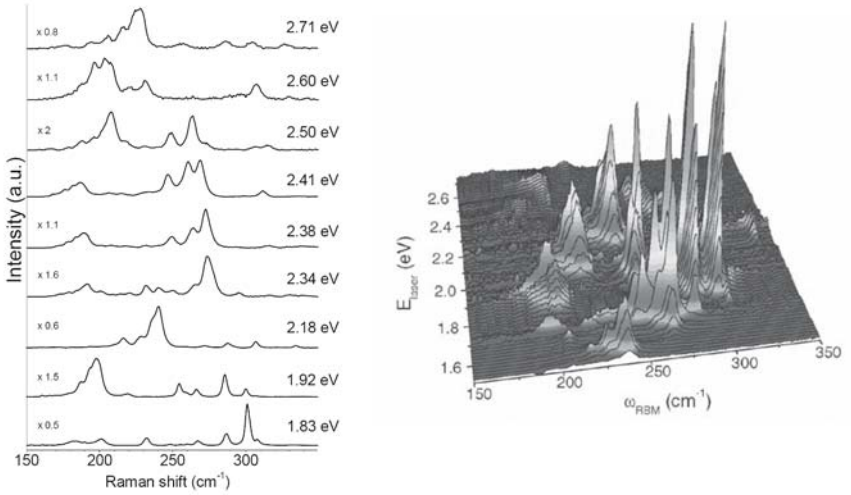

Figure 12. Raman response for the RBM mode of HiPco tubes (left) (after Ref. [16]). Raman cross sections as plotted over a 2D grid of RBM frequency and laser excitation energy (after Ref. [17]).

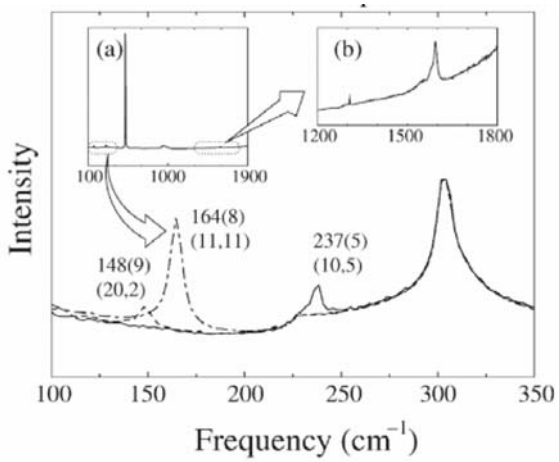

Figure 13. Raman spectra of the RBM modes at 148, 164, and 237 cm^{-1}, respectively. The line at 300 cm^{-1} comes from Si (after Ref. [18]).

3.2.2. *The G-line*

From a theoretical consideration, the G-line in SWCNTs consists of six components with A_1, E_1, and E_2 symmetry and longitudinal or transversal (= circumferential) orientation of the normal coordinates. For the achiral tubes, the index *g* must be added as usual. Experimentally indeed a more or less expressed fine structure has been reported for the G-line pattern. An exact assignment of the fine structure to the A and E modes has not been possible so far. The G-line does not exhibit dispersion except when it comes to the excitation of metallic tubes. However, the G-line exhibits an oscillatory behavior with respect to line intensity if the laser energy is tuned. This is demonstrated Fig. 14, left panel. The set of spectra represent the G-mode response as excited for various lasers. Starting with the highest laser energies, the line intensities increase down to about 2.49 eV. With the further reduction of the energy, the main peak of the G-line decreases but a broad structure appears about 40 cm^{-1} downshifted.

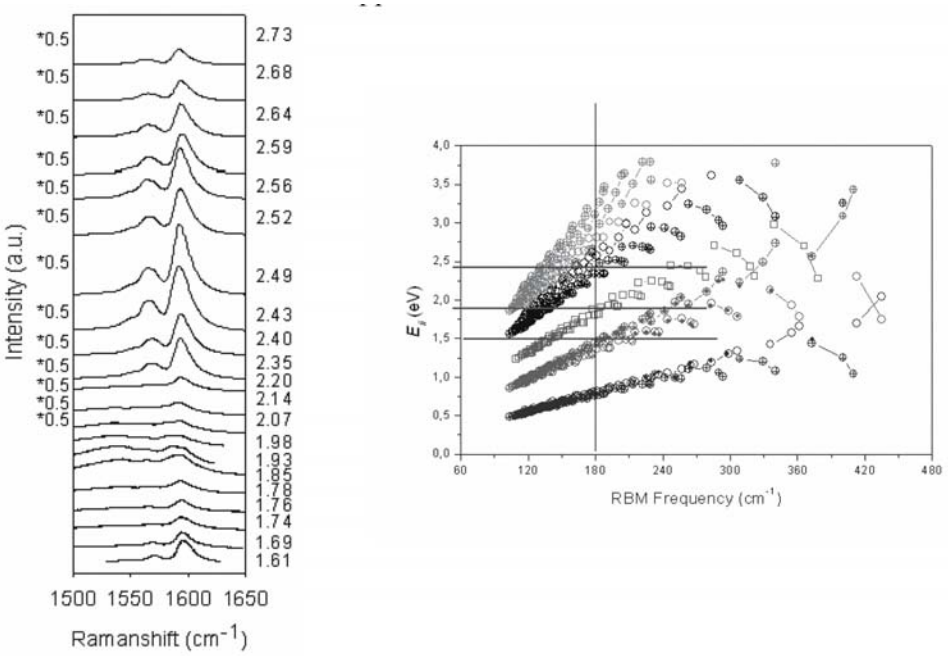

Fiure 14. Left: Raman response for the G-line as excited for various lasers. The spectra are normalized in intensity (after Ref. [19]); Right: Kataura plot of transition energy versus RBM frequency, including curvature effects (after Ref. [20]). The horizontal lines are energy markers.

This broad feature peaks for about 1.93 eV excitation and decreases again for further reduction of the excitation energy. Simultaneously, the main peak of the G-line starts to grow again. The right part of the figure depicts a modified

Kataura plot. The calculation was performed on the level of symmetry-adapted non-orthogonal tight-binding model, which allows one to consider curvature effects. The deviations from the linear behavior are particularly strong for the small diameter tubes (high frequency RBMs). For the tubes used in Fig. 14, left, the mean diameter was 1.4 nm, which corresponds to an approximate RBM frequency of 180 cm^{-1}. The three horizontal lines mark the energies where the main G-line peaks for the first time, where the broad sideband peaks, and where the main G-line peak approaches a peak again. Considering the diameter of the tubes (or the mean RBM frequency of 180 cm^{-1}) it is obvious, that the first peak of the G-line coincides with the resonance at the E_{33}^{S} transition. The maximum of the broad sideband occurs for resonance excitation of metallic tubes at the E_{11}^{M} transition and the re-increase of the main peak takes place when the laser energy comes down to the E_{22}^{S} transition for semi-conducting tubes. A blow-up of the response from the metallic tubes exhibits a Fano-Breit-Wigner line shape demonstrating the strong coupling of this particular line with the free carriers in the metallic tubes.

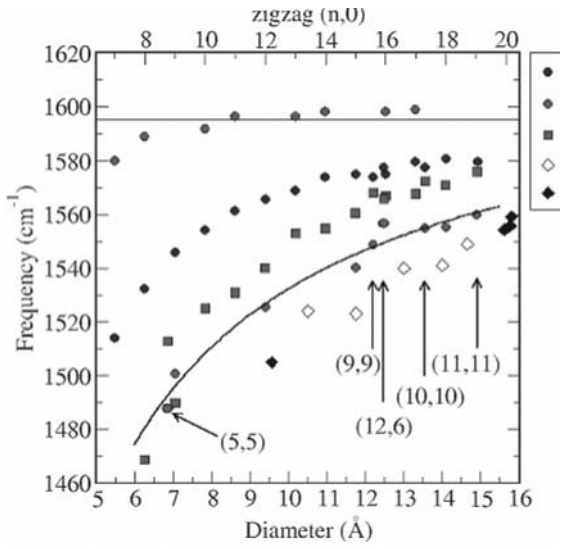

Figure 15. Frequencies for the G-line as calculated using the Vienna Ab-initio Simulation Package (VASP) (after Ref. [21]). The full drawn line is an empirical approximation.

The frequencies of the G-line components were calculated for armchair and zigzag tubes using the density-functional theory code VASP (Vienna Ab-initio Simulation Package). The results are depicted in Fig. 15 for the three selected components $A_1(T)$, $A_1(L)$, and $E_2(L)$. Experimental results for the line position of the metallic tubes are also included in the figure. Two results are striking.

The dependence of line frequency on tube diameter is small for the A modes as long as the tube diameters are rather large. Only for very small tubes, a considerable deviation from the limiting value for large tubes is observed. Only the $E_2(L)$ mode exhibits a considerable down shift with decreasing tube diameter. The other important result is the dramatic drop of line frequencies for the metallic species of the $A_1(L)$ modes. This mode softening corresponds exactly to the experimentally observed downshift of the Raman response for the metallic tubes. A special Peierls-type electron-phonon coupling mechanism was found to be responsible for this softening. This mechanism operates only for the $A_1(L)$ frequencies. The full drawn line represents an empirical law of the form $\nu = 1619 - 866/D$ (Ref. [22]).

There were several reports concerning the change of the G-line Raman response on doping with electron donors and electron acceptors. The general observation is a quenching of the resonance enhancement as a consequence of filling the conduction band (or depleting the valence band). Figure 16 depicts an example where arc-discharge grown SWCNTs were intercalated with Li. A dramatic decrease of the lower frequency components and a weak upshift of the high frequency component are observed. Obviously, the metallic tubes run out of resonance more rapidly.

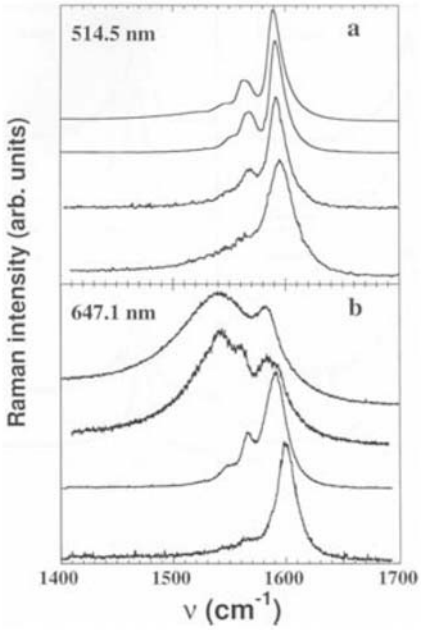

Figure 16. Raman response of the G-line as excited with two different lasers after doping with Li. The Li concentration increases from top to bottom (after Ref. [23]).

3.2.3. *The D-line and the G'-line*

The D-line and the G'-line exhibit a quasi-linear linear dispersion. A set of spectra for both lines is depicted in Fig. 17. The intensity profiles represent again the resonance transitions from the Kataura plot. The right part of the figure shows explicitly the shift of the lines with increasing laser energy. For comparison, the completely flat dispersion for the G-mode is also depicted. The slope of the quasi-linear behavior is 42.3 cm^{-1}/eV for the D-line and 86.4 cm^{-1}/eV for the G'-line. Both values are very similar to the values for graphite. Therefore, it is obvious that the dispersion for the SWCNTs originates from K-point phonons like in graphite. However, since there is a difference in the electronic structure between the two systems, one would expect also some difference in the dispersion. This is indeed the case as we can observe an oscillatory behavior on top of the linear relation. A quantitative analysis revealed indeed that the oscillations originate from the jamming of the electronic states into van Hove singularities.[24] This means that the oscillatory behavior is a consequence of the triple resonance effect relevant for the SWCNTs.

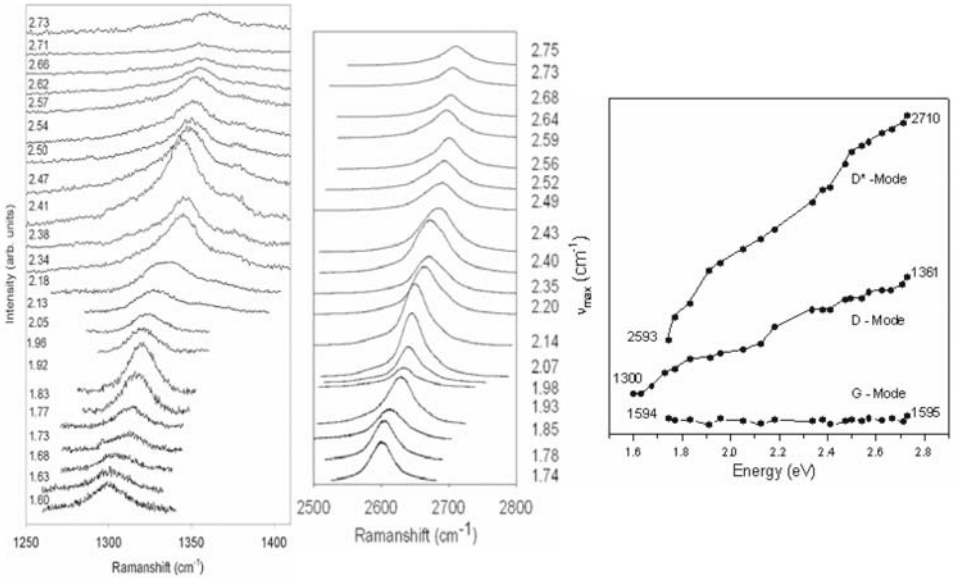

Figure 17. Raman spectra for the D-line (left) and for the G'-line (center) as excited for various lasers. The right part of the figure depicts peak positions of the lines versus laser energy. equivalent to G'. The G-line is included for comparison; after [24].

3.3. FILLING CARBON NANOTUBES (PEAPODS)

One of the many interesting features observed for SWCNTs is the possibility to fill the tubes with other materials. Many different fillers were successfully incorporated into the tubes so far. One of the most exciting filling materials is fullerenes. There is obviously a very strong cohesive force which attracts the fullerenes to the interior of the tubes. The classical and historically first observation of fullerenes inside the tubes came from transmission electron microscopy (TEM).[25] However, since the tubes are at least partly transparent to visible light, a Raman response from the fullerenes inside the tubes can also be expected. This has been demonstrated in various reports even though some of the fullerene modes appear as very weak lines. The line position of the pentagonal pinch mode is downshifted by 3 wave numbers as compared to the response from the free C_{60} molecule and exhibits a characteristic line splitting.[26]

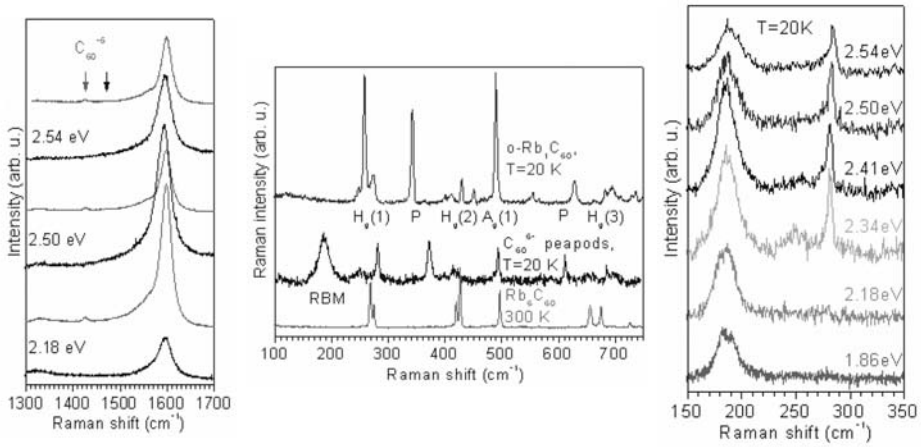

Figure 18. Raman spectra of doped peapods in comparison to un-doped peapods and doped pristine tubes; G-line for doped peapods as compared to doped pristine tubes for three different laser excitations (left); RBM spectral region for doped peapods as compared to polymeric fullerenes and Rb_6C_{60} (center); blow up of RBM spectral region for doped peapods (right) (after Ref. [27]).

Like the empty tubes, the peapods can be doped with electron donors such as Rb. For a reasonably strong doping not only the Raman response from the tubes is modulated as expected from Fig. 16 but also the response from the pentagonal pinch mode is downshifted. For heavy doping the mode shifts by 37 cm^{-1} which corresponds roughly to a charge transfer of 6 electrons. Thus, C_{60} has adopted a charge state –6. This is demonstrated in Fig. 18, left, for excitation with three different lasers. The simultaneously doped pristine tubes do not exhibit the fullerene line. The center of the figure depicts the radial part

of the spectrum and compares the response from the doped peapods with the Raman spectrum of Rb_6C_{60} and the orthorhombic polymeric phase RbC_{60}. In the peapod spectrum two additional lines appear which are assigned as P and clearly indicate that the C_{60}^{-6} molecules inside the tubes are polymerized. Calculations on the tight-binding level suggested that this polymer is single bonded.[28] Interestingly, due to the doping, the resonance behavior for the RBM of the tubes is lost and with it also the dispersion. This is demonstrated in the right panel of Fig. 18.

4. Raman scattering of double-wall carbon nanotubes

Double-wall carbon nanotubes (DWCNTs) are another new species in the family of carbon nanophases. They are of particular interest if grown from peapods, since then there is exactly one inner tube in one outer tube. DWCNTs exhibit several remarkable features. They have the same small size as the SWCNTs but are stiffer and therefore more appropriate as mechanical sensors. Field emission is enhanced. The inner tubes have a very high curvature and allow therefore studying curvature effects in great detail. Inner shell tubes are grown in a highly shielded environment without catalyst and are therefore highly unperturbed. The outer tubes may be subjected to functionalization while the inner tubes remain untouched. Alternatively, as it will be shown below, the inner tubes may be modified, e.g., by isotope substitution whereas the outer tubes remain as grown.

4.1. THE RAMAN RESPONSE FROM THE INNER TUBES

The growth of inner tubes from peapods by annealing at high temperatures was first demonstrated by Smith et al.[29] and proven by TEM. Like in the case of the peapods, Raman spectroscopy is another possibility to study the transition process. Figure 19 depicts a series of spectra which demonstrate the transition from peapods to DWCNTs. Annealing was performed for two hours in high vacuum at 1500 K. The difference in the spectra recorded for peapods and DWCNTs clearly demonstrate the transition. In the spectrum of the DWCNTs, all lines from the fullerenes have disappeared and a new set of very sharp lines have appeared at around 300 cm^{-1}. As the inner tubes have a much smaller diameter, this set of lines is obviously the response from the RBM of the latter. Note that for the red laser, the response from the inner tubes is much larger than the response from the outer tubes even though there is much less carbon material in the former. The right part of the figure depicts a histogram of the diameter distribution. It was drawn under the assumption that the wall to wall distance between inner and outer tube is 0.36 nm which is very close to the

plane to plane distance in graphite. From this figure, three important results can be deduced: Firstly, the number of carbon atoms in the inner tubes is only about one third of the carbon atoms in the outer tubes. Secondly, the distribution of the geometrically allowed tubes is much coarser for the inner tubes as compared to the outer tubes. And finally, there is a cutoff for the inner tube diameters just below d = 0.5 nm. The mean diameter of the inner tubes is about 0.7 nm.

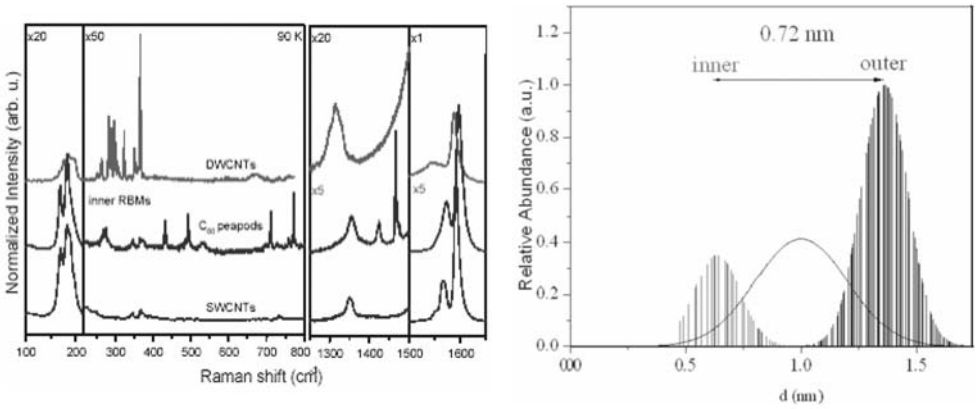

Figure 19. Left: Raman spectra for SWCNTs, as exited with 514 nm (bottom), for peapods as exited with 488 nm (center) and for DWCNTs as excited with 647 nm (top). Right: Diameter distribution plotted as two histograms for outer shell and inner shell tubes and as a curve for HiPco material.

The sharp lines recorded for the Raman response from the inner tubes are surprising. The measurements of the response from these tubes at low temperature and in the high resolution mode of the spectrometer revealed line widths down to 0.4 cm^{-1} after deconvolution from the spectrometer response. An example is depicted in Fig. 22. The narrow lines indicate a long phonon life time and therefore a highly unperturbed tube material. In addition to the small line width, the figure also demonstrates a characteristic line splitting. As a result of this splitting, the number of observed lines is considerably larger than the number of geometrically allowed tubes which can be accommodated in the interior of the host tubes. To a first approximation, this can be explained by the lower density of the geometrically allowed tubes with smaller diameter. Several outer tubes with increasing diameter may be considered as a host before the next larger inner tube can grow for best matching conditions. Since the tube-tube interaction shifts the RBM frequency and since this interaction depends on the wall to wall distance between the tubes, some splitting of the lines can be expected. (See also the discussion below.)

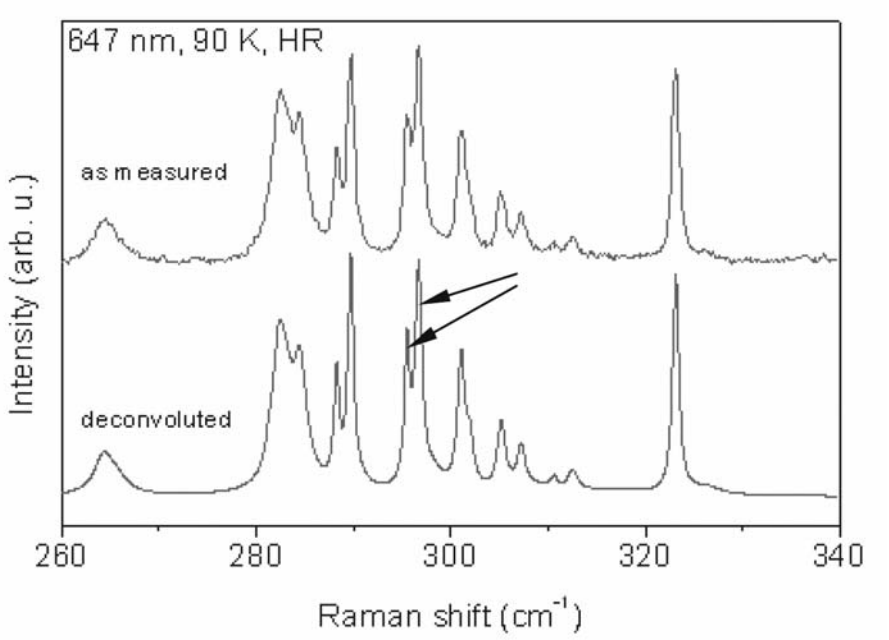

Figure 20. Raman response of the RBM from the inner tubes as recorded with a resolution of 0.5 cm^{-1} (top) and after deconvolution from the spectrometer response (bottom). The arrows indicate line splitting.

4.2. MODE ASSIGNMENT AND HIGH CURVATURE EFFECTS

Recording the Raman response with a large number of laser lines revealed the Raman response from all inner tubes in the diameter range from 1.1 nm down to 0.5 nm. Since the distribution of the RBM frequencies is not a smooth function of the diameters, a best fit search for the assignment of the lines to the (*n*,*m*) values of the corresponding tubes was possible. The result was reported in Ref. [30] and revealed a well-defined straight line for the relation between RBM frequency and inverse tube diameter of the form $\nu_{RBM} = C_1/D + C_2$ with $C_1 = 234$ cm^{-1}nm and $C_2 = 14$ cm^{-1}.

A more dramatic demonstration of the high curvature effects can be obtained from an analysis of the high frequency modes such as the G' mode. The Raman response for this mode as excited with various lasers is depicted in Fig. 21. The dispersion effect is clearly visible for the outer shell tubes (higher frequency peak) and for the inner shell tubes (lower frequency peak). A

quantitative display of the dispersion is depicted in the right panel of the figure. The slopes for the inner and outer tubes are 85.4 and 99.1 cm^{-1}/eV, respectively. From the analysis of the tubes with different diameters in the range of 1 to 1.4 nm, the empirical relation of the form

$$\nu_{G'} = 2536 - 21/D \tag{5}$$

was obtained in Ref. [31] for the dependence of the G' frequency on the tube diameter. This relation yields the correct value of 2684 cm^{-1} for the outer tube if the spectrum is excited with a green laser but a much too high value of 2658 cm^{-1} for the inner tubes. The observed value is 2628 cm^{-1} which means 30 cm^{-1} lower as expected from the extrapolation of Eq. 5. This difference is considered as a breakdown of Eq. 5 for high curvature tubes.

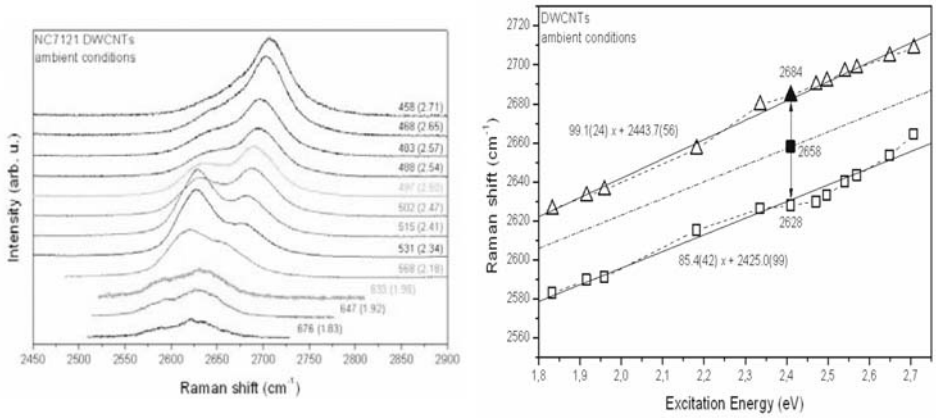

Figure 21. Left: Raman response of the G' mode of DWCNTs for various lasers as indicated. The high and the low frequency peaks come from the outer and inner shell tubes, respectively. The right panel of the figure depicts the dispersion of the two modes. The value of 2658 cm^{-1} for excitation with a green laser (2.42 eV) was obtained for an extrapolation from low curvature tubes.

4.3. ISOTOPE SUBSTITUTION

It was demonstrated recently that the inner tube can be grown as in a highly ^{13}C enriched form by using ^{13}C enriched fullerenes as a filling material[32]. From the mass enhancement all vibrational modes are expected to shift downwards according to the concentration of ^{13}C used. This is demonstrated in Fig. 22, left, for the RBM. The downshift demonstrates the mass enhancement. The ^{13}C enhanced inner shell tubes exhibit dramatic advantages for ^{13}C NMR spectroscopy. Not only that the signal is enhanced by a factor of about ten but it

is also highly selective and originates almost only from the latter. Any response from contaminating carbon phases is strongly suppressed. Figure 24, right, demonstrates this. The top spectrum in the figure displays the response for un-substituted SWCNTs together with the expected line shape resulting from the chemical shift anisotropy of the NMR *g*-factor. The two lower spectra represent the static and the magic angle spinning response for the highly ^{13}C enriched inner tubes. Both lines are downshifted to about 111 ppm as compared to 124 ppm for the un-substituted tube and are also broadened. Both effects are at least partly due to high curvature. The downshift reflects the approach to a sp^3 hybridization for which the ^{13}C NMR resonance is known to appear at 65 ppm. A contribution of the shielding of the magnetic field due to the outer tubes can also contribute to the downshift. The line shape for the response from the static NMR does not represent any more the chemical shift anisotropy. It is rather distorted from the distribution of small tube diameters which correlates to a distribution of sp^2 admixture. The same argument holds for the line broadening of the MAS response.

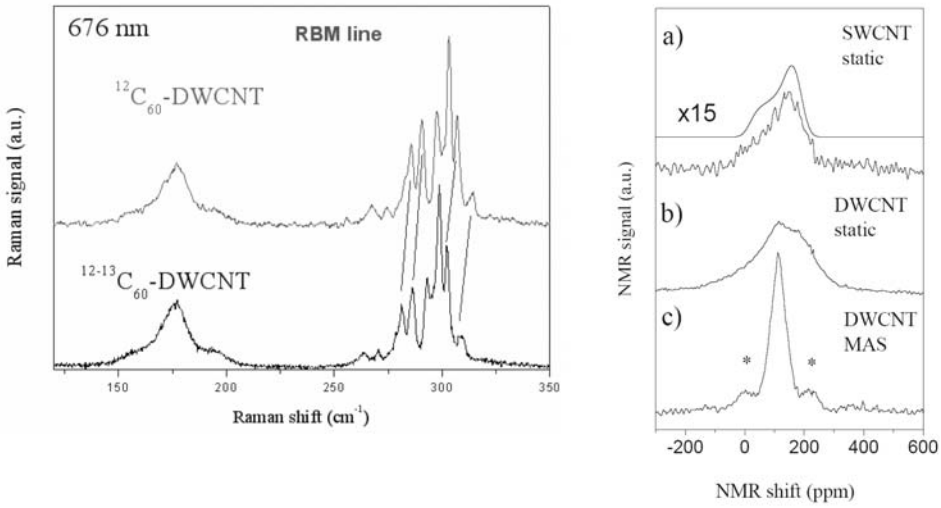

Figure 22. ^{13}C substitution in carbon nanotubes; Left: Raman response for the RBM line; Right: NMR spectroscopy of carbon nanotubes. Top: Response of static NMR for non enriched SWCNTs. The full drawn line is a calculated fit. Center and bottom: static NMR and MAS NMR, respectively, for highly ^{13}C enriched inner shell tubes.

4.4. CLUSTERING OF MODES AND PAIR SPECTRA

The Raman response for the RBM from the inner tubes revealed too many lines which could partly be explained by the different density in the geometrically allowed inner and outer tubes. To take care of the large number of tubes, however, also combinations of inner – outer pairs with not optimized wall to wall distance must be considered. In addition, a comparison of the inner tube RBM spectra to the RBM response from HiPco tubes in the same diameter range revealed a significant absence of lines in the latter material as compared to the signals from the inner shell tubes. This is demonstrated in Fig. 23. In addition, the values obtained for C_1 and C_2 from the assignment procedure described above exhibited some discrepancies with a recent analysis of the RBM in HiPco tubes.[17,33] It was therefore desirable to get a complete frequency and cross-section analysis for the RBM line of the inner tubes. Due to the small diameter of the inner tubes, the tight-binding derived relation between RBM frequency and optical transition energies (Kataura plot from Fig. 9) was expected to be insufficient for this purpose, since it does not include curvature effects. Instead, it turned out that extended tight binding calculations using symmetry adapted non orthogonal tight binding wave functions as reported by V. Popov[20] is a better approach. It reveals dramatic differences to the simple tight binding calculation for tube diameters smaller than 1 nm. Results from such calculations are depicted in Fig. 24 in comparison to results from HiPco tubes. Several striking information can be obtained.

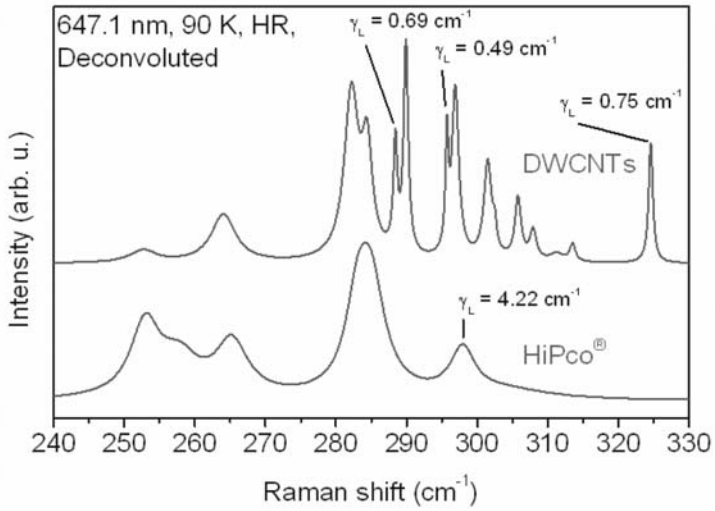

Figure 23. Raman response for the RBM of the inner tubes (upper spectrum) as compared to the response from HiPco tubes (lower spectrum).

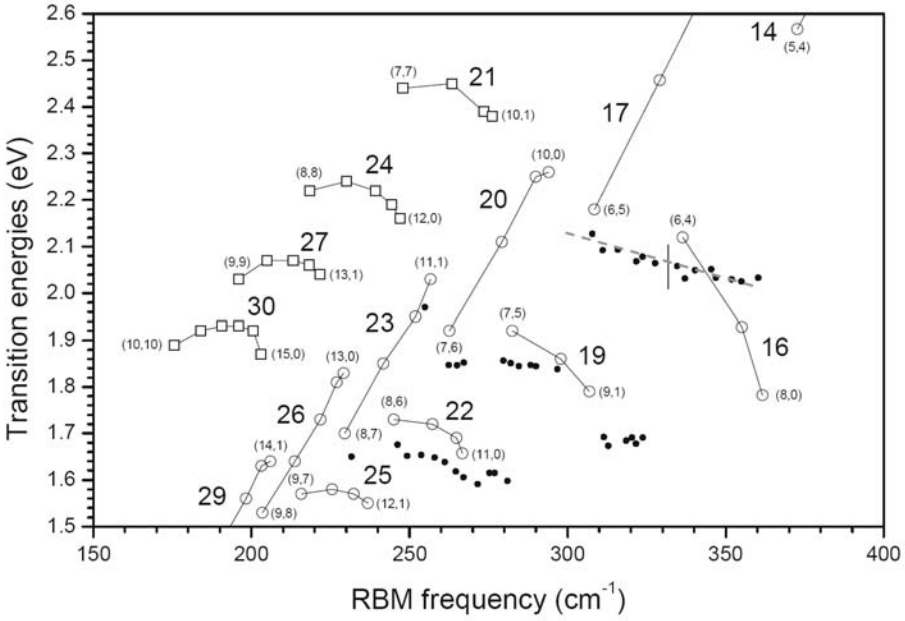

Figure 24. Popov-Kataura plot for the relation between transition energy and RBM frequencies as obtained from an extended tight-binding calculation and HiPco material. Open symbols: averaged for HiPco tubes[17,33] or calculated values. Lines: connect tubes from the same family with family number indicated. Full symbols: observed values for the peak resonance of the inner tubes.

1. The response from the inner tubes follows the same family behavior as the response from the HiPco tubes but the transition energy is generally downshifted by about 50 meV.
2. There is a considerable number of lines which exhibit almost the same resonance transition energy even though the frequencies spread out as much as 30 cm^{-1}.
3. The number of lines in the cluster and thus the width of the cluster increases with decreasing tube diameter.
4. The low frequency end of the clustered lines matches well to the results from the calculation and to the experimental results from HiPco tubes. Therefore the cluster can be assigned to one particular inner tube which has the right resonance energy. This effect is best seen for tube (6,4) of family 16 and tube (6,5) of family 17. These tubes have 14 members in the cluster

as determined from a high resolution measurement at low temperatures (see also Fig. 25).

5. Within the cluster, the resonance energies are slightly decreasing with increasing RBM frequency. The averaged value for the decrease is –2 meV/cm^{-1} as indicated by the dashed line in the figure.

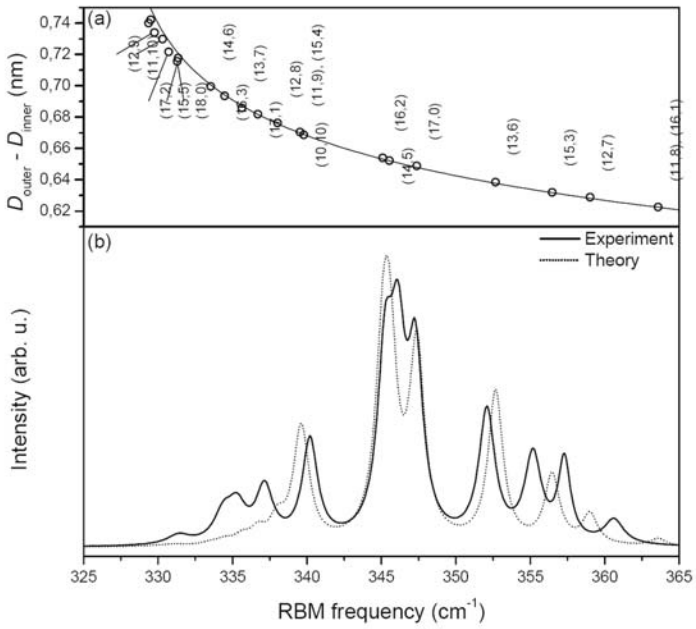

Figure 25. Upper panel: RBM frequencies (x-axis) versus difference in tube diameters (y-axis) as calculated for a (6,4) inner tube and various outer tubes. Lower panel: composed spectrum as observed for the (6,4) cluster (full line) and calculated spectrum where the frequencies from the upper part of the figure were dressed with Lorentzian lines and the intensities were weighted by a Gaussian distribution.

The results can be interpreted in a sense that one inner tube can grow in many, up to 14, different outer tubes and the radial tube-tube interaction is responsible for the line shift. In other words, the outer tubes exert pressure on the inner tubes which causes the line shift. The line shift can be calculated in a continuum model approximation where the tube-tube interactions were described by a Lennard-Jones potential and the dynamical matrix for the frequencies was solved explicitly under these conditions. Results of the calculation are depicted in the upper part of Fig. 25. The lower part of the figure shows the spectrum composed of the contributions of the inner tubes dressed by a Voigtian line. In this way, the spectrum directly represents the population of the pairs of the inner (6,4) tube and the various outer tubes in the cluster. The dotted spectrum was obtained by using the calculated frequencies and dressing them with

Lorentzian lines. The intensities of the lines were taken from an assumed Gaussian distribution.

In detail, the logic is a bit more complicated. During the growth process, various inner tubes are able to grow in a given type of outer tube. This holds for a reasonably large number of outer tubes. Thus, the (6,4) tube exists in a large number of different outer tubes but there is also a large number (maybe ten times more) of the same outer tubes which do not host a (6,4) tube. It is the process of photo-selective Raman scattering which singles out the various (6,4) pairs. In other words, the very strong Raman response of the (6,4) tubes comes only from approximately one tenth of the tube pairs. The higher electron-phonon coupling and the longer lifetime of the excited state are probably the reason for this resonance Raman effect.

5. Summary

In summary, we presented in this contribution some fundamental aspects of Raman scattering of carbon nanotubes with particular emphasis on resonance excitation. A classical and a quantum-mechanical description are provided. The dispersion of the Raman lines and Fano-Breit-Wigner interferences are discussed. In the second part of the manuscript, an extensive description of the Raman scattering from SWCNTs is given. The origin of the quantum oscillation for the RBM, the amount of cross-sectional enhancement and the diameter dependence of the graphitic mode are discussed. This part also contains a review on the Raman response of doped nanotubes upon and of peapod systems. Finally, in the last chapter, the special topic of Raman scattering from the inner shell tubes in DWCNTs is summarized. These systems are special since the inner tubes have a high curvature and an extremely strong Raman effect. By substitution of ^{12}C of the inner tubes with ^{13}C carbons, challenging effects in Raman line shifts and in NMR spectroscopy are reported.

ACKNOWLEDGEMENTS

Work supported by the FWF Nr. 17345 and EU BIN2-2001-00580 and MEIF-CT-2003-501099 projects. Valuable discussions with V. N. Popov are gratefully acknowledged.

References

1. M. Cardona, Light Scattering in Solids, *Topics in Applied Physics* Vol 8, (Springer, Berlin, Heidelberg, 1983)

2. H. Poulet , J.P. Mathieu, Vibrational Spectra and Symmetry of Crystals, (Gordon & Breach, Paris, 1970)
3. H. Kuzmany, Solid State Spectroscopy, (Springer, Berlin, Heidelberg 1999)
4. G. Turell, Infrared and Raman spectra of Crystals, (Academic, London, 1972).
5. D.A. Long, Raman Spectroscopy, (McGraw-Hill, New York 1977).
6. G. Abstreiter, in Light Scattering in Solids IV, M. Cardona, G. Güntherrodt (eds.) *Topics in Appl. Phys*. Vol 54 (Springer, Berlin, Heidelberg 1984).
7. M.L. Bansal, A.K. Sood, and M. Cardona, *Solid State Commun*. 78, 579-582 (1991).
8. D. Olego and M. Cardona, *Phys. Rev. B* 23, 6592-6602 (1981).
9. C. Thomsen and S. Reich, *Phys. Rev. Lett.* 85, 5214 (2000).
10. M. S. Dresselhaus, G. Dresselhaus, and Ph. Avouris, Carbon Nanotubes: Synthesis, Structure, Properties and Applications (Springer-Verlag, Berlin, 2001).
11. R. Saito, G. Dresselhaus, and M. S. Dresselhaus, Physical Properties of Carbon Nanotubes, Imperial College Press (London), 1998.
12. S. Reich, C. Thomsen, J. Maultsch, Carbon Nanotubes, (Wiley-VCH, Weinheim, 2004).
13. H. Kataura, Y. Kumazawa, Y. Maniwa, I. Umezu, S. Suzuki, Y. Ohtsuka, and Y. Achiba, *Synth. Met.* 103, 2555-2558 (1999).
14. R. A. Jishi, L. Venkataraman, M. S. Dresselhaus, and G. Dresselhaus, *Phys. Rev. B* 51, 11176-11179 (1995).
15. H. Kuzmany, W. Plank, M. Hulman, Ch. Kramberger, A. Grüneis, Th. Pichler, H. Peterlik, H. Kataura and Y. Achiba, *Eur. Phys. J. B* 22, 307-320 (2001).
16. A. Kukovecz, Ch. Kramberger, V. Georgakilas, M. Prato and H. Kuzmany, *Eur. Phys. J. B* 28, 223-230 (2002).
17. C. Fantini, A. Jorio, M. Souza, M. S. Strano, M. S. Dresselhaus, and M. A. Pimenta, *Phys. Rev. Lett.* 93, 147406/1-4 (2004).
18. A. Jorio, R. Saito, J. H. Hafner, C. M. Lieber, M. Hunter, T. McClure, G. Dresselhaus, and M. S. Dresselhaus, *Phys. Rev. Lett.* 86, 1118/1-4 (2001)
19. A. Grüneis Diploma work , University of Vienna 2001.
20. V. N. Popov, *New J. Phys*. 6, 17/1-17 (2004).
21. O. Dubay, G. Kresse, H. Kuzmany, *Phys. Rev. Lett*. 88, 235506/1-4 (2002).
22. R. Pfeiffer, 2004, unpublished.
23. J. L. Sauvajol, 2004, unpublished
24. H. Kuzmany, W. Plank, and M. Hulman, *Adv. Solid State Phys.* 40, 194 (2000).
25. B. W. Smith, M. Monthioux, and D. E. Luzzi, *Nature* 396, 323-329 (1998).
26. R. Pfeiffer, H. Kuzmany, T. Pichler, H. Kataura, Y. Achiba, M. Melle-Franco, and F. Zerbetto, *Phys. Rev. B* 69, 035404/1-7 (2004)
27. T. Pichler, H. Kuzmany, H. Kataura, and Y. Achiba, *Phys. Rev. Lett.* 87, 267401/1-4 (2001)
28. S. Pekker, G. Oszlanyi, G. Faigel, *Chem. Phys. Lett.* 282, 435-438 (1998).
29. B. W. Smith, and D. E. Luzzi, *Chem. Phys. Lett.* 321 169-172 (1999).
30. Ch. Kramberger, R. Pfeiffer, H. Kuzmany, V. Zólyomi, and J. Kürti, *Phys. Rev. B* 68, 235404/1-4 (2003).
31. R. Pfeiffer, H. Kuzmany, F. Simon, S. N. Bokova, and E. Obraztsova, *Phys. Rev. B* 71, 155409/1-8 (2005).
32. F. Simon, Ch. Kramberger, R. Pfeiffer, H. Kuzmany, V. Zólyomi, J. Kürti, P. M. Singer, and H. Alloul, *Phys. Rev. Lett.* 95, 017401/1-4 (2005).
33. H. Telg, J. Maultzsch, S. Reich, F. Hennrich, C. Thomsen, *Phys. Rev. Lett.* 93, 177401/1-4 (2004).

RAMAN SPECTROSCOPY OF ISOLATED SINGLE-WALLED CARBON NANOTUBES

THIERRY MICHEL,* MATTHIEU PAILLET, PHILIPPE PONCHARAL, AHMED ZAHAB, JEAN-LOUIS SAUVAJOL
UMR CNRS 5587, Université Montpellier II, Montpellier, France

JANNIK C. MEYER, SIEGMAR ROTH
Max Planck Institute for Solid State Research, Stuttgart, Germany

Abstract. Raman spectra of two isolated single-walled carbon nanotubes with close diameters but different chiral angles are presented and discussed.

Keywords: isolated single-walled carbon nanotubes; Raman spectroscopy

The resonant Raman-scattering technique is a powerful tool for investigating single-wall carbon nanotubes (SWCNTs), for which the radial breathing mode (RBM) and the tangential modes (TM) are the two main features. Recently, several experiments have been devoted to the study of the Raman spectrum at the single-nanotube level (Reich et al. 2004). Here we present a complete experimental procedure and results obtained on two isolated individual SWCNTs with close diameters but different chirality angles.

We developed a complete procedure including the preparation of the substrates, the sample preparation, AFM imaging and Raman spectroscopy (Paillet et al., 2005). Isolated SWCNTs were grown by chemical vapor deposition (Paillet et al. 2004) on lithographically marked substrates. Atomic force microscopy (AFM) was used to check the SWCNT density (< 1 per μm^2), their positions and orientations with respect to the micrometric markers (Fig. 1, left). Room-temperature micro-Raman experiments were performed using the Ar/Kr laser lines at 514.5 nm (2.41 eV) and 647.1 nm (1.92 eV) on a Jobin-Yvon T64000 spectrometer. The Raman spectra of two isolated SWNTs of the same diameter (RBM at 186.4 and 187 cm^{-1}), acquired with two different laser wavelengths (2.41 and 1.92 eV), indicating that one is semiconducting and the other is metallic (Reich et al., 2004), are presented in Fig. 1, right. The profile of the TM of the metallic tube is closer to that of the semiconducting tube than

*To whom correspondence should be addressed. Thierry Michel; e-mail: michel@lcvn.univ-montp2.fr

V.N. Popov and P. Lambin (eds.), Carbon Nanotubes, 121–122.

reported for SWCNT bundles (Reich et al., 2004). Slight differences remain however in the peak positions, relative intensities and widths. These results are a strong experimental evidence for the chirality dependence of TM lineshape and the vanishing of the Breit-Wigner-Fano component in isolated metallic SWCNTs (Paillet et al., 2005).

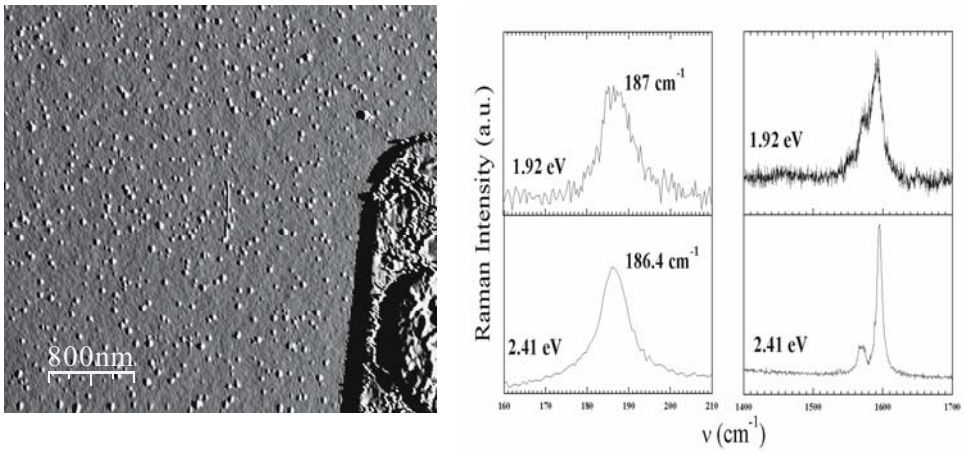

Figure 1. Left: typical AFM image of a low density SWCNT sample synthesized by CVD. Right: Raman spectra of two individual SWCNTs collected using laser photon energy of 1.92 eV (top curves) and 2.41 eV (bottom curves).

In summary, we performed a Raman study of isolated SWCNTs showing the tricky influence of their atomic structure. Experiments involving the combined use of electron diffraction and Raman spectroscopy on the same isolated SWNT are in progress (Meyer et al., 2005) and should allow determining unambiguously the intrinsic response of a specific SWCNT.

References

Reich, S., Thomsen, C., Maultzsch, J., 2004, *Carbon Nanotubes: Basic Concepts and Physical Properties*, John Wiley and Sons, 320 pp.

Paillet, M., Poncharal, P., Zahab, A., Sauvajol, J.-L., Meyer, J. C. and Roth, S., 2005, Vanishing of the Breit-Wigner-Fano component in individual single-wall carbon nanotubes, Phys. Rev. Lett. accepted.

Paillet, M., Jourdain, V., Poncharal, P., Zahab, A., Sauvajol, J.-L., Meyer, J. C., Roth, S., Cordente, N., Amiens, C. and Chaudret, B. 2004, Versatile synthesis of individual individual single-walled carbon nanotubes from nickel nanoparticles for the study of their physical properties, *J. Phys. Chem. B* **108:**17112-17118.

Meyer, J. C., Paillet, M., Sauvajol, J.-L., Duesberg, G. S. and Roth, S. 2005, Lattice structure and vibrational properties of the same nano-object, http://arxiv.org/cond-mat/0501341.

Part III. Electronic and optical properties and electrical transport

ELECTRONIC TRANSPORT IN NANOTUBES AND THROUGH JUNCTIONS OF NANOTUBES

PH. LAMBIN*
Département de Physique, Facultés Universitaires Notre-Dame de la Paix, 61 Rue de Bruxelles, B 5000 Namur, Belgium

F. TRIOZON
DRT/LETI/DIHS/LMNO, CEA, 17 Rue des Martyrs, F 38054 Grenoble Cedex 9, France

V. MEUNIER
Computer Science and Mathematics Division, Oak Ridge National Laboratory, Oak Ridge, TN 37831-6367, USA

Abstract. This chapter briefly reviews the electronic properties of single-wall carbon nanotubes as described by the π-electron tight-binding approximation. The Landauer formalism is introduced next and applied to the study of quantum transport in carbon nanotubes. The electronic properties and electric conductance of intramolecular nanotube junctions are also discussed.

Keywords: electronic structure; density of states; conductivity; transport properties; intramolecular junctions

1. Introduction

The pace of research on carbon nanotubes has been considerably enhanced by the discovery of the extraordinary electronic properties predicted for single-wall nanotubes (SWNTs). These properties are very sensitive to the nanotube atomic structure, namely its diameter and chiral angle (Mintmire et al., 1992; Hamada et al., 1992), or conventionally to the wrapping indices *n* and *m* that label the arrangement of the honeycomb atomic lattice on a seamless cylinder. It was readily predicted that when the difference $n - m$ between the wrapping indices is a multiple of 3, the nanotube is metallic, otherwise there is a semiconducting gap in its band structure (Hamada et al., 1992; Saito et al., 1992). These

*To whom correspondence should be addressed. Philippe Lambin; e-mail: philippe.lambin@fundp.ac.be

V.N. Popov and P. Lambin (eds.), Carbon Nanotubes, 123–142.

properties, and other, can be deduced easily by a simple zone folding of the π-bands of graphite, as demonstrated in Sec. 2. The extreme sensitivity of the electronic properties to the atomic structure of the nanotube is a consequence of the quantization of the π-electron wavevector imposed to the wavefunction by the cyclic boundary condition around the circumference. It follows that a slight change of the couple (n,m) can result in the SWNT being either metallic or semiconducting. Possible applications of nanotubes in nano-electronic devices will have to accommodate and exploit that property (Avouris, 2002).

On a more fundamental point of view, the fact that the nanotubes are one-dimensional systems brings about interesting phenomena. More precisely, carbon nanotubes are quasi one-dimensional systems: the atoms are located on a cylindrical surface in three dimensional space; they do not form a one-dimensional chain, like for instance in polyacetylene. This is important since the Peierls instability responsible for alternating single and double bonds in polyacetylene for example is generally inoperant in the case of carbon nanotubes, except for very small diameter (Connétable et al., 2005). Other one-dimensional effects are predicted to occur in metallic nanotubes, such as the breakdown of the usual Fermi liquid description in favor of Tomonaga-Luttinger behavior dominated by collective excitations (Bockrath et al., 1999).

Nanotubes are remarkable ballistic conductors (Frank et al., 1998). This again is a consequence of the atoms being distributed around the circumference of the tube, which averages defect-induced scattering to a small value. The charge transport in these quasi one-dimensional systems is of quantum origin. It can be described by the Landauer theory, whose formalism is reviewed and illustrated in Sect. 3. Seamless connections between single-walled nanotubes with different helicities can be realized easily, at least on the computer. These so-called intramolecular junctions have interesting electronic properties, which are briefly described in Sect. 4.

2. Zone-folding approximation of graphene band structure

Conceptually, a single-wall nanotube is a rolled-up strip of graphene of which it retains most of its electronic structure. Close to the Fermi energy, the band structure of graphene is dominated by the π states formed by the interacting $2p_z$ orbitals normal to the graphene sheet (Wallace, 1947).

In the Linear Combination of Atomic Orbital (LCAO) approximation, the wavefunction is written as a linear combination of $2p_z$ atomic orbitals Φ_J located on atoms J of the graphene sheet, $\psi = \Sigma_J C_J\Phi_J$. Assuming that the overlap between neighboring orbitals can be neglected, the Schrödinger equation $H\psi = E\psi$ is thus equivalent to a set of linear equations for the LCAO coefficients C_J

$$\sum_J \langle \Phi_I | H | \Phi_J \rangle C_J = E C_I \tag{1}$$

on any site *I*. Due to the periodicity of the graphene layer, the Bloch theorem can be used to relate any coefficient to those of the two atoms in the unit cell shown in Fig. 1(a), C_A and C_B, by simply multiplying the latter by the Bloch factor $\exp(i\mathbf{k}\cdot\mathbf{T})$ where $\mathbf{T}$ is the appropriate translation vector. Equation 1 therefore becomes a set of two linear equations for C_A and C_B. Restricting further the hopping interactions $\langle \Phi_I | H | \Phi_J \rangle$ to first neighbors yields

$$\varepsilon_\pi C_A - \gamma_0 F^*(\mathbf{k}) C_B = E C_A \tag{2a}$$

$$-\gamma_0 F^*(\mathbf{k}) C_A + \varepsilon_\pi C_B = E C_B \tag{2b}$$

where $\varepsilon_\pi = \langle \Phi_A | H | \Phi_A \rangle = \langle \Phi_B | H | \Phi_B \rangle$ is the on-site energy and $\gamma_0 = -\langle \Phi_A | H | \Phi_B \rangle$ is the hopping interaction. In these equations,

$$F(\mathbf{k}) = 1 + \exp(i\mathbf{k}\cdot\mathbf{a}_1) + \exp(i\mathbf{k}\cdot\mathbf{a}_2) \tag{3}$$

with $\mathbf{a}_1$ and $\mathbf{a}_2$ two primitive translation vectors of the graphene hexagonal lattice (see Fig. 1(a)). The two eigenvalues of the set of equations (Eq. 2), given by

$$E_\pm = \varepsilon_\pi \pm \gamma_0 |F(\mathbf{k})|, \tag{4}$$

correspond to the bonding π (minus sign) and the anti-bonding π (plus sign) bands.

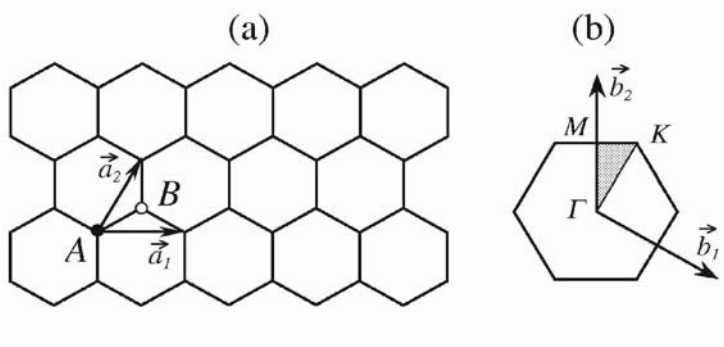

Figure 1. (a) Graphene plane with two primitive translation vectors $\mathbf{a}_1$ and $\mathbf{a}_2$ and its two atoms *A* and *B* in a unit cell. (b) First-Brillouin zone (FBZ) of graphene with its three high-symmetry points Γ, *M*, and *K*. The shaded area corresponds to the irreducible part of the FBZ.

The separation between the π^* and π bands in the reciprocal plane of graphene is shown in Fig. 2(b). These bands cross each other at the corners of the hexagonal first-Brillouin zone shown in Fig. 1(b), conventionally labeled *K*. Indeed, setting

$$\mathbf{k}_K = \frac{1}{3}\mathbf{b}_1 + \frac{2}{3}\mathbf{b}_2 \tag{5}$$

with $\mathbf{b}_1$ and $\mathbf{b}_2$ the reciprocal unit vectors, leads to $F(\mathbf{k}_K) = 1 + \exp(i2\pi/3) + \exp(i4\pi/3)$, which is zero as the sum of the three complex cubic roots of unity. At the corners of the first-Brillouin zone, $E_+ = E_- = \varepsilon_\pi$. For symmetry reasons, the Fermi level coincides with the energy of the crossing. Graphene is a zero-gap semiconductor; its density of states (DOS) at the Fermi energy E_F is zero and increases linearly on both sides of E_F.

In a single-wall nanotube, cyclic boundary conditions apply around the circumference. In the planar development shown in Fig. 2(a), the circumference of the nanotube is a translation vector of graphene, $\mathbf{C} = n\mathbf{a}_1 + m\mathbf{a}_2$, *n* and *m* being the wrapping indices. In the two-dimensional graphene sheet, the wave function at the end point of **C** is the one at the origin multiplied by the Bloch factor $\exp(i\mathbf{k}\cdot\mathbf{C})$. Assuming that the graphene wavefunctions is unaltered in the rolled up structure (zone folding approximation), the cyclic boundary conditions impose $\exp(i\mathbf{k}\cdot\mathbf{C}) = 1$. That condition discretizes the Bloch vector **k** along equidistant lines $\mathbf{C}\cdot\mathbf{k} = 2\pi l$ perpendicular to **C** and therefore parallel to the nanotube axis, where *l* is an integer number. These discretization lines are drawn in Fig. 2(b), for the (5,3) nanotube. Along each of these lines, π^* and π bands of graphene are sampled. Both bands are always separated by a gap, unless one of the discretization lines passes exactly through a corner *K* of the first-Brillouin zone. The nanotube is then a metal, because it contains two bands that cross the Fermi level. The condition for that is $\mathbf{C}\cdot\mathbf{k}_K = 2\pi l$. With the expansion (Eq. 5), this condition becomes $n + m = l$, or equivalently, $n - m$ must be a multiple of 3 to obtain a metallic nanotube, otherwise the nanotube is a semiconductor (Hamada et al., 1992). An armchair nanotube, for which $n = m$, is always a metal. This can be seen directly from Fig. 2(b): a line drawn along the arrow marked *A* always intersects the upper *K* point of the first Brillouin zone.

The band gap of a semiconducting nanotube is easily calculated. Close to the *K* point, the function $F(\mathbf{k})$ can be linearized with respect to the distance $\delta\mathbf{k}$ of the wave vector from the *K* point. To first order in $\delta\mathbf{k}$, Eq. 4 simplifies in

$$E_\pm = \varepsilon_\pi \pm \frac{3}{2}\gamma_0 d_{CC}\left|\delta\mathbf{k}\right| \tag{6}$$

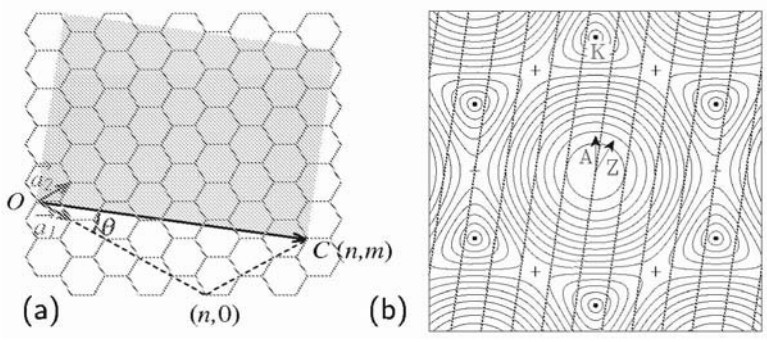

Figure 2. Planar development of the nanotube (*n*,*m*) for $n = 5$ and $m = 3$. In the rolled-up structure, *OC* is the circumference of the nanotube, θ is the chiral angle. (b) Contour plot of the separation between the π^* and π bands of graphene in reciprocal space. The Γ point is at the center of the figure, the corners *K* of the first Brillouin zone are indicated by the black dots, the *M* points are indicated by the crosses. The thick lines across the drawing are discretization lines of the Bloch vector for the (5,3) nanotube, parallel to its axis. The two arrows indicate the axial direction of the armchair (A) and zig-zag (Z) nanotubes.

where d_{CC} is the CC bond length (0.14 nm). As can be seen from Fig. 2(b), the closest distance of the discretization lines to a *K* point for a semiconductor is one third the separation between these lines, which is the reciprocal of the nanotube radius. Setting $\delta\mathbf{k} = 2/3d$ with d the nanotube diameter in the above equation leads to the smallest possible energy of the π^* states and the largest possible value of the π states. The separation between them is the band gap

$$E_g = 2\gamma_0 d_{CC} / d. \tag{7}$$

This formula is asymptotically correct for large d.

The band structure of a nanotube can be obtained directly from Eq. 4 by restricting the wave vector $\mathbf{k}$ to the appropriate discretization lines and therefore making it a one-dimensional good quantum number k (see Fig. 2). The calculations are straightforward in the case of armchair and zig-zag nanotubes, and we find

$$E^{\pm}_{l,\pm}(k) = \pm\gamma_O \sqrt{1 \pm 4\cos(l\pi/n)\cos(ka/2) + 4\cos^2(ka/2)} \tag{8}$$

for the armchair nanotube (*n*,*n*), with $a = \sqrt{3}d_{CC}$ the lattice parameter of graphene (translational axial period of the armchair tube) and

$$E_{l,\pm}^{\pm}(k) = \pm\gamma_O \sqrt{1 \pm 4\cos(l\pi/n)\cos(kc/2) + 4\cos^2(l\pi/n)} \qquad (9)$$

for the zig-zag nanotube (n,0) where $c = 3d_{CC}$ is the axial period. In these expressions, $l = 0, 1 \cdots n - 1$ labels the character of the wavefunction under the rotational symmetry group C_n that both of these non-chiral nanotubes possess. The ± sign in the subscript refers to the ± sign in front of γ_O (corresponding to the π^* and π bands). The other ± comes from additional symmetry of the nanotube. For the armchair nanotube, all the bands have a twofold degeneracy (for instance, $l = 1$ is identical to $l = n - 1$), except for $l = 0$ and possibly $l = n/2$ when n is an even number. This is also true for the zig-zag nanotubes.

The band structure of an armchair (n,n) nanotube is shown in Fig. 3(a) for n = 10. The important characteristics is the presence of two branches that cross each other at the Fermi level (zero of energy) at 2/3 of the Brillouin zone extension. These two branches come from $l = 0$ in Eq. 8. Their wavefunctions are totally symmetric upon a rotation of $2\pi/n$ about the nanotube axis. Their dispersion relation is $E_{0,\pm}^{-}(k) = \pm\gamma_0 \left|2\cos(ka/2) - 1\right|$. The band structures of two zig-zag (n,0) nanotubes, a semiconductor (n = 17) and a metal (n = 18), are shown in Fig. 3(b) and Fig. 3(c), respectively. The highest occupied band and the lowest unoccupied band of the semiconducting nanotube are doubly degenerate; they come from $l = [n/3]$ and $l = n - [n/3]$, where $[x]$ means the nearest integer number to x. For the metallic (n,0) tube, two bands cross each other at the Fermi level at the Γ point. These doubly-degenerate bands correspond to $l = n/3$ and $l = 2n/3$ in Eq. 9. Their dispersion relation is $E_{n/3,\pm}^{-}(k) = \pm 2\gamma_0 \sin(ka/4)$.

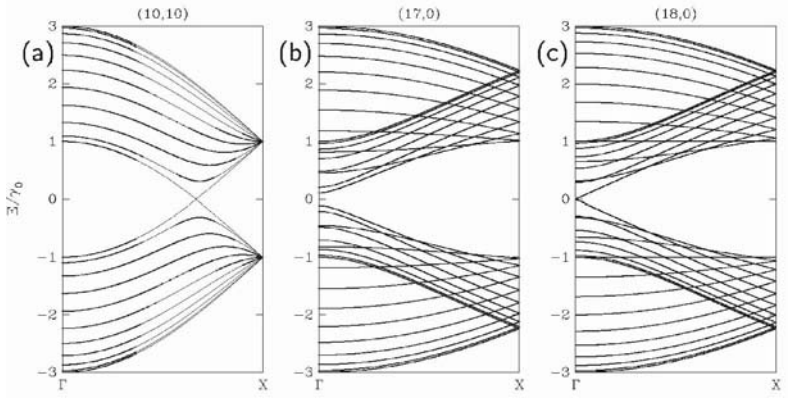

Figure 3. π-electron band structure of (a) the (10,10) nanotube, (b) the (17,0) nanotube, and (c) the (18,0) nanotube. The zero of energy corresponds to ε_π, which is where the Fermi level is located for undoped nanotubes.

In the metallic case, the branches that cross each other at the Fermi level E_F have a nearly linear dispersion in the vicinity the Fermi wavevector. According to Eq. 6, their slope is $dE/dk = \hbar v_F = \pm 3\gamma_0 d_{CC}/2$ where, by definition, v_F is the Fermi velocity. Each of these bands contributes a constant value $1/(\pi |dE/dk|)$ to the density of states per unit length $N(E)$. Multiplying by 4 (number of bands crossing E_F) leads to $N(E) = 8/(3\pi\gamma_0 d_{CC})$, independent on the nanotube radius. Dividing $N(E)$ by the number of atoms per unit length, $4\pi d/(\sqrt{3}d_{CC}^2)$, yields the density of states *per atom*

$$n(E) = \frac{2\sqrt{3}d_{CC}}{\pi^2 \gamma_0 d} \tag{10}$$

which is valid for all metallic nanotubes for $E \approx E_F$. The density of states is constant around the Fermi level and inversely proportional to the tube diameter d.

Using Eq. 6 again, it is readily derived that the highest occupied and lowest unoccupied bands of a semiconducting nanotube (Fig. 3(b)) have a hyperbolic dispersion relation in the neighboring of the wave vector k_m where the band gap is located:

$$E_{\pm}(k) = \varepsilon_\pi \pm \sqrt{\left(E_g/2\right)^2 + \left(3\gamma_0 d_{CC}/2\right)^2 (k - k_m)^2}\,. \tag{11}$$

These relations are valid for all nanotubes, including the chiral ones.

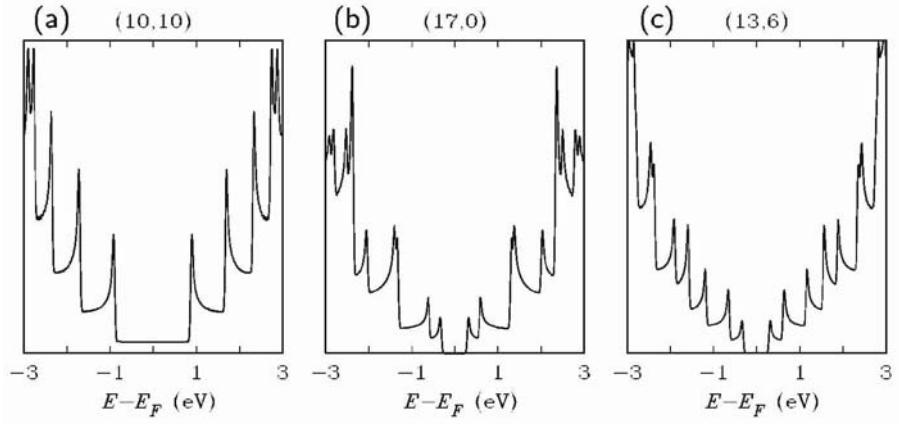

Figure 4. π-electron density of states of (a) the (10,10) nanotube, (b) the (17,0) nanotube, and (c) the (13,6) nanotube. The calculations have been performed with γ_0 = 2.9 eV and ε_π = 0, which corresponds to the Fermi level for undoped nanotubes.

The density of states of three nanotubes is shown in Fig. 4. For the (10,10) nanotube (Fig. 4(a)), the plateau of density of states (Eq. 10) is clearly seen on both side of the Fermi level. The width of this plateau is three times larger than the corresponding band gap of a semiconductor nanotube having the same diameter, namely

$$w = 6\gamma_0 d_{CC} / d \tag{12}$$

The other two nanotubes in Fig. 4 are semiconductors with approximately the same diameter, with a band gap of about 0.6 eV. An essential characteristics of the density of states of nanotubes is the series of asymmetric spikes, called van Hove singularities, arising at all energies where a branch has a horizontal slope in the band structure. These singularities form intrinsic and easy-to-observe fingerprints of the nanotube. Their positions can be measured by scanning tunneling microscopy (STS) (Wildoer et al., 1998; Odom et al., 1998; Kim et al., 1999), which sometimes makes it possible to assign a pair of wrapping indices to the nanotube, or simply to determine the nanotube diameter from Eq. 7 or Eq. 12 (Venema et al., 2000), depending on the metallic or semiconductor character of the tube.

An optical absorption spectrum of single-wall carbon nanotubes is mainly determined by electronic transitions between van Hove singularities, where there is a large accumulation of states. These optical transition energies can be measured experimentally (Kataura et al., 1999). For light polarized parallel to the nanotube axis, transitions between symmetric states with respect to ε_π are allowed. Among these, the transition across the direct band gap of the semiconducting nanotubes has the lowest energy. It correspond to a first optical absorption band at $E_{11}^S = E_g \approx 0.6\,\text{eV}$ for usual nanotubes (those with diameter around 1.4 nm). The zone-folding approximation predicts another absorption band at about twice this energy $E_{11}^S = 2E_g$ still for the semiconducting nanotubes. As for the metallic single-wall nanotubes, the transition between the van Hove singularities located on both sides of the metallic plateau in their density of states (see Fig. 4(a)) has an energy $E_{11}^M = w$, which is typically 1.8 eV.

At the time of writing, there is no real consensus on the actual value of the hopping interaction γ_0. Measurements of the dispersion relation of the two metallic crossing bands by STS in armchair nanotubes (Ouyang et al., 2002) gives γ_0 = 2.5 eV, whereas resonant Raman scattering, which probes the first optical transition energies, lead to γ_0 = 2.9 eV (Souza et al. 2004). The origin of the discrepancy between these two determinations is not known. Of course, the zone-folding approximation is only valid asymptotically for large nanotube diameter. But, even with more refined techniques such as non-orthogonal tight binding model, which incorporates the four valence electrons of carbon, the

optical transition energies measured experimentally are larger than the calculated ones by 0.3 eV (Popov, 2004). For not too small diameters, the correction to the band-structure model is attributed to self-energy and excitonic effects, which seem to partly compensate each other (Kane and Mele, 2004).

3. Transport properties

The transport properties of a single-wall nanotube, either a metallic or a doped semiconductor, may deviate significantly from Ohm's law (Kong et al., 2001). Mesoscopic effects appear when the length of the nanotube between the contact electrodes (see Fig. 5) is smaller than the so-called coherence length. The coherence length is the average distance between two *inelastic* collisions with phonons, for instance. This distance increases by decreasing temperature simply because the number of thermally excited phonons is a decreasing function of temperature. For a metallic single-wall nanotube, the coherence length can be of the order of 1 μm at room temperature. Below that length, the electron wave function conserves memory of its phase, even if the electrons are *elastically* scattered by static defects and impurities. Even though, the resistance of the nanotube is not zero. The reason is that the nanotube offers only a few propagating states in comparison with the macroscopic contact electrodes that have many such states.

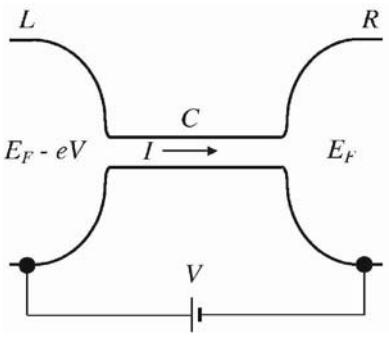

Figure 5. Thin wire connection (*C*) between two contact electrodes (*L* and *R*).

The conductance of the nanotube is proportional to the probability (transmission coefficient) that it transmits charges from one electrode to the other through its available electronic states ψ_n. In a long, perfect nanotube, these are Bloch states corresponding to the energy bands shown in Fig. 3. The total current flowing from the left electrode to the right electrode is

$$I = \int \sum_n T_n(E) f_L(E - E_F + eV)[1 - f_R(E - E_F)] I_{n+}(E) dE + \int \sum_n T_n(E) f_R(E - E_F)[1 - f_L(E - E_F + eV)] I_{n-}(E) dE \quad (13)$$

where $f_R(E)$ and $f_L(E)$ are the Fermi-Dirac distribution functions of the left and right electrodes, respectively, $T_n(E)$ is the transmission coefficient for the state ψ_n of the nanotube at the energy E, $I_{n+}(E)$ and $I_{n-}(E)$ are the forward and backward currents per energy unit that state ψ_n can carry. For one-dimensional systems, it turns out that $I_{n\pm}(E) = \mp 2e/h$, irrespective of the state (band) index n and energy E, provided E be located in the energy interval spanned by this state (Datta, 1995) (otherwise both T_n and $I_{n\pm}$ vanish). Then,

$$I = \frac{2e}{h} \int \sum_n T_n(E)[f_R(E - E_F) - f_L(E - E_F + eV)] dE \quad (14)$$

At zero temperature, this formula further simplifies into

$$I = \frac{2e}{h} \int_{E_F - eV}^{E_F} \sum_n T_n(E) dE \quad (15)$$

At small bias, $I = \left(2e^2/h\right) V \sum_n T_n(E_F)$, which can be identified with the law $I = GV$, where the differential conductance G is given by

$$G = \frac{2e^2}{h} \sum_n T_n(E_F) \quad (16)$$

Here the sum is over all nanotube electronic states n that encompass the Fermi energy E_F and that can carry a current in one direction (also called conducting channels). Equation 16 is the well-known Landauer-Büttiker formula (Landauer, 1970).

In the case of a perfect, infinite nanotube, $T_n = 1$ for all states, and

$$G = G_0 M \quad (17)$$

where $G_0 = 2e^2/h$ is the quantum of conductance and M is the number of branches that cross E_F with a positive dE/dk slope in the band structure. The electrical resistance is therefore $G^{-1} = G_0^{-1}/M = 12.9/M$ kΩ. It is length-independent (ballistic transport) and quantized due to the finite number M of conducting channels. For a metallic nanotube $M = 2$ when E_F is close to the charge-neutrality energy ε_π. There are indeed two branches with positive slope in the band structure ("right" or "left" going branches) crossing ε_π, one at a positive k (shown in Fig. 3(a)), the other at the symmetric wave vector $-k$. And

indeed, two quanta of conductance have been measured experimentally in some metallic nanotubes (Kong et al., 2001).

When moving away from the Fermi energy, more bands are able to transport the current, an effect that gives a corresponding increase in G. In reality, since a nanotube is never perfect, the propagating electrons will be scattered by lattice defects, phonons, structural deformations of the nanotube or at the contacts. This leads to an unavoidable reduction of the transmission probability $T_n(E)$ and in turn of the conductance. In practice, the resistance of a metallic nanotube can be significantly larger than 6.45 kΩ when there are poor coupling contacts with the external electrodes.

The collision of electrons with phonons and defects is expected to increase the electrical resistance. Indeed, the resistance of a nanotube increases slightly with increasing temperature above room temperature, due to the back-scattering of electrons by thermally excited phonons (Kane et al., 1998). At low temperature, the resistance of an isolated metallic nanotube also increases *upon cooling* (Yao et al., 1999). This unconventional behavior for a metallic system may be the signature of electron correlation effects first observed in SWNT ropes (Luttinger liquid, typical of one-dimensional systems) (Bockrath et al., 1999). A single impurity, like B or N, in a metallic nanotube affects only weakly the conductivity close to ε_π (Choi et al., 2000). The same holds true with a Stone-Wales defect, which transforms four adjacent hexagons in two pentagons and two heptagons. Interestingly, even long-range disorder induced by defects like substitutional impurities has a vanishing back-scattering cross section in metallic nanotubes, at least when E_F is close to ε_π (Ando and Nakanishi, 1998; White and Todorov 1998). This is not true with doped semiconducting nanotubes, where scattering by long-range disorder is effective.

A reduction of conductance will also happen when molecules (either chemisorbed or physisorbed molecules, i.e. dopants) interact with the tube (Meunier and Sumpter, 2005). For a non-perfect nanotube, it is clear that the conductance cannot simply be evaluated from counting the bands for a given electron energy but requires an explicit calculation of the transmission function. The difficulty arises from the fact that this type of calculation must be performed in an open system (nor finite or periodic), consisting of a conductor connected to the macroscopic world via two (or more) leads. Practically, the transmission coefficients can be evaluated efficiently using a Green's function and transfer-matrix approach for computing transport in extended systems Buongiorno Nardelli, 1999), which can be generalized for multi-terminal transport (Meunier et al., 2002). This method is applicable to any Hamiltonian that can be described with a localized-orbital basis.

A two-terminal system like in Fig. 5 can be partitioned into a left lead (L), the conductor (C), and a right lead (R). Assuming an orthogonal, localized-orbital basis, the Green function equation writes

$$\begin{pmatrix} \varepsilon - H_L & -H_{LC} & 0 \\ -H_{CL} & \varepsilon - H_C & -H_{CR} \\ 0 & -H_{RC} & \varepsilon - H_R \end{pmatrix}^{-1} = \begin{pmatrix} G_L & G_{LC} & 0 \\ G_{CL} & G_C & G_{CR} \\ 0 & G_{RC} & G_R \end{pmatrix} \tag{18}$$

where H and G with appropriate indices refer to corresponding blocks of the Hamiltonian and Green'function, and ε is a complex energy (see below). From the Green functions, the self-energies of the leads can be calculated in the form $\Sigma_L = H_{CL} g_L H_{LC}$ and similarly for the right electrode, where $g_L = (\varepsilon - H_L)^{-1}$. The coupling Hamiltonian H_{LC} is very short-ranged thanks to the localized-orbital basis. As a consequence, the calculation of Σ_L requires a few elements of the Green function g_L of the perfect, periodic and semi-infinite lead. Using the self-energies, the Green function of the conductor writes

$$G_C = \left(\varepsilon - H_C - \Sigma_L - \Sigma_R\right)^{-1} \tag{19}$$

The total transmission coefficient $T = \sum_n T_n$ between the two leads can be calculated as a trace

$$T = Tr\left(\Gamma_L G_C^r \Gamma_R G_C^a\right)^{-1} \tag{20}$$

and the current between the leads follows from Eq. 14. The coupling operator Γ_L between the conductor and the left lead is expressed as a function of the advanced (a) and retarded (r) self-energies, $\Gamma_L = i\left(\Sigma_L^r - \Sigma_L^a\right)$, and similarly for the right electrode. In all these equation, $\varepsilon = E \pm i\eta$ where the arbitrarily small imaginary part η is added or subtracted to the energy E for the retarded or advanced Green's functions, respectively.

Recent reports in the literature underline the dramatic role played by the interface between electrodes and the nanotube (Leonard and Tersoff, 2000). For instance, it has recently been shown that the electrical properties of junctions between a semiconducting carbon nanotube and a metallic lead dominate the overall electrical characteristics of nanotube based field-effect transistors (Appenzeller et al., 2002; Heinze et al., 2002; Martel et al., 2001; Meunier et al., 2002). In order to focus on the properties of the conductor itself, i.e., its intrinsic properties, one usually relies on modeling. Fortunately, theoretical methods conveniently offer the possibility to separate the effects of the intrinsic properties of the conductor from the effects of its connection to metallic leads. The effect of the heterogeneous contact between carbon nanostructures and metallic leads by seamlessly connecting the conductor to the electron reservoirs

by semi-infinite nanotube leads is illustrated in Fig. 6 for the case of a (5,5) nanotube. In this case, the transmission curve (solid line) is a step-like function that is merely a signature of the available bands in the system, each contributing for one channel of conductance (Eq. 17). When the conductor is connected to reservoirs by metallic leads, the solution of the Schrödinger equation of the perfect tube is no longer valid for the full system made up of the metallic leads and the nanotube portion; it follows that there is a reduction of the transmission probability (dashed line Fig. 6). In this case the interface between the device and the electrodes acts a scattering center.

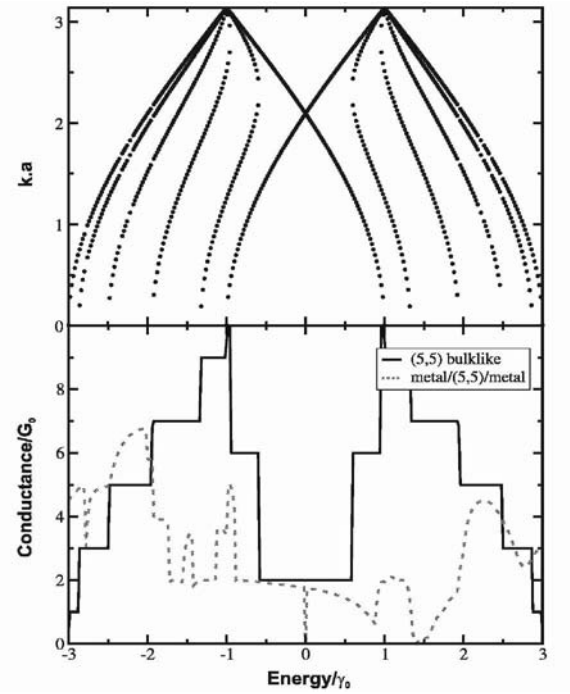

Figure 6. Top: Electronic band structure of a perfect (5,5) carbon nanotube, where *ka* is the product of the Bloch wavevector *k* and the axial period *a* of the tube. The π and π^* bands are crossing at 2/3 of the FBZ. The energy, in units of γ_0, is relative to the charge neutrality level. Bottom: Electron transmission in a (5,5) carbon nanotube, seamlessly connected to an identical nanotube in a bulk-like fashion (full curve) and connected to heterogeneous metallic leads (dotted curve). The bulk-like conductance curve corresponds to a mere counting of the allowed bands for any given energy, since the Bloch states of the leads are also solutions of the Schrödinger equation of the full system. When connected to heterogeneous metallic leads the Bloch states are no longer solution of the whole system, and the conductance can take any values, including non-integer ones.

4. Nanotube junctions

The possibility of realizing seamless connections between single-walled nanotubes with different helicities has stimulated a great interest for about ten years, because metal-semiconductor junctions with simple interfaces can be obtained in this way. Rectifying current properties were predicted for these systems (Service, 1996), like in a diode, which was further verified experimentally (Yao et al., 1999). A simple end to end connection between two different nanotubes, called an intramolecular junction, can be realized by the incorporation of an equal number of pentagons and heptagons. In the simplest case, this junction has just one pair of them (Dunlap, 1992; Saito et al., 1996). More complex structures can be formed, still by incorporating pentagons and heptagons in the otherwise perfect honeycomb arrangement of the carbon atoms. For instance, ideal T or Y junctions can be realized with an excess of six heptagons over the pentagons (Ferrer et al., 1999).

Single-wall intramolecular junctions have been occasionally identified by AFM and STM in samples produced by laser ablation (Yao et al., 1999; Ouyang et al., 2001; Kim et al., 2003). Kinked nanotube junctions, which probably have their pentagon and heptagon at opposite sides, have been observed in a relatively large amount in catalytic CVD samples (Han et al., 1998) and also in arc-discharge samples (Hassanien et al., 2003). It is believed that intramolecular junctions can also be produced, perhaps in a controlled way, by electron irradiation of individual single-wall nanotubes (Hashimoto et al., 2004).

If a two-terminal device like a metal-semiconductor intramolecular junction offers little interest for logical circuits compared to all-transistor devices, it presents the advantage of being a simple object to deal with. On the theoretical side, intramolecular junctions are ideal systems to consider for the study of the electronic structure of metal/semiconductor (Lambin et al., 1995; Chico et al., 1996; Charlier et al., 1996; Ferreira et al., 2000), metal-metal (Tamura and Tsukada, 1997), and semiconductor/semiconductor (Kim et al., 2003) interfaces, to investigate the Schottky barrier formation in such junctions (Odintsov, 2000; Yamada, 2002), and to calculate their transport properties (Saito et al., 1996; Chico et al., 1996b; Buongiorno Nardelli, 1999; Rochefort and Avouris, 2002).

As an example, we discuss here the electronic properties of a straight connection between a metallic (5,5) nanotube and a semiconductor (10,0) nanotube (Rochefort and Avouris, 2002). This connection requires five pentagon-heptagon pairs, distributed all around the structure, in such a way that the hybrid system conserves a five-fold symmetry that both constituents have. The atomic structure is shown in Fig. 7(a). The local density of states computed

with π electrons around the rings of atoms labeled *a*, *b* … *s* are displayed in Figs. 7(b) and (c). As Fig. 7(b) demonstrates, the band gap rapidly forms as one proceeds into the semiconducting part of the junction, except that there is a well-localized metal-induced gap state (MIGS) 0.28 eV below the ε_π level taken as zero of energy. This state exists between locations labeled *b* and persists in the metallic section up to ring *n* in Fig. 7(c). In the metallic part, back-scattering of the wavefunctions whose energy falls within the band gap of the semiconductor lead to interferences typical of armchair nanotubes (Lambin et al., 1995; Meunier et al., 1998). These interferences lead to oscillations of the density of states in the region of the plateau of density of states, between -1.8 and +1.8 eV. Interestingly, the Landauer conductance calculated for this junction drops to zero in an interval of energy larger than the band gap of the (10,0) semiconducting part (Rochefort and Avouris, 2002). This is due to the fact that the wave functions of connected nanotubes have characters upon the C_{5v} symmetry group of the junction that are not compatible in an energy window corresponding to the metallic plateau of the DOS of the (5,5) nanotube. As a consequence, the transmission probability vanishes there, like in the (6,6)-(12,0) metal-metal system with six-fold symmetry (Chico et al., 1996b). The MIGS being below the Fermi level is occupied and is responsible for a charging effect, which amounts to 1.5 electron in the semiconducting part (rings *a*-*g*) and 0.8 electron in the metallic part.

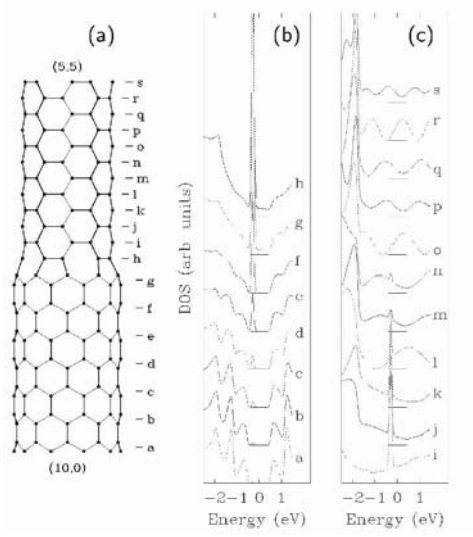

Figure 7. (a) Atomic structure of a straight and symmetric connection between (10,0) and (5,5) nanotubes. (b) and (c) Local π-electron densities of states averaged over the atoms forming the rings labeled *a*, *b* … *s* in (a).

By combining two intramolecular junctions in series, a quantum dot can be obtained when the metallic part is sandwiched between two semiconducting tubes (Chico et al., 1998). This system presents discrete peaks of conductance due to the finite number of electronic states localized in the metallic island (Lu et al., 2004). More interesting perhaps is the metal/semiconductor/metal structure, which may behave like a field effect transistor (Hyldgaard and Lundqvist, 2000). The conceptual simplicity of this device makes it attractive, at least for theoretical calculations. However, controlling the synthesis and growth of a double intramolecular junction of that sort would be extremely difficult. Another way to achieve the same effect, which could possibly be achieved experimentally, is by inducing a metal-semiconductor transformation by a local radial deformation of the central part of a metallic armchair nanotube (Lu et al., 2004). From the theoretical side, however, the structure of the squashed tube is more difficult to address than that of a perfect semiconducting tube sandwiched between two metallic ones.

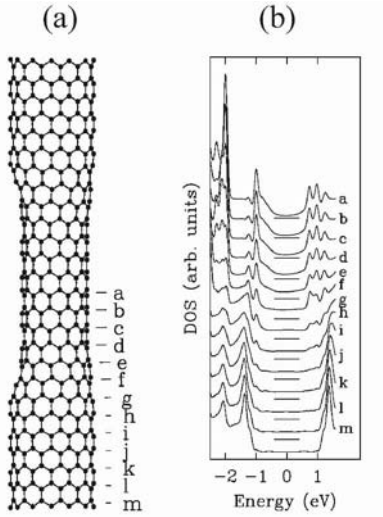

Figure 8. (a) Atomic structure of a metal-semiconductor-metal double junctions constructed with (12,0) and (11,0) zig-zag nanotubes. (b) Local π-electron densities of states averaged over the atoms forming the rings labeled *a*, *b* … *m* in (a). Reproduced from another work (Triozon et al., 2005) of the authors published by IOP Publishing Ltd.

As an example of the latter system, we present here the case of a semiconducting (11,0) nanotube sandwiched between two semi-infinite metallic (12,0) tubes of helicity (12,0). Each (12,0)-(11,0) junction includes a single pentagon-heptagon pair aligned parallel to the axis. In the model shown in Fig. 8, the (11,0) section has 5 unit-cells and length L = 2.1 nm. The local DOS, averaged on successive carbon rings of the (11,0)-(12,0) junction, are plotted in

Fig. 8. Close to the interface, there is a finite DOS in the gap of the semiconductor due to the presence of MIGS's. The weight of these states decreases exponentially with the distance from the interface, with a decay length of order of 1 nm. Apart from the MIG states, there is another interesting feature in the local DOS of the semiconducting section: Several peaks are observed close to –1 and +1 eV, which can be attributed to discrete states confined between the two interfaces.

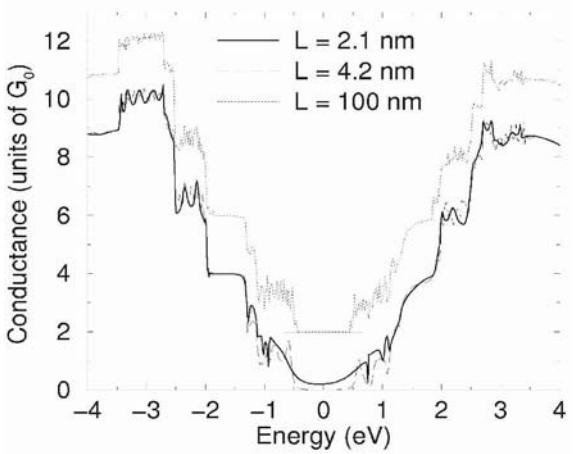

Figure 9. Variation of the conductance of the double-junction (12,0)-(11,0)-(12,0) for three values of the length L of the semiconducting portion. Reproduced from another work of the authors (Triozon et al., 2005) published by IOP Publishing Ltd.

The energy-dependent conductance $G(E)$ was calculated for different lengths L of the semiconducting section using Eq. 20, where the self-energies and the Green functions were obtained by the so-called dissemination technique, as described elsewhere (Triozon et al., 2005). Variations of G with energy make sense if one considers shifting the Fermi level by a gate electrode and/or for transport under a large bias voltage. In both cases, conducting channels far from the charge neutrality point $E = \varepsilon_\pi = 0$ will contribute to the current. The results are shown in Fig. 9. For a short semiconducting section (L = 2.1 nm), electrons with energies falling in the gap can cross the semiconducting section. This is due to the overlap of the MIGS's from the two interfaces. This overlap is much smaller for L = 4.2 nm. Besides, out of the gap, we observe small oscillations of the conductance at $E \approx 1$ eV, corresponding to the peaks observed in the local DOS. These peaks are the signature of electronic states mostly localized in the semiconducting section, like in a quantum box. The density of states in the connected metallic (12,0) tubes is indeed small at

these energies, giving rise to quasi-localized states that provide conducting channel through the semiconducting island. When L increases, the separation energy between these discrete confined states gets smaller, roughly like $1/L$, leading to faster oscillations of the conductance, especially near the edges of the gap. It is interesting also to remark the asymmetry of the conductance curve, which is due to the pentagons and heptagons that destroy the electron-hole symmetry.

ACKNOWLEDGEMENTS

The authors acknowledge M. Buongiorno Nardelli, V.N. Popov, and S. Roche for fruitful discussions. This research is supported in part by the IUAP project P5/01 "Quantum size effects in nanostructured materials" of the Belgian Science Policy Programming (Ph.L) and in part by the Division of Materials Science, U.S. Department of Energy under Contract No. DEAC05-00OR22725 with UT-Battelle, LLC at Oak Ridge National Laboratory (VM).

References

Mintmire, J. W., Dunlap, B. I., and White, C. T., 1992, Are fullerene tubules metallic ?, *Phys. Rev. Lett.* **68:**631-634.

Hamada, N., Sawada, S. I., and Oshiyama, A., 1992, New one-dimensional conductors: graphitic microtubules, *Phys. Rev. Lett*. **68:**1579-1581.

Saito, R., Fujita, M., Dresselhaus, G., and Dresselhaus, M. S., 1992, Electronic structure of chiral graphene tubules, *Appl. Phys. Lett.* **60:**2204-2206.

Avouris, Ph., 2002, Carbon nanotube electronics, *Chem. Phys.* **281:**429-445.

Connétable, D., Rignanese, G. M., Charlier, J. C., and Blasé, X., 2005, Room temperature Peierls distortion in small diameter nanotubes, *Phys. Rev. Lett.* **94:**015503/1-4.

Bockrath, M., Cobden, D. H., Lu, J., Rinzler, A. G., Smalley, E. E., Balents, L., and McEuen, P. L., 1999, Luttinger-liquid behavior in carbon nanotubes, *Nature* **397:**598-601.

Frank, S., Poncharal, Ph., Wang, Z. L., and de Heer, W. A., 1998, Carbon nanotube quantum resistors, *Science* **280:**1744-6.

Wallace, P. R., 1947, The band theory of graphite, *Phys. Rev.* **71:**622-634.

Wildoer, J. W. G., Venema, L. C., Rinzler, A. G., Smalley, R. E., and Dekker, C., 1998, Electronic structure of atomically resolved carbon nanotubes, *Nature* **391:**59-62.

Odom, T. W., Huang, J. L., Kim, Ph., and Lieber, Ch. M., 1998, Atomic structure and electronic properties of single-walled carbon nanotubes, *Nature* **391:**62-64.

Kim, Ph., Odom, T. W., Huang, J. L., and Lieber, C. M., 1999, Electronic density of states of atomically resolved single-walled carbon nanotubes: Van Hove singularity and end states, *Phys. Rev. Lett.* **82:**1225-1228.

Venema, L. C., Meunier, V., Lambin, Ph., and Dekker, C., 2000, Atomic structure of carbon nanotubes from scanning tunneling microscopy, *Phys. Rev. B* **6**1:2991-2996.

Kataura, H., Kumazawa, Y., Maniwa, Y., Umezu, I., Suzuki, S., Ohtsuka, Y., and Achiba, Y., 1999, Optical properties of single-wall carbon nanotubes, *Synt. Metals* **103:**2555-2558.

Ouyang, M., Huang, J. L., and Lieber, C. M., 2002, One-dimensional energy dispersion of single-walled carbon nanotubes by resonant electron scattering, *Phys. Rev. Lett.* **88:**066804/1-4.

Souza Filho, A. G., Chou, S. G., Samsonidze, G. G., Dresselhaus, G., Dresselhaus, M. S., An, L., Liu, J., Swan, A. K., Unlu, M. S., Goldberg, B. B., Jorio, A., Gruneis, A., and Saito, R., 2004, Stokes and anti-Stokes Raman spectra of small-diameter isolated carbon nanotubes, *Phys. Rev. B* **69:**115428/1-8.

Popov, V. N., 2004, Curvature effects on the structural, electronic and optical properties of isolated single-walled carbon nanotubes within a symmetry-adapted non-orthogonal tight-binding model, *New J. Phys.* **6:**17/1-17.

Kane, C. L., and Mele, E. J., 2004, Electron interactions and scaling relations for optical excitations in carbon nanotubes, *Phys. Rev. Lett.* **93:**197402/1-4.

Kong, J., Yenilmez, E., Tombler, T. W., Kim, W., Dai, H., Laughlin, R. B., Liu, L., Jayanthi, C. S., and Wu, S. Y., 2001, Quantum interference and ballistic transmission in nanotube electron waveguides, *Phys. Rev. Lett.* **87:**106801/1-4.

Datta, S., 1995, *Electronic Transport in Mesoscopic Systems*, Cambridge University Press, Cambridge, 1995, pp. 1-377.

Landauer, R., 1970, Electrical resistance of disordered one-dimensional lattices, *Phil. Mag.* **21:**863-867.

Kane, C. L., Mele, E. J., Lee, R. S., Fischer, J. E., Petit, P., Dai, H., Thess, A., Smalley, R. E., Verschueren, A. R. M., Tans, S. J., andDekker, C., 1998, Temperature-dependent resistivity of single-wall carbon nanotubes, *Europhys. Lett.* **41:**683-688.

Yao, Z., Postma, H. W. Ch., Balents, L., and Dekker, C., 1999, Carbon nanotube intramolecular junctions, *Nature* **402:**273-276.

Choi, H. J., Ihm, J., Louie, S. G., and Cohen, M. L., 2000, Defects, quasibound states, and quantum conductance in metallic carbon nanotubes, *Phys. Rev. Lett.* **84:**2917-2920.

Ando, T., and Nakanishi, T., 1998, Impurity scattering in carbon nanotubes - Absence of back scattering, *J. Phys. Soc. Japan* **67:**1704-1713.

White, C. T., and Todorov, T. N., 1998, Carbon nanotubes as long ballistic conductors, *Nature* **393:**240-242.

Meunier, V., and Sumpter, B. G., 2005, Amphoteric doping of carbon nanotubes by encapsulation of organic molecules: electronic properties and quantum conductance, *J. Chem. Phys.*, in press.

Buongiorno Nardelli, M., 1999, Electronic transport in extended systems: Application to carbon nanotubes, *Phys. Rev. B* **60:**7828-7833.

Meunier, V., Buongiorno Nardelli, M., Bernholc, J., Zacharia, T., and Charlier, J. C., 2002, Intrinsic electron transport properties of carbon nanotube Y-junctions, *Appl. Phys. Lett.* **81:**5234-5236.

Leonard, F., and Tersoff, J., 2000 Role of Fermi-level pinning in nanotube Schottky diodes, *Phys. Rev. Lett.* **84:**4693-4696.

Appenzeller, J., Knoch, J., Derycke, V., Martel, R., Wind, S., and Avouris, Ph., 2002, Field-modulated carrier transport in carbon nanotube transistors, *Phys. Rev. Lett.* **89:**126801/1-4.

Heinze, S., Tersoff, J., Martel, R., Derycke, V., Appenzeller, J., and Avouris, Ph., 2002, Carbon nanotubes as Schottky barrier transistors, *Phys. Rev. Lett.* **89:**106801/1-4.

Martel, R. V., Lavoie, C., Appenzeller, J., Chan, K. K., Tersoff, J., and Avouris, Ph., 2001, Ambipolar electrical transport in semiconducting single-wall carbon nanotubes, *Phys. Rev. Lett.* **87:**256805/1-4.

Service, R. F., 1996, Mixing nanotube structures to make a tiny switch, *Science* **271:**1232.

Dunlap, B. I., 1992, Connecting carbon tubules, *Phys. Rev. B* **46:**1933-1936.

Saito, R., Dresselhaus, G., and Dresselhaus, M. S., 1996, Tunneling conductance of connected carbon nanotubes, *Phys. Rev. B* **53:**2044-2050.

Melchor Ferrer, S., Khokhriakov, N. V., and Savinskii, S. S., 1999, Geometry of multi-tube carbon clusters and electronic transmission in nanotube contacts, *Molec. Eng.* **8:**315-344.

Ouyang, M., Huang, J. L., and Lieber, Ch. M., 2001, Atomically resolved single-walled carbon nanotube intramolecular junctions, *Science* **291:**97-100.

Kim, H., Lee, J., Kahng, S. J., Son, Y. W., Lee, S. B., Lee, C. K., Ihm, J., and Kuk, Y., 2003, Direct observation of localized defect states in semiconductor nanotube junctions, *Phys. Rev. Lett.* **90:**216107/1-4.

Han, J., Anantram, M. P., Jaffe, R. L., Kong, J., and Dai, H., 1998, Observation and modeling of single-wall carbon nanotube bend junctions, *Phys. Rev. B* **57:**14983-14989.

Hassanien, A., Holzinger, M., Hirsch, A., Tokumoto, M., and Venturini, P., 2003, Ropes of carbon nanotubes intramolecular junctions, *Synthetic Metals* **137:**1203-1204.

Hashimoto, A., Suenaga, K., Gloter, A., Urita, K., and Iijima, S., 2004, Direct evidence for atomic defects in graphene layers, *Nature* **430:**870-873.

Lambin, Ph., Fonseca, A., Vigneron, J. P., Nagy, J. B., and Lucas, A. A., 1995, Structural and electronic properties of bent carbon nanotubes, *Chem. Phys. Lett.* **245:**85-89.

Chico, L., Crespi, V. H., Benedict, L. X., Louie, S. G., and Cohen, M. L., 1996, Pure carbon nanoscale devices: Nanotube heterojunctions, *Phys. Rev. Lett.* **76:**971-974.

Charlier, J. C., Ebbesen, T. W., and Lambin, Ph., 1996, Structural and electronic properties of pentagon-heptagon pair defects in carbon nanotubes, *Phys. Rev. B* **53:**11108-11113.

Ferreira, M. S., Dargam, T. G., Muniz, R. B., and Latge, A., 2000, Local electronic properties of carbon nanotube heterojunctions, *Phys. Rev. B* **62:**16040-16045.

Tamura, R., and Tsukada, M., 1997, Conductance of nanotube junctions and its scaling law, *Phys. Rev. B* **55:**4991-4998.

Odintsov, A. O., 2000, Schottky barrier in carbon nanotube heterojunction, *Phys. Rev. Lett.* **85:**150-153.

Yamada, T., 2002, Modeling of kink-shaped carbon-nanotube Schottky diode with gate bias modulation, *Appl. Phys. Lett.* **80:**4027-4029.

Chico, L., Benedict, L. X., Louie, S. G., and Cohen, M. L., 1996b, Quantum conductance of carbon nanotubes with defects, *Phys. Rev. B* **54:**2600-2606.

Rochefort, A., and Avouris, Ph., 2002, Quantum size effects in carbon nanotube intramolecular junctions, *Nano Lett.* **2:**253-256.

Meunier, V., Henrard, L., and Lambin, Ph., 1998, Energetics of bent carbon nanotubes, *Phys. Rev. B* **57:**2591-2596.

Chico, L., Lopez Sancho, M. P., and Munoz, M. C., 1998, Carbon-nanotube-based quantum dots, *Phys. Rev. Lett.* **81:**1278-1281.

Liu, H., and Tao, Y., 2003, Size effect of quantum conductance in single-walled carbon nanotube quantum dots, *Eur. Phys. J. B* **36:**411-418.

Hyldgaard, P., and Lundqvist, B. I., 2000, Robust nanosized transistor effect in fullerene-tube heterostructure, *Solid State Commun.* **116:**569-573.

Lu, J. Q., Wu, J., Duan, W., and Gu, B. L., 2004, Metal-to-semiconductor transition in squashed armchair carbon nanotubes, *Appl. Phys. Lett.* **84:**4203-4205.

Triozon, F., Lambin, Ph., and Roche, S., 2005, Electronic transport properties of carbon nanotube based metal/semiconductor/metal intramolecular junctions, *Nanotechnology* **16:**230-233.

ELECTRONIC TRANSPORT IN CARBON NANOTUBES AT THE MESOSCOPIC SCALE

SYLVAIN LATIL
Department of Physics, Facultés Universitaires Notre-Dame de la Paix, 61 Rue de Bruxelles, B 5000 Namur, Belgium

FRANÇOIS TRIOZON
DRT/LETI/DIHS/LMNO, CEA, 17 Rue des Martyrs, F 38054 Grenoble Cedex 9, France

STEPHAN ROCHE
DSM/DRFMC/SPSMS/GT, CEA, 17 Rue des Martyrs, F 38054 Grenoble Cedex 9, France

Abstract. This chapter deals with the electronic transport in carbon nanotubes under the influence of a static disorder. The approach used is the Kubo formalism that is based on fluctuation-dissipation theory developed in real space.

Keywords: electronic transport; Kubo formalism; defects

1. Introduction and motivation

A carbon nanotube (CNT) is a one-dimensional graphitic structure that can be either metallic or semiconductors, owing to its geometry (Saito et al., 1998). In addition to this unusual electronic structure, CNTs also exhibit remarkable quantum transport properties,[1] which present them as serious candidates for emerging nanoelectronics. First basic components have been synthesized:

[1] Electronic transport in carbon nanotubes seems to be very robust under static disorder (Franck et al., 1998). Theoretical works have nicely explained such unusual property (White and Todorov, 1998).

*To whom correspondence should be addressed. Sylvain Latil; e-mail: sylvain.latil@fundp.ac.be

V.N. Popov and P. Lambin (eds.), Carbon Nanotubes, 143–165.

junction nanodiode (Zhou et al., 2000) and logic gate (Derycke et al., 2001). Physical studies of such nanojunctions are full of promise.[2]

In order to tailor the electronic properties of CNTs, the Fermi level can be tuned by chemical doping, which can be achieved by different approaches: intercalation of alkali metal atoms (Fischer, 2002), substitution of boron or nitrogen in carbon nanotubes. Carbon nanotubes doped either with nitrogen or boron (Terrones et al., 1996; Czerw et al., 2001; Carroll et al., 1998) substitutions have been synthesized. When substituting a carbon atom, the boron atom (resp. nitrogen) acts as an acceptor (resp. donor) impurity in the nanotube, as revealed by thermopower measurements (Choi et al., 2003).

On the other hand, the chemical sensing capabilities of carbon nanotubes-based devices appear very promising (Star et al., 2003a). Indeed, beyond the standard covalent bonding (Bahr et al., 2001) that is responsible for a significant perturbation of the CNT, functional groups can specifically be attached to the carbon nanotube surface by physisorption (Star et al., 2001b). On the other hand, the π-stacking of π-conjugated organic molecules on the nanotube sidewalls is an example of non-covalent functionalization involving a weaker binding energy (Tournus, et al., 2005). The induced scattering is thus expected to be low and molecular-dependent in opposition to the electrochemical covalent functionalization. Consequently, a good knowledge of the CNTs reactivity and of the impact of the physisorption on the quantum transport is needed to guarantee their potential application as chemical sensors.

One notes that the chemical reactivity of nanotube/metal interface is also an important issue of concern, when investigating the behaviors and performances of nanotubes-based field effects transistors. By means of a suited chemical treatment of contacts, optimization of charge injection properties was endeavored (Auvray et al., 2004).

In this lecture, we present an approach to study the electronic transport in disordered carbon nanotubes (and any 1D material). The method we use and the related Kubo formalism are discussed in Section 2. Section 3 presents the first application of this formalism to atomic substitutions of boron in nanotubes. We will extract the electronic transport quantities of nanotubes as a function of the density of dopants. In Section 4, we present results on nanotubes with a random coverage of π-conjugated molecules and establish that the HOMO-LUMO gap of the adsorbed molecular entities is a crucial parameter for backscattering.

[2]Electronic properties of nanotubes (with the tight-binding or zone folding Hamiltonian), junctions and the Landauer formalism are presented in the Chapter by P. Lambin, V. Meunier and F. Triozon.

2. The Kubo formalism in real space

The conductivity of a bulk material of volume Ω is defined for frequency ω as the tensorial ratio between the applied field and the resulting electronic current: $\mathbf{j}(\omega) = \sigma(\omega)\mathbf{E}(\omega)$. Since we will perform calculations on 1D materials, oriented along the *z*-axis, only the diagonal element will be taken into account: $j_z(\omega) = \sigma(\omega)E_z(\omega)$.

The Kubo approach is a technique to calculate linear responses of materials (optical, electric, etc.). It is based on the *fluctuation-dissipation theorem* that establishes a correspondence between the *dissipative* out-of-equilibrium response (namely, the conductivity) and the *fluctuations* at the equilibrium (the correlation function of the charge carrier velocities). In this situation, the Kubo formula of conductivity reads (Kubo et al., 1985)

$$\sigma(\omega) = \frac{2\pi e^2 \hbar}{\Omega} \int_{-\infty}^{+\infty} \frac{f(E) - f(E+\hbar\omega)}{\hbar\omega} \mathrm{Tr}\left[\hat{\mathrm{V}}_z \delta(E - \hat{\mathrm{H}}) \hat{\mathrm{V}}_z \delta(E - \hat{\mathrm{H}} + \hbar\omega) \right] dE \qquad (1)$$

where $\hat{\mathrm{H}}$ is the Hamiltonian operator, $\hat{\mathrm{V}}_z$ is the operator for the electronic velocity along the *z*-axis and $f(E)$ is the Fermi distribution function. The DC conductivity corresponds to the limit $\omega = 0$. Using the property

$$\lim_{\omega \to 0} \frac{f(E) - f(E+\hbar\omega)}{\hbar\omega} = -\frac{\partial f}{\partial E} = \delta(E - E_F) \qquad (2)$$

and after a Fourier transform (Roche and Mayou, 1997), the diagonal conductivity writes in real space:

$$\sigma_{DC} = e^2 n(E_F) \lim_{t \to 0} \left[\frac{1}{t} \left\langle \Delta Z^2(t) \right\rangle_E \right] \qquad (3)$$

where $n(E_F)$ is the density of states per unit of volume and $\left\langle \Delta Z^2(t) \right\rangle_E$ is the measure of the electronic quadratic spreading at energy E.[3] It is defined like:

$$\left\langle \Delta Z^2(t) \right\rangle_E = \frac{\mathrm{Tr}\left[\delta(E - \hat{\mathrm{H}}) \left(\hat{Z}(t) - \hat{Z}(0) \right)^2 \right]}{\mathrm{Tr}\left[\delta(E - \hat{\mathrm{H}}) \right]} \qquad (4)$$

[3] In term of fluctuation-dissipation theory, the movement of an electronic wave packet due to an external electric field (i.e., dissipation under non equilibrium conditions) is related to the spreading of the wave packet without any external electric field (i.e., fluctuations at the equilibrium).

where $\hat{Z}(t)$ is the position operator along the *z*-axis, written in the *Heisenberg representation* for the time *t*. In view of simplifications, we will modify equation (4). Firstly, using the time-reversal symmetry and the properties of the Trace, it is straightforward to demonstrate that

$$\mathrm{Tr}\left[\delta(E-\hat{\mathrm{H}})\left(\hat{Z}(t)-\hat{Z}(0)\right)^2\right]=\mathrm{Tr}\left[A^+(t)\delta(E-\hat{\mathrm{H}})A(t)\right] \tag{5a}$$

$$A(t)=\left[\hat{Z},\hat{u}(t)\right]=\hat{Z}\hat{u}(t)-\hat{u}(t)\hat{Z} \tag{5b}$$

where $\hat{Z}$ is the position operator in the *Schrödinger representation* and $\hat{u}(t)=\exp(-i\hat{\mathrm{H}}t/\hbar)$ is the usual evolution operator. Secondly, the Traces in equation (4) are approximated by expectation values on wave-packets (Triozon et al., 2002) that are treated as random-phase states:[4]

$$Tr[...]\rightarrow\langle wp|...|wp\rangle$$

and the spreading (4) can finally be rewritten as

$$\left\langle \Delta Z^2(t)\right\rangle_E=\frac{\langle wp|A^+(t)\delta(E-\hat{\mathrm{H}})A(t)|wp\rangle}{\langle wp|\delta(E-\hat{\mathrm{H}})|wp\rangle}. \tag{6}$$

Equation (6) is now suitable for order *O*(*N*) numerical techniques and calculation of the transport properties are possible. We leave the technical details in Appendices A and B and turn now to the physical discussion about this approach.

In fact, the quadratic spreading (6) is a key quantity as it is directly related to the diffusion coefficient (or diffusivity)

$$D_E(t)=\left\langle Z^2(t)\right\rangle_E\cdot\frac{1}{t} \tag{7}$$

whose time dependence fully determines the transport mechanism. It is worth also to define the electronic spreading

$$Z_E(t)=\sqrt{\left\langle Z^2(t)\right\rangle_E}=\sqrt{tD_E(t)}. \tag{8}$$

[4] Random phase states are expanded on all the orbitals $|n\rangle$ of the basis set and defined like

$$|wp\rangle=\frac{1}{\sqrt{N}}\sum_{n=1}^{N}\exp(2i\pi\alpha(n))|n\rangle\,,$$

where $\alpha(n)$ is a random number in the [0,1] range. An average over 10 to 20 random phases states is sufficient to calculate the expectation values.

Three main categories of transport mechanisms can be interpreted, as illustrated in Fig. 1. The *ballistic regime* represents the ideal case of a perfect 1D lattice. Electrons travel through the systems without any scattering: the correlation of their group velocities is perfect after any time, and both $D_E(t)$ and $Z_E(t)$ are linear functions, with a slope equal respectively to v_f^2 and v_f (Fig. 1, left). Such electronic transport is characterized by a quantum conductance that does not decrease with length, and a step-like curve for $G(E)$.

The *diffusive regime* is characterized by a saturation of $D_E(t \to \infty)$, owing to identify a relaxation time $\tau(E)$, after what $D_E(t)$ is constant and $Z_E(t) \sim \sqrt{t}$ (Fig. 1, center). For typical times longer than τ, a semi-classical interpretation allows the recovery of the Einstein formula for conductivity (Ashcroft and Mermin, 1976) like

$$\sigma_{DC} \cong e^2 n(E_F) D_{E_F}.$$

The most useful tools to characterize a diffusive motion at energy E are the electrons group velocity $\langle v \rangle_E$ and the elastic mean-free-path $l_e(E)$

$$l_e(E) = \langle v \rangle_E \tau(E) \tag{9a}$$

and

$$\langle v \rangle_E = \sqrt{\frac{D_E(t)}{t}} \tag{9b}$$

with

$$t << \tau(E).$$

The conductance of diffusive 1D systems (whose length is longer than l_e) linearly decreases with their length.

The *localized regime* is a pure quantum regime that does not allow any semi-empirical explanation. In very disordered systems, the electronic wave function cannot propagate because of destructive interferences. Conducting electrons are then "trapped" onto limited regions and the diffusivity behaves like ~1/*t*. Spreading $Z_E(t)$ reaches an asymptotic value (we can identify to the size of the "trapping" regions) that is called the localization length $\zeta(E)$ (Fig. 1, right)

$$\zeta(E) = \lim_{t \to \infty} Z_E(t). \tag{10}$$

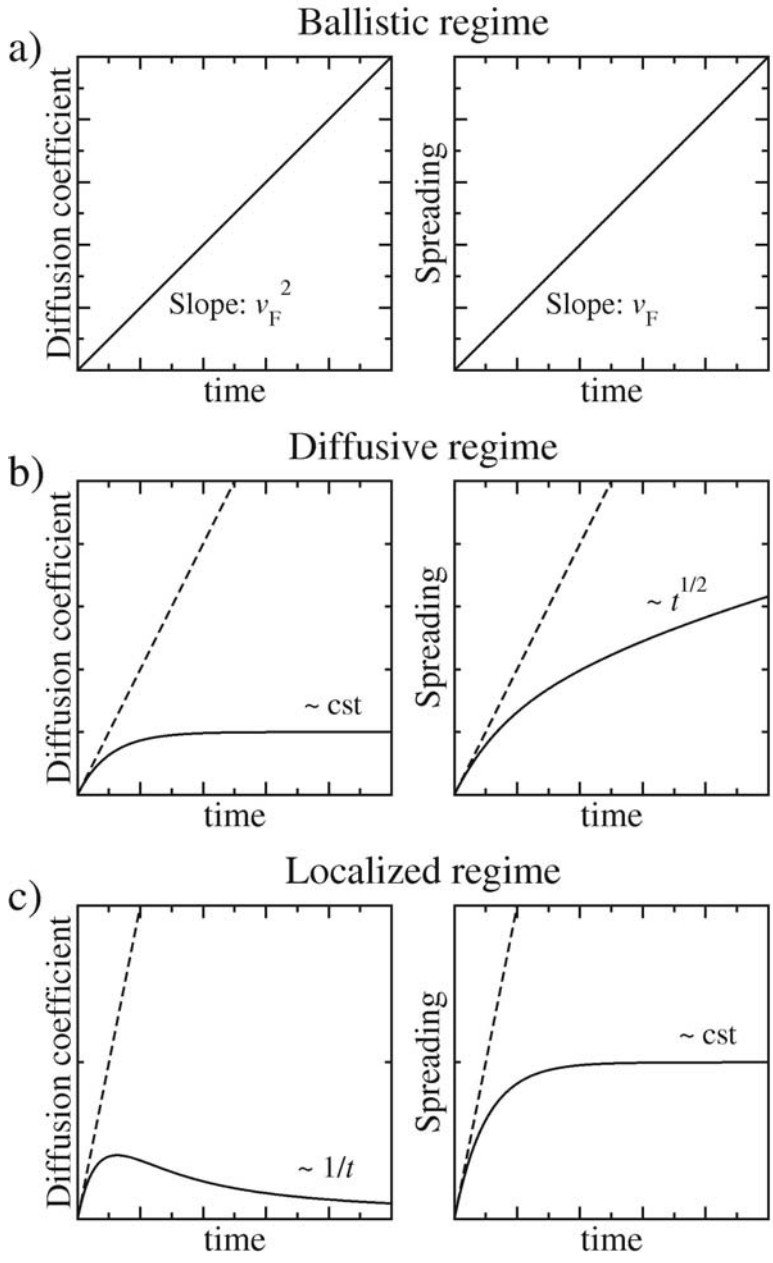

Figure 1. Typical behavior of the diffusion coefficient $D_E(t)$ and the spreading $Z_E(t)$, given by equations (7) and (8) for the three characteristic regimes: ballistic (a), diffusive (b) and localized (c).

Let's turn now to an important remark. All the dynamic of the system will be driven by the $\hat{H}$ operator that will be set up following the tight binding approach.[2] Since the Hamiltonian is constructed with the presence of static disorder (e.g., randomly located defects), the *elastic scattering* will be taken automatically onto account. Our aim is to quantify this scattering by calculating its length scales: elastic mean-free-path, localization length, etc. But, as we can see, the system remains Hamiltonian: its total energy is conserved. In this situation, an eigenstate of $\hat{H}$ possesses an infinite lifetime. In reality, power dissipation *must* occur somewhere: in the contacts or in the system (due to an energy exchange with the phonons), and conducting electrons loose their phase due to any *inelastic scattering* that does not conserve the energy. The resulting phase coherence length L_φ cannot be computed within this approach and has to be seen as an arbitrary parameter.

We will always consider that L_φ is much longer than the size of the studied system, i.e., that the decoherence process is negligible in the system and the dissipation occurs only in the contacts. In this quantum coherent regime, from the Kubo formula, and since the system is one-dimensional, the generic conductance of a device of length L_{dev} writes:

$$G(E, L_{dev}) = 2e^2 n(E) \frac{D_E(\tau_{dev})}{L_{dev}}, \tag{11}$$

where $n(E)$ is the electronic DOS per unit length and $\tau_{dev}(E)$ is the time spent by the wave packet (at the considered energy E) to spread over a distance equal to L_{dev}. Following the fluctuation-dissipation framework, it is also equivalent to the time needed for an electron to travel through the device.[5]

3. Boron substitutions

In this section, the generic transport properties of boron-doped nanotubes such as conduction mechanisms, mean-free-paths and conductance scalings, are computed as a function of the density of dopants.

Electronic calculations have been carried on (10,10) nanotubes, with 2500 cells and periodic boundary conditions (10^5 atoms). To use equation (6), the zone folding (ZF) Hamiltonian has been used. This method is an orthogonal tight-binding (TB) approach, which takes into account only one orbital $p_\perp$ per atom, and describes correctly the usual electronic properties of pristine carbon

[5] This approach is equivalent to the Landauer formula, assuming reflectionless contacts (Fisher and Lee, 1982; Datta, 1995).

nanotubes.[2] The presence of the gap, due to the local curvature, in the band structure of "metallic" nanotubes (Ouyang et al., 2001) is not predicted by ZF calculations, but since this work addresses doped systems, a truly metallic behavior should be recovered. Within this framework, the Hamiltonian operator writes as follows

$$\hat{\mathrm{H}} = \sum_{n=1}^{N} \left[H_{nn} |n\rangle\langle n| + \sum_{p} H_{np} |n\rangle\langle p| \right] \tag{12}$$

where the first sum runs on all the $p_{\perp}$ orbitals in the system while the second runs on the first neighbors of the *n* site. In expression (12), the matrix elements H_{nn} are the on-site energies and H_{np} are the hopping integrals.

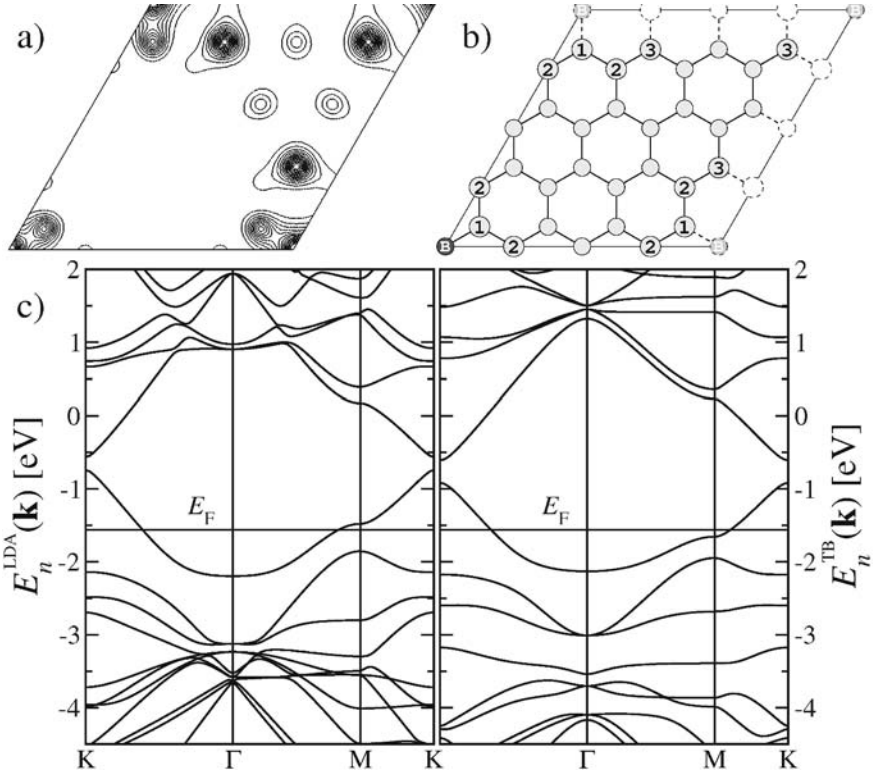

Figure 2. Electronic properties of a boron substitution in a graphene sheet. a) Isodensity plot of the last (half) occupied band, at Γ point calculated with DFT-LDA. Plane is shifted from the graphitic sheet (0.625 Å). Electronic density is mainly distributed on the B atom, up to the third neighbor. b) The renormalized atoms used our model are labeled: 1st, 2nd and 3rd neighbors of the boron (B) atom. c) Comparison between the electronic band structures of the doped graphene sheet calculated with DFT-LDA (left) and our modified TB model (right) with the renormalized on-site energies (see text).

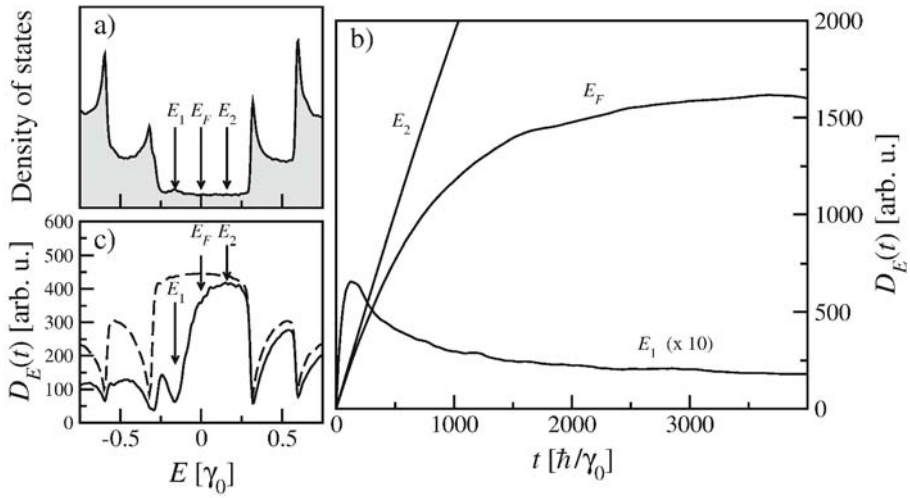

Figure 3. a) Electronic diffusion in a (0.1 %) B-doped (10,10) CNT. The DOS illustrates in (a) the characteristic acceptor peek located below the Fermi level (here $E_F = 0$). b) The diffusivity $D_E(t)$ given by equation (7), as a function of time, (b) for the three ranges of energy, indicated by arrows in (a). The diffusion coefficient for energy E_1 is ten times magnified. c) Diffusivity $D_E(t)$ as a function of energy for a time $t = 200\hbar/\gamma_0$ for the same B-doped CNT (solid line) and a pristine CNT (dashed line).

In order to apply this ZF technique to boron-doped carbon nanotubes, the electronic properties in the vicinity of an atomic substitution need to be accurately described. Tight-binding methods (like the ZF) are usually not suitable for predicting charge transfer, especially, in the chosen case of hetero-atomic substitutions. However, by adding a corrective electrostatic potential to the on-site energies, this technique can handle electric fields, charge transfer or electric dipole moments. The correction (added to the on-site energies) is usually calculated by a self-consistent loop on the electric charge (Krzeminski et al., 2001). Unfortunately, as the present $O(N)$ technique does not allow to use such a self-consistent scheme, an alternative approach is explained below for the case of a B-doped CNT.

In our modified ZF model, the values of the matrix elements in equation (12) are supposed to vary depending on the involved species. These elements are labeled ε_C, ε_B,… (for the on-site energies H_{nn}) and γ_{CC}, γ_{BC},…(for the hopping integrals H_{np}). Practically, these parameters were defined by fitting the

ZF band structure on DFT-LDA calculations.[6] In this *ab-initio* approach, standard norm-conserving pseudo-potentials were used, and the cutoff energy for the plane waves expansion was set to E_{cut} = 30 Ha. Since the curvature of the graphene sheet is neglected in the ZF approximation, the LDA calculations were performed on flat "graphene-like" systems. At first, the electronic structure of a supercell containing 31 carbon atoms and a single B atom was studied within a spin-averaged LDA approach, in order to simulate the electronic states of a doped carbon system in the vicinity of the B impurity. As shown in Fig. 2a, the electronic density $\rho(r)$ for the last (half) occupied band is distributed only on the $p_{\perp}$ orbitals for atoms located close to the impurity, up to the third neighbor of the B atom. This localization of the HOMO-LUMO band allows considering that the correction on the on-site energies affects carbon atoms only up to the third neighbors of the impurity. Moreover, this result suggests that the hopping integral between sites will not be affected by the charge transfer in assumption that the π atomic orbitals are not polarized by the local electric field. In addition, the boron atom is supposed to be "carbon-like"[7], i.e., $\gamma_{CC} = \gamma_{BC} = \gamma$. The geometry of the model is presented in Fig. 2b, where the boron and the renormalized carbon atoms are labeled. In this situation, only 6 parameters need to be adjusted: the unique hopping integral γ, the carbon and boron on-site energies ε_C and ε_B, and the renormalized carbon on-site energies ε_3, ε_2, and ε_1 (resp. third, second and first neighbors of the boron atom, as shown in Fig. 2b).

These adjustments were performed using least square energy minimization scheme between LDA and ZF band structures. At first, the LDA electronic structure of an isolated graphene sheet was used to fit the hopping. Its value was kept further as a constant. As only a low density of boron atoms in a graphene sheet is considered and given that this supercell is supposed to be in electronic equilibrium with the surrounding nanotube, the chemical potentials (Fermi energies) of the two subsystems have to be equal. Since the Fermi energy of a graphene sheet (or a nanotube described with ZF technique) is ε_C, this leads to $\varepsilon_C = E_{F,supercell} = E_{F,CNT}$. The band structure obtained with the optimal parameters is compared to the LDA band structure in Fig. 2c. The optimal hopping integral is γ =2.72 eV and the Fermi level $E_F = \varepsilon_C$. The on-site energies are ε_B = +2.77

[6]The DFT-LDA calculations were done with the ABINIT code. This program is a common project of the Université Catholique de Louvain, Corning Incorporated, and other contributors (http://www.abinit.org). Electronic states are expanded on a plane wave basis set (energy cutoff is 35 Hartree) and standard norm-conserving pseudopotentials have been used (Troullier and Martins, 1991).

[7]Since the electronic density for a C and a B atom at a distance d = 1.42 Å is roughly the same, this approximation is valid.

eV, ε_1 = –0.16 eV, ε_2 = +0.21 eV, and ε_3 = –1.56 eV. At last, the whole spectrum is shifted to have E_F = 0 eV.

As shown in Fig. 3a, the density of states (DOS) of a (0.1%) B-doped (10,10) CNT exhibits the typical acceptor peak (E_1) in agreement with previous *ab-initio* studies (Choi et al., 2000). On Fig. 3b, three different transport regimes are illustrated for a (0.1%) B-doped nanotube. At Fermi energy (E_F), the diffusion coefficient saturates at long times where $D(E_F,t) \rightarrow D_0 \sim l_e v_F$, indicating a diffusive regime. In contrast, at the resonance energy (E_1) of the quasi-bounded states, the diffusivity exhibits $a \sim 1/t$ behavior, typical of a strong localization regime. Finally at energy E_2 above the Fermi level, the electronic conduction remains nearly insensitive to dopants, as shown by the quasi-ballistic diffusion law. In Fig. 3c, the energy-dependent diffusivity clearly manifests such asymmetry in conduction.

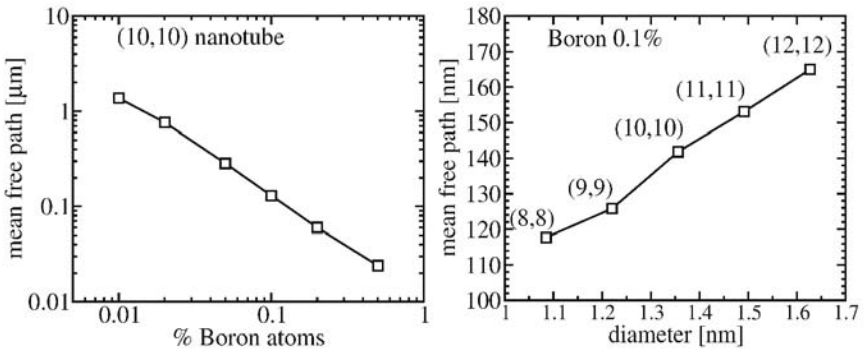

Figure 4. Scaling of the mean free path l_e at the Fermi level for a B-doped (n,n) nanotube. Left: in the case of a (10,10) nanotube with various boron concentrations, l_e behaves like the inverse of the doping rate. Right: for a fixed concentration of B atoms, l_e is roughly a linear function of the diameter.

From a physical point of view, the relevant information is that a low density of dopants yields diffusive regimes, with a mean-free-path decreasing linearly with dopant concentration following Fermi golden rule (Fig. 4, left), and increasing linearly with nanotube diameter (Fig. 4, right) following theoretical predictions based on Anderson-like[8] disorder modeling (White and Todorov, 1998). Moreover, in very good agreement with experimental data (Liu et al.,

[8]In the Anderson model, the disorder is not properly created by localized scattering centers but acts as a random modulation of the on-site energies. It then can be seen as a "white noise", affecting equally the whole energy spectrum (Anderson, 1958).

2002), from our calculations, we estimate mean-free-paths in the order of 175–275 nm for boron-doped nanotubes with diameters in the range 17–27 nm, and 1% of doping.

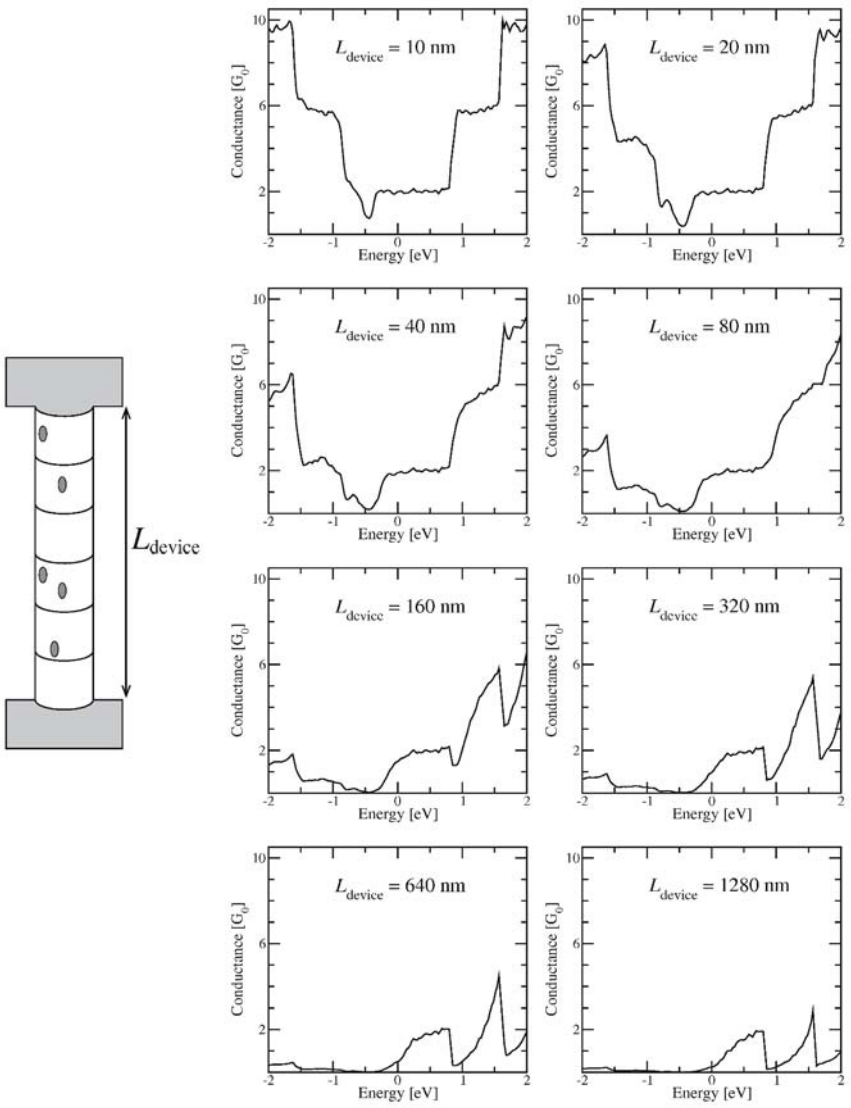

Figure 5. Quantum conductance of a device made from a single (10,10) nanotube containing 0.1% of boron impurities. The conductance is plotted as a function of the energy, for different lengths of the device. A decrease of the conductance is observed near the energies of donor states, and near the Van Hove singularities.

The main remarkable conductance features for B-doped (10,10) nanotubes are illustrated in Fig. 5. As the typical length L_{dev} increases from the nanometric scale (~10 nm) to the mesoscopic scale (~ 1 μm), the quantum interference effects beyond the diffusive regime are correspondingly enhanced. A strong asymmetric damping of the electronic conductance follows.

Moreover, our results show that the generic conductance $G(E,L_{dev})$ of B-CNT at Fermi level exhibit a positive derivative with respect to energy. Similar study on nitrogen doped nanotubes indicates that localized states around the nitrogen substitution, are responsible for backscattering *above* the Fermi level (Latil et al., 2004). Such a difference between N- and B-doped CNTs suggests that the thermopower measurements[9] originate from a diffusion mechanism only (Choi et al., 2003). Gate-dependent studies on individual undoped carbon nanotubes have recently revealed a quantum connection between conductance modulations and thermopower (Small et al., 2003). Similar studies on chemically doped SWNTs would be desirable to confirm these theoretical predictions.

4. Adsorption of π-conjugated molecules

In this section, the effect of molecular physisorption on the diffusion mechanisms of metallic CNTs is theoretically investigated. As in Section 3, the results will be achieved by combining DFT calculations with tight-binding models. The focus is made on the evaluation of the scattering strength and the resulting transport length scales produced by a random coverage of π-conjugated hydrocarbon molecules (benzene (C_6H_6) and azulene ($C_{10}H_8$)).

In order to adjust the parameters of the semi-empirical Hamiltonian, and since the interaction between the CNT and each molecule is geometry-dependent, an ab initio study of the adsorption has been carried out prior to the TB analysis (Tournus et al., 2005). Assuming that the adsorption on a CNT or on graphene are equivalent, the atomic model is simplified when using a 5 x 5 graphene supercell with one adsorbed benzene or azulene molecule, instead of the cylindrical structure.

[9]The thermopower S gives important information about the sign of charge carriers and the conductance modulations close to the Fermi level:

$$S = \frac{-\pi^2 k_B^2 T}{3eG(E_F)}\left(\frac{dG}{dE}\right)_{E=E_F} \quad \text{(Mott formula)}$$

where $G(E)$ is the conductance at Fermi level, k_BT the temperature energy scale.

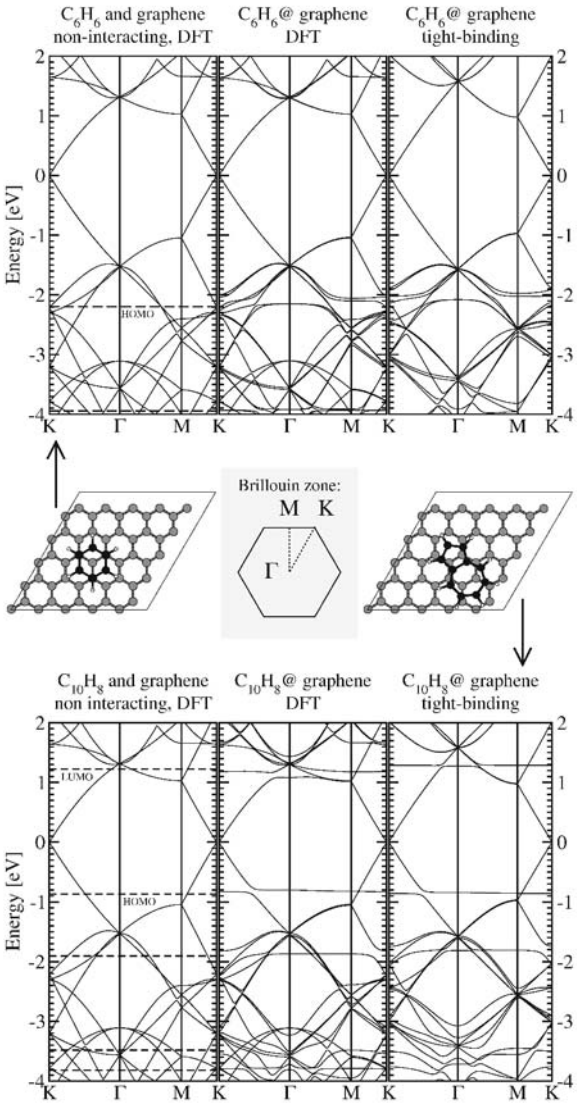

Figure 6. The electronic structures of a graphene 5 x 5 supercell with one adsorbed π-conjugated molecule. Top: the HOMO eigenstate of the isolated benzene C_6H_6 molecule (shown with a dashed line in the left hand frame) mixes up with the band structure of the graphene layer, to form a complex band structure (central frame). Bottom: an azulene $C_{10}H_8$ molecule is physisorbed on the graphene sheet; the mixing also occurs for HOMO and LUMO eigenstates. Although a weaker dipersion is observed than for the benzene case, the smaller gap of azulene will allow a perturbation of the CNT electronic diffusion at the Fermi level (here $E_F = 0$). Note that in both cases, our TB model gives an excellent description (right frame) compared to the *ab-initio* calculation.

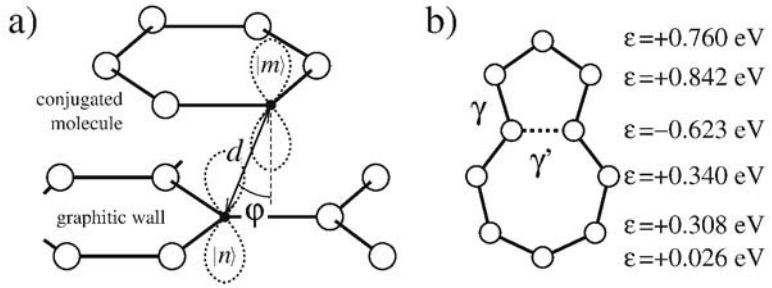

Figure 7. Schematic view of the graphene-molecule interaction described by equation (14). The distance d and the angle φ are drawn. b) The modified Hückel model for the azulene molecule. The on-site energies ε are corrected in order to take screening into account and the hopping integrals are $\gamma = -2.63$ eV and $\gamma' = -2.08$ eV, respectively.

Here, electronic calculations have been performed with the density functional theory within its local density approximation to predict the optimal geometry, and extract its electronic structure.[10] From the optimized geometries[11] (displayed in the center of Fig. 6), the LDA band structures are plotted for both isolated and interacting systems. The interaction acts as a mixing of the molecular single states with the underlying band structure, resulting in hybrid eigenstates with low group velocity. However, due to the relatively large gaps of the isolated molecules (5.217 eV and 2.089 eV for benzene and azulene, respectively) only weak disturbance is induced around the Fermi energy, and the linear band dispersion is preserved.

Following the same procedure as in Section 3, the zone folding model is used for defining the Hamiltonian of the nanotube. The π-conjugated molecules are treated by the Hückel model (Salem, 1966) and the tight-binding Hamiltonian of the complete system, containing the interaction between CNT and N_{mol} molecules, reads

$$\hat{\mathrm{H}} = \hat{\mathrm{H}}_{\mathrm{CNT}} + \sum_{M=1}^{N_{mol}} \left[\hat{\mathrm{H}}_{mol}(M) + \hat{\mathrm{V}}(M) \right] \tag{13}$$

where $\hat{\mathrm{H}}_{\mathrm{CNT}}$ is the usual zone folding Hamiltonian, equivalent to equation (12) and $\hat{\mathrm{H}}_{mol}(M)$ is the Hückel hamiltonian related to the Mth molecule. The

[10] The AIMPRO code (Briddon and Jones, 2000) has been used with standard norm-conserving pseudopotentials (Bachelet et al., 1982) and a 3 x 3 x 1 k-points sampling for the Brillouin zone integrations. The basis used is sufficient to obtain correct adsoption curves (C atoms contain five s- and p-like and three d-like orbitals, and H atoms contain four s- and p-like orbitals).

[11] Equilibrium distances (energies of adsorption) are found to be 3.25 Å (25.1 kJ.mol^{-1}) for the benzene, and 3.28 Å (37.6 kJ. mol^{-1}) for the azulene molecules.

$\hat{V}(M)$ term in equation (13) corresponds to the interaction between the *M*th molecule and the CNT, and is expressed as follow:

$$\hat{V}(M) = \sum_{m\in \mathrm{CNT}} \sum_{m\in M} \beta \cos(\varphi) \exp\left(\frac{d-\delta}{l}\right) |n\rangle\langle m| \qquad (14)$$

Such coupling term was optimized to accurately reproduce the interaction between shells in a multi-walled CNT (Lambin et al., 2000). In Eq. (14), d corresponds to the distance between sites, while φ is the angle defined in Fig. 4a. The parameters related to the interaction are: δ = 3.34 Å, l = 0.45 Å and β = –0.36 eV.

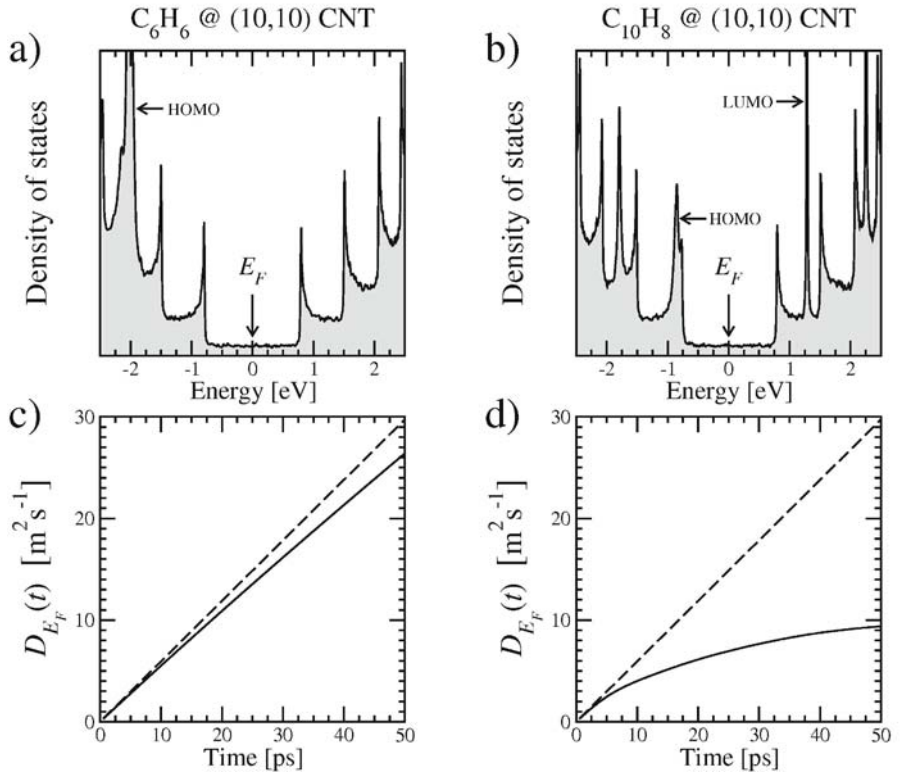

Figure 8. a) DOS of the (10,10) CNT with a benzene density coverage of 16.3%. The HOMO molecular state is located by an arrow. b) Same as in a) but for an azulene density coverage of 11.5%. HOMO and LUMO levels are identified by arrows. c) Time-dependent diffusion coefficient (at Fermi level) for the C_6H_6@CNT system, showing quasi-ballistic behavior (solid line). Ballistic conduction for pristine CNT case is also reported (dashed line). d) Time-dependent diffusion coefficient for the $C_{10}H_8$@CNT structure, showing saturation at large times (diffusive regime).

The tight-binding parameters (on-sites energies ε and hopping integrals γ) are adjusted to reproduce the band structure of graphene sheet and the energy levels of isolated benzene and azulene molecules, calculated within LDA. A standard procedure have been used to set the parameters for the graphene or the CNT: $\varepsilon_{CNT} = 0$ eV, $\gamma_{CNT} = -2.56$ eV, as well as for the benzene molecule: $\varepsilon_{benz} = +0.411$ eV, $\gamma_{benz} = -2.61$ eV.

Due to an inhomogeneous charge distribution along the azulene molecule, the TB model has to be refined to properly account for screening effects. By adding an electrostatic correction, proportional to the net charge on each carbon atom (calculated with LDA), renormalized on-site energies for the azulene molecule have been deduced. The on-sites and the adjusted hopping integrals are given in Fig. 4b. Within this approach, the TB value of the azulene HOMO-LUMO gap is 2.198 eV. Finally, the band structure computed with this modified TB model is compared to the previous ab initio results. As presented in Fig. 6, this reparametrized semi-empirical model gives an excellent description of the electronic states for both benzene and azulene adsorption cases.

The density of states (DOS) of a (10,10) carbon nanotube, with random coverage of adsorbed molecules is calculated within this framework. Fig. 8 presents the DOS for a nanotube with benzene coverage density of 16.3% (such density corresponds to the ratio of adsorbed mass of the molecule over CNT mass) and with azulene coverage density of 11.5%.Since the coupling intensity is weak, the DOS plotted in Fig. 8 displays the reminiscent discrete molecular levels, slightly enlarged by the mixing with the underlying continuum of π- or π*-bands. Peaks arising from molecular HOMO and LUMO levels are labeled.

In the case of the benzene adsorption, the DOS is weakly affected at charge neutrality point, and the computed diffusion coefficient shows almost no deviation from the linear scaling in time (ballistic regime). Elastic backscattering induced by benzene molecules is thus vanishingly low at Fermi level (also shown in Fig. 8), and does not produce sufficient deviation to determine an elastic mean free path below ~100 μm.

In contrast, in the case of azulene molecules, the HOMO level is located in the close vicinity of the last occupied Van Hove singularity of the CNT. Although the total DOS remains basically unaffected around the Fermi energy, the azulene adsorption turns out to impact more significantly on the intrinsic electronic current. Indeed, as shown in Fig. 8, the diffusion coefficients of propagating electrons at Fermi level depart more strongly from the ballistic regime.

The non-linear time dependence of $D_E(t)$, calculated with equation (7) allows to extract the elastic relaxation time τ and, knowing the Fermi velocity v_F, the corresponding electronic mean free path l_e. Fig. 9 presents the evolution

of l_e as a function of the azulene coverage density, both at Fermi level (charge neutrality point) and for an energy closer to the HOMO resonance [$E = -0.2\gamma \approx -0.54$ eV].

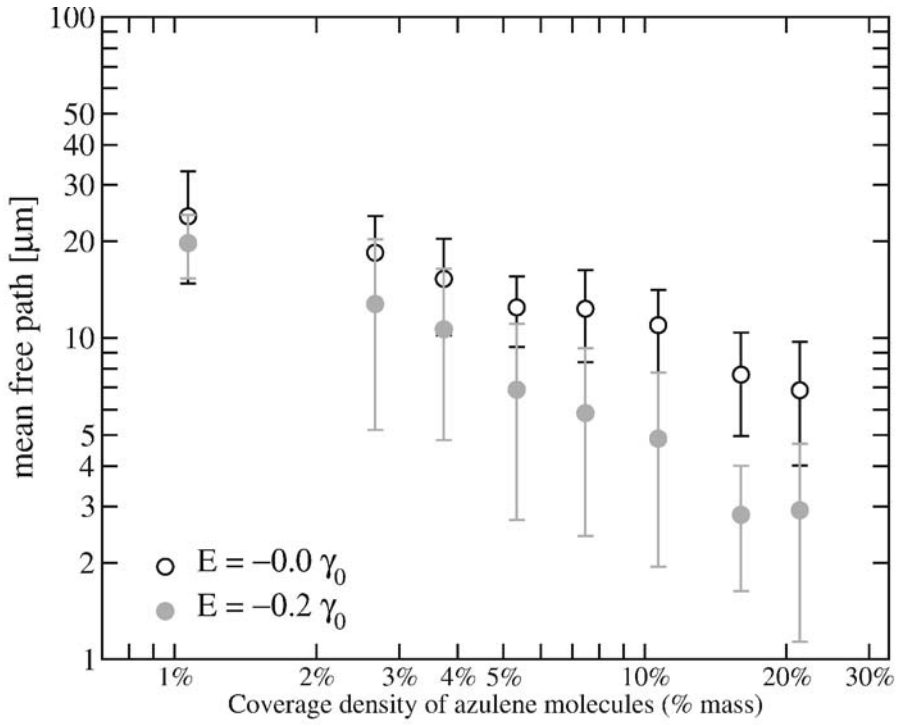

Figure 9. Electronic mean free path of a $C_{10}H_8$@CNT nanostructure versus the density of physisorbed molecules and for two different Fermi level positions. The origin of the error bars is the use of the random phase states for the expectation values in equation (6).

AKNOWLEDGEMENTS

We acknowledge fruitful discussions and collaborations with Prof. Didier Mayou, Prof. Jean-Christophe Charlier, Prof. Philippe Lambin, Dr. Xavier Blase and Prof. Malcolm I. Heggie. S. L. acknowledges financial support from the Belgian Francqui Fundation for Scientific Research.

A. THE RECURSION TECHNIQUE

As we have established in Section 2, the main issue of our numerical technique is to compute expectation values, like the local density of states on a given ket $|\varphi\rangle$ related to the retarded Green's function:

$$\langle\varphi|\delta(E-\hat{\mathrm{H}})|\varphi\rangle = -\frac{1}{\pi}\lim_{\varepsilon\to 0^+}\left[\mathrm{Im}\langle\varphi|\frac{1}{E+i\varepsilon-\hat{\mathrm{H}}}|\varphi\rangle\right] \tag{15}$$

We use the real-space recursion technique, which avoids diagonalization or inversion of the Hamiltonian and has a numerical cost which grows linearly with the system size (order N) (Haydock et al., 1972). Starting from a normalized ket $|\varphi\rangle$, an orthonormal basis $\{|\varphi_0\rangle, |\varphi_1\rangle, \ldots\}$ is constructed from the recurrence relations:

$$\hat{\mathrm{H}}|\varphi_0\rangle = a_0|\varphi_0\rangle + b_0|\varphi_1\rangle \tag{16a}$$

$$\hat{\mathrm{H}}|\varphi_n\rangle = a_n|\varphi_n\rangle + b_{n-1}|\varphi_{n-1}\rangle + b_n|\varphi_{n+1}\rangle \tag{16b}$$

with $|\varphi_0\rangle = |\varphi\rangle$. At any step n, a_n is given by $\langle\varphi_n|\hat{\mathrm{H}}|\varphi_n\rangle$, hence it is a real number. Then b_n and $|\varphi_{n+1}\rangle$ are uniquely determined by the normalization condition for $|\varphi_{n+1}\rangle$ and the choice of a real positive b_n.

In this basis, the Hamiltonian is tridiagonal. The Green's function element mentioned above is simply the first diagonal element of the inverse of the tridiagonal matrix:

$$\begin{pmatrix} E+i\varepsilon-a_0 & -b_0 & & \\ -b_0 & E+i\varepsilon-a_1 & -b_1 & \\ & -b_1 & E+i\varepsilon-a_2 & . \\ & & . & . \end{pmatrix}$$

It is obtained by a continued fraction expansion:

$$\langle\varphi_0|\frac{1}{E+i\varepsilon-\hat{\mathrm{H}}}|\varphi_0\rangle = \cfrac{1}{z-a_0-\cfrac{b_0^2}{z-a_1-\cfrac{b_1^2}{\ldots}}} \tag{17}$$

With N_{recurs} recursion steps, an energy resolution of order of W/N_{recurs} is obtained for the density of states, where W is the energy bandwidth of the system. In the single-band case, a_n and b_n converge and the continued fraction is terminated by the approximation $a_{N+1} = a_\infty$ and $b_{N+1} = b_\infty$. A more sophisticated termination can be used in a multi-band system, as detailed in (Roche, 1999).

B. COMPUTATION OF $A(t)\left|wp\right\rangle$ BY CHEBYCHEV POLYNOMIALS EXPANSION

This section presents the method used to apply the operator $A(t)=\left[\hat{Z},\hat{u}(t)\right]$ on a state vector $\left|\varphi\right\rangle$, in view of solving numerically the equation (6), with time steps Δt. The concept consists in expanding the evolution operator $\hat{u}(\Delta t)$ on polynomials of the Hamiltonian operator like:

$$\hat{u}(\Delta t)=\sum_{n=0}^{\infty}c_n(\Delta t)Q_n(\hat{\mathrm{H}}) \tag{18}$$

Practically, sums are limited to N_{poly} (hence, the exponential in the evolution operator is approximated by a polynomial of order N_{poly} and Q_n are the Chebychev polynomials, which follow the simple recursive rules

$$bQ_{n+1}(\hat{\mathrm{H}})=\left(\hat{\mathrm{H}}-a\right)Q_n(\hat{\mathrm{H}})-bQ_{n-1}(\hat{\mathrm{H}}) \tag{19a}$$

$$Q_0(\hat{\mathrm{H}})=1\,,.\,Q_1(\hat{\mathrm{H}})=\frac{1}{b\sqrt{2}}\left(\hat{\mathrm{H}}-a\right) \tag{19b}$$

The real numbers a and b are parameters defining a density function on the mathematical domain $[a-2b,\, a+2b]$

$$N(E)=\frac{1}{2\pi b\sqrt{1-\left(\dfrac{E-a}{2b}\right)^2}} \tag{20}$$

It is then crucial to choose a and b to fit all the spectrum of $\hat{\mathrm{H}}$ within the domain.

The expansion coefficients $c_n(\Delta t)$ in equation (18) are then the scalar product like

$$c_n(t)=\int N(E)Q_n(E)\exp(-\frac{i}{\hbar}E\Delta t)dE \tag{21}$$

and can be computed. To simplify the equations (18) and (19), we will introduce the two sets of kets

$$\left|\alpha_n\right\rangle=Q_n(\hat{\mathrm{H}})\left|\varphi\right\rangle \tag{22a}$$

$$\left|\beta_n\right\rangle=\left[\hat{\mathrm{Z}},Q_n(\hat{\mathrm{H}})\right]\left|\varphi\right\rangle \tag{22b}$$

that obeys the recursion rules

$$b\left|\alpha_{n+1}\right\rangle = \left(\hat{\mathrm{H}} - a\right)\left|\alpha_n\right\rangle - b\left|\alpha_{n-1}\right\rangle \tag{23a}$$

$$\left|\alpha_0\right\rangle = \left|\varphi\right\rangle,\ \left|\alpha_1\right\rangle = \frac{1}{b\sqrt{2}}\left(\hat{\mathrm{H}} - a\right)\left|\varphi\right\rangle \tag{23b}$$

and

$$b\left|\beta_{n+1}\right\rangle = \left[\hat{\mathrm{Z}}, \hat{\mathrm{H}} - a\right]\left|\beta_n\right\rangle - b\left|\beta_{n-1}\right\rangle \tag{24a}$$

$$\left|\beta_0\right\rangle = 0 \times \left|\varphi\right\rangle,\ \left|\beta_1\right\rangle = \frac{1}{b\sqrt{2}}\left[\hat{\mathrm{Z}}, \hat{\mathrm{H}}\right]\left|\varphi\right\rangle \tag{24b}$$

They can be calculated from the starting ket $\left|\varphi\right\rangle$ by applying $\hat{\mathrm{Z}}$ [12] and $\hat{\mathrm{H}}$.

Once we know $\left|\alpha_n\right\rangle$ and $\left|\beta_n\right\rangle$, the application of the operators on $\left|\varphi\right\rangle$ is simply

$$\hat{u}(\Delta t)\left|\varphi\right\rangle = \sum_{n=0}^{N_{\mathrm{poly}}} c_n(\Delta t)\left|\alpha_n\right\rangle \tag{25a}$$

$$\left[\hat{\mathrm{Z}}, \hat{u}(\Delta t)\right]\left|\varphi\right\rangle = \sum_{n=0}^{N_{\mathrm{poly}}} c_n(\Delta t)\left|\beta_n\right\rangle \tag{25b}$$

Finally, when the equations (25) are solved for a given time t,[13] the following step $t + \Delta t$ is calculated by applying the Chebychev expansion on solution at time t like

$$\hat{u}(t + \Delta t)\left|\varphi\right\rangle = \hat{u}(\Delta t)\hat{u}(t)\left|\varphi\right\rangle \tag{26a}$$

$$\left[\hat{\mathrm{Z}}, \hat{u}(t + \Delta t)\right]\left|\varphi\right\rangle = \left[\hat{\mathrm{Z}}, \hat{u}(\Delta t)\right]\hat{u}(t)\left|\varphi\right\rangle + \hat{u}(\Delta t)\left[\hat{\mathrm{Z}}, \hat{u}(t)\right]\left|\varphi\right\rangle \tag{26b}$$

and so on. The evolution of $A(t)\left|\varphi\right\rangle$ and $\hat{u}(t)\left|\varphi\right\rangle$ can be calculated step by step from any starting $\left|\varphi\right\rangle$.

[12] The choice of an orthogonal basis set (within the TB approach) simplifies the action of the position operator, assuming that $\left\langle n\left|\hat{\mathrm{Z}}\right|p\right\rangle = \delta_{np} Z_n$.

[13] This means that the two vectors $\hat{u}(t)\left|\varphi\right\rangle$ and $\left[\hat{\mathrm{Z}}, \hat{u}(t)\right]\left|\varphi\right\rangle$ have already been calculated.

References

Anderson, P. W., 1958, Absence of Diffusion in Certain Random Lattices, *Phys. Rev.* **109**: 1492.

Ashcroft, N. W., and Mermin, N. D., 1976, *Solid State Physics*, Saunders College, Philadelphia.

Auvray, S., Borghetti, J., Goffman, M. F., Filoramo, A., Derycke, V., Bourgoin, J.-P., and Jost, O., 2004, Carbon nanotube transistor optimization by chemical control of the nanotube-metal interface, *Appl. Rev. Lett*. **84**: 5106.

Bachelet, G. B., Haman, D. R., and Schlüter, M., 1982, Pseudopotentials that work: From H to Pu, *Phys. Rev. B* **26**: 4199.

Bahr, J. L., Yang, J. P., Kosynkin, D. V., Bronikowski, M. J., Smalley, R. E., and Tour, J. M., 2001, Functionalization of Carbon Nanotubes by Electrochemical Reduction of Aryl Diazonium Salts: A Bucky Paper Electrode, *J. Am. Chem. Soc.* **123**: 6536.

Briddon, P. R. and Jones, R., 2000, LDA calculations using a basis of gaussian orbitals, *Phys. Status Solidi B* **217**: 131.

Carroll, D. L., Redlich, P., Blase, X., Charlier, J.-C., Curran, S., Ajayan, P., Roth, S., and Rühle, M., 1998, Effects of Nanodomain Formation on the Electronic Structure of Doped Carbon Nanotubes, *Phys. Rev. Lett.* **81**: 2332.

Choi, H. J., Ihm, J., Louie, S. G., and Cohen, M. L., 2000, Defects, Quasibound States, and Quantum Conductance in Metallic Carbon Nanotubes, *Phys. Rev. Lett.* **87**: 2917.

Choi, Y.-M., Lee, D.-S., Czerw, R., Chiu, P.-W., Grobert, N., Terrones, M., Reyes-Reyes, M., Terrones, H., Charlier, J.-C., Ajayan, P. M., Roth, S., Carroll, D. L., and Park, Y.-M., 2003, Nonlinear Behavior in the Thermopower of Doped Carbon Nanotubes Due to Strong, Localized States, *Nano Lett.* **3**: 839.

Czerw, R., Terrones, M., Charlier, J.-C., Blase, X., Foley, B., Kamalakaran, R., Grobert, N., Terrones, H., Tekleab, D., Ajayan, P. M., Blau, W., Ruhle, M., and Carroll, D. L., 2001, Identification of Electron Donor States in N-Doped Carbon Nanotubes, *Nano Lett.* **1**: 457.

Datta, S., 1995, *Electronic Transport in Mesoscopic Systems*, Cambridge Univesity Press, Cambridge.

Derycke, V., Martel, R., Appenzeller, J., and Avouris, P., 2001, Carbon Nanotube Inter- and Intramolecular Logic Gates, *Nano Lett.* **1**: 453.

Fischer, J. E., 2002, Chemical doping of single-wall carbon nanotubes, *Acc. Chem. Res.* **35**: 1079.

Fisher, D., and Lee, P. A., 1982, Relation between conductivity and transmission matrix, *Phys. Rev. B* **23**: 6852.

Frank, S., Poncharal, P., Wang, Z., and de Heer, W., 1998, Carbon nanotube quantum resistors, *Science* **280**: 1744.

Haydock, R., Heine, V., and Kelly, M., 1972, Electronic structure based on the local atomic environment for tight-binding bands, *J. Phys. C: Solid State Phys.* **5**: 2845.

Krzeminski, C., Delerue, C., Allan, G., Vuillaume, D., and Metzger, R. M., 2001, Theory of electrical rectification in a molecular monolayer, *Phys. Rev. B* **64**: 085405.

Kubo, R., Toda, M., and Hashitsume, N., 1985, *Statistical Physics II*, Springer, Berlin.

Lambin, P., Meunier, V., and Rubio, A., 2000, Electronic structure of polychiral carbon nanotubes, *Phys. Rev. B* **62**: 5129.

Latil, S., Roche, S., Mayou, D., and Charlier, J.-C., 2004, Mesoscopic Transport in Chemically Doped Carbon Nanotubes, *Phys. Rev. Lett.* **92**: 256805.

Liu, K., Avouris, P., Martel, R., and Hsu, W. K., 2002, Electrical transport in doped multiwalled carbon nanotubes, *Phys. Rev. B* **62**: 161404.

Ouyang, M., Huang, J.-L., Cheung, C. L., and Lieber, C. M., 2001, Energy Gaps in Metallic Single-Wall Carbon Nanotubes, *Science* **292**: 702.

Roche, S., 1999, Quantum transport by means of O(N) real-space methods, *Phys. Rev. B* **59**: 2284.

Roche, S., and Mayou, D., 1997, Conductivity of Quasiperiodic Systems: A Numerical Study, *Phys. Rev. Lett.* **79**: 2518.

Saito, R., Dresselhaus, G., and Dresselhaus, M. S., 1998, *Physical Properties of Carbon Nanotubes*. Imperial College Press, London.

Salem, L., 1966, *The Molecular-Orbital theory of π-conjugated systems*. Benjamin, Reading.

Small, J. P., Perez, K. M., and Kim, P., 2003, Modulation of Thermoelectric Power of Individual Carbon Nanotubes, *Phys. Rev. Lett.* **91**: 256801.

Star, A., Han, T. R., Gabriel, J. C., Bradley, K., and Gruner, G., 2003a, Interaction of Aromatic Compounds with Carbon Nanotubes: Correlation to the Hammett Parameter of the Substituent and Measured Carbon Nanotube FET Response, *Nano Lett*. **3**: 1421.

Star, A., Liu, Y., Grant, K., Ridvan, L., Stoddart, J. F., Steuerman, D. W., Diehl, M. R., Boukai, A., and Heath, J. R., 2003b, Noncovalent Side-Wall Functionalization of Single-Walled Carbon Nanotubes, *Macromolecules* **36**: 553.

Terrones, M., Benito, A. M., Manteca-Diego, C., Hsu, W. K., Osman, O. I., Hare, J. P., Reid, D. G., Terrones, H., Cheetham, A. K., Prassides, K., Kroto, H. W., and Walton, D. R. M., 1996, Pyrolytically grown $B_xC_yN_z$ nanomaterials: nanofibres and nanomaterials, *Chem. Phys. Lett.* **257**: 576.

Tournus, F., Latil, S., Heggie, M. I., and Charlier, J.-C., 2005, π-stacking interaction between carbon nanotubes and organic molecules, *Phys. Rev. B* **72**: 075431.

Triozon, F., Vidal, J., Mosseri, R., and Roche, S., 2002, Quantum dynamics in two- and three-dimensional quasiperiodic tilings, *Phys. Rev. B* **65**: 220202.

Troullier, N., and Martins, J. L., 1991, Efficient pseudopotentials for plane-wave calculations, *Phys. Rev. B* **43**: 1993.

White, C. T., and Todorov, T. N., 1998, Carbon nanotubes as long ballistic conductors, *Nature* **393**: 240.

Zhou, C., Kong, J., Yenilmez, E., and Dai, H., 2000, Modulated Chemical Doping of Individual Carbon Nanotubes, *Science* **290**: 1552.

WAVE PACKET DYNAMICAL INVESTIGATION OF STM IMAGING MECHANISM USING AN ATOMIC PSEUDOPOTENTIAL MODEL OF A CARBON NANOTUBE

GÉZA I. MÁRK,* LEVENTE TAPASZTÓ, LÁSZLÓ P. BIRÓ
Research Institute for Technical Physics and Materials Science, H-1525 Budapest, P.O.B. 49, Hungary

ALEXANDRE MAYER
Département de Physique, Facultés Universitaires Notre-Dame de la Paix, 61 Rue de Bruxelles, B-5000 Namur, Belgium

Abstract. Scanning tunneling microscopy (STM) is capable of providing information on both the geometrical and electronic structure of a carbon nanostructure. Utilizing a pseudopotential model of a nanotube we investigated the three-dimensional wave packet (3D WP) tunneling process through an STM tip – nanotube – support model for different atomic arrangements representing metallic and semiconducting nanotubes.

Keywords: Scanning tunneling microscopy; carbon nanotube; local pseudopotential

Scanning Tunneling Microscopy (STM) images of nanosystems contain both the effect of the geometry and the electronic structure. To investigate geometrical effects in the STM imaging mechanism, formerly we performed wave packet dynamical simulations[1,2] for jellium models of STM tip – carbon nanotube (CNT) – support tunnel junctions. We were able to explain some geometrical effects frequently seen in STM images. In the present paper we extend the 3D WP calculation to include the details of the atomic structure.

A local one electron pseudopotential[3] was used for the CNT. The STM tip of 0.5 nm radius and the conductive support surface was modeled by constant potential jellia.[2] The time development of a Gaussian WP approaching the tunnel junction from inside the tip bulk was calculated by numerically solving the time dependent 3D Schrödinger equation. The time-dependent probability

*To whom correspondence should be addressed. Géza I. Márk; e-mail: mark@sunserv.kfki.hu

V.N. Popov and P. Lambin (eds.), Carbon Nanotubes, 167–168.

density is visualized by snapshots of a constant density surface. In the panel t = 0.0 fs of Fig. 1 the initial WP is shown – still in the tip bulk region. At t = 0.6 fs the WP has already penetrated into the tip apex region. At t = 1.8 fs the WP has already tunneled from the tip into the tube and is beginning to flow around the tube circumference. The WP flows along the C-C bonds with negligible density at the centers of the hexagons. At t = 3.02 fs the WP already has flown around the tube circumference and is beginning to spread along the tube. Spreading is faster for the metallic tube than for the semiconducor tube.

These preliminary results show that the 3D WP tunneling simulation is a useful tool for interpreting experimental data and predicting the likely behavior of nanodevices.

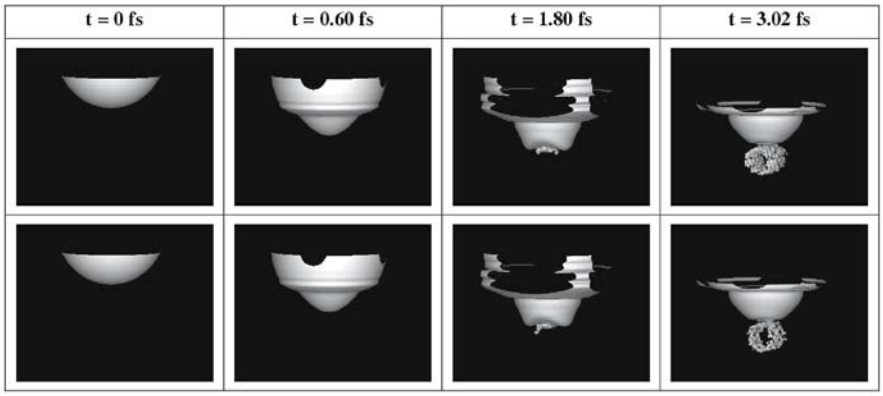

Figure 1. Details of tunneling of a wave packet approaching the STM junction from the tip bulk and tunneling into the nanotube. Constant probability density surface is shown. Upper row: (10,0) tube, lower row: (6,6) tube. The isosurface is clipped at the presentation box boundaries.

This work was partly supported by OTKA grants T 43685 and T 43704 in Hungary and the Belgian PAI P5/01 project on "Quantum size effects in nanostructured materials". The calculations were done on the Sun E10000 supercomputer of the Hungarian IIF.

References

1 G. I. Márk, L. P. Biró, and J. Gyulai, Simulation of STM images of 3D surfaces and comparison with experimental data: carbon nanotubes, *Phys. Rev. B* 58, 12645-12648 (1998).

2 G. I. Márk, L. P. Biró, and Ph. Lambin, Calculation of axial charge spreading in carbon nanotubes and nanotube Y junctions during STM measurement, *Phys. Rev. B* 70, 115423/1-11 (2004).

3 A. Mayer, Band structure and transport properties of carbon nanotubes using a local pseudopotential and a transfer-matrix technique, *Carbon* 42(10), 2057-2066 (2004).

CARBON NANOTUBE FILMS FOR OPTICAL ABSORPTION

EVA KOVATS,* ARON PEKKER, SANDOR PEKKER,
FERENC BORONDICS, KATALIN KAMARAS
Research Institute for Solid State Physics and Optics, 29-33 Konkoly-Thege M. Street H-1121 Budapest, Hungary

Abstract. Ultrathin, transparent, and pure nanotube films have great importance in the optical studies. The samples are free-standing, which eliminates the difficulties caused by the various substrates in wide-range optical measurements. We prepared uniform homogenous thin films from hole-doped and functionalizated single-wall carbon nanotubes (SWNTs) with a simple process. We examined the spectra from the infrared to the ultraviolet range on the same sample. The vibrational transitions of the sidewall groups indicated the chemical composition. The changes in the electronic properties were followed simultaneously by Near-infrared/Visible/Ultraviolet (NIR/VIS/UV) spectroscopies.

Keywords: carbon nanotube thin film; optical spectroscopy; absorption

Carbon nanotubes have unique electronic properties, which have been widely investigated on isolated SWNTs as well as on bundled nanoropes. Here we describe wide-range optical studies on SWNTs prepared as free-standing films.

Free-standing nanotube films were produced by vacuum filtration of dilute nanotube suspensions.[1] After the dissolution of the filter, the films were transferred to a frame with a hole. The films were thin enough to be optically transparent (100-200 nm) and wide enough to have a sufficient surface area (0.5-1 cm^2).

The optical measurements were made in the spectral range from 600 to 30000 cm^{-1}. For the mid- and near-infrared regions we used Bruker a IFS 66v spectrometer. The visible and UV data were obtained on a Jasco V550. The molecular vibrations can be detected up to 4000 cm^{-1} and above this wavenumber the electronic transitions can be observed.

*To whom correspondence should be addressed. Eva Kovats, Research Institute for Solid State Physics and Optics, 29-33 Konkoly-Thege M. Street H-1121 Budapest, Hungary; e-mail: kovatse@szfki.hu

V.N. Popov and P. Lambin (eds.), Carbon Nanotubes, 169–170.

We examined two chemically modified nanotube samples. In the purification process, the SWNTs were treated with concentrated nitric acid, which causes charge transfer doping. In the absorption spectra, we detected increase of the M_{00} band intensity. We explain this with the increase of the number of free charge carriers.

The other sample, butylated SWNTs, was prepared by reductive alkylation.[2,3] In the 2800-3100 cm^{-1} region, several C-H modes of butyl sidegroups were detected. The occupation of the van Hove singularities decreased due to less π-electrons.[4] The slight change is due to the small degree of functionalization (1,8%, Ref. [3]).

We measured the transmittance of pure nanotube films and calculated the optical conductivity.[5] The simultaneous optical transparency and DC conductivity make nanotube films ideal materials for transparent electrodes.[1]

In summary, we prepared transparent free-standing nanotube films, which made possible wide-range optical absorption measurements on the same sample. The change of the electronic properties was detectable. For example, in the case of ionic doping, the M_{00} absorption bands of electronic transitions increased because of more free electrons; the effect of functionalization causes the decrease of the S_{11}, S_{22}, M_{11} bands because of less π-electrons. Because of the high DC conductivity and high transmittance, these films are ideal candidates for transparent electrodes.

References

1. Z. Wu, Z. Chen, X. Du, J. M. Logan, J. Sippel, M. Nikolou, K. Kamaras, J. R. Reynolds, D. B. Tanner, A. F. Hebard, and A. G. Rinzler, Transparent, conductive carbon nanotube films, *Science* 305, 1273-1276 (2004).
2. S. Pekker, J.-P. Salvetat, E. Jakab, J.-M. Bonard, and L. Forro, Hydrogenation of Carbon Nanotubes and Graphite in Liquid Ammonia, *J. Phys. Chem. B* 105, 7938-7943 (2001).
3. F. Borondics, E. Jakab, M. Bokor, P. Matus, K. Tompa, S. Pekker, Reductive Functionalization of Carbon Nanotubes, *Fullerenes, Nanotubes and Carbon Nanostuctures* 13, 375 (2005)
4. K. Kamarás, M. E. Itkis, H. Hu, B. Zhao, R. C. Haddon, Covalent Bond Formation to a Carbon Nanotube Metal, *Science* 301, 1501 (2003).
5. F. Borondics, K. Kamaras, Z. Chen, A. G. Rinzler, M. Nikolou, D. B. Tanner, Wide range optical studies on transparent SWNT films, Electronic properties of synthetic nanostructures, *AIP Conference Proceedings* 723, 137-140 (2004).

INTERSUBBAND EXCITON RELAXATION DYNAMICS IN SINGLE-WALLED CARBON NANOTUBES

C. GADERMAIER,* C. MANZONI, A. GAMBETTA,
G. CERULLO, G. LANZANI
ULTRAS – INFM, Dipartimento di Fisica, Politecnico di Milano, P. za L. da Vinci 32, 20133 Milan, Italy

E. MENNA, M. MENEGHETTI
Department of Chemical Sciences, University of Padova, 35131 Padova, Italy

Abstract. We study excited state dynamics of semiconducting single-walled carbon nanotubes (SWNTs) by two-color pump-probe experiments. We find a time constant of 40 fs for the intersubband energy relaxation from EX2 to EX1.

Keywords: pump-probe spectroscopy; carbon nanotubes; excitons

Time-resolved photoemission,[1] pump-probe,[2-4] and fluorescence spectroscopy[5] reveal that semiconducting SWNTs excited to their lowest excitonic state (EX1) show a fast recovery to the ground state due to non-radiative decay channels.

Our study complements these findings by resolving the relaxation from the second sub-band exciton (EX2) to EX1. Transient oscillations due to coherent excitation of the radial breathing mode are seen in some of the time traces.

The setup used consists of an amplified Ti:sapphire laser driving two non-collinear optical parametric amplifiers (NOPAs) which generate pulses tunable in the near IR and visible. We studied samples of SWNTs grown by the high pressure carbon monoxide procedure, functionalized with PEG-amine and embedded in polymethylmethacrylate: films were cast on glass cover slips.

Figure 1 shows $\Delta T/T$ dynamics at two different pump and probe energies, 0.9 eV and 2.1 eV, respectively. The two pump energies are resonant with the EX1 and EX2 transitions.

We propose the following simple assignment of the various signals to rationalize the observations. The positive signals are due to photobleaching of

*To whom correspondence should be addressed. Christoph Gadermaier; e-mail: christoph.gadermaier@fisi.polimi.it

V.N. Popov and P. Lambin (eds.), Carbon Nanotubes, 171–172.

the EX1 and EX2 transitions respectively. The PA at 2.1 eV is attributed to a transition between the first and third conduction/valence subbands as conjectured by Korovyanko et al. (Ref. [6]).

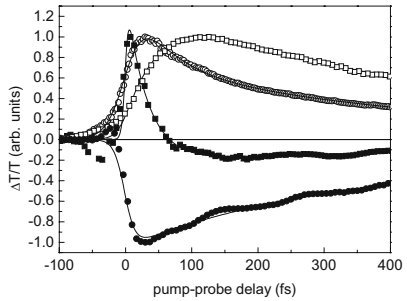

Figure 1. Transient differential transmission of SWNT sample at 0.9 eV pump and 0.9 eV probe (open circles), 2.1 eV probe (closed circles), 2.1 eV pump and 0.9 eV probe (open squares) and 2.1 eV probe energies (closed squares). Solid lines show fits to the data.

Excitation of either EX1 or EX2 leads to an instantaneous bleaching of the respective transition. The relaxation of EX1 to the ground state occurs with a time constant of 400 fs, in good agreement with previous measurements[4] EX2, on the other hand, relaxes towards EX1 with a time constant[7] of 40 fs. This is responsible for the fast decay of the EX2 bleaching concomitant with a buildup of both the EX1 bleaching and the EX1-EX3 absorption.

References

1. T. Hertel and G. Moos, Electron-phonon interaction in single-wall carbon nanotubes: A time-domain study, *Phys. Rev. Lett.* 84, 5002-5005 (2000).
2. Y.-C. Chen, N. R. Raravikar, L. S. Schadler, P. M. Ajayan, Y.-P. Zhao, T.-M. Lu, G.-C. Wang, and X.-C. Zhang, Ultrafast optical switching properties of single-wall carbon nanotube polymer composites at 1.55 μm, *Appl. Phys. Lett.* 81, 975-977 (2002).
3. H. Han, S. Vijayalakshmi, A. Lan, Z. Iqbal, H. Grebel, E. Lalanne, and A. M. Johnson, Linear and nonlinear optical properties of single-walled carbon nanotubes within an ordered array of nanosized silica spheres, *Appl. Phys. Lett.* 82, 1458-1460 (2003).
4. O. J. Korovyanko, C.-X. Sheng, Z.V. Vardeny, A. B. Dalton, and R. H. Baughman, Ultrafast spectroscopy of excitons in single-walled carbon nanotubes, *Phys. Rev. Lett.* 92, 017403 (2004).
5. F.Wang, G. Dukovic, L.E. Brus, and T.F. Heinz, Time-resolved fluorescence of carbon nanotubes and its implication for radiative lifetimes, *Phys. Rev. Lett.* 92, 177401 (2004).
6. C. Manzoni, A. Gambetta, E. Menna, M. Meneghetti, G. Lanzani, and G. Cerullo, Intersubband exciton relaxation dynamics in single-walled carbon nanotubes, *Phys. Rev. Lett.* 94, 207401 (2004).

PECULIARITIES OF THE OPTICAL POLARIZABILITY OF SINGLE-WALLED ZIGZAG CARBON NANOTUBE WITH CAPPED AND TAPERED ENDS

O. V. OGLOBLYA
Kyiv National Shevchenko University, Kyiv 01033, Ukraine
G. M. KUZNETSOVA
Scientific Center of Radiation Medicine, Kyiv 04050, Ukraine

Abstract. Computer modeling of the linear optical polarizability of single-walled carbon nanotubes (SWCNTs) of the zigzag type (*n*,0) with different diameter capped at one end by half of fullerene and tapered at the other end so that it can be connected with different (*n*,*n*) armchair nanotubes is carried out. The calculations were carried out within the Su-Schrieffer-Heeger model. It is shown that the localized states demonstrate the nonlinear aspects of excited states in that system. It is found that the molecules with different radius have strong oscillating dependence of the optical polarizability on the incident light energy. The effect of the length, capping of the tube end, and the Coulomb repulsion on the optical polarizability spectrum is studied.

Keywords: optical polarizability; carbon nanotube; Su-Schrieffer-Heeger model

The Su-Schrieffer-Heeger (SSH) model (Ma and Yuan, 1998) was used in the numerical calculations of the optical and electronic properties of an individual SWCNT and its modifications. We introduced new parameters $\xi = \alpha^2/(Kt)$, $u = U/t$, and $v = V/t$. The values ξ = 0.32 and t = 3.2 eV were used in the calculations as in a previous work (Prylutsky and Ogloblya, 2004). Within the independent electron approximation and sum-over-states approach, the linear polarizability is expressed as

$$\alpha(\omega) = \sum_{n\in occ., p\in unocc.} \mu_{np}\mu_{pn} 2\varepsilon_{pn}(\varepsilon_{pn}^2 - \omega^2)/[(\varepsilon_{pn}^2 - \omega^2)^2 + \Gamma^2\omega^2]$$

where μ_{np} is the dipole momentum. To account for the radiative widening of electron levels, we used Γ = 32 meV. The main attention was devoted to the spatially averaged polarizability $\alpha = (|\alpha_{xx}|^2 + |\alpha_{yy}|^2 + |\alpha_{zz}|^2)/3$.

V.N. Popov and P. Lambin (eds.), Carbon Nanotubes, 173–174.

We investigated zigzag (15,0) nanotube, capped at the ends with caps made from C_{180} fullerene. The results of the computations of α for nanotubes with length 6 and 8 periods are depicted in Figs. 1a and 1b, left. As we can see from these figures, the uncapped nanotube has additional low-energy peaks that are due to dangling bonds at the opened ends of nanotubes. The length decrease or the uncapping of the nanotube shifts the peaks of the polarizability towards the high energy region and suppresses their values.

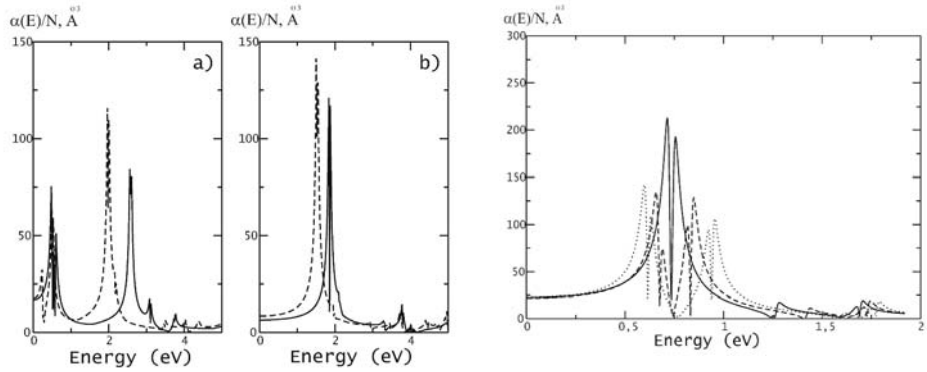

Figure 1. Left: polarizability of (a)open (15,0) and (b)capped at both ends nanotubes with length of 6 (solid line) and 8 (dotted line) periods (u = 0.3, v = 0.15). Right: polarizability of capped-tapered nanotube with u = 0; v = 0 (solid line), u = 0.3; v = 0.15 (dashed line), u = 0.6; v = 0.3 (dotted line).

We also considered the tapered configuration of the closing fragment (Saito et al., 1996). These authors describe a general way to connect nanotubes with different diameter by a knee configuration with a heptagon-pentagon defect. We used this procedure and built a knee that connects a capped (10,0) nanotube with length 8 with a (2,2) nanotube, which was not completed and four bonds remained dangling. The results are depicted in Fig. 1, right, which demonstrates the influence of the Coulomb repulsion. A splitting of the main peak of the polarizability can be observed, which is larger for higher values of the Coulomb repulsion.

References

Ma, J., and Yuan, R. K., 1998, Electronic and optical properties of finite zigzag carbon nanotubes with and without Coulomb interaction, *Phys. Rev. B* **57:**93439348.

Prylutsky, Yu. I., and Ogloblya, O. V., 2004, Computer modelling of the optical absorption spectrum of single-walled carbon nanotube bundles, *Ukr. J. Phys.* **49:**A17-A20.

Saito, R., Dresselhaus, G., and Dresselhaus, M. S., 1996, Tunneling conductance of carbon nanotubes, *Phys. Rev. B* **53:**2044-2050.

THIRD-ORDER NONLINEARITY AND PLASMON PROPERTIES IN CARBON NANOTUBES

A. M. NEMILENTSAU,* A. A. KHRUTCHINSKII,
G. YA. SLEPYAN, S. A. MAKSIMENKO
Institute for Nuclear Problems, Belarus State University,
Bobruiskaya 11, 220050 Minsk, Belarus

Abstract. Nonlinear optical properties in single-wall carbon nanotubes (CNTs) illuminated by an external electromagnetic field were investigated using quantum kinetic equations for the density matrix of the π-electrons. In the regime of weak driving field, these equations were solved by the perturbation method and the spectra of the third-order polarizability were calculated. In the case of high-intensive driving field, numerical simulation of the processes in the time-domain was carried out. The π-plasmons excitation was analyzed.

Keywords: carbon nanotubes; third-order polarizability; plasmon

We investigated the nonlinear optical effects, which take place in an infinitely long rectilinear single-wall carbon nanotube (CNT) exposed to an external electromagnetic field. To calculate the nonlinear response of CNT, the quantum kinetic equations for the π- electrons motion in single-electron approximation were obtained.[1] We assumed that the CNT is illuminated by a normally incident electromagnetic field, polarized along the tube axis. To avoid the destruction of the CNT by the driving field, its strength should be smaller than the atomic field strength. The driving field was assumed to be uniform over the CNT. Then its wavelength should be much greater than the CNT cross-sectional radius.

In the regime of weak driving field, the quantum kinetic equations were solved by the perturbation method and the third-order polarizability $\alpha^{(3)}_{zzzz}\left(-3\omega;\omega,\omega,\omega\right)$ of the single-wall CNT was calculated. The spectra of this polarizabillity were plotted in the frequency range from 1.35 to 1.9 eV for four different types of the CNTs: armchair (8,8), metallic zigzag (15,0), and semiconductor zigzag (16,0) and (38,0). The obtained spectra of the third-order

*To whom correspondence should be addressed. A. M. Nemilentsau, Institute for Nuclear Problems, Belarus State University, Bobruiskaya 11 220050, Minsk, Belarus; e-mail: nemili_1982@yahoo.com

V.N. Popov and P. Lambin (eds.), Carbon Nanotubes, 175–176.

polarizability contain a number of resonant lines whose position and magnitude are strongly dependent on the CNT type. However, in spite of this fact, there are several spectral maxima whose location does not depend on the tube radius. They are the resonant lines caused by the plasmon with respect to the third harmonic of the driving field frequency. Our result is in a good agreement with the experiment on the third-order harmonic generation in the solution comprising CNTs illuminated by the fundamental and second harmonics of the ND:YAG laser.[2]

In the regime of high-intensity driving field, the quantum kinetic equations were solved numerically in the time-domain with initial and boundary conditions. The initial conditions reflect the fact that at ambient temperature the electrons in the CNT are distributed according to the Fermi equilibrium distribution. The boundary conditions are the conditions of the periodicity of the solution in the quasi-momentum space. We considered the interaction of the CNT with the femtosecond laser pulse in the vicinity of the plasma resonance. The spectra of the induced current density were obtained. All calculations were performed for the metallic zigzag (9,0) CNT. Practically complete suppression of the high-order harmonic generation near this resonance was observed. The temporal behavior of the induced current was investigated in the case of exact resonance. Quasi-periodic relaxation of the induced current was revealed with time intervals much longer than the input pulse. Similar behavior was observed in metallic clusters. Thus, it is possible to conclude, that the carrier dynamics in CNTs, exposed to electromagnetic pulses, exhibits properties common with those of plasma.

The research was partially supported by INTAS and the State Committee for the Science and Technology of Belarus under project 03-50-4409, and by the NATO Science for Peace Program under project SfP--981051. A. M. N. is grateful to the World Federation of Scientists for the financial support.

References

1. G. Ya. Slepyan, A. A. Khrutchinskii, A. M. Nemilentsau, S. A. Maksimenko, and J. Herrmann, High-order optical harmonic generation on carbon nanotubes: quantum-mechanical approach, *Intern. J. Nanoscience* 3, 343-354 (2004).
2. X. Liu, J. Si, B. Chang, G. Xu, Q. Yang, Z. Pan, S. Xie, P. Ye, J. Fan, and M. Wan, Third-order optical nonlinearity of the carbon nanotubes, *Appl. Phys. Lett.* 74, 164-166 (1999).

HYDRODYNAMIC MODELING OF FAST ION INTERACTIONS WITH CARBON NANOTUBES

DUNCAN J. MOWBRAY, SANGWOO CHUNG, ZORAN L. MIŠKOVIĆ
Department of Applied Mathematics, University of Waterloo, Waterloo, Ontario, Canada N2L 3G1

Abstract. We use the two-fluid, two-dimensional hydrodynamic model, proposed in (Mowbray et al., 2004), to describe the collective response of a carbon nanotube's σ and π electrons to fast ions moving parallel to the nanotube. In the present contribution, two extensions of this model are being made: (1) to the case of multi-walled carbon nanotubes, where the inter-wall electrostatic interaction gives rise to rich plasma spectra, and (2) generalization to include a dielectric medium surrounding the nanotube.

Keywords: hydrodynamic modeling; carbon nanotubes; ion channeling

The two-fluid model (Mowbray et al., 2004) treats the π and σ electrons of a single wall nanotube (SWNT) as separate two-dimensional fluids confined to the same cylindrical surface, while the electrostatic interaction between these fluids gives rise to a splitting of the plasmon energies in qualitative agreement with experiments.

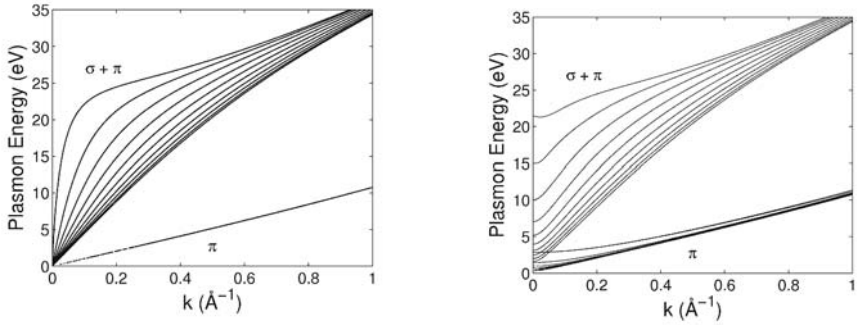

Figure 1. A MWCNT with ten walls of inner radius a_{in} = 3.6 Å and inter-wall separation Δ = 3.4 Å exhibits dispersion curves (in eV) for the $\sigma + \pi$ and π plasmons, shown versus longitudinal momentum k (in Å^{-1}) for (left) m = 0 and (right) m = 1.

V.N. Popov and P. Lambin (eds.), Carbon Nanotubes, 177–178.

The plasmon dispersion curves for a MWCNT with a number of walls N = 10 are shown in Fig. 1. The two-fluid model reproduces the $\sigma + \pi$ bands found by Yannouleas et al. in (Yannouleas et al., 1996), as well as the quasi-acoustic π bands. Note that the ten π bands from each wall coincide for $m = 0$ as shown in Fig. 1, left, while splitting of the acoustic bands occurs for higher m values as shown in Fig. 1, right, for $m = 1$.

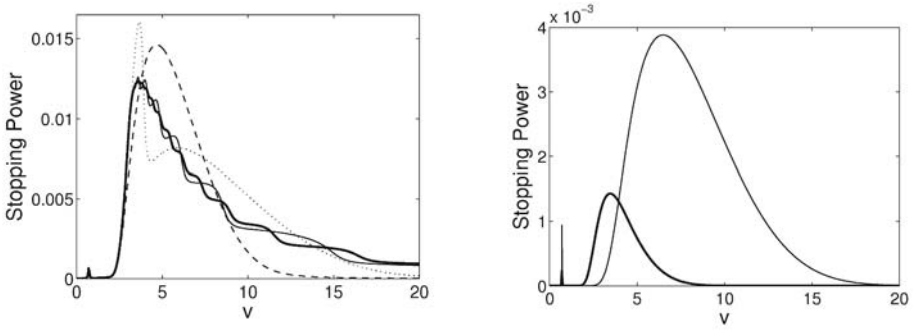

Figure 2. Stopping Power (in atomic units) for an ion moving with speed v along the nanotube axis is shown for (left) a MWCNT with a_{in} = 3.6 Å and inter-wall separation Δ = 3.4 Å in vacuum for N = 1 (dashed line), 2 (dotted line), 10 (thin line), and 20 (thick line) walls and (right) a SWCNT with a_{in} = 7 Å in vacuum (thin line) and embedded in a dielectric media of ε = 4 (thick line). The low-velocity peaks correspond to energy-loss to the quasi-acoustic plasmons.

The two-fluid model stopping power for N = 1, 2, 10, and 20 walls is shown in Fig. 2, left, for an ion traversing the carbon nanotube axis. We notice that as the number of walls increases, the stopping power becomes much more pronounced at higher velocities. In Fig. 2, right, we find that an embedding dielectric media of ε = 4 causes the stopping power of a SWCNT to both decrease and shift to lower velocities, as found for metallic nanotubes (Prodan et al., 2002). These results suggest that using SWCNTs and an embedding dielectric media may be employed to reduce the stopping power in the high velocity regime and facilitate channeling of fast ions.

References

Mowbray, D. J., Mišković, Z. L., Goodman, F. O., and Wang, Y. N., 2004, Interactions of fast ions with carbon nanotubes: two-fluid model, *Phys. Rev. B* **70:**195418/1-7.

Prodan, E., Nordlander, P., and Halas, N. J., 2002, Effects of dielectric screening on the optical properties of metallic nanoshells, *Chem. Phys. Lett.* **368:**94-101.

Yannouleas, C., Bogachek, E. N., and Landman, U., 1996, Collective excitations of multishell carbon microstructures: Multishell fullerenes and coaxial nanotubes, *Phys. Rev. B* **53(15)**:10255-10259.

LOCAL RESISTANCE OF SINGLE-WALLED CARBON NANOTUBES AS MEASURED BY SCANNING PROBE TECHNIQUES

BRETT GOLDSMITH, PHILIP G. COLLINS*
Department of Physics and Astronomy, University of California at Irvine, Irvine CA 92697-4576

Abstract. Single-walled carbon nanotube (SWCNT) resistance arising from point defects can be directly imaged using scanning probe techniques. Here, we combine Scanning Gate Microscopy (SGM) and Kelvin Force Microscopy (KFM) to electronically identify defect sites and study their contributions to SWCNT resistances.

Keywords: carbon nanotube; Kelvin gate microscopy; scanning gate microscopy; defect; local resistance

A ballistic SWCNT is theoretically predicted to have a 6.5 kΩ resistance based on the presence of two one-dimensional channels for conduction. In real devices, however, the experimental resistance is typically higher than this measured value. Various mechanisms contribute to this increased resistance. In long SWCNTs, diffusive scattering plays a significant role. In shorter SWCNTs, contact effects can be dominant. In short devices with ohmic contacts, however, a significant number of devices continue to exhibit unexpectedly large resistances. This variability poses a major problem for both the fundamental understanding and commercial application of SWCNT circuits.

Scanning probe techniques provide a novel way to directly image the electric potential gradients along a SWCNT and identify the sources of resistance.[1,2] In this study, the contact resistance was minimized through proper processing of the SWCNT circuit and devices were selected which nevertheless had large, gate-dependent resistances. Nearly 10% of the devices from a wafer-scale fabrication batch met these criteria.

Figure 1, left, shows an example of two voltage profiles acquired along a particular SWCNT device using KFM. At different source-drain biases, the SWCNT exhibits localized voltage drops at particular points along its length. It

*To whom correspondence should be addressed. Philip G. Collins; e-mail: collinsp@uci.edu

V.N. Popov and P. Lambin (eds.), Carbon Nanotubes, 179–180.

is immediately apparent that the SWCNT does not smoothly ramp from 2 to 0V as for a diffusive conductor. Instead, sudden jumps and changes in slope are observed. Furthermore, KFM cannot identify a difference between the surface potential of the electrode and that of the SWCNT near the contact, indicating that the majority of the resistance is not due to contact effects. Instead, all of the surface potential gradients occur along the SWCNT body.

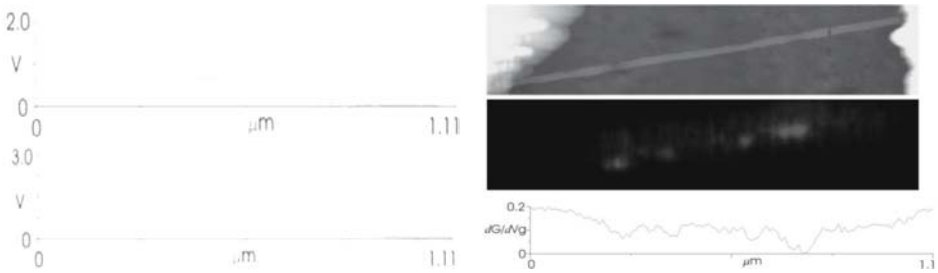

Figure 1. Left: KFM voltage profile along a SWCNT biased at 2.0V (top) and at 3.0V (bottom). Both profiles exhibit sharp voltage drops identifying locally resistive sites. Source and drain electrodes connect the SWCNT near the edges of both plots. Right: A SWCNT imaged topographically by AFM (top) and electronically by SGM (middle). A linescan parallel to the SWCNT identifies local regions dominating the transconductance (bottom).

The same SWCNT can also be characterized by SGM, in which the AFM tip is used as a local gate as shown in Fig. 1, right. The lack of gate-sensitive Schottky barriers in this figure confirms that this sample is likely to be metallic, despite two-terminal behavior of a field-effect transistor. The SGM measurement identifies nearly all of the gate-dependence as being due to local points of resistance along the SWCNT body. These effects are consistent with what we might expect form a defects in or near the SWCNT wall.

Further analysis indicates that the sites of gate sensitivity in Fig. 1, right, have a one-to-one correspondence with the sites of local resistance identified in Fig. 1, left. The primary conclusion is that defects in SWCNTs are statistically relevant and, when present, they can dominate the electronic characteristics of a device, even causing metallic SWCNTs to behave like semiconducting ones.

References

1. M. Freitag, A. T. Johnson, S. V. Kalinin, and D. A. Bonnell, Role of single defects in electronic transport through carbon nanotube field-effect transistors, *Phys. Rev. Lett.* 89, 216801 (2002).
2. A. Bachtold, M. S. Fuhrer, S. Plyasunov, M. Forero, E. K. Anderson, A. Zettl, and P. L. McEuen, Scanned probe microscopy of electronic transport in carbon nanotubes. *Phys. Rev. Lett.* 84(26), 6082-6085 (2000).

BAND STRUCTURE OF CARBON NANOTUBES EMBEDDED IN A CRYSTAL MATRIX

P. N. D'YACHKOV, D. V. MAKAEV
Institute of General and Inorganic Chemistry, Russian Academy of Sciences, Leninskii pr. 31, 119991 Moscow, Russia,

Abstract. The electronic structure of single-wall carbon nanotubes (SWCNTs) embedded in a crystal matrix is calculated in terms of a linear augmented cylindrical wave method (LACW). In the case of armchair nanotubes, the delocalization of the nanotube electrons into the matrix region is responsible for the high energy shift of the σ-states and growth of the electron density of states at the Fermi level. For the semiconducting nanotubes, it causes a decay of the minimum energy gap and a formation of a metallic state.

Keywords: Electronic structure; carbon nanotube; crystal matrix; nanotube metallization effect; linear augmented cylindrical wave method

There have been attempts to integrate SWCNTs in conventional 2D or 3D semiconductor systems. For example, encapsulated single-walled SWCNTs in epitaxially grown semiconductor heterostructures were found promising for the realization of new semiconductor hybrid devices such as a SWCNT contacted by a two-dimensional electron gas.[1]

Here, we present a simple model for electronic structure of embedded SWCNTs.[2] Our approach is based on a LACW method.[3] The method is just a reformulation of the well-known linear augmented plane wave theory for cylindrical multiatomic systems. In the LACW method, the one-electron potential is constructed using the muffin-tin approximation. The one-electron potential is spherically symmetric in the region of the atoms and is constant in the interstitial region up to the two cylindrical potential barriers. In the case of embedded SWCNT, there is no vacuum but a matrix region outside the tubule. The potential barrier V_m between the SWCNT and the matrix is penetrable so that an electronic tunneling exchange between the SWCNT and matrix is possible. For simplicity, we treat the matrix as a homogenous medium with a constant potential neglecting the atomic structure of the matrix and the

V.N. Popov and P. Lambin (eds.), Carbon Nanotubes, 181–182.

complicated structure of the potential barrier on the interface between the SWCNT and the matrix. It is a model of a SWCNT in contact with an electron gas. Then we solve the one-electron Schrödinger equation for the orbitals and the electronic energies of the SWCNT in the matrix, the potential V_m being treated as a parameter.

According to the LACW calculations, the delocalization of electrons of the armchair nanotube into the matrix region results in a strong band structure perturbation. A high energy shift of the σ-states relative to the π-bands is the most significant effect of the embedding. As a result, these electrons can take part in the SWCNT charge transfer through the mechanism of electron tunneling into the matrix. The interaction with the matrix results in a growth of the electronic density of states at the Fermi level. The electron tunneling into the matrix does not destroy the metallic character of the armchair nanotube band structure.

In the case of semiconducting SWCNT, the minimum energy gap is very sensitive to the matrix effect. The gap decreases with decreasing V_m. Finally, the gap is closed up and the semiconducting behavior breaks down.

The metallization of the embedded SWCNTs is consistent with the measured transport properties of the tube-semiconductor devices with carbon nanotubes encapsulated in a semiconductor crystal using the molecular beam epitaxy.[1] The presented results from a collection of 20 measured devices displayed no gate voltage dependence of the conductance at room temperature, i.e., the incorporated nanotubes were metallic.[1] A Luttinger liquid behavior confirmed that the leak currents through the substrate can be neglected and the electronic transport is dominated by the properties of the embedded metallic SWCNTs.[1]

This work was supported by RBRF (grant 04-03-32251).

Refrences

1. A. Jensen, J. R. Hauptmann, J. Nygerd, J. Sadowski, and P. E. Lindelof, Hybrid devices from single wall carbon nanotubes epitaxially grown into a semiconductor heterostructures, *Nano Lett*. 4, 349-352 (2004).
2. P. N. D'yachkov and D.V. Makaev, Electronic structure of embedded carbon nanotubes, *Phys. Rev. B*. 71, 081101(R) (2005).
3. P. N. D'yachkov, Augmented waves for nanomaterials, in *Encyclopedia of Nanoscience and Nanotechnology*, edited by N. S. Nalwa, (American Scientific Publishers, New York, 2004), v. 1, pp. 191-212.

MAGNETOTRANSPORT IN 2-D ARRAYS OF SINGLE-WALL CARBON NANOTUBES

V. K. KSENEVICH*
Department of Physics, State University of Belarus, 220050 Minsk, Belarus

J. GALIBERT
Laboratoire National des Champs Magnétiques Pulsés BP 14245 143, Avenue de Rangueil F-31432 TOULOUSE CEDEX 4, France

L. FORRO
Ecole Polytechnique Federal de Lausanne, DP-IGA, PH Ecublens, CH-1015, Lausanne, Switzerland

V. A. SAMUILOV
Department of Materials Science, State University of New York at Stony Brook, N.Y. 11794-2275, U.S.A.

Abstract. Magnetotransport properties of two-dimensional (2D) arrays of single-wall carbon nanotubes (SWCNTs) were investigated. The magnetoresistance (MR) in pulsed magnetic fields and the temperature dependence of the resistance of 2D arrays of SWCNTs were measured in the temperature range 1.8–300 K and in fields up to 9 T. The crossover between metallic and non-metallic temperature dependence of the resistance was observed at $T \approx 125$ K. At low temperature, positive MR was observed with decreasing amplitude with the increase of temperature.

Keywords: SWCNTs arrays; magnetoresitance; weak localization

We report magnetotransport measurements on SWCNT arrays. We used Langmuir-Blodgett (LB) technique for self-assembling SWCNTs. Chemical functionalization of the SWCNTs[1] was realized in order to reach high solubility of the nanotubes in organic solvents and to obtain a monolayer on the water surface. The monolayers of SWCNTs were transferred to the substrate with in-

*To whom correspondence should be addressed. V.K.Ksenevich, Department of Physics, State University of Belarus, 220050 Minsk, Belarus; e-mail: ksenevich@bsu.by

V.N. Popov and P. Lambin (eds.), Carbon Nanotubes, 183–184.

plane macroscopic finger-shaped electrodes. Minimum on the temperature dependence of the resistance of the SWCNTs arrays, $R(T)$, was observed at $T \approx$ 125K. At $T >$ 125 K, $R(T)$ was found to have a metallic-type behavior ($dR/dT > 0$). In the low-temperature range ($T \sim$ 4.2-50 K), $R(T)$ is an inherent for weak localization power law with an exponent of –0.60. Such type of dependence can be interpreted in terms of heterogeneous model for conduction, where the presence of structural defects and intertube connections gives rise to low temperatures localization effects.[2] The conductivity of the system at high temperatures is determined by the charge transport trough metallic nanotubes. Positive MR with decreasing amplitude was observed with the increase of the temperature in the low temperature range, as shown in Fig. 1. The localization effects in the SWCNTs arrays are confirmed by the shape of the MR curves.

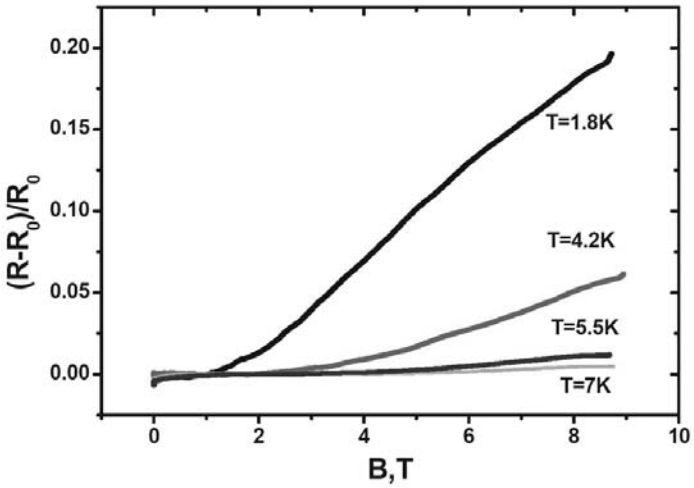

Figure 1. Magnetoresistance of the SWCNTs array for magnetic field parallel to the surface.

This work was supported by the INTAS grant #03-50-4409.

References

1. P.W. Chiu, G.S. Duesberg, U. Dettlaff-Weglikowska, S. Roth. Interconnection of carbon nanotubes by chemical functionalization, *Appl.Phys.Lett.*, 80, 3811-3813 (2002).
2. A.B. Kaiser, G. Duesberg, S. Roth. Heterogeneous model for conduction in carbon naotubes, *Phys. Rev. B* 57, 1418-1421 (1998).

COMPUTER MODELING OF THE DIFFERENTIAL CONDUCTANCE OF SYMMETRY CONNECTED ARMCHAIR-ZIGZAG HETEROJUNCTIONS

O. V. OGLOBLYA
Kyiv National Shevchenko University, Kyiv 01033, Ukraine
G. M. KUZNETSOVA
Scientific Center of Radiation Medicine, Kyiv 04050, Ukraine

Abstract. Computer modeling of the differential conductance of symmetry connected armchair (n,n) and zigzag ($2n$,0) nanotubes was carried out in the framework of the surface Green's function matching (SGFM) method. It is shown that the heterojunctions (n,n)/($2n$,0) have a band gap in the electron energy spectrum. It is demonstrated that the *I-V* curve increases with constant values with the increase of the voltage. The height of the *I-V* curve plateau is bigger for heterojunctions of larger diameter. It is shown that the maximum of the differential conductance of heterojunctions with bigger diameter is at comparatively low voltage.

Keywords: differential conductance; nanotube; heterojunction

In order to calculate the conductance of a zigzag/armchair nanotube and a symmetry-connected (n,n)/($2n$,0) heterojunction, we use the Kubo formula (Datta, 1995). The conductance is related to the current via $I = GV$ and is given by the Landauer formula $G = (2e^2/h)T$. Here T is the transmission function expressed as $T = \mathrm{Tr}[\Gamma_R G^+ \Gamma_L G^-]$, where $G^{+/-}$ are the retarded and advanced Green's functions, and $\Gamma_{R,L}$ describe the coupling of the conductor to the leads.

We used the recurrence formulas derived for layered systems (Sancho et al., 1985) in order to calculate the retarded and advanced Green's functions $G^{+/-}$ and self energies $\Sigma^{+/-}$ of isolated nanotubes. Knowing Σ_L (self-energy function of a left semi-infinite tube) and Σ_R (same but for a right semi-infinite tube) we can find the coupling functions Γ_L and Γ_R: $\Gamma_{\{L,R\}} = i[\Sigma^+_{\{L,R\}} - \Sigma^-_{\{L,R\}}]$.

We considered the symmetry connection of armchair (n,n) and zigzag ($2n$,0) nanotubes. The nanotubes are positioned on the same axes and connected by n

V.N. Popov and P. Lambin (eds.), Carbon Nanotubes, 185–186.

topological defects (5/7). In order to calculate the conductance of such heterojunction, we used the SGFM method based on the formula

$$\begin{pmatrix} G_L & G^+ \\ G^- & G_R \end{pmatrix} = \begin{pmatrix} \varepsilon - H_L - \Sigma_L & H_{LR} \\ H_{LR}^+ & \varepsilon - H_R - \Sigma_R \end{pmatrix}^{-1}$$

In this formula, $H_{\{LR\}}$ is the hopping matrix between the two nanotubes, H_L and H_R are the Hamiltonians of the unit cell of armchair and zigzag nanotubes. Σ_L and Σ_R are calculated using published formulas (Sancho et al., 1985). The formula above enables us to find $G^{+/-}$ necessary for the calculation of the conductance by the Kubo formula. The results of our calculation for a (4,4)/(8,0) heterojunction are shown on Fig.1, left. We calculated the differential conductance $\partial I / \partial V$ assuming phase-coherent transmission and a constant potential within the whole sample (Liang et al., 2001).

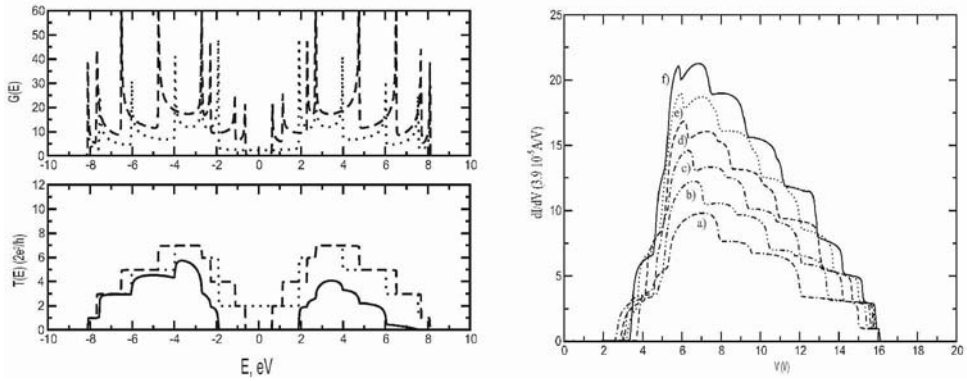

Figure 1. Left: density of states (top) and conductivity in units of $2e^2/h$ (bottom) for the (4,4) (dotted line) and (8,0) (dashed line) nanotubes and for the heterojunction (4,4)/(8,0) (solid line). Right: Differential conductance for (a) (4,4)/(8,0), (b) (5,5)/(10,0), (c) (6,6)/(12,0), (d) (7,7)/(14,0), (e) (8,8)/(16,0), (f) (9,9)/(18,0).

The results of the calculation of the differential conductance of $(n,n)/(2n,0)$ heterojunctions of different diameter are shown in Fig. 1, right. The maximum of the conductance for larger diameter heterojunctions shifts to lower voltage.

References

Datta, S., 1995, *Electronic Transport in Mesoscopic Systems*, Cambridge University Press, Cambridge.

Lopez Sancho, M. P., Lopez Sancho, J. M., and Rubio, J., 1985, Highly convergent schemes for the calculation of bulk and surface Green functions, *J. Phys. F* **15:**851-858.

Liang, W., Bockrath, M., and Borovic, D., 2001, Fabry-Perot interference in a nanotube electron waveguide, *Nature* **411:**665-669.

Part IV. Molecule adsorption, functionalization and chemical properties

MOLECULAR DYNAMICS SIMULATION OF GAS ADSORPTION AND ABSORPTION IN NANOTUBES

ANA PROYKOVA*
University of Sofia, Faculty of Physics, 5 J. Bourchier Blvd., Sofia-1126, Bulgaria

Abstract. Physi- and chemisorption are considered within the framework of classical and quantum molecular dynamics and density functional theory. We analyze coating (adsorption of metal monolayer) of carbon nanotubes as the cause of gas adsorption enhancement. Coarse-graining of less relevant degrees of freedom to obtain Hamiltonians spanning large length and time scales is a successful approach. The diffusion of adsorbed substances is modeled as well. Carbon nanotubes are regarded as mass conveyors as an application of diffusion. Charge fluctuations of electron density of the adsorbed molecules and of the carbon tube are the sources of metastability of the physisorption states.

Keywords: adsorption; simulations of carbon nanotubes; Molecular Dynamics method; coarse-graining technique; ab-initio calculations; time-scales

1. Adsorption – general characteristics

Adsorption of one or more of the components at one or more of the phase boundaries of a multicomponent, multiphase system is said to occur if the concentrations in the interfacial layers are different from those in the adjoining bulk phases, so that the overall stoichiometry of the system deviates from that corresponding to a *reference system* of homogeneous bulk phases whose volumes and/or amounts are defined by suitably chosen dividing surfaces or by a suitable algebraic method.

*To whom correspondence should be addressed. Ana Proykova, University of Sofia, Faculty of Physics, 5 J. Bourchier Blvd., Sofia-1126, Bulgaria; e-mail: anap@phys.uni-sofia.bg

V.N. Popov and P. Lambin (eds.), Carbon Nanotubes, 187–207.

1.1. PHYSISORPTION AND CHEMISORPTION

A qualitative distinction is usually made between *chemisorption* and *physisorption*. The problem of distinguishing between chemisorption and physisorption is basically the same as that of distinguishing between chemical and physical interaction in general. No absolutely sharp distinction can be made and intermediate cases exist, for example, adsorption involving strong hydrogen bonds or weak charge transfer. In terms of the relative binding strengths and mechanisms, a strong 'chemical bond' is formed between the adsorbate atom or molecule and the substrate. In the case of chemisorption the adsorption energy, E_a, of the adatom is of a few eV/atom.

Physisorption (or *physical adsorption*) results from the presence of van der Waals attractive forces due to fluctuating dipole (and higher order) moments on the interacting adsorbate and substrate with no charge transfer or electrons shared between atoms. These intermolecular forces, usually between closed-shell systems, are of the same kind as those responsible for the imperfection of real gases and the condensation of vapours.

Table 1. The following features characterize physisorption and chemisorption.

Physisorption	Chemisorption
Evidence for the perturbation of the electronic states of adsorbent and adsorbate is minimal	Changes in the electronic state
The chemical nature of the adsorptive is not altered by adsorption and subsequent desorption	The chemical nature of the adsorptive(s) may be altered, i.e. the chemisorption may not be reversible.
Energies are of order 50-500 meV/atom	The energy is of the same order of magnitude as the energy change in a chemical reaction between a solid and a fluid, eV/atom
The elementary step in physisorption from a gas phase does not involve activation energy	The elementary step in chemisorption often involves *activation energyi* (*adsorption sites*)
multilayer adsorption or filling of micropores	one layer of chemisorbed molecules is formed

Physisorption energies are of order 50-500 meV/atom. As they are small, they can be expressed in K/atom, via 1 eV ≡ 11604K, omitting Boltzmann's constant in the corresponding equations. One can see that these energies are comparable to the sublimation energies of rare gas solids.

The physical adsorption is believed to serve as a precursor, which enhances the transition to the chemisorption state. A first, *precursor* stage, has all the characteristics of physisorption, but this state is metastable. In this state the molecule may re-evaporate, or it may stay on the surface long enough to transform *irreversibly* into a chemisorbed state.

This transition from physisorption to chemisorption usually results in a split of the molecule and adsorption of individual atoms: *dissociative chemisorption*. If the heat of adsorption is given up suddenly and is imparted to the resulting adatoms, then the dissociation stage is explosive as it is in the case of F_2. The adsorption energies for the precursor phase are similar to phyisorption of rare gases, but may contain additional contributions from the dipole, quadrupole, or higher molecular multipoles.

1.2. LOCALIZED ADSORPTION AT LOW COVERAGE

Equilibrium phenomena are described by thermodynamics, which is the dynamics of heat or by statistical mechanics, which works well for large (on the order of Avogadro's number) numbers of particles – atoms and /or molecules. However, many properties of nanosized (small number of particles, away from the thermodynamics limit) materials are concerned with kinetics, where the rate of change of metastable structures (or their inability to change) is dominant (Proykova et al., 2001; Proykova, 2002). An equilibrium effect is the vapor pressure of a crystal (pure element). A kinetic effect is crystal growth from the vapor.

The *surface coverage* for both monolayer and multilayer adsorption is defined as the ratio of the amount of adsorbed substance to the ***monolayer capacity***. *For chemisorption* the monolayer capacity is defined as the amount of adsorbate, needed to occupy all adsorption sites as determined by the adsorbent structure and by the chemical nature of the adsorptive; *for physisorption* it is the amount needed to cover the surface with a complete monolayer of molecules in a close-packed array (Venables, 2000).

The sublimation of a pure solid at equilibrium is given by the condition $\mu_v = \mu_s$, where μ_v is the chemical potential of the vapor and μ_s is the chemical potential of the solid. At low pressure p, μ_v is:

$$\mu_v = -kT \ln(kT / p\lambda^3), \tag{1}$$

where $\lambda = h/(2\pi mkT)^{1/2}$ is the thermal de Broglie wavelength; h is the Planck constant; k is the Boltzmann constant; m is the electron mass.

The equilibrium vapor pressure p_{eq} in terms of the chemical potential of the solid is

$$p_{eq} = (2\pi m / h^2)^{3/2} (kT)^{5/2} \exp(\mu_s / kT). \tag{2}$$

To calculate the vapor pressure we usually model μ_s at a low pressure assuming harmonic vibrations of the solid at a given lattice constant. The free energy per particle is

$$F / N = \mu_s = U_0 + < 3h / 2 > + 3kT < \ln(1 - \exp(-h / kT)) >, \quad (3)$$

where < > denote averaged values. The (positive) sublimation energy at zero temperature is

$$L_0 = -(U_0 + < 3h\nu / 2 >), \quad (4)$$

where the first term is the (negative) energy per particle in the solid relative to vapor, and the second is the (positive) energy due to zero-point vibrations.

The vapor pressure is important at high temperatures, where the Einstein model (all $3N\nu$s are the same) of the solid becomes realistic if thermal expansion is taken into account in U_0. This model gives

$$< \ln(1 - \exp(-h / kT)) > = < \ln(h / kT) >, \quad (5)$$

so that $\exp(\mu_s/kT) = (h\nu/kT)^3 \exp(-L_0/kT)$ and

$$p_{eq} = (2\pi m\nu^2)^{3/2} (kT)^{-1/2} \exp(-L_0 / kT). \quad (6)$$

Thus $p_{eq}T^{1/2}$ follows the Arrhenius law and the pre-exponential factor depends on the lattice vibration frequency as ν^3. The missing Planck's constant h shows a classical effect with equipartitioning of energy. Since the $T^{1/2}$ term slowly varies most tabulations of vapor pressure give the constants A and B from $\log_{10} p_{eq} = A - B/T$. The values for L_0 and ν are obtained along these lines.

The chemical potential μ_a of the adsorbed layer satisfies two possible conditions: $\mu_a = \mu_v$ for equilibrium with the vapor or $\mu_a = \mu_s$ for equilibrium with the solid.

The canonical partition function for the adsorbed atoms is $Z_a = \sum_i \exp(-E_i/kT)$ with $F = -kT\ln Z$. For N_a adsorbed atoms distributed over N_0 sites with the same adsorption energy E_a, $Z_a = Q(N_a,N_0)\exp(N_aE_a/kT)$, where Q is the configurational (and vibrational) degeneracy. The *configurational entropy* appears since, at low coverage, there are many ways to arrange the adatoms on the available adsorption sites, (Hill 1987): $Q = N_0!/(N_a!)(N_0 - N_a)!$ multiplied by q^{Na} if vibrational effects are included. The expression for $\ln Q$ is evaluated using Stirling's approximation for $N! = N\ln N - N$ to give $\mu_a = F/N_a = -(kT/N_a)\ln Z_a = kT\ln(\theta/(1 - \theta)) - E_a - kT \ln q$ and $\theta = N_a/N_0$. The first term is the configurational contribution in terms of the adatom coverage θ, the second term is the adsorption energy (measured positive with the vacuum level zero), and the last term is the (optional) vibrational contribution. The density of adatoms is determined by $\mu_s = 3kT\ln(h\nu/kT) - L_0 = \mu_a$ in the high temperature Einstein model. Thus at low coverage, θ is

$$\theta = N_a / N_0 = C \exp[(-L_0 + E_a) / kT], \quad (7)$$

where the pre-exponential function depends on vibrations in the solid, and the important exponential term depends on the difference between the sublimation and the adsorption energy. If C is unknown, we usually put it equal to 1 to obtain a first estimate of θ at a given temperature.

The *Langmuir Adsorption Isotherm* results from $\mu_a = \mu_v$. Using this to calculate the vapor pressure p in equilibrium with the adsorbed layer we get

$$p = C_1\theta/(1-\theta)\exp(-E_a/kT), \tag{8}$$

or $\theta = \xi(T)p/[1 - \xi(T)p]$, with $\xi(T) = C_1^{-1}\exp(E_a/kT)$; the constant $C_1 = kT/q\lambda^3$. The coverage is linearly proportional to p for small p approaching 1 as $p \to \infty$.

The other limit of isolated adatom behaviour is the 2D gas (Venables 2000). This case is appropriate to a very smooth substrate, with shallow potential wells. The mobile adatoms see the *average adsorption energy* E_0, and gain additional entropy from the gaseous motion. The chemical potential is now $\mu_a = -E_0 + kT\ln(N_a\lambda^2/Aq_z)$, where this expression is valid at sufficiently low density for the distinction between classical Bose-Einstein and Fermi-Dirac statistics not to be important. The derivation involves evaluating the partition function by summing over 2D momenta, analogously to a 3D gas, while retaining the z-motion partition function q_z. **The 3D to 2D difference accounts for λ^2 rather than λ^3, and the N_a/A, the number of adsorbed atoms per unit area, is the 2D version of the 3D density N/V, as in $pV = NkT$.**

The perfect gas law has the 2D form $\Phi A = N_a kT$, where Φ is the *spreading pressure* (Venables 2000). This means that $\mu_a = -E_0 + kT\ln(\Phi\lambda^2/kT)$, or $\mu_a = -E_0 + \mu_2 + kT\ln\Phi$, where $\mu_2 = -kT\ln(kTq_z/\lambda^2)$ is the standard free energy for the 2D gas. This makes the correspondence between 3D gases and 2D adsorption clear: $p \leftrightarrow \Phi$, $\mu_0 \leftrightarrow \mu_2$; the energy is lower in the 2D case by E_0. The various q's are dimensionless and often skipped.

Henry's Law for 2D gas adsorption is obtained by putting $\mu_a = \mu_v$:

$$p = C_2(N_a/A)\exp(-E_0/kT), \tag{9}$$

or $(N_a/A) = \chi'(T)p$ with $\chi'(T) = C_2^{-1}\exp(E_0/kT)$ and $C_2 = kT/q_z\lambda$.

The 2D gas form has (N_a/A) proportional to p, whereas the localized form has the coverage $\theta = N_a/N_0$ proportional to p. These could be reconciled if we write $(N_a/A) = \theta(N_0/A)$. The monolayer coverage (N_0/A) and the area density of adsorbed atoms (N_a/A) have been defined as constants. Both N_0 and N_a are numbers, not area densities, although they are densities for $A = 1$. One can re-write the 2D gas equation as

$$p = (kTN_0/Aq_z\lambda)\exp(-E_0/kT), \tag{10}$$

which is in a form that can be compared directly with the corresponding equation for localized adsorption. This comparison shows that there is a

transition from localized to 2D gas-like behaviour as T is raised, because $E_a > E_0$, whereas the pre-exponential (entropic) term is larger for the 2D gas. The ratio of coverages at a given p for the two states is

$$\begin{aligned} \theta_{gas} / \theta_{loc} &= (2\pi mkT / h^2 q_x q_y)(A / N_0)\ \exp[(E_0 - E_a)/kT] \\ &= (2\pi ma^2 \nu_d^2 / kT)\ \exp[(E_0 - E_a)/kT], \end{aligned} \tag{11}$$

where the length a is an atomic dimension ($a^2 = A/N_0$), and the last equality is only true for the high temperature limit where equipartition of energy holds (no term in h). We can state that the localized atoms will vibrate with amplitude $\Re$ and $4\pi^2 m\Re^2 \nu_d^2$ is the energy associated with this 2D oscillation, which equals $2kT$ at high T, assuming a harmonic approximation is valid. Thus, the pre-exponential is just a ratio of *free areas* ($a^2/\pi\Re^2$), the numerator associated with the 2D gas, and the denominator with the potential well in which the adatom vibrates. This is the basis of *cell models* of lattice vibrations, introduced originally by Lennard-Jones and Devonshire in 1937 (Hill, 1986). The free area is defined by integrating the Boltzmann factor over the 'cell' in which the atom vibrates; in 3D this produces a *free volume*. **This approximate classical theory is very effective in computations, since it includes thermal expansion** (the response to the spreading pressure exerted by the vibrations), which more sophisticated models ignore. It also does not rely on a harmonic approximation; for these reasons at least, it deserves to be better known.

1.3. SPECIFICITY OF ADSORPTION ON SWCNT AND SWCNT BUNDLES

One of the most interesting issues in adsorption is the basic question of the system dimensionality. A specified nanotube adsorption problem can exhibit behavior characteristic of one, two or three dimensions depending on thermodynamic (temperature and number of particles) or microscopic (atomic size relative to nanotube radius) parameters, and geometry (independent tubes or bundles).

The study of adsorption of atoms on nanotube surfaces is also essential for nano-electronics aiming to achieve low resistance ohmic contacts to nanotubes and to fabricate functional nanodevises. It is important for nanotechnology to produce nanowires with controllable sizes. While the adsorption on the surface of a SWCNT is a two-dimensional process, the diffusion of substances in the tubes is one-dimensional process.

1.3.1. *Adsorption on SWCNT*

It was shown with the help of first-principles gradient-corrected density-functional calculations (Pati et al., 2002) that the adsorption of water molecules

on a SWCNT causes a reduction of the electronic conduction due to charge transfer between the adsorbate and the SWCNT: 0.03e is transferred from a single water molecule to the nanotube. The authors conclude a physisorption although they claim a weak bond between a hydrogen atom of a water molecule and one C atom.

A systematic study of single atoms adsorption on a carbon nanotube has been performed by Durgun et al., 2003. Higher coverage and decoration of adsorbed foreign atoms can produce nanostructures such as nanomagnets, nanometer size magnetic domains, one-dimensional conductors and thin metallic connects, which could be used in technological applications as spintronics and high density data storage. The *d*-orbitals of the transition metal atoms are responsible for a relatively high binding energy that displays a variation with the number of filled *d*-states.

The main result of the experimental study of Zhang et al. (2000, 2000a) that continuous nanowires of any metal can be obtained by coating the SWCNT with titanium. The strong interaction between Ti and SWCNT can be understood in the frame of density functional theory, which will be described in some detail in the Section 2.1.

The average exchange time between methane molecules adsorbed inside SWCNTs and the free gas outside is estimated to be about 80 ms from nuclear magnetic resonance measurements (Kleinhammes et al., 2003).

1.3.2. *Adsorption in bundles of SWCNT*

Experimental results of methane adsorption on closed-ended single-wall nanotube bundles (Talapatra, 2002) give the isosteric heat of adsorption as a function of the amount of methane adsorbed on the SWNT substrate for coverage in the first layer. The isosteric heat of adsorption is found to decrease with increasing coverage. This behavior provides an explanation for differences in previously reported values for this quantity. Substantial agreement was found with previous reports on the temperature dependence of the pressures at which the two first-layer sub-steps occur for methane adsorbed on SWNT bundles.

Grand canonical MonteCarlo simulations with a Lennard-Jones potential have been performed to study the adsorption of methane, X and Ar onto bundles of closed SWCNT (Shi, 2003). The results agree with the experiments of Talapatra, et al., 2002: four different adsorption sites have been identified on bundles of SWCNTs – internal (endohedral), interstitial channels (ICs), external groove sites, and external surfaces. The main conclusion is that the ICs become important in the case of heterogeneous bundles. However, there is no obvious plateau region corresponding to groove site filling for the heterogeneous bundles for methane and Ar and the authors conclude that the groove sites for both homogeneous and heterogeneous bundles are very similar.

The kinetics of adsorption and desorption of methane, Xe, SF6, and other weakly bonded gases from SWCNT bundles has been compared with that from graphite by Hertel (2001). The observed trends in the binding energies of gases with different van der Waals radii suggest that the so-called groove sites on the external bundle surface are the preferred low coverage adsorption sites due to their higher binding energy. The measured sticking coefficients can be related to the diffusion kinetick of adsorbates into the bulk of the nanotube samples.

1.3.3. *Adsorption of methane on graphene*

Methane is of great interest both as a greenhouse gas and as a possible source of hydrogen for fuel cells. A lot of articles have been published on the properties of methane. Our interest in methane has been rooted in the ability of methane to form clathrates or gas hydrates in very cold water under a high pressure. We have re-visited the problem of hydrophobic-molecule influence on liquid and solid water structures (Daykova, 2002) in order to understand the competition between the enthalpy and the entropy of clathrate formation. We have suggested a statistical model of the rearrangement of water molecules when methane molecules are introduced in the ideal tetrahedral hydrogen-bond network. The most important basis of that model, which considered the methane molecules as rigid objects, has been the hydrophobic interaction. Methane molecules are less rigid if they interact with carbon atoms.

The electronic structure of graphene, a single planar sheet of sp^2-bonded carbon atoms, provides the basis for understanding the electronic structure of single-walled carbon nanotubes. Recently a lot of efforts have been put into developing applications of SWCNT as gas sensors as the electronic and transport properties of the SWCNTs are significantly changed if they are exposed to gases (Collins 2000). The gas molecules are either physisorbed or chemisorbed depending on the reactivity of the gas.

A microscopic theory of physisorption applied for the noble He atoms on variety of free electron metals showed a little influence of the boundary conditions for a non-local model on the equilibrium distance (Landman, 1975). This justifies the study of adsorption of methane (resembling the noble gases in interaction with other atoms) on an isolated piece of graphene sheet.

Extensive time-dependent density-functional calculations (DFT) have been performed (Daykova, 2005) with the real-space DFT code (Chelikowsky, 2000) to study the mechanism of adsorption of methane and to check the influence of the slab finite size on the dynamics of the process and the electron distribution as a result of open "ends" of the slab. Thus, no boundary conditions have been introduced. The computations without periodic boundary conditions are more demanding. Hence, a preliminary research for the volume and its shape should be done. In the present study a cubic box with a side-length of 17.46 Å has been

chosen for the graphene slab with a diameter of 8.98 Å, Figure 1 (a). The grid of calculations is 110 x 110 x 110 with a space-step of 0.3 Bohr = 0.1587 Å; the cut-off radius is 5.29 Å; the time step of electron density integration is 1.2 fs; constant-temperature molecular dynamics (MD) calculations at each time step with a friction-mass of 0.0004 a.u. is used for optimizing the configuration at T = 0 K. Under these conditions the electron density at the cut-off radius reduces to 5.4 10^{-9} with a respect to the maximum density. There is no need for increasing the box size or the cut-off radius. Details of procedure have been published by the code authors (Vassiliev et al., 2002) and (Proykova, 2003).

The center of mass of methane molecule is above the point 0 on the graphene sheet, Fig. 1 (a), initially at a height of 2.91 Å. The height is optimized with a combined DFT and MD calculations to be 3.07 Å. We have considered two different orientations of the methane molecule relative to the graphene surface. Case 'F', Fig. 1 (b), is characterized with a binding energy of 120 ± 10 meV, which shows a physisorption and agrees surprisingly well with previous calculations of Muris et al. (2001) based on a constant-temperature Monte Carlo method. They have found that the binding energy for a single methane molecule is –121 ± 10 meV for the curved graphitic surface; for planar graphite it is –143 ± 10 meV.

The case 'V' denotes a methane molecule rotated at 180° with respect to the position in Fig, 1 (b). In this case, one C-H bond is closer to the graphene slab and the other three are further. The binding energy is larger manifesting a configuration dependence reported for Li adsorbed on CNT (Udomvech, 2005).

The methane-graphene interaction induces a local curvature of the graphene: in the 'F' case it is hardly seen, Figure 1 (b), while in the 'V' case it is essential.

The oscillations of CH4 center of mass in Fig, 1 (c) reveal a faster dynamics in the 'F' case. This result combined with the smaller adsorption energy in the 'F' case, shows that this case is less stable.

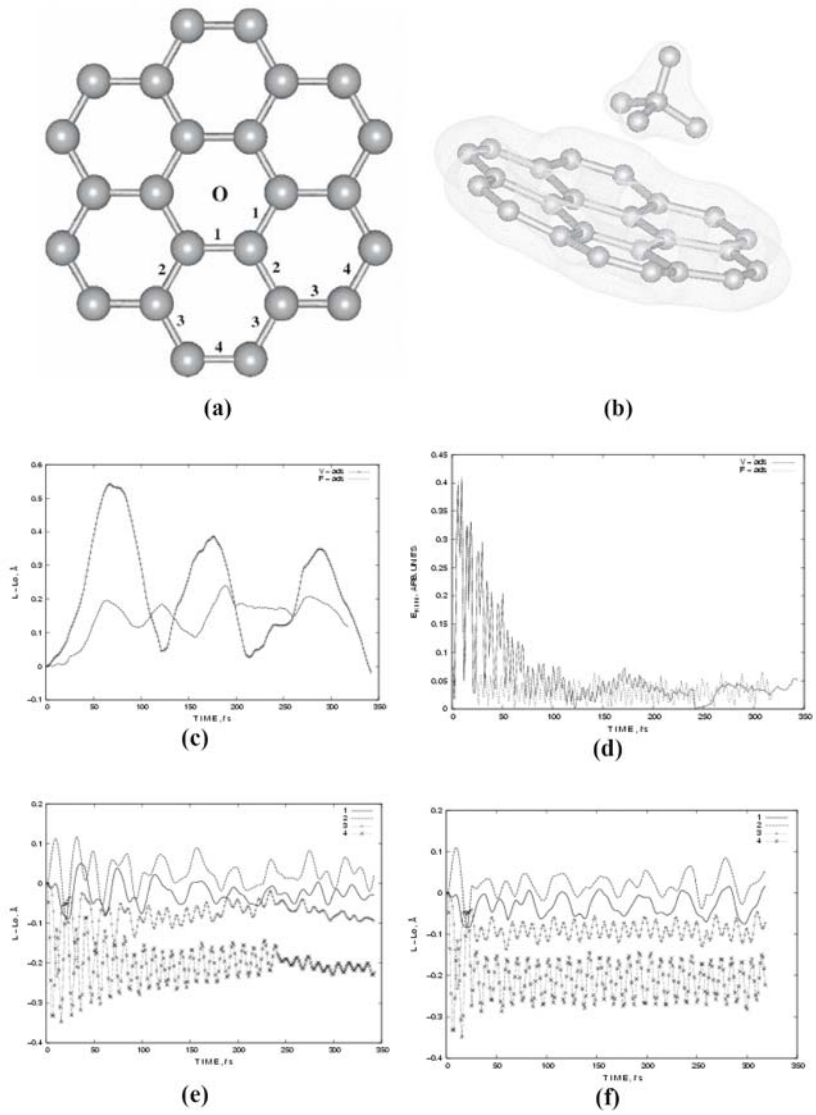

Figure 1. The CH_4 molecule is initially at $r_0 = 2.91$ Å above point 0 in the graphene sheet (a); 1, 2, 3, and 4 label the bonds between C atoms in the sheet and appear in the figures (e) and (f); (b) the 'F' orientation of CH_4; (c) the relative amplitude of induced oscillations of the CH_4 center of mass for the cases 'F' and 'V'; (d) the kinetic energy of the system (molecule and graphene) as a function of time: after 150 fs the temperature is almost 0 K; the oscillations of graphene bonds '1', '2', '3', and '4' for 300 fs: (e) 'V' case; (f) 'F' case.

To find out the mechanism of adsorption we study the electron distribution change in both methane and graphene slab due to methane-graphene interaction. Additionally, changes of the fundamental modes of methane bring information about the interaction. We compare our calculations with the experimentally determined values for the fundamental modes of methane obtained by Allan (2005) with the help of electron energy loss spectroscopy, Table 2.

Table 2. Vibrational modes of methane (symmetry T_d).

Mode	Symmetry species	Type	Frequency (meV)	Line width (meV)	Activity
ν_1	A_1	Symmetric stretch	361.7		Raman
ν_2	E	Twisting	190.2	30	Raman
ν_3	T_2	Asymm. stretch	374.3		IR
ν_4	T_2	Scissoring	161.9	16	IR

Note that the outer graphene bonds (lines 3 and 4 in Fig. 1, (e) and (f)) oscillate with a period of ≈11 fs, which is the same as the asymmetric stretch mode 11.05 fs (374.3 meV) of the methane molecule. Summation of the two wave processes cause beating which we see in the dynamics of the electron distribution in the methane molecule.

1.4. RELATIONSHIP OF POTENTIAL ENERGY CURVES TO ELECTRONIC SPECTRA OF A DIATOMIC MOLECULE ADSORBED ON A SURFACE

To understand differences in adsorption of various atoms/molecules we inspect the potential energy (Morse) curve, Fig. 2 (a), for a diatomic molecule versus the inter-nuclear distance. The minimum and maximum values for the bond distance for the vibrational state are at A and B (see caption to the figure). At those points the atoms change direction, so the *Vibrational Kinetic* energy is zero. At r_e (equilibrium internuclear distance) the *Vibrational Kinetic* energy has a maximum value and the *Vibrational Potential* energy is zero. Each horizontal line represents a vibrational state. The ground state is v_0 and thee excited states are v_1, v_2, v_3, etc. Each excited state contains a series of different vibrational energy levels and may be represented by a Morse curve. Each vibrational level v_n is described by a vibrational wave function Ψ_{vib}. The square of wave function gives the probability distribution, and in this case Ψ_{vib}^2 indicates the probable internuclear distance for a particular vibrational state (the dotted line). The higher the line the more probable the internuclear distance is. The most probable distance for a molecule in the ground state is r_e, while there

are two probable distances that correspond to the two maxima in the next vibrational state; three in the third, Fig. 2 (b). In the excited vibrational levels for the ground state and the excited electronic states, there is a high probability of the molecule having an inter-nuclear distance at the ends of the potential function.

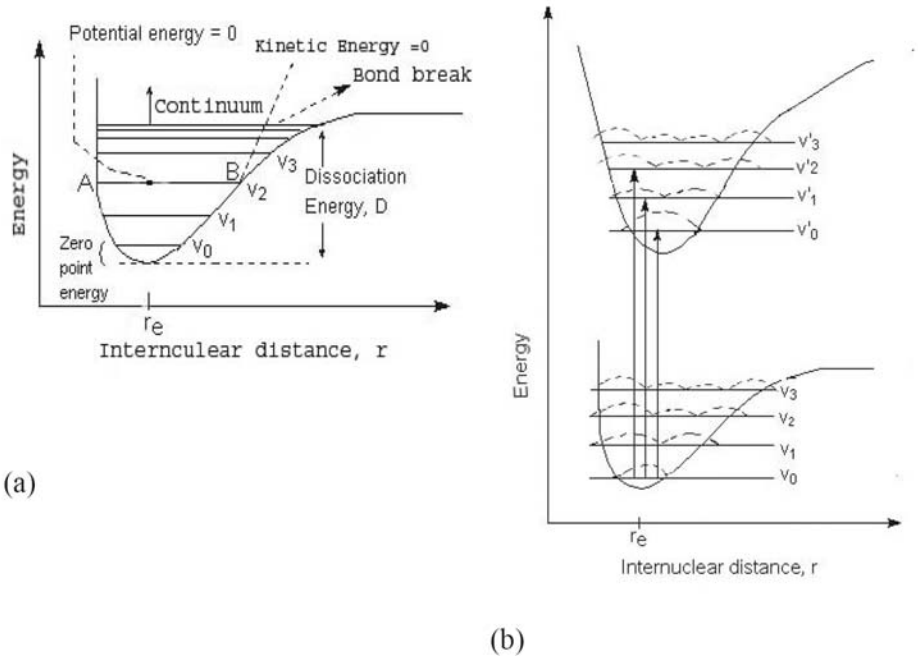

Figure 2. (a) Morse curve: Along the A-B line we see that the energy is constant while the bond distance (b) is changing, that means the molecule is vibrating, and A-B is a vibrational state.

2. Time-scales in Molecular Dynamics. Ab-initio (quantum) Molecular Dynamics and coarse graining techniques

To determine properties of materials one needs to approximate both atomic and electronic interactions. However, these interactions have completely different time and space scales. Because of the large difference between the masses of electrons and nuclei and the fact that the forces on the particles are the same, the electrons respond instantaneously to the motion of the nuclei. Thus, the

$$\Psi(\mathbf{R}_I, \mathbf{r}_n) = \Psi_{el}(\{\ \mathbf{r}_n\ \}; \{\mathbf{R}_I\})\ \Psi_I(\{\mathbf{R}_I\})$$

nuclei are adiabatically treated and separated from the electrons. The many-body wave function is factorized within the Born-Oppenheimer approximation.

The adiabatic principle reduces the many-body problem in the solution of the dynamics of the electrons in a frozen-in configuration $\{\mathbf{R}_I\}$ of the nuclei. This is an example of how some degrees of freedom are eliminated in the multi-scale modeling.

The structure of matter is continuous when viewed at large length scales and discrete at an atomic scale. Modeling techniques are being developed to bridge the gap between the length-scale extremes. Nanotechnology challenges the researchers to develop and design nanometer to micrometer-sized devices for applications in new generations of computers, electronics, photonics and drug delivery systems. Theory and modeling play more and more important role in these areas to reduce costs and increase predictability for the new properties. Multi-scale materials modeling approaches are required to combine the atomistic and continuum scale. A detailed overview of recent achievements has been completed by Ghoniem and collaborators (Ghoniem et al., 2003).

The SWCNT is a good example of the dual behavior of the matter. Their functionalization is done at an atomic level (bonding manipulation) while their elastic modulus shows up at the continuous level.

2.1. DENSITY FUNCTIONAL AND MOLECULAR DYNAMICS METHOD

The Car-Parrinello (CP) method was applied to perform both dynamic and static calculations. The method performs the classical MD, which computes a time dependent trajectory of all the atomic motions by numerically integrating equation of motion, and simultaneously applies DFT to describe the electronic structure, using an extended Lagrangian formulation. The characteristic feature of the Car-Parrinello approach is that the electronic wave function, *i.e.* the coefficients of the plane wave basis set, are dynamically optimized to be consistent with the changing positions of the atomic nuclei. The actual implementation involves the numerical integration of the equations of motion of second-order Newtonian dynamics. A crucial parameter in this scheme is the fictitious mass associated with the dynamics of the electronic degrees of freedom. Nosé (1984) has modified Newtonian dynamics so as to reproduce both the canonical and the isothermal-isobaric probability densities in the phase space of an N-body system. Nosé did this by scaling time (with s) and distance (with $V^{1/D}$ in D dimensions) through Lagrangian equations of motion. The dynamical equations describe the evolution of these two scaling variables and their two conjugate momenta p_s and p_v. In practice, the fictitious mass has to be chosen small enough to ensure fast wave function adaptation to the changing nuclear positions on one hand and sufficiently large to have a workable large time step on the other. In our work (Daykov and Proykova, 2001) the equations

of motion were usually integrated using the Verlet algorithm (Verlet, 1967). The fictitious mass limits the time step.

The CP simulations can be performed using the CP-PAW code package developed by Blöchl (Blöchl, 1994). It implements the ab-initio (from first-principles) molecular dynamics together with the **projector augmented wave** (PAW) method. The PAW method uses an augmented plane wave basis for the electronic valence wave functions, and, in the current implementation, frozen atomic wave functions for the core states. Thus it is able to produce the correct wave function and densities also close to the nucleus, including the correct nodal structure of the wave functions. The advantages compared to the pseudopotential approach are that transferability problems are largely avoided, that quantities such as hyperfine parameters and electric field gradients are obtained with high accuracy (Petrilli et al., 1998; Blöchl, 2000) and, most important for the present study, that a smaller basis set as compared to traditional norm-conserving *pseudopotentials* is required.

It is well known that most physical properties of solids are dependent on the valence electrons to a much greater degree than that of the tightly bound core electrons. It is for this reason that the *pseudopotential* approximation is introduced. This approximation uses this fact to remove the core electrons and the strong nuclear potential and replace them with a weaker pseudopotential which acts on a set of pseudo wavefunctions rather than the true valence wavefunctions. In fact, the pseudopotential can be optimised so that, in practice, it is even weaker than the *frozen core potential* (Lin et al., 1993).

The frozen core approximation was applied for the 1s electrons of C and O, and up to 2p for Cl. For H, C and O, one projector function per angular-momentum quantum number was used for **s**- and **p-**angular momenta. For Cl, two projector functions were used for **s**-and one for **p-**angular momenta. The Kohn-Sham (Kohn and Sham 1965) orbitals of the valence electrons were expanded in plane waves up to a kinetic energy cutoff of 30 Ry.

Static DFT calculations can be performed using the atomic-orbital based ADF package (Baerends et al., 1973). In these calculations, the Kohn-Sham orbitals were expanded in an uncontracted triple-Slater-type basis set augmented with one 2p and one 3d polarization function for H, 3d and 4f polarization functions for C, O, and Cl.

For heavy atoms, relativistic effects become important because electrons near the nuclei move at speeds that are a significant fraction of the speed of light. The electron wave functions near the nuclei must therefore be described by the Dirac equation. However, the pseudopotential method can also be applied here. To determine the radial wave functions, one must work with a generalization of the radial Kohn-Sham equations that correspond to the Dirac equation. The steps in creating a pseudopotential are now modified as follows:

Step 1 - one must write down and solve a version of the Kohn-Sham equations that generalizes the Dirac equation; Step 2 - one draws smooth replacements for the original wiggly wave functions. One can take the original nonrelativistic Kohn-Sham equation and put a pseudopotential in it that produces the wave functions obtained in the previous step. Now the pseudopotential is not only compensating for the smoothing procedure of step 2 that removed wiggles from the wave function, but also is compensating for the differences between the Dirac equation and the Schroedinger equation. That is, the pseudopotential is chosen to produce a wave function for the Schroedinger equation that is also a solution of the original Dirac equation.

DFT and MD methods have been simultaneously applied to study conductivity and mechanical properties of (10,0) SWCNT (Iliev et al., 2005). Molecular dynamics simulations have shown that the distribution of the vacancies, not only their concentration, is important for the mechanical strength of the tube. Our calculations demonstrate that the band gap shrinks in a defective tube and the external field changes the band gap differently depending on the axis of application.

Insight of carbon nanotube growth has been gained from DFT and tight binding studies (Krasheninnikov et al., 2004). They have found that the adsorption and migration energies strongly depend on the nanotube diameter and chirality, which makes the model of carbon adatom on a flat graphene sheet inappropriate. This result is consistent with our finding (Daykova et al., 2005) that adsorption of methane on a small graphene sheet induces curvature of the sheet, which is not flat anymore. Krasheninnikov and collaborators have used the PAW method to describe the core electrons and the generalized gradient approximation (Perdew and Wang, 1992, Perdew et al., 1992). They have found that adatom migration is a different mechanism from the kick-out mechanism as it was previously derived from analytical potential calculations (Maiti, 1967).

2.2. SPACE-TIME DISCRETE POINTES

For the numerical solution of time-dependent wave propagation problems that appear both in DFT and *ab initio* MD one has to deal with complex geometries with very different evolution scales. The time step of the computations is determined by the fastest process in order to predict reliable results. For a comparison, the electronic degrees of freedom should be integrated in the atto-second domain, while the nuclear degrees of freedom are in the femto-second domain. If a uniform time-step (fastest process) Δt is used two problems appear. First, the computational cost is high. Second, the ratio $c\Delta t$/(space_step) in the coarser grid will be much smaller than its optimal value. This generates dispersion errors in most numerical schemes. To avoid these problems, it is

advisable to keep the ratio constant meaning that Δt is different in the various space domains determined by the density distribution of the original system. The Figure 3 shows replacement of a uniform time-space mesh with a refined mesh for a complex structure, which is much denser in the middle of the area than at the boarders. At different time-steps (they could be very different) one can use various space discrete steps.

The mesh refinement is an opposite approach to coarse-graining techniques, which we will consider in the next section. At the end of the present section we must underline that the use of local time step raises new practical and theoretical problems that are very delicate in the case of hyperbolic equations. There are plenty of articles on the subject, see for example (Manfrin, 1996) and the references therein.

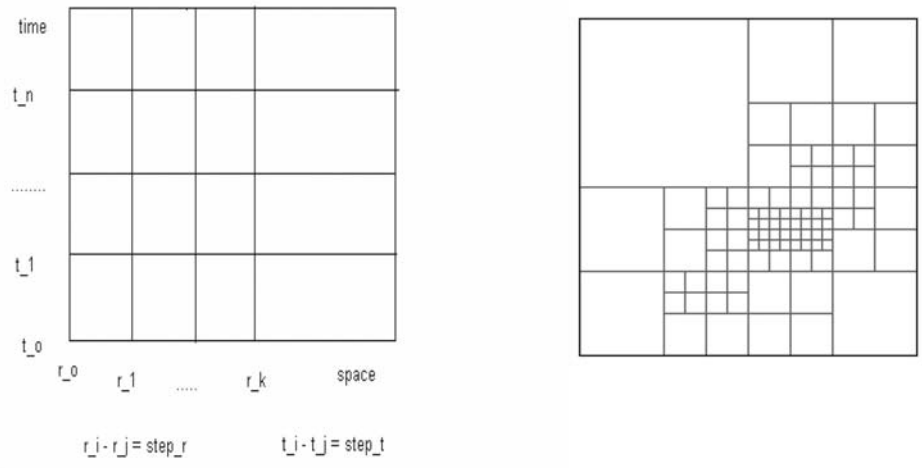

Figure 3. The uniform time-space mesh (left) is replaced by a suitable dynamic mesh (right).

2.3. COARSE-GRAINING TECHNIQUE: TIME/TEMPERATURE DEPENDENT PHENOMENA

The study of time/temperature dependent phenomena is more difficult and requires the development of a dynamics for a system with an inhomogeneous level of coarse graining. A nice job has been completed by Stefano Curtarolo in his dissertation for the degree of PhD in material science (Curtarolo 2003). The technique suggested is different from both microscopic (quantum mechanics) and macroscopic (thermodynamics) descriptions. By removing the unnecessary

degrees of freedom, the author constructs a local thermodynamics associated with dynamics and interaction between regions.

An example useful for the carbon nanotubes is the following. Let us consider a finite one dimensional chain of atoms that interact through nearest neighbor pair potentials. It is possible to remove every second atom by considering each of these atoms as part of a local system with its own local partition function. The local degrees of freedom can be removed by integrating over all the possible configurations of the particular atom. The integration produces a local partition function, local free energy and local entropy, which equals the information that has been locally removed from the system. This construction 'converts' the second neighbors into first neighbors with an effective potential which is the microscopic analogy of the pressure for thermodynamic systems. The procedure can be iterated until a multi-scale description of the systems is achieved. This approach is rigorously correct at equilibrium being an approximate one to slow dynamics description.

Coarse graining requires both a scheme to remove atoms and a recipe for constructing potentials between the remaining atoms. One way is the integration of bond motion similarly to the Migdal-Kadanoff approach in renormalization group theory (Migdal, 1975; Kadanoff, 1976; Kadanoff, 1977). New potentials can be differently defined satisfying the requirements: a) the coarse-grained system ultimately evolves to the same equilibrium state of the atomistic one; b) the information removed from the original system is quantified by the entropy contribution of each coarse graining. Curtarolo has used as a criterion for the definition of a new potential: the partition function should be unchanged in the coarse graining procedure.

3. Diffusion of the adsorbed gases

An important observation has been that adsorbed atoms (adatoms) form small clusters which diffuse on metal surfaces by undergoing possible cluster configurations. The nature of the motion depends on the surface morphology. Examples are one-dimensional diffusion of W on the (211) W surface and two-dimensional diffusion of Pt on W. What is the dimensionality of gas diffusion on/in nanotubes?

Different approaches – experimental, computational, and theoretical – give supplementary information on the specific features of particle diffusion on/in CNT and SWCNT bundles.

Theoretically one solves the generic diffusion equation

$$\partial c / \partial t - \nabla.(D\nabla c) = Q, \tag{12}$$

where $c = N_a/A$ is the concentration of the ad-atoms, D is the diffusion coefficient and Q is a volume source, may be anisotropic in which case D is a 2x2 matrix. The boundary conditions can be of Dirichlet type, where the concentration on the boundary is specified, or of Neumann type, where the flux $n.(D\nabla c)$ is specified. It is also possible to specify a generalized Neumann condition. It is defined by $n.(D\nabla c) + qc = g$, where q is a transfer coefficient. This approach does not reflect the discrete nature of SWCNTs, which restricts its applications.

Recent research reveals that binary gases and fluids diffuse differently at the nano-scale than many other polyatomic molecules. For example, *n*-butane and isobutene are predicted to have substantially different separation behaviors when they are mixed with methane molecules in a single-wall carbon tube (Moe, 2001). Further studies to determine the exact mechanisms responsible for this unique trait are, however, a great challenge due to the difficulty of detecting and determining the behavior of the molecules experimentally.

Atomistic simulations (Skoulidas et al., 2002) for both self- and transport diffusivities of methane and hydrogen in CNT predict orders of magnitude faster transport than that in zeolites. The high rates in CNT result from the inherent smoothness of the nanotubes. The authors used equilibrium dynamics to obtain the diffusion coefficients.

There is an interest in Li adsorption and diffusion on/in CNT in relation with Li batteries production. Frontera and collaborators (Garao et al., 2003) studied molecular interaction potential between Li^+ and small-diameter arm-chair SWCNT based on *ab-initio* calculations. They observed a channel that would allow ion mobility inside the nanotube. Since the Li atom and cation prefer to localize near the carbon nanotube sidewall, small-diameter carbon nanotubes are more advantageous than the larger ones for batteries usage.

The rate of diffusion is inversely related to the binding energy. Density functional computations based on the B3LYP functional and all-electron basis set centered on atoms show that the binding energy depends on the configuration rather than on the diameter size (Udomvech et al., 2005). This result contradicts the finding of Krasheninnikov and thus needs an independent study.

To complete this section it is important to note that the diffusion process is the basis of various phenomena including carbon nanotube growth by carbon diffusion; convey of nanoscale materials with the help of SWCNT; migration of defects; gas separation and filtration.

One of the future challenges is the development of explicit links between the atomistic scales and the continuum level in all numeric techniques included in the present paper. The issue of computational efficiency must be also

addressed so that truly large-scale simulations on thousands of processors can be effectively performed.

ACKNOWLEDGEMENTS

Computations on the methane adsorption on graphene have been performed with a partial support from HPC-Europe (CINECA, Italy). The results for the influence of external electric field on defective SWCNT have been calculated under the Taiwan-Bulgarian project. A Grant from the Ministry of Education and Science (У-Ф-03/03) and a grant from the University of Sofia (2005) have been used for calculations of mechanical strength of carbon nanotubes.

References

Allan, M., 2005, Excitation of the four fundamental vibrations of CH4 by electron impact near threshold, *J. Phys. B: At. Mol. Opt. Phys.* **38:**1679-1685.

Baerends, E. J.; Ellis, D. E.; and Ros, P., 1973, Self-consistent molecular Hartree—Fock—Slater calculations I. The computational procedure**,** *Chem. Phys.* **2**:41-51.

Bienfait, M., Zeppenfeld, P., Dupont-Pavlovsky, N., Muris, M.R., Wilson, T., DePies, M., and Vilches, O.E., 2004, Thermodynamics and structure of hydrogen, methane, argon, oxygen, and carbon dioxide adsorbed on sigle wall carbon naotube bundles, *Phys. Rev. B* **70:**035410/1-10.

Blöchl, P. E., 1994, Projector augmented-wave method, *Phys. Rev. B* **50:**17953-1797.

Blöchl, P. E., 2000, First-principles calculations of defects in oxygen-deficient silica exposed to hydrogen *Phys. Rev. B* **62:**6158-6179.

Car, R., Parrinello, M., 1985, Unified approach for Molecular Dynamics and Density-Functional Theory, *Phys. Rev. Lett.* **55:**2471-2474.

Chelikowsky, J. R., 2000, The pseudopotential-density functional method applied to nanostructures, *J. Phys. D: Appl. Phys*. **33:**R33-R50 http://jrc.cems.umn.edu/codes.htm.

Collins, P. G., Bradley, K., Ishigami, M., and Zettl, A., 2000, Extreme Oxygen Sensitivity of electron properties of carbon nanotubes, *Science* **287:**1801-1804.

Curtarolo, Stefano, 2003, Coarse-Graining and Data Mining Approaches to the prediction of structures and their dynamics, Ph.D. Thesis, MIT (USA).

Daykov, I., and Proykova, A., 2001, Cluster size dependence of the temperature interval of coexisting phases observed in plastic molecular clusters, in: *Meetings in Physics at University of Sofia*, A. Proykova, ed., vol. 2, Heron Press Science Series, Sofia, pp. 31-35.

Daykova, E., Pisov, S., and Proykova, A., 2005, First-principles and molecular dynamics simulations of methane adsorption on graphene, NATO Science Series II, Springer, submitted.

Daykova, E. , Proykova, A., and Ohmine, I., 2002, Statistical Calculations of Entropy of Methane Clathrate, in: Meetings in Physics @ University of Sofia, A. Proykova, ed., vol. 3, Heron Press Science Series, Sofia, pp. 44 -48.

Durgun, E., Dag, S., Bagci, V. M. K., Gulseren, O., Yildirim, T., and Ciraci, S., 2003, Systematic study of adsorption of single atoms on a carbon nanotube, *Phys. Rev. B* **67:**201401-201404.

Garao, C., Frontera, A., Quinonero, D., Costa, A., Ballester, P., Deya, P.M., 2003, Lithium diffusion in single-walled carbon nanotubes: a theoretical study, *Chem. Phys. Lett.* **374:**548-553.

Ghoniem, N., Busso, E., Kiossis, N., and Huang, H., 2003, Multiscale modeling of nanomechanics and micromechanics: an overview, *Philosophical Magazine* **83:**3475-3528.

Hertel, T., Kriebel, J., Moos, G., and Fasel, R., 2001, Adsorption and desorption of weakly bonded adsorbates from single-wall carbon nanotube bundles, AIP Conference Proceedings 590, Nanonetwork Materials, Fullerenes, Nanotubes and Related Systems, S. Saito, T. Ando, Y. Iwasa, K. Kikuchi, M. Kobayashi, Y. Saito, eds., Kamakura, Japan, p.181.

Hill, T. L., 1987, *Statistical Mechanics: Principles and Selected Applications*, Dover, New York.

Hill, T. L., 1986, *An Introduction to Statistical Thermodynamic,*.Dover, New York.

Hill, T. L., 1994, *Thermodynamics of Small Systems*, Parts I and II, Two Volumes in One. Dover, New York.

Iliev, H., and Proykova, A., 2004, Mechanically induced defects in single-wall carbon nanotubes, in *Meetings in Physics at University of Sofia*, A. Proykova, ed., vol. 5, Heron Press Science Series, Sofia, pp. 87-91.

Iliev, H., Li, F.-Yin, and Proykova, A., 2005, Carbon nanotubes with vacancies under external mechanical stress and electric field, NATO Science Series II, Springer, submitted.

Kadanoff, L. P., 1976, Notes on Migdal's Recursion Formulas, *Ann. Phys.* **100:**359-394.

Kadanoff, L. P., 1977, The Application of Renormalization Group Techniques to Quarks and Strings, *Rev. Mod. Phys.* **49:**267-296.

Kleinhammes, A., Mao, S.-H., Yang, X.-J., Tang, X.-P, Shimoda, H., Lu, J.P., Zhou, O., and Wu, Y., 2003, Gas adsorption in single-walled carbon nanotubes studied by NMR, *Phys. Rev.* ***B*** **68:**075418/1-6.

Kong, J., Franklin, N.R., Zhou, C., Chapiline, Peng, S., Cho, K., and Dai, H., 2000, Nanotube Molecular Wires as Chemical Sensors, *Science* **287:**622-625.

Kohn, W. and Sham, L.J., 1965, Self-consistent equations including exchange and correlation effects, *Phys. Rev.* **140:**A1133-A1138**.**

Krasheninnikov, A.V., Nordlund, K., Lehtinen, P.O., Foster, A.S., Ayuela, A., and Nieminen, R.M., 2004, Adsorption and migration of carbon adatoms on carbon nanotubes: Density-functional *ab initio* and tight-binding studies, *Phys. Rev.* B **69:**073402/1-4.

Landman, Uzi and Kleinman, George, 1975, Local and non-local effects in the theory of physisorption, *J. Vac. Sci. Technol.* **12:**206-209.

Lin, J. S. , Qteish, A., Payne, M. C. and Heine, V., 1993, Optimized and transferable nonlocal separable *ab initio* pseudopotentials, *Phys. Rev. B* **47:**4174-4180.

Maiti, A., Brabec, C.J., and Bernholc, J., 1997, Kinetics of metal-catalyzed growth of single-walled carbon nanotubes, *Phys.Rev.* B **55:**R6097-R6100.

Manfrin, R. (1996) On the gevrey regularity for weakly hyperbolic equations with space-time degeneration of oleinik type, *Rendiconti di Matematica* **16:**203-231.

Migdal, A.A., 1975, *Zh.Eksp. Teor. Fiz.* **69:**1457.

Moe, Zugang and Susan B. Sinnott, 2001, *Separation of Organic Molecular Mixtures in Carbon Nanotubes and Bundles: Molecular Dynamics Simulations*, The University of Kentucky, 177 Anderson Hall, Lexington, Kentucky 40506-0046.

Muris, M., Bienfait, M., Zeppenfeld, P., Dupont-Pavlovsky N., Wass, P., Johnsons, M., Vilches, O.E., and Wilson, T., 2001, http://www.ill.fr/AR-01/p-82.htm and references there in

Nosé, S.J., 1984, Constant temperature molecular dynamics methods, *J. Chem. Phys.* **81:**511-519.

Pati, R., Zhang, Y., and Nayak, S., 2002, Effect of H2O adsorption on electron transport in a carbon nanotube, *Appl. Phys. Lett.* **81:**2638-2640.

Perdew, J. and Wang Y., 1992, Accurate and simple analytic representation of the electron-gas correlation energy, *Phys. Rev.* B **45:**13244-13249.

Perdew, J. P., Chevary, J. A., Vosko, S. H., Jackson, K. A. Pederson, M. R., Singh, D. J., and Fiolhais, C., 1992, Atoms, molecules, solids, and surfaces: Applications of generalized gradient approximation for exchange and correlation, *Phys.Rev.* B **46:**6671-6687.

Petrilli, H. M.; Blöchl, P. E.; Blaha, P.; Schwarz, K., 1998, Electric-field-gradient calculations using the projector augmented wave method, *Phys. Rev. B* **57**:14690-14697.

Proykova, A., Pisov, S., Radev, R., Mihailov, P., Daykov, I., and R. S.Berry, 2001, Dynamical Phase Coexistence of Molecular Nano-clusters: Kinetics versus Thermodynamics, in: *Nanoscience&Nanotechnolgy*, E. Balabanova, I. Dragieva, eds., Heron Press Science Series, Sofia, pp.18-20.

Proykova, A., 2002, The role of metastable states in the temperature driven phase changes of molecular nano-clusters*, Vacuum* **68**:97-104.

Proykova, A., Pisov, S., Dragieva, I., and Chelikowski, J., 2003, DFT Calculations of optimized structures of some coordination compounds, in: *Nanoscience&Nanotechnolgy'03*, E. Balabanova, I. Dragieva, eds., Heron Press Science Series, Sofia.

Proykova, A., and Iliev, H., 2004, Simulated stress and stretch of SWCNT, in: *Proceedings of SIMS*, B. Elmegaard, J. Sporring, K. Erleben, K. Sorensen, eds., Copenhagen, pp. 273-279.

Shi, Wei and Johnson, J. Karl, 2003, Gas adsorption on Heterogeneous Single-Walled Carbon Nanotube Bundles, *Phys. Rev. Lett.* **91**:015504/1-4.

Skoulidas, A., Ackerman, D., Johnson, J.K., and Sholl, D., 2002, Rapid transport of gases in carbon nanotubes, *Phys. Rev. Lett.* **89**:185901/1-4.

Spurling, T. H., De Rocco, A. G., and Storvick, T. S., 1968, Intermolecular Forces in Globular Molecules. VI. Octopole Moments of Tetrahedral Molecules, *J. Chem. Phys. J. Chem. Phys.* **48:**1006-1008.

Talapatra, S. and Migone, A.D., 2002, Adsorption of methane on bundles of closed-ended single-wall carbon nanotubes, *Phys. Rev.* B **65:**045416/1-6.

Udomvech, A., Kerdcharoen, T., Osotchan, T., 2005, First principles study of Li and Li+ adsorbed on carbon nanotube: Variation of tubule diameter and length, *Chem. Phys. Lett.* **406:**161-166.

Vassiliev, I., Ogut, S., and Chelikowsky, J. R., 2002, First-principles density-functional calculations for optical spectra of clusters and nanocrystals, *Phys. Rev.* B **65:**115416/1-18.

Venables, John A., 2000, *Introduction to Surface and Thin Film Processes*, Cambridge University Press, Cambridge.

Verlet, L., 1967, Computer "experiments" on classical fluids. I. Thermodynamical properties of Lennard-Jones molecules, *Phys. Rev.* **159:**98-103.

Zhang, Y. and Dai, H., 2000, Formation of metal nanowires on suspended single-wall carbon nanotubes, *Appl. Phys. Let*. **77**:3015-3017.

Zhang, Y., Franklin, N. W., Chen, R. J., and Dai, H., 2000a, Metal coating on suspended carbon nanotubes and its implication to metal-tube interaction, *Chem.Phys. Lett*. **331:**35-41.

FIRST-PRINCIPLES AND MOLECULAR DYNAMICS SIMULATIONS OF METHANE ADSORPTION ON GRAPHENE

EVGENIYA DAYKOVA, STOYAN PISOV, ANA PROYKOVA*
Faculty of Physics, University of Sofia, Sofia, Bulgaria

Abstract. First-principle real-space calculations within a time-dependent local density approximation show fluctuating charge distribution in a methane molecule physisorbed on a finite-size graphene sheet, which in turn bends forming a concave surface under multipole-multipole interaction and the carbon network vibrates in a complex way: a metastable physisorbed state occurs.

Keywords: methane adsorption; graphene; Molecular Dynamics; ab-initio calculation

This paper presents results from first-principles simulations of methane adsorption on graphene. One aim of the study is to quantify the difference in adsorption on a graphene sheet compared to adsorption on carbon nanotubes – perfect and defective. Comparisons show (Stan et al., 1998) a stronger binding of the adsorbate in the tubes than at the planar surface of graphite. Another goal is to find out if the adsorption makes a metastable state.

Methane molecules (tetrahedra) resemble rare gases: CH_4 - CH_4 interaction is classically described with a Lennard-Jones potential, inherent for the noble atoms. Our previous Molecular Dynamics simulations showed that the interaction energy is orientationally dependent (Daykova et al., 2004). The current real-space density functional calculations with the Chelikowski's code (Chelikowski, 2000) and an ultrasoft pseudopotential for carbon atoms generated with the fhi98PP code (Kratzer et al., 1998) do not manifest any dependence of the interaction energy on the CH4 orientation with respect to the initially flat graphene surface: case "F" with 3 bonds closer to the sheet; case "V" with 1 bond. The methane molecule is initially located in either "F" or "V" position above point 0 on the finite piece of a graphene sheet (Fig. 1a). After ~ 30 fs of relaxation, the CH_4 center of mass stabilizes its position above the sheet

*To whom correspondence should be addressed. Dr. Ana Proykova, Department of Atomic Physics, University of Sofia, 5 James Bourchier Blvd, 1164 Sofia, Bulgaria; e-mail: anap@phys.uni-sofia.bg

V.N. Popov and P. Lambin (eds.), Carbon Nanotubes, 209–210.

(Fig. 1b) (the upper curve is for case "F"). The interaction induces a dipole moment in CH_4 (Fig. 1c) that fluctuates with the CH_4 center of mass with a certain delay due to inertia. Larger moment is produced in case "V". The two orientations might be Raman distinguishable. The charge distribution at 20% level of the electron density 60 fs after the run start is presented in Fig. 1d. The preliminary results show that CH_4 behaves differently on a tube.

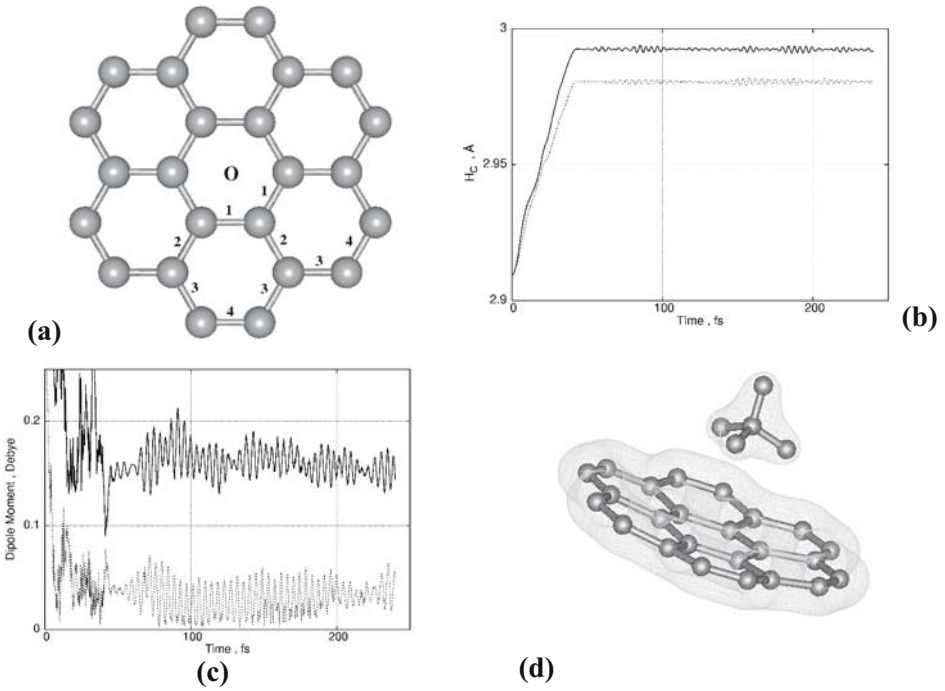

Figure 1. Initial (a) and stabilized (b) position of the CH_4 molecule above the graphene sheet, (c) induced dipole moment of the molecule, and (d) charge distribution of the relaxed configuration.

References

Daykova, E., and Proykova, A., 2004, A peculiar structure of free methane clusters at low temperatures, *Meetings in Physics @ University of Sofia*, **5**:69-75.

Chelikowsky, J. R., 2000, The pseudopotential-density functional method applied to nanostructures, *J. Phys. D: Appl. Phys*. **33**: R33-R50 http://jrc.cems.umn.edu/codes.htm.

Kratzer, P., Morgan, C.G.,Penev, E., Rosa, A.L., Schindlmayr, A.,Wang, L.G.,Zywietz,T.,1998, *Computer code for density-functional theory calculations for poly-atomic systems*, http://www.fhi-berlin.mpg.de/th/fhi98md/fhi98PP/.

Stan, G., and Cole, M. W., 1998, Low Coverage Adsorption in cylindrical pores, *Surf. Sci.* **395**:280.

EFFECT OF SOLVENT AND DISPERSANT ON THE BUNDLE DISSOCIATION OF SINGLE-WALLED CARBON NANOTUBES

SILVIA GIORDANI,* SHANE D. BERGIN, ANNA DRURY, ÉIMHÍN NÍ MHUIRCHEARTAIGH, JONATHAN N. COLEMAN AND WERNER J. BLAU
Molecular Electronics and Nanotechnology Group, Physics Department, Trinity College, Dublin 2, Ireland

Abstract. Single-wall carbon nanotubes (SWNT) are severely restricted in their applications, as they exist in rope-like bundles. Recently, J. Coleman et al. demonstrated a spectroscopic method to monitor bundle dissociation in low concentration NT-polymer composites.[1] In this work we present the results we obtained with 2,5-dioctyloxy-1,4-distyrylbenzene (pDSB), a short-chain analogues of the well known PPV. We found a strong dependence of the concentration at which individual SWNTs become stable with the nature of the solvent.

Keywords: Single-wall carbon nanotubes; dispersion; de-bundling; fluorescence; microscopy

pDSB was synthesised in the house. It is strongly fluorescent, displays minimal self-aggregation and disperses SWNTs in the organic solvents. Stock solutions of pDSB and of SWCNT were made in the different solvents, and were subject to sonication. Two identical solutions of pDSB in each solvent were made and pure HiPCO SWNTs were added to one solution. Each solution was then diluted, serially, on the order of twenty times to give a broad range of CNT concentrations (10^{-2}–10^{-8} kg/m^3). Each solution was sonicated and then allowed to stand for 24 hours to come to equilibrium. No sedimentation was observed over this period. The absorption and emission spectra of each solution were recorded. The addition of the SWNTs to the pDSB results in a visible quenching of the emission, indicating interaction between the two. The molecule exists in two forms, free and bound to the SWNT. The PL efficiency for the bound form is expected to be extremely low as any photo-generated

*To whom correspondence should be addressed. Silvia Giordani, Molecular Electronics and Nanotechnology Group, Physics Department, Trinity College, Dublin 2, Ireland; e-mail: giordans@tcd.ie

V.N. Popov and P. Lambin (eds.), Carbon Nanotubes, 211–212.

singlet excitons preferentially decay non-radiatively through the fast vibrational manifold of the nanotubes. Thus any observed PL from the composite solutions is due to the free form only. For all concentrations, the fraction of free molecule in each solvent was calculated from the PL intensity ratio of composite solution to that of the pure molecule solution. Figure 1 reports the results obtained with pDSB in three different solvents. The solid black lines represent the response of an individual-SWNT system as deduced from Coleman's model, fitted for the results obtained in chloroform and in N-methyl-2-pyrrolidone (NMP). In the case of the chlorinated solvent the experimental data deviates from this curve at SWNT concentrations higher than 1 x 10^{-7} kg/m^3 indicating that bundles occur above this limit. In the case of the amide solvents the response does not deviate from the solid curve, indicating that individual SWNTs or small bundles of SWNTs are present up to the limit of the experiment. Preliminary AFM and TEM results agreed with the spectroscopic results. There is a clear shift in the bundle size distribution, to smaller bundles, in the amide solvent versus the chlorinated solvent. The dominant feature is the presence of small SWNT bundles at relatively high SWNT concentrations in the case of the amide solvent.

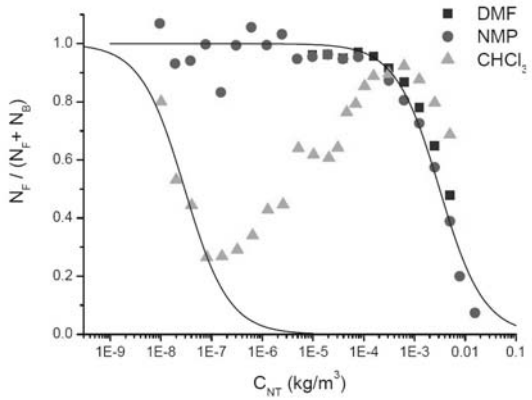

Figure 1. Graph of the fraction of free molecules as a function of concentration for pDSB in the different solvents.

References

1. J. N. Coleman, A. Fleming, S. Maier, S. O'Flaherty, A. Minett, M. S. Ferreira, S. Hutzler, W. J. Blau, Binding Kinetics and SWNT Bundle Dissociation in Low Concentration Polymer – CNT Dispersions, *J. Phys. Chem. B* 108, 3446-3450 (2004).

CARBON NANOTUBES WITH VACANCIES UNDER EXTERNAL MECHANICAL STRESS AND ELECTRIC FIELD

HRISTO ILIEV, ANA PROYKOVA*
Department of Atomic Physics, University of Sofia, Bulgaria
FENG-YIN LI
National Chung Hsing University, Taiwan

Abstract. Reduction of the gap in a (10,0) carbon nanotube with vacancies is obtained with the CASTEP 4.2 code. Molecular Dynamics simulations show that the vacancy distribution is important for the tube stability under stress.

Keywords: carbon nanotubes; defects; vacancies; electronic structure

The regular graphene structure that comprises carbon nanotubes (CNT) determines their extraordinary mechanical and electronic properties. In the presence of defects, the single-wall CNTs are less robust and their band structure can be changed. Understanding the role of the defects on the CNT properties is important for the development of CNT based nanodevices.

The structural defects in CNTs can roughly be divided into topological defects and vacancies. We present a few results from Molecular Dynamics (MD) simulations of CNTs with different distributions and amounts of vacancies under an external load and a result from DFT calculations of the band-structure of a single-wall (10, 0) CNT with ~ 1% vacancies.

Classical MD simulations with a velocity Verlet algorithm for integration of the Newtonian equations of motion were performed to study defective CNTs response to an external field. Details of the simulations were published in the Ref. [1].

The simulations show that vacancies reduce the tensile strength of a SWCNT depending on their distribution and concentration as it is shown in Fig. 1. It might happen that different amounts of vacancies could have the same effect if they are properly distributed.

*To whom correspondence should be addressed. Ana Proykova; e-mail: anap@phys.uni-sofia.bg

V.N. Popov and P. Lambin (eds.), Carbon Nanotubes, 213–214.

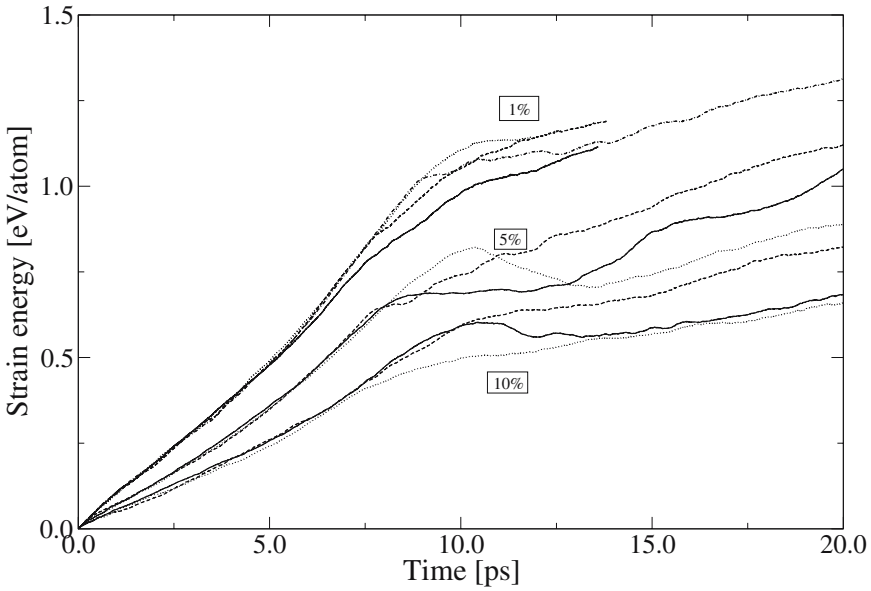

Figure 1. The strain energy per atom in a (10,0) SWCNT with 2000 atoms and various defect concentrations (1%, 5% and 10%). For every concentration we present several curves corresponding to different defect distributions generated randomly.

We have also demonstrated with DFT calculations (CASTEP code) that a zigzag (10,0) SWNT with a mono-vacancy defect responds quite differently to a transverse electric field applied in different directions. The defect site of the defective nanotube provides a conducting band minimum with a lower energy (0.19 eV) than in the corresponding perfect nanotube (0.4 eV). Our results indicate that the band gap can be modulated by rotating a SWNT with a mono-vacancy defect under a transverse electric field. Upon application of a strong electric field, the band gap becomes similar to that found in the corresponding perfect nanotubes. This also provides some flexibility to select a suitable band gap for some specific applications because the band gap can increase or decrease depending on the direction and strength of the transverse electric field.

References

1. Hristo Iliev and Ana Proykova, Mechanically induced defects in single-wall carbon nanotubes, in: *Meetings in Physics @ University of Sofia*, edited by A. Proykova, vol. 5 (Heron Press, Sofia, 2004) pp. 87-91.

Part V. Mechanical properties of nanotubes and composite materials

MECHANICAL PROPERTIES OF THREE-TERMINAL NANOTUBE JUNCTION DETERMINED FROM COMPUTER SIMULATIONS

ELENA BELOVA,* LEONID A. CHERNOZATONSKII
Institute of Biochemical Physics of RAS, Kosygin St. 4, 119991 Moscow, Russia

Abstract. The mechanical properties of a three-terminal nanotube "bough" junction are described. Interatomic Tersoff-Brenner potential and intermolecular Lennard-Jones potential were used to obtain the strain energy of the "bough" junction upon loading the "branch". At small strain, the energy increases quadratically with the strain and the "branch" reverts to its initial position without external force. For strains higher than the critical one, the junction falls to a metastable state “branch stuck to stem".

Keywords: Nanotube junctions; Mechanical properties; Molecular dynamics simulations; Tersoff-Brenner potential

In this paper, the mechanical characteristics of a three-terminal (19,0)&(9,9) nanotube junction (Fig. 1a) are considered. This nanotube "bough" (B) junction[1,2] consists of a "stem" nanotube with a "branch". The connection of two nanotubes is formed by defects (6 heptagons) introduced into the perfect hexagonal nanotube lattice. The topological defects create an angle of ~30° between the "stem" and the "branch".

The atomic interactions were modeled by the Tersoff-Brenner potential[3] and the "stem"-"branch" nanotube interaction was described by a Lennard-Jones potential.[4] The compression strain was created by a graphene plane parallel to the "stem" axis. The plane was shifted towards the "branch" by small steps and the junction was relaxed by a conjugate-gradient method keeping the "stem" ends constrained. The strain ε was defined as $\varepsilon = (r_0 - r)/r_0$, where r_0 is the "stem"-"branch" distance in initial state and r is the distance for "branch" under loading. The strain energy of this B-junction for different strains was obtained.

At strains $\varepsilon < 0.5$, the strain energy of junction increases as $E(\varepsilon) = ½\ E''\varepsilon^2$, where E'' = 17 eV (Fig. 1c). In this case, the B-junction is similar to a spring.

*To whom correspondence should be addressed. Elena Belova, Institute of Biochemical Physics of RAS, Kosygin St. 4, 119991 Moscow, Russia; e-mail: elenamih@mail.ru

V.N. Popov and P. Lambin (eds.), Carbon Nanotubes, 215–216.

The "branch" returns to its initial position after removal of the plane. If the strain is more than critical value $\varepsilon_{cr} \sim 0.75$, the B-junction converts to a new metastable state "branch stuck to stem" (Fig. 1b). In this state, the "branch" remains parallel to the "stem" by van der Waals interactions. The distance between the "stem" and the "branch" is equal to the interlayer graphite distance at normal conditions of 0.34 nm. This new junction state is steady up to 2000 K heating with the "branch" oscillating near equilibrium position but not returning to the initial position.

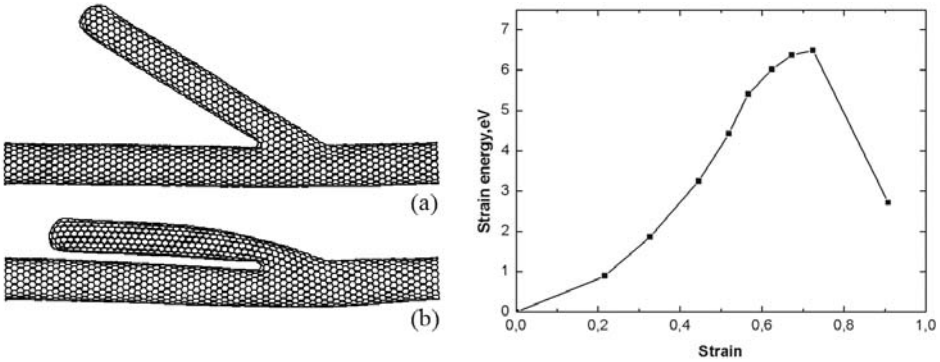

Figure 1. A (19,0)&(9,9) B-junction in (a) initial state and (b) "branch stuck to stem" state. (c) Strain energy vs. strain for the B-junction.

In summary, our simulations show two possible types of behavior of three-terminal nanotube "bough"-junction under compression strain. In the case of a small strain, this junction can be used as a "nanospring". However, we must take into account molecular effects appearing for atomic-scale objects, e. g., the effect of "branch stuck to stem" in the nanotube B-junction.

This work is supported by the Russian Foundation for Fundamental Investigation (grants № 05-02-17443).

References

1. N. Gothard, C. Daraio, J. Gaillard, R. Zidan, S. Jin, and A. M. Rao, Controlled growth of Y-junction nanotubes using Ti-doped vapor catalyst, *Nano Lett.* 4, 213-217 (2004).
2. L. A. Chernozatonskii, Three-terminal junctions of carbon nanotubes: structures, properties and applications, *J. Nanoparticle Res.* 5, 473-484 (2003).
3. D. W. Brenner, Empirical potential for hydrocarbons for use deposition of diamond films, *Phys. Rev. B* 42, 9458-9471 (1990).
4. S. B. Sinnott, O. A. Shenderova, C. T. White, and D. W. Brenner, Mechanical properties of nanotubule fibers and composites determined from theoretical calculations and simulations, *Carbon* 36, 1-9 (1998).

OSCILLATION OF THE CHARGED DOUBLEWALL CARBON NANOTUBE

VICTOR LYKAH
Dept. of Physics and Technology, National Technical University "Kharkiv Polytechnic Institute", Kharkiv 61002, Ukraine

EVGEN S. SYRKIN*
B. I. Verkin Institute for Low Temperature and Engineering, Nat'l Academy of Sciences of Ukraine, Kharkov 61103, Ukraine

Abstract. The oscillation frequency of charged doublewall semiconducting carbon nanotubes (DWCNTs) is found as function of the nanotube mass and geometry. The linear and nonlinear oscillations are analyzed.

Keywords: carbon nanotube; electronanomechanics; oscillation

Recent experiments in nanomechanic oscillations of the multiwall carbon nanotubes[1,2] open perspectives in the Gigahertz range. The single molecule C_{60} transistor shows electromechanic oscillations.[3]

In this report, we consider the mechanical telescope oscillations of a DWCNT due to a charge (electron or hole) on it. The energy of the system is the sum of the Van der Waals interaction energy between the nanotubes (averaged and smoothened[3]) and the energy of the extra carrier interaction with the nanotube. For the nonresonant nanotube lengths, the ponderomotive electrostatic attractive forces give the main contribution to the potential of the oscillations of the DWCNT. The system geometry is illustrated in Fig. 1, when the length $2l$ of the external short tube is longer than the resonance one and a hole is localized on the external shorter tube. An electron is localized in the space between two tubes where the potential well is about 1 eV (Ref. [4]).

The electrostatic energy of CNT is $W_{NT} = (1/2)\int \varepsilon(r)\varepsilon_0 dV$, where $\varepsilon(r)\varepsilon_0$ is the tube electric permeability. For small shift ξ of the short tube and for $l, \xi << L$, the nonlinear oscillation equation for the tube due to charge q is found as

*To whom correspondence should be addressed: Evgen Syrkin; e-mail: syrkin@ilt.kharkov.ua

V.N. Popov and P. Lambin (eds.), Carbon Nanotubes, 217–218.

$$M\ddot{\xi} + \frac{q^2 S}{32\pi^2 \varepsilon_0}(1-\frac{1}{\varepsilon})[\frac{1}{(L-\xi)^4} - \frac{1}{(L+\xi)^4}] = 0$$

Here M is the oscillating tube mass, S is the longer tube cross-sectional area. The expansion in series leads to the oscillation equation $\ddot{\xi} + \omega_0^2 \xi[1+\xi^2/L^2] = 0$.

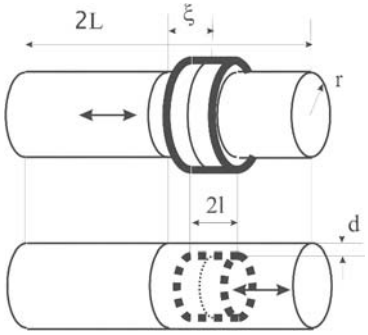

Figure 1 DWCNT geometry. The long (short) CNT has length 2*L* (2*l*). The distance between the middles of the tubes is *ξ*. The arrows show the direction of the telescopic oscillation. The shorter CNT can be external (for holes and electrons) or internal (only for electrons).[1,2]

The frequency ω_0 of DWCNT oscillation is a function of tube parameters $\omega_{0L}^2 \cong \left(q^2/4\pi^2\varepsilon_0\rho\right)(1-1/\varepsilon)(1/L^6)$ and $\omega_{0S}^2 \cong \omega_{0L}^2(N_L/N_S)$. Here $L(S)$ is for moving long (short) tube; $M \cong 2\pi rLd\rho$, $S \cong 2\pi rd$ is used. $\rho \cong m_0/da^2$ is the mass density. m_0 and a are carbon atom mass and the C-C bond length. $N_L \sim r_L L$ ($N_S \sim r_S l$) is number of atoms in the tube. The evaluation yields $\omega_{0L} \sim 10^8 \div 10^{11}$ rad/s for $\varepsilon \cong 6$, $L \sim 10 \div 100$ Å. The moving short tube can have considerably higher frequencies because $N_L >> N_S$. For relatively larger amplitudes, the nonlinearity gives rise to higher stiffness: $\omega^2 = \omega_0^2(1+\xi^2/L^2)$.

The considered setup differs qualitatively from Refs. [1,2] where pure mechanical tube oscillations need large amplitude and extruding of tube core.

References

1. S. B. Legoas, V. R. Coluci1, S. F. Braga, P. Z. Coura, S. O. Dantas, and D. S. Galvao, Molecular Dynamics Simulations of Carbon Nanotubes as Gigahertz Oscillators. Phys. Rev. Lett. 90, 055504, 2003.
2. Q. Zheng, J. Z. Liu, Q. Jiang. Excess van der Waals interaction energy of a multiwalled CNT with an extruded core and the induced core oscillation. Phys. Rev. B 65, 245409, 2002.
3. H. Park, J. Park, A. K. L. Lim, E. H. Anderson, A. P. Alivisatos, Paul L. McEuen. Nanomechanical oscillations in a single-C60 transistor. Nature 407, 57, 2000.
4. C. L. Kane, E. J. Mele, and A. T. Johnson. Theory of scanning tunneling spectroscopy of fullerene peapods. Phys. Rev. B 66, 235423, 2002.

POLYMER CHAINS BEHAVIOR IN NANOTUBES: A MONTE CARLO STUDY

K. AVRAMOVA,* A. MILCHEV
Institute for Physical Chemistry, Bulgarian Academy of Sciences, 1113 Sofia, Bulgaria

Abstract. We study the equilibrium properties of flexible polymer chains confined in a *soft* tube by means of extensive Monte Carlo simulations.

Keywords: Monte Carlo computer simulations; polymer chains; elastic nanotubes; scaling; chain dynamics

The confinement of polymers in cylindrical tubes has attracted considerable attention by researchers during the last two decades in view of the broad class of applications such as protein transport through channels in membranes, etc. However, the behavior of linear polymers under conditions of geometric constraints is also a challenge for the basic research.

We used an off-lattice bead-spring model for the Monte-Carlo (MC) simulations with periodic boundary conditions in a box of size 128x128x128. The linear polymer chain consists of N = 32 to 256 effective monomers in a hexagonal-coordinated tube with 246 stacked rings in the box with D_{id} = 3.08 to 10.9 in units of the maximum bond length (Fig. 1).

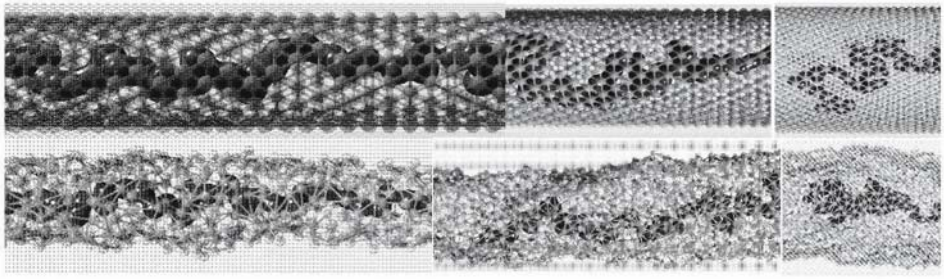

Figure 1. Snapshots of a polymer chain of length N = 128 in a tube of diameter D_{id} = 3.08, 6.12, and 10.9 (from left to right) with hard (above) and soft (below) walls.

*To whom correspondence should be addressed. Kati Avramova, Institute for Physical Chemistry, Bulgarian Academy of Sciences, 1113 Sofia, Bulgaria; e-mail: kati@ipc.bas.bg

V.N. Popov and P. Lambin (eds.), Carbon Nanotubes, 219–220.

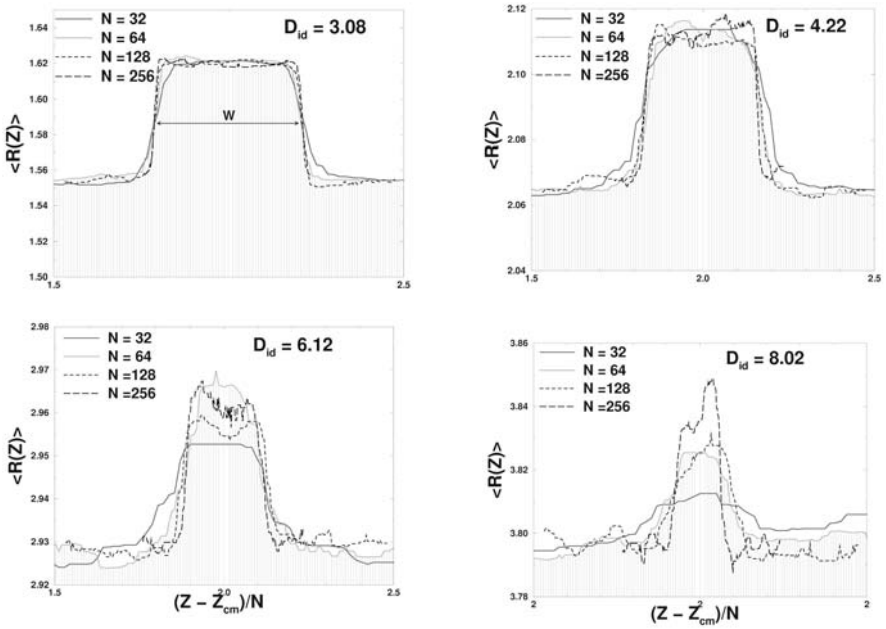

Figure 2. Profiles of the swollen region of the soft tube with radius $R(Z)$ containing polymer chains of different length N = 32, 64, 128, and 256 along the tube axis Z. The four graphs correspond to four different diameters D_{id} of unperturbed tubes containing no polymer.

Figure 2 shows a side view of the tube wall deformation in the vicinity of the enclosed polymer chain centered at the center of mass of the chain whereby the z axis is scaled proportionally to the number of monomers N in the polymer. Four tube diameters D_{id} and data for chains with $32 < N < 256$ are displayed. A good collapse of all curves on a cigar-like master profile of width $W \propto N$ is observed. The sides of the bulge are almost perpendicular to the tube axis whereas its plateau is almost independent of N, at least for the narrow tubes, $D_0/R_g << 1$, R_g being the gyration radius of the chain. The deformation of the walls in the vicinity of the bulge is negligible. Thus it appears that the observed cigar-like shape of the wall deformation around the polymer chain agrees with our theoretic conclusions that the free energy cost for a cylindrically shaped deformation of the soft tube will always be lower than that for a globular deformation provided the number of repeat units N is large enough: $F_{cyl}^{eq} \propto NkT(kb^2)^{2/5}$ and $F_{glob}^{eq} \propto v^{2/5}(kb^2)^{3/5}N^{18/15}$.

The polymer chain performs reptational movement along the tube with relaxation time $\tau \propto N^3$ and diffusion coefficient $D_{diff} \propto 1/N$. The chains diffuse more slowly in a soft tube than in a hard one since they are coupled to a local deformation of the tube wall.

CARBON NANOTUBES AS CERAMIC MATRIX REINFORCEMENTS

CSABA BALÁZSI, FERENC WÉBER, ZSUZSANNA KÖVÉR, PÉTER ARATO
Ceramics and Composites Laboratory, Research Institute for Technical Physics and Materials Science, Hungary, H-1525 Budapest, P.O. Box 49

ZSOLT CZIGÁNY
Thin Film Physics Laboratory, Research Institute for Technical Physics and Materials Science, Budapest, Hungary

ZOLTÁN KÓNYA, IMRE KIRICSI
Department of Applied and Environmental Chemistry, University of Szeged, Hungary

ZSOLT KASZTOVSZKY
Department of Nuclear Research, Institute of Isotope and Surface Chemistry, Chemical Research Center, Budapest, Hungary

ZOFIA VÉRTESY, LÁSZLÓ PÉTER BIRÓ
Laboratory for Nanostructures Research, Research Institute for Technical Physics and Materials Science, Budapest, Hungary

Abstract. Silicon nitride based composites with different amount (1, 3 and 5 wt%) of carbon nanotubes have been prepared. Optimization of the manufacturing processes has been conducted to preserve the carbon nanotubes in composites and to avoid damaging during high temperature processing. The first results show that carbon nanotubes have a good contact to the surface of silicon nitride grains. Moreover, carbon nanotubes may serve as crystallization sites and seeds for silicon nitride grain growth. With increasing the carbon nanotube content a lower densification rate was obtained together with the deterioration of the mechanical characteristics of composites. In the case of 1wt% and 3 wt% carbon nanotube addition, the increase of gas pressure resulted in increase of bending strength.

*To whom correspondence should be addressed. Csaba Balazsi, Ceramics and Composites Laboratory, Research Institute for Technical Physics and Materials Science, Hungary, H-1525 Budapest, P.O. Box 49; e-mail: balazsi@mfa.kfki.hu

V.N. Popov and P. Lambin (eds.), Carbon Nanotubes, 221–222.

Keywords: carbon nanotubes; ceramic matrix composites; silicon nitride; mechanical properties

This study is focusing on the exploration of new preparation processes for tailoring the microstructure of carbon nanotube (CNT) reinforced silicon nitride-based ceramic composites. Because CNTs present exceptional mechanical, thermal and electrical properties, it is expected that the addition of CNTs will radically improve the quality of ceramic matrix composites. In order to get the full use of the benefits provided by CNTs it is crucial to retain CNT un-attacked in the composites and to optimize the interfacial bonding between CNT and matrix.

The preparation of composites is described in details elsewhere.[1] The fracture surfaces of HIP samples are presented in Fig. 1. As can be observed, well-developed β-Si_3N_4 grains with length 1-3 μm evolved during the hot isostatic pressing. Incorporated CNTs in the middle of the silicon nitride grains, evidently serving as seeds for crystal growth, can also be observed. As can be seen in Fig. 1, higher strength values were achieved by increasing the pressure from 2 MPa to 20 MPa.

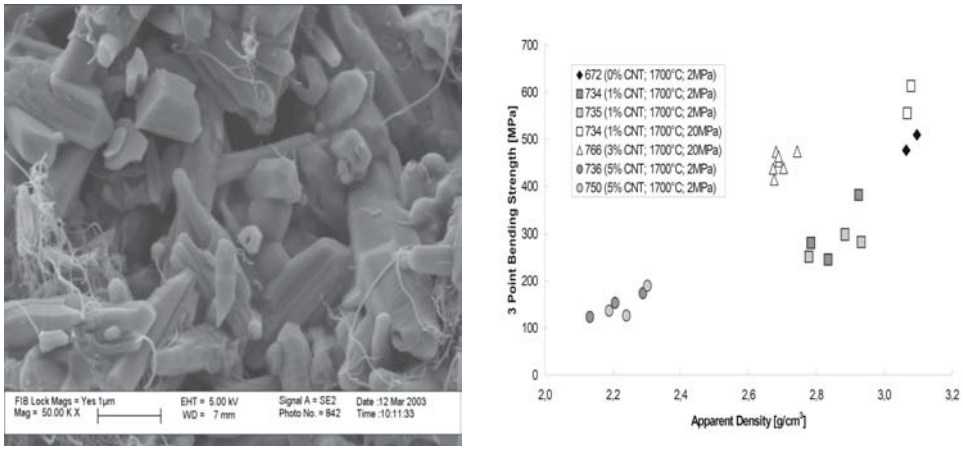

Figure 1. Fracture surface of a composite (left) and three point bending strength of composites in function of apparent density (right).

References

1. Cs. Balázsi, Z. Kónya, F. Wéber, L. P. Biró, P. Arató, Preparation and characterization of carbon nanotube reinforced silicon nitride composites, *Mat. Sci. Eng. C* 23(6-8), 1133-1137 (2003).

CARBON NANOTUBES AS POLYMER BUILDING BLOCKS

FIONA M. BLIGHE, MANUEL RUETHER, RORY LEAHY, WERNER J. BLAU
Molecular Electronics and Nanotechnology Group, Physics Department, Trinity College, Dublin 2, Ireland

Abstract. Carbon Nanotubes were successfully functionalised with different chemical groups, which allowed them to act as an initiator for the polymerisation reaction of a Bisphenol A epoxy resin. Functionalised with traditional amino hardeners they became the "building blocks" for the amino cured epoxy.

Keywords: Carbon Nanaotube; Functionalisation; Composite; Epoxy

Through previous research carbon nanotubes have been found to have several properties that make them potentially useful in extremely small scale electronics and mechanical applications.[1,2] However, after over a decade of research the full potential of CNT incorporation within polymer systems has not been fully realized. Insufficient dispersion is often cited as a process limitation and the key diminishing factor of the composites mechanical properties.[3,4,5] Chemical fictionalization is an attractive option when tying to disperse nanotubes as it can improve solubility and processibility, while allowing the unique properties of the CNTs to be coupled to those of other materials.[6]

MWNT-COOH were reacted with $SOCl_2$ in the presence of DMF under reflux for 24hrs to form -COCl side groups.[7] The functional groups were then modified with three different amino hardeners NH_2-A/B/C-NH_2 (HA/HB/HC) to produce tubes functionalised with longer groups with amino ends to cure the epoxy. The amino hardener functionalized Carbon Nanotube/Epoxy composite material softens at around 80^{o}C but is hard at room temperature, suggesting that it is partially cured. The use of an additional hardener (which was added after 12 hours to allow the tubes and the epoxy time to interact) is necessary to fully cure the epoxy resin. The fully cured composites show improved mechanical performances double that of the pure epoxy (Fig.1, left). The glass transition

*To whom correspondence should be addressed. Fiona Blighe, Molecular Electronics and Nanotechnology Group, Physics Department, Trinity College, Dublin 2, Ireland; e-mail: fblighe@tcd.ie.

V.N. Popov and P. Lambin (eds.), Carbon Nanotubes, 223–224.

temperature was seen to stabilize and shows an increase rather than the more usual decrease on the addition of the functionalized CNTs (Fig.1, right). A general increase in the decomposition temperature of the composites gives further evidence of the NTs behaving as covalently bonded "building blocks". A comparison study of composites prepared without the 12 hour gap before hardener addition is being undertaken at present. SEM pictures indicate a system in which the NTs are properly wet by the polymer and fully incorporated into the matrix, contrasting with those of the one-step composites that show protruding bundles of nanotubes.

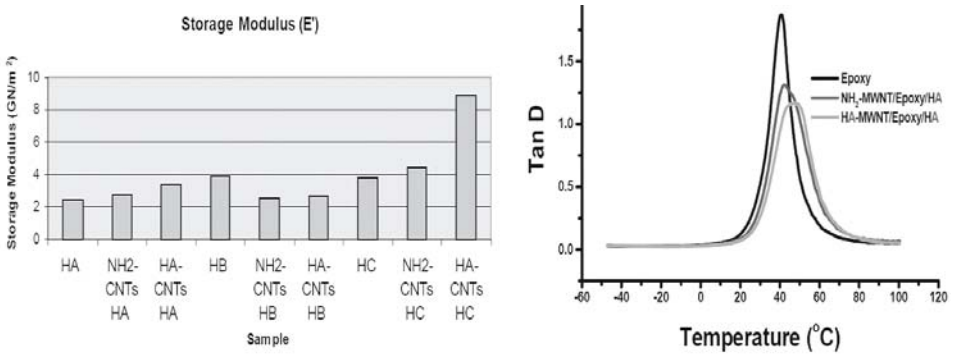

Figure 1. Left: Storage Moduli of Composites. Right: Shift in Glass Transition Temperature of Composites (tan δ; from DMA measurements).

References

1. V. N. Popov, Carbon Nanotubes: Properties and Applications, *Materials Science and Engineering R* 43, 61-102 (2004).
2. R. H. Baughman, A. A. Zakhidov, and W. A. de Heer, Carbon nanotubes—the route toward applications, *Science* 297, 787-792 (2002).
3. R. Andrews and M. C. Weisenberger, Carbon nanotube polymer composites, *Current Opinion in Solid State and Material Science* 8, 31-37 (2004).
4. Y. S. Song and J. R. Youn, Influence of dispersion states of carbon nanotubes in the nanocomposites, *Carbon* 43, 1378-1385 (2005).
5. A. Star, J. F. Stoddart, D. Steuerman, M. Diehl, A. Boukai, E. W. Wong, X. Yang, S. W. Chung, H. Choi, and J. R. Heath, Preparation and properties of polymer-wrapped single-walled carbon nanotubes, Angew. Chem. Int. Ed. 40(9), 1721-1725 (2001).
6. J. Liu, A. G. Rinzler, H. Dai, J. H. Hafner, R. K. Bradley, P. J. Boul, A. Lu, T. Iverson, K. Shelimov, C. B. Huffman, F. Rodriguez-Macias, Y.-S. Shon and T. R. Lee, D. T. Colbert, R. E. Smalley, Fullerene Pipes, *Science* 280, 1253-1256 (1998).
7. J. Chen, M. A. Hamon, H. Hu, Y. Chen, A. M. Rao, P. C. Eklund, and R. C. Haddon, Solution Properties of Single-Walled Carbon Nanotubes, *Science* 282, 95-98 (1998).

SYNTHESIS AND CHARACTERIZATION OF EPOXY-SINGLE-WALL CARBON NANOTUBE COMPOSITES

DANIEL VRBANIC,* MARJAN MARINSEK, STANE PEJOVNIK
Faculty of Chemistry and Chemical Technology, University of Ljubljana, Askerceva 5, Ljubljana, Slovenia

ALOJZ ANZLOVAR
National Institute of Chemistry, Hajdrihova 19, Ljubljana, Slovenia

POLONA UMEK, DRAGAN MIHAILOVIC
Jozef Stefan Institute, Jamova 39, Ljubljana, Slovenia

Abstract. We present a study on the composite of 1 wt% single-wall carbon nanotubes (SWNTs) in epoxy resin. Composites were prepared by solution mixing of epoxy resin XY 444 (Vantico), polyamine hardener XV 279 (Vantico) and single-wall carbon nanotubes (SWNTs), as a thin film. We observed that addition of surfactant together with sonification were necessary in order to obtain more uniform composite. We used several techniques to investigate the nanocomposite material, such as scanning electron microscopy (SEM) and differential scanning calorimetry (DSC). The observed changes of the glass transition temperature (T_g) and electron micrographs indicate that the compatibility and interfacial adhesion between the nanotubes and epoxy resin are poor.

Keywords: carbon nanotubes; epoxy resin; composite

The purification of SWNTs prepared by the arc-discharge method is needed to enable detailed characterization and applications of the material. Therefore, we purified the SWNTs by seven-step process using chemical (solvents, acids) and physical (sonication, filtration) treatment as described elsewhere.[1] The composites were carefully prepared in the form of thin films (thickness 0.08 - 0.1 mm). We focused on composites with low loading of nanotubes (1 wt%) in

*To whom correspondence should be addressed. Daniel Vrbanic; e-mail: daniel.vrbanic@fkkt.uni-lj.si

V.N. Popov and P. Lambin (eds.), Carbon Nanotubes, 225–226.

order to study well-dispersed tubes in the matrix. We used a non-ionic surfactant (polyoxyethylene 23 lauryl ether) to improve the compatibility of the nanotubes and the epoxy and to enhance the interfacial adhesion. The addition of surfactant decreases the T_g and the storage modulus. This was expected because of the surfactant function as a plasticizer. The most likely role of the surfactant is to function as a dispersing agent. Naturally, the addition of the surfactant also has an effect on the wetting behavior and on the interfacial adhesion (samples SC3 to SC5). In Table 1, glass transition temperatures and mechanical properties of epoxy composites are summarized.

Table 1. Glass transition temperatures (T_g) and mechanical properties of different types of SWNTs-epoxy composites.

Sample	T_g (℃)	Tensile strength (MPa)	Young's modulus (MPa)
pristine epoxy	98.8	45.4	9.51
epoxy+SWNTs	105.6	35.6	8.26
SC3	85.6	43.2	9.63
SC4	83.1	46.3	9.35
SC5	80.0	45.6	9.50

SC4- supernatant of the suspension in acetone sonicated for 24 hours and centrifugated 2 times at 2000 rotations per minute for 15 min

SC5- precipitate of the suspension in acetone sonicated for 24 hours and centrifugated 2 times at 2000 rotations per minute for 15 min

The changes of T_g and the mechanical properties indicated that the compatibility and interfacial adhesion between nanotubes and epoxy resin were poor. The addition of non-ionic surfactant, solvent (acetone) and sonication helped in the dispersion of the SWNTs. The tensile strength and Young's modulus of the composites are in most cases reduced compared to those of pure epoxy resin. There are no breaks of nanotubes, which indicate that the load transfer from polymer to nanotube was not sufficient to fracture the nanotubes. Modification of nanotube is therefore necessary to improve the connection between the polymer and the nanotubes.

References

1. P. Umek, D. Vrbanic, M. Remskar, T. Mertelj, P. Venturini, S. Pejovnik, and D. Mihailovic, An effective surfactant-free isolation procedure for single-wall carbon nanotubes, *Carbon* 40, 2581-2585 (2002).

VAPOUR GROWN CARBON NANO-FIBERS – POLYPROPYLENE COMPOSITES AND THEIR PROPERTIES

V. CHIRILA,* G. MARGINEAN, W. BRANDL
University of Applied Sciences Gelsenkirchen, Department of Materials Science, Neidenburger Str. 10, 45877 Gelsenkirchen, Germany

T. ICLANZAN
University "Politehnica" Timisoara, Faculty of Mechanical Engineering, Blv. Mihai Viteazu 1, 300222 Timisoara, Romania

Abstract. The influence of the oxygen chemical plasma treatment parameters on the water contact angle and surface energy of vapor grown carbon nanofibers (VGCFs) was studied. Tensile properties of the composites containing untreated and plasma treated fibers were measured.

Keywords: Vapour Grown Carbon Nanofibers; Wettability; Tensile Properties

In order to modify the relatively weak mechanical properties of polymer materials carbon fibers are very commonly used as reinforcement for an effective improvement of the mechanical properties[1].

In the present work the wettability and surface energy of carbon nanofibers before and after an oxygen plasma treatment as well as the composite morphology were characterized and the mechanical properties of the composites were measured.

Polypropylene powder from Sabic Polyolefine GmbH and VGCFs (GANF – commercial fibers) from Grupo Antolin Ingeniria S.A, Spain, with diameters 50-150μm and length less than 80 μm were used. The morphology of the composites was studied by scanning electron microscopy. The oxygen plasma treatment was carried out in a plasma reactor equipped with a microwave generator. Three types of composites were manufactured: PP+5wt.% VGCFs as grown and plasma treated and PP+10wt.% VGCFs as grown. Fig. 1 shows the water contact angle (a) and surface energy (b) of the carbon fibers after oxygen

*V. Chirila, University of Applied Sciences Gelsenkirchen, Department of Materials Science, Neidenburger Str. 10, 45877 Gelsenkirchen, Germany; e-mail: valentin_chirila@yahoo.com

V.N. Popov and P. Lambin (eds.), Carbon Nanotubes, 227–228.

plasma treatment as a function of the plasma treatment parameters. Whereas the composites manufactured with plasma treated fibers show a good adhesion between fibers and polypropylene, Fig. 2a, the occurrence of fiber pullout, Fig. 2b, indicates a weak adhesion between untreated VGCFs and PP matrix. The tensile properties of composites are presented in Fig. 3. The composite with 5 wt.% treated fibers has a higher tensile strength than composites containing 5 or even 10 wt.% untreated fibers.

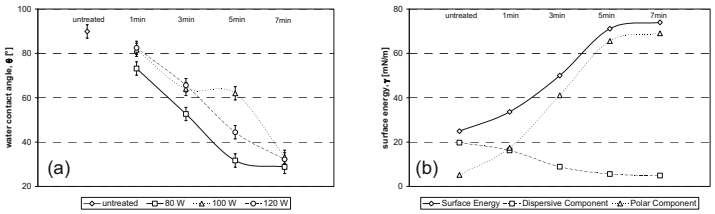

Figure 1. Water contact angle (a) and surface energy (b) as a function of plasma parameters.

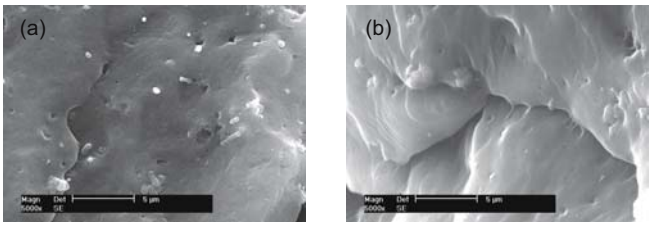

Figure 2. SEM micrographs of the PP containing 5 wt.% untreated (a) and plasma treated (b) fibers.

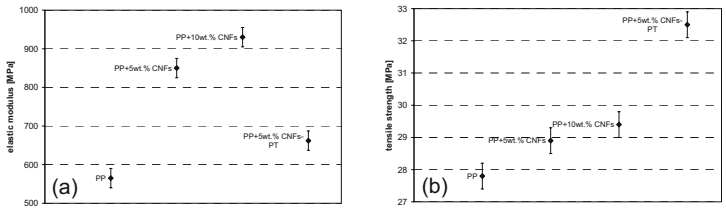

Figure 3. Elastic modulus (a) and tensile strength (b) of the obtained composites.

References

1. A. R. Bhattacharyya, T. V. Sreekumar, T. Liu, S. Kumar, L. M. Ericson, R. H. Hauge, and R. E. Smalley, Crystallization and orientation studies in polypropylene/single wall carbon nanotube composite, *Polymer* 44, 2373–2377 (2003).

Part VI. Applications

NANOTECHNOLOGY: CHALLENGES OF CONVERGENCE, HETEROGENEITY AND HIERARCHICAL INTEGRATION

A. VASEASHTA
Nanomaterials Processing & Characterization Laboratories
Marshall University, Huntington, WV 25755- 2570, USA

Abstract. The purpose of this investigation is to accentuate the global impact of nanotechnology which encompasses convergence of disciplines, heterogeneity in synthesis routes, metrology, and applications, and pose hierarchical challenges. A global perspective to develop a seamless integration in advancing the field of nanotechnology beyond its fundamental limit is presented.

Keywords: nanotechnology; convergence; heterogeneity; hierarchical integration

The dimensionality of a system has a profound influence on its physical behavior. Recent progress in synthesis and characterization of nanostructured materials and continuously emerging nanotechnologies have demonstrated tremendous potential for development of new materials, devices and sensor designs with unique capabilities. Nanostructures exhibit unique properties and morphological flexibility, which renders them inherently multifunctional and compatible with organic and inorganic systems. An increased awareness of the potential for inadvertent or deliberate contamination of the environment, food, and agricultural products has made distributed sensing a research priority for several federal agencies. Efficiencies in acquiring research results calls for decentralized laboratory facilities and conducting clinical trials employing direct reading, portable, lab-on-chip systems. Recent progress in nanostructured materials and wireless sensors have significantly impacted data collection, processing, and recognition allowing direct detection of chemical-biological agents in a label-free, highly multiplexed format over a broad dynamic range.

Nanotechnology deploys convergence of several disciplines, rendering it of paramount importance that the scientific community identifies critical barriers and research needs, and to facilitate dynamic and valuable collaborations. Increased funding in nanotechnology initiatives indicates high priority on a

*To whom correspondence should be addressed. Prof. A. Vaseashta, Nanomaterials Proc. & Charact. Lab., Marshall University, Huntington, WV 25755-2570, USA, e-mail: vaseashta@marshall.edu

V.N. Popov and P. Lambin (eds.), Carbon Nanotubes, 229–230.

global basis. Scientific breakthroughs in fields ranging from agriculture, medicine, defense to national security, are envisaged employing nanostructured materials that can be designed to suit specific applications. Its potential in education and training is becoming a key component of the long-term objective of nanotechnology initiatives worldwide. Partnerships are continuously being formed because of the diversity of this area and the need for multi disciplinary research by focus interest groups. The growing pace of nanotechnology has further prompted several agencies worldwide to develop a unified nomenclature and standards that address materials, devices and system level interoperability.

The development of synthesis routes are goals of current nanotechnology initiatives.[1] Structures, devices, and systems employing nanoelements face challenges in integration, interoperability, standardization, design, verification, and failure analysis. Successful implementation requires precise control of growth at desired sites with desired size, structure, doping, orientation, and formation of reliable contacts. The capability to examine single-molecule properties offers new insight into electro-optical and biological systems. Furthermore, platforms that are designed to detect molecular binding with exquisite sensitivity and selectivity without the need for chemical labels, amplification or complex sample preparation must also be capable of detecting a broad range of single molecules such DNA, RNA, proteins, ions, small molecules, cells and pH values, while being multiplexable enough to allow for the parallel detection of multiple agents. Recent efforts to develop NRAM, flat panel displays, cold cathode X-ray sources, and distributed sensor networks herald distinct potential for the technology, however major developments are needed before these discrete systems are integrated with the process flow, ASICs, or instrumentation. Although nanotechnology offers ultra-low power consumption capability for sensors (motes), system-level integration, hardware reconfiguration, and sensor-network infrastructures pose challenges. Promising nano-biological initiatives such as functionalized nanoparticles within therapeutic templates and communication mechanisms for the central nervous systems is an example of one nanotechnology application that has triggered social concern regarding adverse affects of nanotechnologies thus warranting government based studying of societal implications.

References

1. A. Vaseashta, in: Nanostructured and Advanced Materials, for Applications in Sensor, Optoelectronic and Photovoltaic Technology, edited by A. Vaseashta, D. Dimova-Malinovska, and J. M. Marshall (Springer, Dordrecht, 2005), pp. 424.

BEHAVIOR OF CARBON NANOTUBES IN BIOLOGICAL SYSTEMS

DMYTRO G. KOLOMIYETS
Faculty of Radiophysics, National Taras Shevchenko University of Kiev, 64, Vladimirskaya str., Kiev, 01033, Ukraine

Abstract. Our main subject is CNTs and their interaction with DNA biomolecular gel. The electronic properties and vibration modes of CNT and DNA/CNT systems were investigated by TEM and Raman spectroscopy. From the UV-VIS-NIR absorption spectra the principal electronic absorption bands have been estimated. The effect of DNA is revealed by the existence of the 2.5-3eV and 2 eV bands and shifting of the minima at 2.96 eV, 3.05, 3.34 eV. Using these results, we assert that a system of electronic levels is self-formed at the DNA/CNT interface. The structure of the CNT/DNA blocks is reviewed.

Keywords: carbon nanotubes; DNA; interaction

The technological development allows scientists to use self-assembly techniques to develop nanoscale structures with specific dimensions and chemical properties.[1]

The first technique is implementing DNA-nanotube hybrids as architectural elements, using the chemical selectivity of DNA to control the assembly of nanotubes, nanowires, and other nano-objects.[2] The immobilization of DNA, proteins and enzymes onto CNT, the helical crystallization and the interaction of proteins with CNT may be used for development of new biosensors.

For the application of MWCNT in biomedical systems and to construct simple logic circuits, it is necessary to create their layers. These layers have been created by DNA technology on Au and Si substrates. For the experiment we used MWCNT/(Si or Au) and MWCNT/DNA structures.

Investigation of the Stokes, anti-Stokes processes, D- and G- bands by Raman spectroscopy (1000-2000 cm^{-1}) was carried out. The results show that intensity of the G-band does not depend on the substrate, but the intensity of the D-band shows some dependence on the substrate. The additional bands at 1094, 1216, 1777 cm^{-1} were observed on (MWCNT+DNA)/Au layers.

*To whom correspondence should be addressed. Dmytro G. Kolomiyets; e-mail: dimako@ipnet.kiev.ua

V.N. Popov and P. Lambin (eds.), Carbon Nanotubes, 231–232.

In the experimental IR-spectra, the vibration modes at 360, 450, 650, 864, 1231, 1400, 1444, 1575 cm^{-1}, which were theoretically predicted for MWCNTs with diameter 10-40 nm, we assigned to modes of the DNA/MWCNT composite layer. In these spectra, the presence of added DNA bases group was detected.

Optical reflectance spectroscopy measurements were used for detection of electronic transitions of MWCNT and MWCNT:DNA structures. From the UV-VIS-NIR (300-1000 nm) absorption spectra, obtained for MWCNT and DNA/MWCNT layers, the principal electronic absorption bands were evaluated (2.95, 3.06, 3.95, 3.33, 3.38 eV), The behavior of the absorption curve for the DNA/MWCNT layer is determined by the ratio of DNA and MWCNT volumes. The band gap of DNA/MWCNT is about 0.78-0.84 eV (Fig. 1).

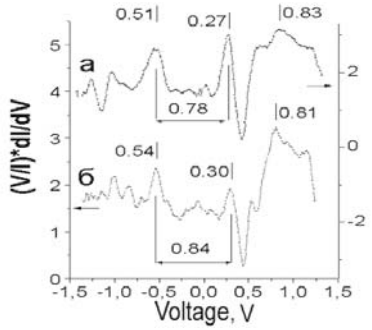

Figure 1. Current-voltage characteristics of DNA/MWCNT sample. (a) Pt tip, (b) Ir tip.

The current-voltage characteristics of metal (Pt/Ir) tip - DNA/MWCNT - metal (Pt/Ir) tip have the behaviour of a diode type. The value of the conductivity is determined by the ratio of the DNA and MWCNT volumes. The dependence of the normalized conductivity $(V/I)*dI/dV$ on V for the MWCNT, MWCNT/DNA structures was calculated.

Using these results, we assert that a system of electronic levels is self-formed at the (DNA+MWCNT) interface.

References

1. X. Zhao, Y. Ando, Y. Liu, M. Jinno, and T. Suzuki, Carbon nanowire made of a long linear carbon chain inserted inside a multiwalled carbon nanotube, *Phys. Rev. Lett.* 90, 187401 (2003).
2. A. Karlash, Ya. Shtogun, T. Veblay, A. Gorchinsky, O. Matyshevska, E. Buzaneva, M. Lositsky, S. Prylutska, and V. Yashchuk, Self-organized DNA molecules/carbon nanotubes layer: UV, IR-Spectroscopy, *Visnyk of Kyiv University, Series: Phys.-Math. Science* 2, 412-421 (2000).

MOLECULAR DYNAMICS OF CARBON NANOTUBE-POLYPEPTIDE COMPLEXES AT THE BIOMEMBRANE-WATER INTERFACE

KONSTANTIN V. SHAITAN,* YEGOR V. TOURLEIGH, DMITRIY N. GOLIK
Lomonosov Moscow State University, Dept. of Bioengineering

Abstract. Molecular dynamics simulation of a system consisting of a hydrated lipid bilayer, a nanotube with a cap at one end, and a polypeptide to be pushed through the membrane is reported. This construction is considered to be a delivery vehicle (nanosyringe) which drives the peptide to the membrane surface. Tuning the nanotube (by adding functional groups) one may achieve the selectivity of the nanotube landing area on the cellular membrane. The pressure expulsing the peptide could arise as a result of a chemical reaction that makes the reaction mixture volume increase in the nanotube. As an analogue of the explosive component, blowing Van der Waals spheres are proposed. Different regimes of the penetration are simulated.

Keywords: molecular dynamics; nanotubes; biomembranes; peptides; drug delivery

Methods of molecular dynamics currently are widely applied in the study of the most fundamental topics of natural sciences as well as in nanotechnology research. A molecular device able to selectively inject molecules through the cell membrane is described. This nanosyringe is a nanovehicle, which carries not too big molecules to the membrane (Fig. 1). The molecules are protected by the wall of a carbon nanotube. In the next step, the nanotube interacts with a receptor site on the membrane in accordance with the molecular tuning of the free end of the nanosyringe. Then, the active agent can be shot from the nanosyringe through the membrane structure. The nanosyringe is filled with an olygopeptide and a working medium, which is represented by an active compound increasing its volume due to a chemical reaction. As a model of the microexplosive agent, a set of Van der Waals spheres was taken. The spheres

*To whom correspondence should be addressed. Konstantin V. Shaitan, Bioengineering Department, Moscow State University, Leninskie Gory, 1/12, 119992, Moscow, Russia; e-mail: shaitan@moldyn.org

V.N. Popov and P. Lambin (eds.), Carbon Nanotubes, 233–234.

were enlarging their volumes at a certain rate. Some dynamical aspects of these processes are reported below.

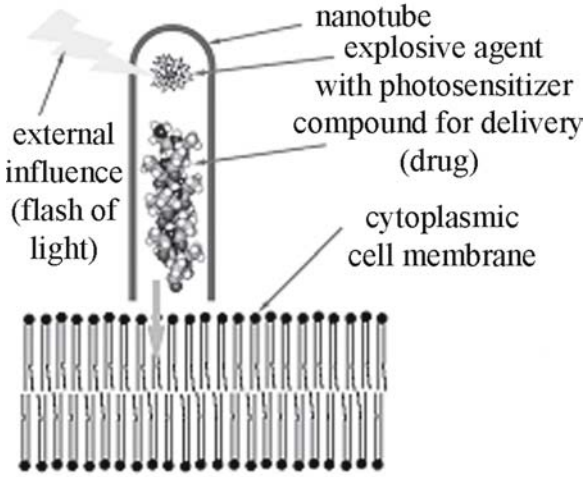

Figure 1. Scheme of the nanosyringe in action.

The uptake of the peptide to the nanotube is energetically favorable and can take place spontaneously. The time of self-assembly at 300 K was estimated as 40 microseconds. Under the shock action, the polyalanine alpha helix greatly changed the conformation (Fig. 2) and partially denaturated. In the model system, the delivery of a compound to the membrane under the action of a nanoexplosion turned out to be possible.

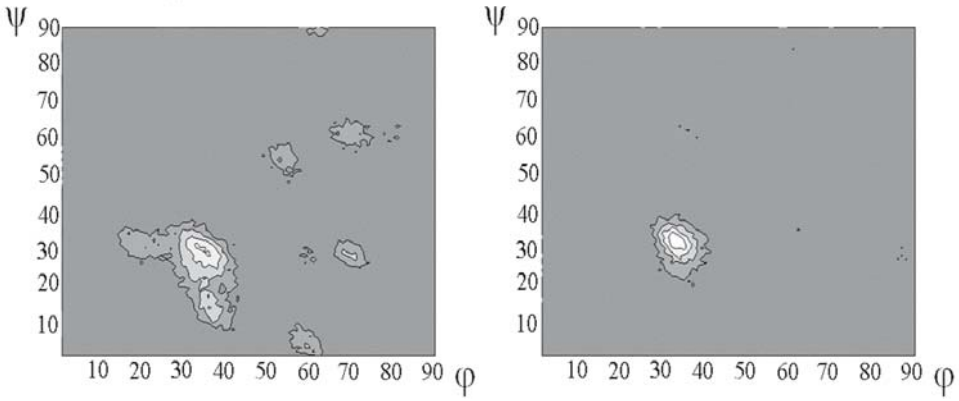

Figure 2. Poincare sections for the φ and ψ angles averaged over all polyalanine residues under the extrusion to the membrane at 13 ps (left) and 26 ps (right) from the beginning of the spheres enlargement.

THERMAL CONDUCTIVITY ENHANCEMENT OF NANOFLUIDS

A. CHERKASOVA, J. SHAN
Department of Mechanical and Aerospace Engineering, Rutgers, State University of New Jersey, 98 Brett Road, Piscataway, NJ 08854-8058, USA

Abstract. It has been recognized that nanofluids, a suspension of nanoparticles or nanotubes with size on the order of nanometers, can exhibit very unusual properties. The thermal conductivity of an individual single wall carbon nanotube is 5-10 times greater than that of very conductive materials such as aluminum or copper. It is not surprising that the thermal conductivity of nanofluids has been reported to be much higher then of their base fluid, even with very low particle concentration. The increase has been reported to have very strong temperature dependence and cannot be explained by existing macroscale theories. We report on initial experiments on the thermal conductivity of nanofluids consisting of different base fluids and a wide range of carbon nanotubes concentrations.

Keywords: nanotube; nanofluid; thermal conductivity enhancement

Since the discovery of carbon nanotubes (CNTs) in 1991, a growing realization of their remarkable properties has led to interest in their application to diverse areas, including high-strength materials, sensors, electronics, and fuel storage. Recent experiments have reported that carbon nanotubes greatly increase the thermal conductivity of fluids. For suspension consisting of distilled water (DW) and only 0.6% of multiwall CNTs (MWNTs), a 38% increase in thermal conductivity was reported.[1] At 1.0% volume fraction of MWNTs in DW, ethylene glycol (EG) and decene (DE) thermal conductivity enhancement of 7.0%, 12.7% and 19.6%, respectively, were reported.[2]

Although recent experiments on nanofluids have demonstrated enormous heat transfer enhancement, such increases cannot be explained by existing macroscale theories. All these models depend only on thermal conductivities of particles and base fluid and particle volume fraction, not on the particle size and the interface between particle and fluid. Although the conventional models can

V.N. Popov and P. Lambin (eds.), Carbon Nanotubes, 235–236.

be used with large particles, they under-predict the thermal conductivities of nanofluids.

The thermal conductivity of CNT suspensions in most previously reported experiments was measured by transient hot-wire method. To compare results obtained by different measurement techniques, we choose a parallel plate method to conduct our experiment. This method also allows us to avoid natural convection. The sample fluid was kept in the gap between two thin copper plates of the apparatus. An electric resistance heater producing a prescribed heat flux was placed on the upper plate. The temperature of the bottom plate was maintained constant by cooling or heating with water from thermal bath. The temperature difference across the nanofluid-filled gap was measured, and, the steady-state analytical solution of the heat conduction equation can be used to obtain the thermal conductivity of fluid.

Nanotubes are hydrophobic, aggregate easily and cannot be dispersed into many fluids.[3] To obtain well-mixed and stable solutions, some additional processing techniques, such as adding a surfactant or solution sonication should be used. Utilization of different types and concentrations of surfactant has a great impact on nanotubes dissolution. Different sonication techniques and times also have a great influence on preparing well-dispersed solution.

Preliminary experiments with 0.1% SWNTs in EG and water showed no measurable thermal conductivity enhancement. Multi-walled nanotube solutions of 0.6% in DW and EG showed large amounts of visible agglomerates after short sonication times. Longer sonication times can possibly break nanotubes to very short parts[1]. Further experiments are in progress to prepare stable, well-dispersed nanotube suspensions of MWNTs. Such nanofluids will be tested in our parallel-plate apparatus to provide comparison with previous measurements of thermal conductivity, and provide data for the development of a theoretical description of nanofluid thermal conductivity.

References

1. M. J. Assael, C.-F. Chen, I. Metaxa, W. A. Wakeham, Thermal Conductivity of Suspensions of Carbon Nanotubes in Water, Int. J. Thermophys. 25(4), 971-985 (2004).
2. H. Xie, H. Lee, W. Youn, and M. Choi, Nanofluids Containing Multiwalled Carbon Nanotubes and Their Enhanced Thermal Conductivities, *J. Appl. Phys.* 94(8), 4967-4971 (2003).
3. M. F. Islam, E. Rojas, D. M. Bergey, A. T. Johnson, and A. G. Yodh, High Weight Surfactant Solubilization of Single-Wall Carbon Nanotubes in Water, *Nano Lett.* 3(2), 269-273 (2003).

CARBON NANOTUBES AS ADVANCED LUBRICANT ADDITIVES

F. DASSENOY,* L. JOLY-POTTUZ, J. M. MARTIN
LTDS, Ecole Centrale de Lyon, 69134 Ecully cedex, France

T. MIENO
Shizuoka University, Department of Physics, 836 Ooya, 422-8529 Shizuoka, Japan

Abstract. Single wall carbon nanotubes (SWNTs) present interesting tribological properties under boundary lubrication at ambient temperature. Used as additives to polyalphaolefin (PAO) base oil, they lead to a drastic decrease of both friction and wear of antagonist steel surfaces. These results are obtained with only 1 wt% of nanotubes dispersed in oil but with a minimal contact pressure of 0.83 GPa indicating that a structural modification is necessary for such improvements. Characterization of nanotubes by analytical TEM and Raman spectroscopy before and after friction is used to understand how nanotubes behave in the contact area.

Keywords: Single wall carbon nanotubes; tribology; friction; wear; additives

SWNTs were prepared by electric arc technique.[1] Nanotubes grow in long bundles. Their mean diameter is close to 10 nm. Effect of nanotube concentration in PAO was studied with a pin on flat tribometer (pin and flat made of steel). Tests were performed in ambient air, at room temperature, with a sliding velocity of 2.5 mm/s.

Figure 1a shows the influence of the nanotube concentration on the friction coefficient for a contact pressure of 0.83 GPa. With 1 wt% and 2 wt%, a drastic decrease of 70 % of the friction coefficient was observed. The influence of the contact pressure on the friction coefficient (test performed with a dispersion of 1 wt% of nanotubes in oil) reveals that a minimal contact pressure of 0.83 GPa must be applied to reach a very low and stable friction coefficient (Fig. 1b). This suggests that the efficiency of SWNTs is due to structural changes induced by the friction. Addition of nanotubes in oil induces also a strong reduction of the wear of the rubbing surfaces which is three times smaller than that observed without nanotubes.

*To whom correspondence should be addressed. Fabrice Dassenoy; e-mail : Fabrice.Dassenoy@ec-lyon.fr

V.N. Popov and P. Lambin (eds.), Carbon Nanotubes, 237–238.

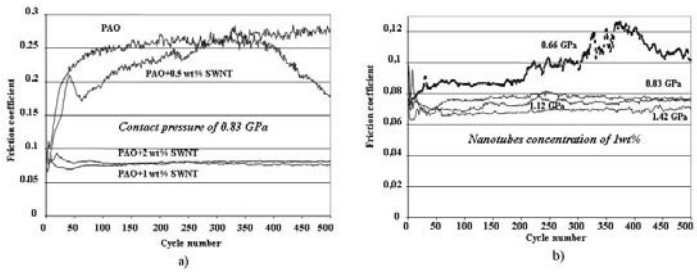

Figure 1. Influence of a) nanotubes concentration and b) contact pressure on the friction coefficient of the lubricant.

Wear particles collected from the pin and the flat were observed by TEM. Figure 2a shows the presence of amorphous carbon containing well-dispersed catalyst particles. The comparison of the Raman spectrum of the wear particles with that of the nanotubes (Fig. 2b) shows clearly the disappearance of the RBM modes at low frequencies and the growth of the D-band characteristic of disordered carbon.

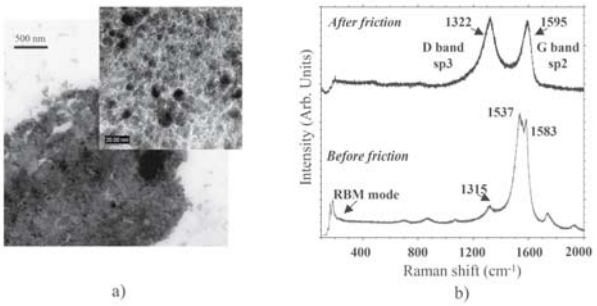

Figure 2. a) TEM images of carpet-like wear debris collected from the pin; b) Raman spectra (λ = 632.8 nm) obtained before friction on the SWNTs and after friction from wear debris.

These analyses prove the strong alteration of the SWNTs structure during the friction. The mechanism of lubrication by the nanotubes can be explained by a crushing of the nanotubes followed by a sliding under shearing. The wear reduction can be due to the formation on the antagonist surfaces of a protective amorphous carbon layer containing metallic particles of catalyst, similar to a Ni-doped DLC like material, well known for its good tribological properties.

References

1. C. Journet, W. K. Maser, P. Bernier, A. Loiseau, M. Lamy de la Chapelle, S. Lefrant, P. Deniard, R. S. Lee and J. E. Fischer, Large scale production of single-wall carbon nanotubes by the electric arc technique, *Nature* 388, 756 (1997).

SYNTHESIS AND CHARACTERIZATION OF IRON NANOSTRUCTURES INSIDE POROUS ZEOLITES AND THEIR APPLICATIONS IN WATER TREATMENT TECHNOLOGIES

MIROSLAVA VACLAVIKOVA,* MAREK MATIK, STEFAN JAKABSKY, SLAVOMIR HREDZAK
Institute of Geotechnics, Slovak Academy of Sciences, Watsonova 45, 043 53 Kosice, Slovakia

GEORGE GALLIOS
Lab. Gen. & Inorg. Chemical Technolgy, School of Chemistry, Aristotle University, GR-540 06 Thessaloniki, Greece

Abstract. A new sorbent with magnetic properties and anion removal ability has been produced by incorporating iron oxide based nanoparticles into the pores of zeolite crystals. The sorbent has been tested for the removal of arsenic (V) species from model aqueous solutions in batch–type equilibrium experiments. Good sorption was observed with maximum capacity of 73.32 mg of As per g of sorbent at pH 3.5.

Keywords: arsenic; iron oxides; nanoparticles; magnetically modified zeolite; sorption

Nanotechnology is developing fast, with much impact on a wide variety of technological areas. Inclusion of guests into a well-organized host matrix is a powerful method to form new nano-sized materials. Nanoporous and microporous crystals, such as molecular sieves (zeolites) are ideal hosts for accommodation of organic and inorganic molecules, polymer chains, etc., because of their uniform pore size and their ability to adsorb molecular species. It is well known that zeolites possess a negatively charged surface and are therefore good sorbents of cations. The modification of their surface can create localized functional groups with a good affinity to inorganic anions too.

* To whom correspondence should be addressed. Miroslava Vaclavikova, Institute of Geotechnics, Slovak Academy of Sciences, Watsonova 45, 043 53 Kosice, Slovakia; e-mail: vaclavik@saske.sk

V.N. Popov and P. Lambin (eds.), Carbon Nanotubes, 239–240.

Iron oxide magnetic nanoparticles were synthesized by co-precipitation of Fe(III) and Fe(II) in the presence of zeolite – clinoptilolite 40-60% with particle size 0.045-0.09 mm as described in Vaclavikova et al. (2004). The new magnetic sorbent produced was tested for the removal of As(V) species from model aqueous solutions in batch–type equilibrium experiments. The test conditions were: initial As(V) concentration 20–1000 $mg.L^{-1}$; sorbent dosage 2 $mg.L^{-1}$; pH 3.5; sorption time 24 h in a rotary shaker; analysis of As by AAS.

Figure 1 presents the adsorption isotherm for As (equilibrium concentration of As versus uptake). The solid line represents the Langmuir model and the dashed line represents the Freundlich model. The solid points represent the experimental data. Magnetically modified zeolite was found to be a good sorbent for arsenic oxyanions with sorption capacity calculated from Langmuir model to 73.32 mg As/g of sorbent. Both models Langmuir as well as Freundlich fit well the experimental data with coefficient of determination R^2 of 0.96 and 0.97 respectively.

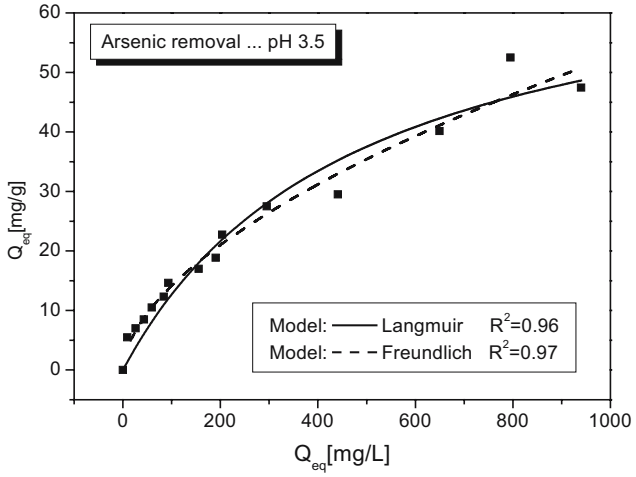

Figure 1. Sorption isotherm – As uptake by sorbent.

Research presented by this paper was supported by the Science and Technology Assistance Agency under the contract No. APVT-51-017104 as well as by the NATO Collaborative Linkage Grant EST.EAP.CLG 981103.

References

Vaclavikova, M., Jakabsky, S., Hredzak, S., 2004, Magnetic Nanoscale particles as sorbents for removal of heavy metal ions, in: Nanoengineered Nanofibrous Materials, NATO Science Series II, Mathematics, Physics and Chemistry, 169, Kluwer Academic Book Publishers, Dordrecht, Netherlands, Ed. S. I. Guceri, Y. Gogotsi, and V. Kuzentsov, pp. 479–484.

NANOSTRUCTURED CARBON GROWTH BY AN EXPANDING RADIOFREQUENCY PLASMA JET

S. I. VIZIREANU, B. MITU, R. BIRJEGA, G. DINESCU
National Institute for Lasers, Plasma and Radiation Physics, Bucharest, Romania

V. TEODORESCU
National Institute for Physics of Materials, Magurele, Bucharest

Abstract. Carbon deposition from acetylene injection into plasma jet onto sputtered nickel on silicon is investigated. The whole methodology, including the deposition of catalyst, its etching to islands followed by the carbon growth, is implemented in the same reactor. The investigation of structure and morphology shows the formation of nickel particles coated with graphitic layers.

Keywords: Nanostructured carbon; Nickel catalyst; expanding radiofrequency plasma; Plasma-enhanced vapour deposition (PECVD)

Several methods have been developed for synthesis of various forms of nanostructured carbon. The growth of nanostructured carbon using a radio-frequency (RF) plasma jet injected with acetylene, as a variant of PECVD technique, is described. The characteristics of the Ni layers are described by X-ray diffraction (XRD) and atomic force microscopy (AFM). The structured carbon on the Ni catalyst is characterized by AFM and TEM.

A setup[1] consisting of expanding RF plasma jet (vertically) and a small size magnetron source (laterally) were combined into the same reactor. The Si substrates were treated 10 min at 700 °C in ammonia plasma and exposed up to 5 min to the magnetron sputtering source. After cooling down to room temperature and re-heating at 700 °C, an additional ammonia plasma treatment was performed to insure the fragmentation of Ni film and creation of catalytic islands.[2] For the carbon deposition, the argon RF plasma jet, generated at 200 - 400 W power, was injected with acetylene and ammonia gas at various flow ratios.

The deposition rate for the Ni films was 10 nm/min. Films with thickness in the range 50-60 nm were deposited. In Fig. 1a, the XRD diffractograms of a

V.N. Popov and P. Lambin (eds.), Carbon Nanotubes, 241–242.

thermally treated and additionally ammonia etched Ni films indicate that nickel crystallites are formed. The grain size of the sample additionally etched in ammonia plasma was almost half of that obtained for only thermally treated sample (decrease from 29 to 16 nm), while the new sharp peak appearing at 2θ = 47.3° indicated the silicide presence.

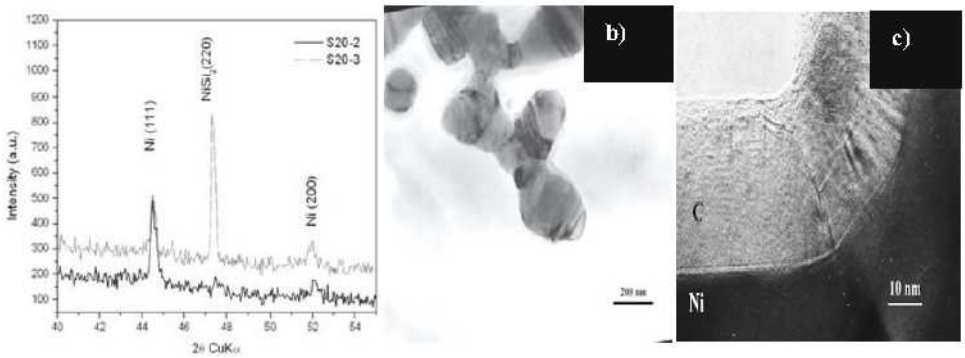

Figure 1. (a) Diffractograms of the Ni covered substrates: (S20-2) thermal and (S20-3) thermal and ammonia treatment. TEM images of Ni particles encapsulated in graphitic layers (b) and detail showing the graphitic structure with the graphene sheaths spaced by 0.34 nm and parallel to the surface (c).

The AFM investigation of Ni covered Si (Rrms ~ 10 nm) and carbon covered Ni show the increasing of the roughness (Rms~30 nm).

Material scratched from the carbon coverd Ni was investigated by TEM. Particles consisting of a dense core, completely surrounded by a less dense sheath of material (Fig. 2b), were observed. The high magnification image (Fig. 2c) proves that the dense core is formed from Ni, which is encapsulated in nanostructured graphitic layers, aligned to the metal surface and having almost 30 nm thickness.

Carbon nanotubes are not formed under the present conditions. This is caused by the large dimension of the Ni islands and the strong adhesion force with the Si substrate enhanced by the nickel silicide formation.[2]

References

1. S. I. Vizireanu, B. Mitu, and G. Dinescu, Nanostructured carbon growth by expanding rf plasma assisted CVD Ni-coated silicon substrate, *Surface & Coatings Technology* 200(1-4), 1132-1136 (2005).
2. I. K. Song, W. J. Yu, Y. S. Cho, G. S. Choi, and D. Kim, The determining factors for the growth mode of carbon nanotubes in the chemical vapour deposition process, *Nanotechnology* 15, S590-S595 (2004).

DESIGN AND RELATIVE STABILITY OF MULTICOMPONENT NANOWIRES

TRAIAN DUMITRICĂ
Department of Mech. Engineering, University of Minnesota
VERONICA BARONE, MING HUA, BORIS I. YAKOBSON
Center for Nanoscale Science and Technology, Rice University

Abstract. The stability of free standing hexagonal Sc silicide wires is discussed based on *ab-initio* calculations. It is shown that Sc presence dramatically increases stability.

Keywords: nanowires; silicides; nanotubes

Nearly 1D forms of matter, nanotubes (NT) and nanowires (NW), attracted interest due to potential applications in nano-electronics. While C forms narrow NT (with diameters as small as 3 Å), another critical element, Si, can form NW with diameters one order of magnitude larger. A new class of epitaxial growth experiments (Chen et al., 2000) produced subnanometer height NW of Si combined with metal (Sc, Er, Dy). Besides introducing novel optical, electric, or magnetic properties, we argue that metal (M) addition has a major role in the NW stability as this report will show.

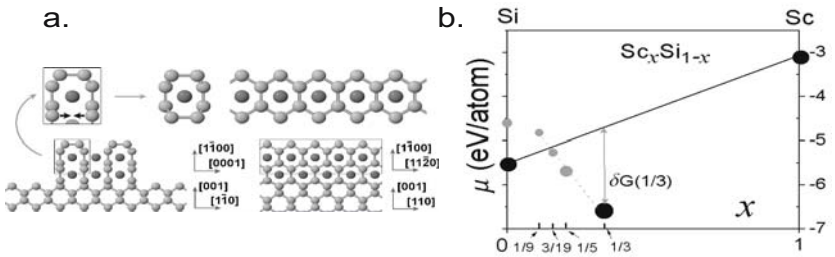

Figure 1. a) Bottom shows axial (left) and side (right) views of a two--monolayer high Sc (dark ball) @ Si (gray ball) NW grown on the Si substrate. Upper inset contains a Si substrate. Upper is a detail of framed portion, which upon detachment gives the (2,2) Sc@Si NW. b) E_c function of Sc fraction x. Gray dots are NW, black ones are bulk Si(x = 0), $ScSi_2$ (x = 1/3), and Sc (x = 1).

V.N. Popov and P. Lambin (eds.), Carbon Nanotubes, 243–244.

Calculations were performed with density functional theory within the local density approximation using GAUSSIAN03 (Frish et al., 2003). Imposing proper periodic boundary conditions we optimized: three Sc@Si NW cut from $ScSi_2$ bulk, a chain of fullerenelike Si_{20} clusters, along with bulk Si (diamond), $ScSi_2$ (hcp), and Sc (hcp). Obtained NW cohesive energies (Table 1) vary as $E_c = -7.96x - 3.93$ eV/atom with the Sc fraction $x \in [1/9, 1/3]$.

The decisive role of Sc addition is most evident in the thinnest attainable form of Si (Dumitrică et al., 2004), Fig. 1a (upper panel). The shell Si structure, isomorphic to a properly rescaled (2,2) CNT, would be unstable without the extra bonding provided by the axially placed Sc atoms. Connection with the experimental NW is shown in Fig. 1a (bottom). The framed portion of the Sc-silicide, if lifted off would make exactly a (2,2) Sc@Si NW. Following the same logic we designed the other two Sc@Si NW, the one-monolayer height Sc_3Si_{16} (or $x = 3/19$) and two-monolayer height Sc_6Si_{24} (or $x = 1/5$).

To compare NW with different x one must lay down a proper criteria. We propose comparing the Gibbs free energies of formations $\delta G(x) = E_c(x) - x\mu_{Sc} - (1 - x)\mu_{Si}$. The constituent chemical potentials, μ_{Sc} and μ_{Si}, depend on the experimental conditions. In the diagram of Fig. 1b we set them at the bulk values, E_c[Si] and E_c[Sc]. Bulk $ScSi_2$ appears most stable as the line of positive slope E_c[Sc] – E_c[Si] clears above the $ScSi_2$ point with $\delta G(1/3) = -1.9$ eV/atom. Moving to Sc@Si NW, δG increases and changes sign, indicating that NW become less stable as they get narrower. The thinnest (2,2) Sc@Si NW is the weaker in this series, with $\delta G(1/9) = 0.41$ eV/atom. However, when this NW is compared with the chain of Si_{20} clusters of similar thickness and having $\delta G(0) = 0.93$ eV/atom, the advantage of Sc addition becomes evident.

Work carried out at the University of Minnesota Supercomputing Institute.

Table 1. Cohesive energies E_c (eV/atom) for the computed NW and bulk structures.

	NW				Bulk		
Unit cell	$ScSi_8$; Sc_2Si_{16}	Sc_3Si_{16}	Sc_6Si_{24}	Si_{30}	Si_2	$ScSi_2$; Sc_2Si_4	Sc_2
x	1/9	3/19	1/5	0	0	1/3	1
E_c	–4.82; –4.84*	–5.23	–5.65	–4.57	–5.50	–6.59; –6.65*	–3.06

*Spin multiplicity is 2. In the rest of the calculation, it was taken 1.

References

Chen, Y., Ohlberg, D. A. A., Ribeiro, G. M., and Chang, Y. A. (2000), *Self-assembled growth of epitaxial erbium disilicide nanowires on silicon* (001), Appl. Phys. Lett. 76: 4004.

Dumitrică, T., Hua, M., and Yakobson, B. I. (2004), *Endohedral silicon nanotubes as thinnest silicide wires*, Phys. Rev. B (R) 72: 241303.

Frisch, M. J. (2003), *Gaussian 03 Revision A.1* (Pittsburgh PA).

MODELING OF MOLECULAR ORBITAL AND SOLID STATE PACKING POLYMER CALCULATIONS ON THE BI-POLARON NATURE OF CONDUCTING SENSOR POLY(P-PHENYLENE)

IOANNIS RABIAS,* PANAGIOTIS DALLAS, DIMITRIOS NIARCHOS
Institute of Materials Science, NCSR "Demokritos", 15310 Athens, Greece

Abstract. From the large class of poly-conjugated aromatic polymers which upon doping with electron donors or electron acceptors display metallic conductivities, poly (p-phenylene) is one of the experimentally most investigated systems. This work reports on a combined theoretical investigation of their solid state packing structure of oligomers of poly (p-phenylene). The influence of the torsion angle along the chains has been well documented as having an effect on the electronic and geometric structure of oligomers of poly (p-phenylene). A study of ionization potential, band width and energy gap was performed as a function of the torsion angle along the chains. It demonstrates the evolution of the electronic properties, which are of interest in the conducting polymer area. The coplanar conformation is obviously the ideal for the pi-overlap and therefore maximum conductivity.

Keywords: ab-initio calculations; solid state packing calculations; poly(p-phenylene)

Molecular Orbital Calculations were performed on MOPAC V6.0 and Gaussian 94 using the QM Utilities interface of Molecular Simulations CERIUS[2] package. Initial models of poly(p-phenylene) oligomers were constructed[1] using the 3D-Builder module of CERIUS[2]. Gaussian calculations using a 3-21G basis set were performed on neutral benzenoid $(PP)_n$ and quinonoid $(QPP)_n$ oligophenyls for n = 2–11 in the gas phase. A schematic structure of the oligomer for the case n = 7 is shown in Figure 1.

Calculations on the evolution of the carbon-carbon bond length between the rings as a function of the torsion angle were performed at the *ab-initio* 3-21G and AM1 and PM3 level on the oligomers. All subsequent analysis of the

*To whom correspondence should be addressed. Ioannis Rabias; e-mail: irabias@ims.demokritos.gr

V.N. Popov and P. Lambin (eds.), Carbon Nanotubes, 245–246.

calculations was also performed with the QM Utilities to visualize the eigenvalues and eigenvectors. The atomistic calculations were used to provide parameters for the solid-state calculations. The molecules considered contained a number of phenyls ranging from $n = 2$ to $n = 11$.

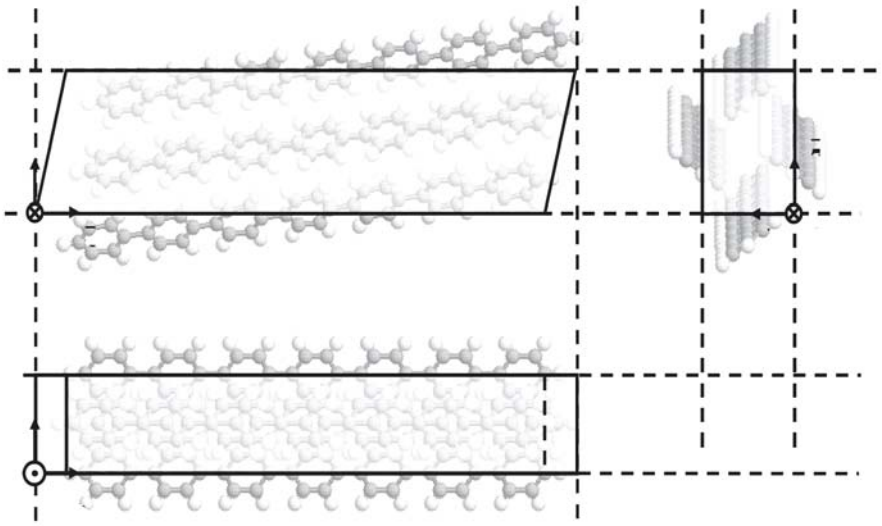

Figure 1. Representation of the monoclinic crystalline cell of planar septiphenyl.

By considering the series of neutral oligophenyls nPPP and model molecules QnPPP, a distinct energy difference between the oligophenyls was observed in the gas phase calculations. The energetic reason for this behaviour lies in the substantially larger energy difference between benzenoid and quinonoid valence isomers in the case of the gas phase PPP series. Because of this larger energy difference, it is energetically more unfavourable to sustain the quinonoid structure over a larger spatial region. The trends in the ionisation potential, band width and energy gap were studied as a function of the torsion angle along the chains and demonstrated the evolution of electronic properties. As the torsion angle between adjacent rings increases, the ionisation potential and band gap values increase and the bandwidth of the highest occupied bands decreases.

References

1. Rabias, I., Howlin, B. J., Provata, A., and Theodorou, D., Modelling of Structural and Vibrational Properties of Poly(p-phenylene), 2000, *Mol. Simul.* **24:**95-109.

ND:LSB MICROCHIP LASER AS A PROMISING INSTRUMENT FOR RAMAN SPECTROSCOPY

VADIM PARFENOV*
SE Laser Physics, Res.Ctr. "Vavilov State Optical Institute", St.Petersburg 199034, Russia

Abstract. A compact diode-pumped Q-switched Nd:LSB microchip laser was developed for use in Raman spectrometers. In the paper, the performance of the laser and results of its application for spectrometric analysis of carbon nanotubes are reported.

Keywords: Raman spectroscopy; lasers; diode-pumped lasers; Nd:LSB microchip laser; carbon nanotubes

One of effective methods of investigation of carbon nanostructures is the Raman scattering spectroscopy (RSS), which can be used, in particular, for *in situ* analysis of the growth of carbon nanotubes. Presently, compact, reliable and low-cost lasers generating in the visible range of spectrum are needed for the RSS spectroscopy in order to replace the previously used ion (Argon and Krypton), He-Ne, copper-vapor and dye lasers, which have limited power and lifetime, and long warm up time.

Among the most promising modern lasers, that can be used in Raman spectrometers, are the so-called microchip lasers based on Nd-doped crystals. The microchip lasers are small, robust, compact, high-performance, diode-pumped, all-solid-state lasers that can be manufactured in large quantity at low cost. The main advantage of the microchip lasers is that they can provide a very high peak power with a diffraction limited output beam in case of the generation in the Q-switched regime.

We developed a compact, high-effective, 100 mW passively Q-switched Neodymium-Lanthanum-Scandium-Borate (Nd:LSB) microchip laser that emits at the wavelength of 531 nm. This laser was built using an original All-in-One laser technology, which allows one to put the pump laser diode, gain medium

*To whom the correspondence should be addressed. Vadim Perfenov; e-mail: vadim_parfenov@mail.ru

V.N. Popov and P. Lambin (eds.), Carbon Nanotubes, 247–248.

and saturable Q-switched absorber in one miniature package that provides a very high compactness of the laser (Fig. 1).

Pumped with a 1-W CW diode laser, our microchip laser produces short pulses (in the range of 5-20 ns depending on the pump power level), high peak power (up to about 1-5 KW), repetition rate of 5-50 KHz, and it has excellent beam quality ($M^2 < 1.4$) and spectral bandwidth of about 6 cm^{-1}.

The laser was applied for investigation of carbon nanotubes as an exciting light source in the Raman spectrometer. Measured spectra of single-wall carbon nanotubes are shown in Fig. 2. The results of these experiments allow to draw the conclusion that the Nd:LSB microchip laser is a very promising instrument for Raman spectroscopy.

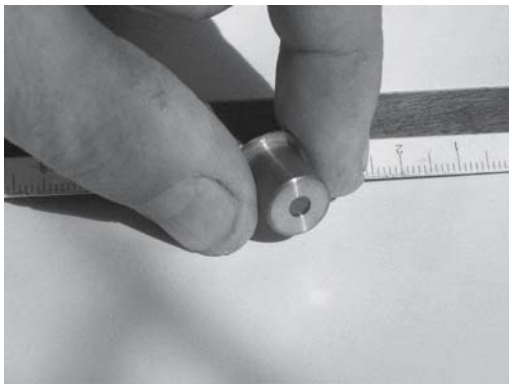

Figure 1. General view of Nd:LSB microchip laser.

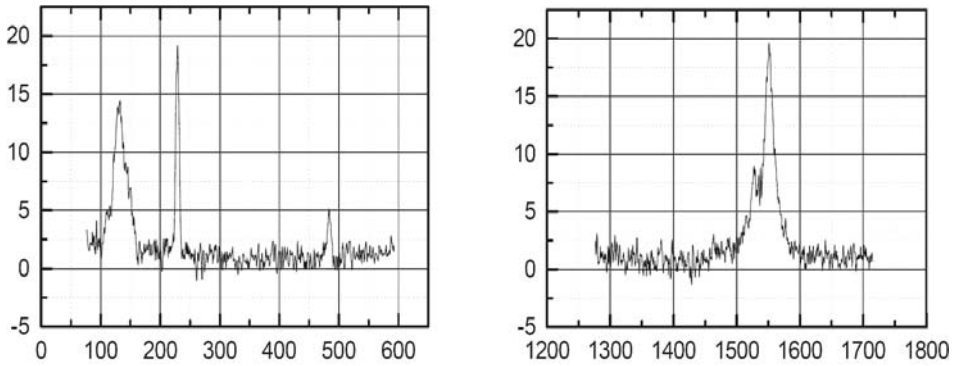

Figure 2. Raman spectra of nanotubes (Raman intensity in arb. units against the wavenumber in cm^{-1}) measured with Nd:LSB microchip laser.

The author would like to thank Dr. K. El'tsov (Institute of General Physics, Russian Academy of Sciences, Moscow) for providing the results of the Raman spectroscopy analysis of carbon nanotubes carried out using the Nd:LSB microchip laser described above.

SUBJECT INDEX

Ab-initio techniques, 70, 76, 84, 85, 107, 150, 152, 153, 155−157, 159, 164, 187, 194, 195, 198−201, 204, 206, 207, 209, 243, 245
AFM, 44, 121, 122, 136, 180, 212, 241, 242
Chemisorption, 65, 187, 188, 189
Composite materials, 9, 19, 57, 66, 69, 77, 80, 211, 221, 223−228, 232
CVD, 1, 43, 44, 47, 49, 53, 57, 59, 60, 63, 64, 122, 136, 242
CCVD, 45
PECVD, 55, 56, 60, 241
Defects, 8, 14, 19, 20, 28, 35, 37, 49, 50, 75, 94, 95, 101, 124, 131, 133, 143, 149, 174, 179, 180, 184, 186, 204, 205, 215
Diffraction, 9, 11, 43, 44, 122, 241, 247
DMA, 224
DNA, 230, 231, 232
Doping, 13, 30, 89, 94, 95, 108, 110, 144, 153, 154, 169, 170, 230, 245
EELS, 47
Electric arc discharge, 1−4, 15, 26, 49, 237
Electrochemistry, 57, 144, 164
Exciton, 171, 211
Fibers, 49, 50, 66, 216, 227, 228
Field emission, 111
Filling, 3, 12, 28, 101, 108, 110, 114, 188, 193
Fluorescence, 171, 172, 211
Functionalization, 38, 111, 144, 170, 183, 199
Gas adsorption, 187, 191
Helicity, 20, 29, 30, 34, 43, 44, 90, 99, 100, 121, 122, 138, 201
LASER ablation, 1−4, 6, 9, 15, 16, 29, 49, 101, 136
Lithography, 43, 50, 55
Mechanical properties, 50, 57, 201, 215, 216, 221, 223, 226, 227
Nanoelectronics, 19, 39, 143
Nanowire, 67, 192, 193, 207, 231, 243
NMR, 89, 114, 115, 119, 206
Optical properties, 140, 178
Optical spectroscopy, 9, 13, 130, 169, 170, 174
Peapods, 38, 89, 110−112, 119
Phonon, 14, 69, 73−78, 80, 83−87, 90−92, 95−97, 102, 108, 109, 112, 119, 131, 133, 149
Physisorption, 67, 144, 155, 187−189, 192, 194, 195
Plasmon, 177, 178
Purification, 9, 11, 12, 15, 63, 64, 169, 225
Raman scattering, 9, 14, 15, 45, 46, 74−76, 84−87, 89−106, 108−116, 119, 121, 122, 130, 197, 210, 231, 237, 238, 247, 248
Schottky barrier, 136, 180
Sensor, 69, 111, 144, 194, 229, 230, 235, 245

Separation, 2, 30, 45, 76, 85, 126, 127, 140, 177, 178, 204
Simulation techniques, 67, 77, 187, 195, 200, 201, 209, 215, 219, 233
Solubility, 53, 183, 223
STM, 19, 21−29, 31−38, 136, 167, 168
STS, 19, 21, 24, 26−30, 34, 36, 38, 130
TEM, 9, 11, 14, 19, 34, 43−50, 53, 54, 65, 110, 111, 212, 231, 237, 238, 241, 242
HRTEM, 44, 62
Tight-binding approach, 28, 33, 35, 36, 67, 69, 70, 76, 79, 81, 88, 107, 111, 116, 117, 123, 130, 144, 149, 151, 155, 157, 159, 201
Transistor, 134, 136, 138, 144, 165, 180, 217
Transport properties, 9, 10, 28, 43, 46, 77, 78, 123, 124, 131−133, 136, 139, 143−147, 149, 153, 155, 170, 183, 194, 201, 204, 219, 232, 235, 236, 245
XRD, 241, 242

AUTHOR INDEX

Alvisi, M., 59
Angelucci, R., 61
Anzlovar, A., 225
Arato, P., 221
Avramova, K., 219
Balázsi, C., 221
Barone, V., 243
Behler, K. D., 45
Belova, E., 215
Bergin, S. D., 211
Bichara, C., 67
Birjega, R., 241
Biró, L. P., 19, 53, 167, 221
Blau, W. J., 211, 223
Blighe, F. M., 223
Bonnot, A.-M., 47
Borondics, F., 169
Bouchiat, V., 47
Brandl, W., 227
Brichka, S., 65
Carbone, D., 57
Casella, M., 51
Caudillo, R., 49
Cech, J., 1
Cerullo, G., 171
Cherkasova, A., 235
Chernozatonskii, L. A., 215
Chirila, V., 227
Chung, S., 177
Coleman, J. N., 211
Collins, Ph. G., 179
Corticelli, F., 61
Cuffiani, M., 61
Czigány, Z., 221
Dallas, P., 245
Darabont, A., 53
Dassenoy, F., 237
Daykova, E., 209
De Riccardis, M. F., 57
Dettlaff, U., 1
Dikonimos Makris, Th., 57, 59
Dimovski, S., 45
Dinescu, G., 241
Drury, A., 211
Dumitrică, T., 243
D'yachkov, P. N., 181
Engstler, J., 63
Fanetti, M., 51
Fiawoo, M.-F., 47
Forro, L., 183
Gadermaier, C., 171
Galibert, J., 183
Gallios, G., 239
Gambetta, A., 171
Gavioli, L., 51
Giordani, S., 211
Giorgi, L., 59
Giorgi, R., 57, 59
Gogotsi, Y., 45
Goldsmith, B., 179
Golik, D. N., 233
Guerri, S., 61
Haluska, M., 1
Hornbostel, B., 1
Horváth, Z. E., 53
Hredzak, S., 239
Hua, M., 243
Hulman, M., 89

Iaia, A., 47
Iclanzan, T., 227
Iliev, H., 213
Jakabsky, S., 239
Joly-Pottuz, L., 237
José-Yacaman, M., 49
Kamaras, K., 169
Kasztovszky, Z., 221
Katok, K., 65
Kertész, K., 53
Kholmanov, I. N., 51
Khrutchinskii, A. A., 175
Kiricsi, I., 221
Kolomiyets, D. G., 231
Kónya, Z., 221
Koós, A. A., 53
Kovats, E., 169
Kövér, Z., 221
Ksenevich, V. K., 183
Kuzmany, H., 89
Kuznetsova, G. M., 173, 185
Lambin, Ph., 19, 69., 123
Lanzani, G., 171
Latil, S., 143
Leahy, R., 223
Li, F.-Y., 213
Lisi, N., 57
Lisi, N., 59
Loiseau, A., 43, 47
Lykah, V., 217
Makaev, D. V., 181
Maksimenko, S. A., 175
Maksimova, N. I,. 63
Malesevic, A., 55
Man, H. T., 43
Manzoni, C., 171
Marginean, G., 227
Marinsek, M., 225
Márk, G. I., 167
Marques, M. A. L., 49
Martin, J. M., 237
Matik, M., 239
Mayer, A., 167
Meneghetti, M., 171
Menna, E., 171
Meunier, V., 123
Meyer, J. C., 121
Mhuircheartaigh, É. N., 211
Michel, Th., 121
Mieno, T., 237
Mihailovic, D., 225
Milchev, A., 219
Mišković, Z. L., 177
Mitu, B., 241
Morpurgo, A., 43
Mowbray, D. J., 177
Nemes Incze, P., 53
Nemilentsau, A. M., 175
Niarchos, D., 245
Ogloblya, O. V., 173, 185
Osváth, Z., 53
Paillet, M., 121
Pailloux, F., 43
Parfenov, V., 247
Pejovnik, S., 225
Pekker, A., 169
Pekker, S., 169
Pellenq, R. J. M., 67
Pfeiffer, R., 89
Pisov, S., 209
Poncharal, Ph., 121
Popov, V. N., 69
Preusche, D., 43
Prikhod'ko, G., 65
Proykova, A., 187, 209., 213
Rabias, I., 245
Rizzo, A., 59
Rizzoli, R., 61
Roche, S., 143
Roth, S., 1, 121
Roussel, Th. J., 67
Rubio, A., 49

Ruether, M., 223
Salernitano, E., 57, 59
Samuilov, V. A., 183
Sancrotti, M., 51
Sárközi, Z., 53
Sauvajol, J.-L., 121
Schneider, J. J., 63
Shaitan, K. V., 233
Shan, J., 235
Simon, F., 89
Slepyan, G. Ya., 175
Strunk, C., 43
Syrkin, E. S., 217
Tapasztó, L., 53, 167
Teodorescu, V., 241
Tertykh, V., 65
Thibault, J., 47
Thune, E., 43
Tourleigh, Y. V., 233
Triozon, F., 123, 143
Troiani, H. E., 49
Umek, P., 225
Vaclavikova, M., 239
Van Haesendonck, C., 55
Vanhulsel, A., 55
Vaseashta, A., 229
Veronese, G., 61
Vértesy, Z., 53, 221
Vizireanu, S. I., 241
Vrbanic, D., 225
Wéber, F., 221
Yakobson, B. I., 243
Ye, H., 45
Zahab, A., 121